

https://dspace.org/

Additive Manufacturing of Tungsten Carbide cemented in a Nickel-alloy binder utilizing the Laser Engineered Net Shaping (LENS®) process

Davoren, Brandon

2020
https://hdl.handle.net/10539/30897

Downloaded from a DSpace repository. https://dspace.org/

Additive Manufacturing of Tungsten Carbide cemented in a Nickel-alloy binder utilizing the Laser Engineered Net Shaping (LENS®) process



Brandon Davoren

A thesis submitted to the Faculty of Engineering and the Built Environment, University of the Witwatersrand, Johannesburg, in fulfilment of the requirements for the degree of Doctor of Philosophy in Engineering.

August 2020

Declaration

I declare that this report is my own work. It is to be submitted for the Doctor of Philosophy in Engineering at the University of the Witwatersrand, Johannesburg. This report has never been submitted before for any degree or examination in any other University

Student Name: Brandon Davoren; Student No.:1728622

Student Signature:_____

Abstract

Additive manufacturing is the keystone of what has been termed the 4th industrial revolution. With this prestigious title comes the need for additive manufacturing technologies to be applied to new material combinations to advance that which is possible by conventional manufacturing processes. Laser Engineered Net shaping (LENS®), a powder blown additive manufacturing process, was used to develop a process to deposit WC-9.2 wt.% Monel 400. A design of experiments matrix was successfully utilized to produce thin wall depositions which, with the application of ANOVA regression, were used to determine the best starting parameters for further refinements. Alterations to the laser beam power, laser beam spot size, z-increment, hatch overlap percentage, powder feed rate, traverse speed and stage temperature were all used to obtain an optimal parameter set. The lowest porosity of 2.5% was obtained using a laser beam power of 220 W, traverse speed of 4.5 mm/s, powder feed rate of 11.9 g/min, hatch overlap of 50% and a z-increment of 0.4 mm, with the 2.5% porosity contribution being attributed due to lack of fusion and oxygen entrapment during deposition. Multiple microstructures were observed with eutectic, fishbone and Fe/W-rich dendrites present in the fusion zone, needle-like, triangular and blocky carbides in the central region and acicular in the top region. These variations in the microstructure resulted in a gradient hardness profile from the substrate to the top layer as the grain size refined. The LENS® process was also successful in the fabrication of drill bits, which were tested against a commercially available drill bit in terms of hole circularity, hole depth, and hole diameter. The fabricated drill bits did not compare well to the commercial drill bit and had tip failure in all the tested cases due to regions of lack-of-fusion porosity which caused weakness in the component, but with further refinement with an emphasis on product development a LENS® fabricated drill bit can be competitive with a commercially manufactured drill bit. This study showed that with a well structured design of experiments and a mathematical parameter refinement process, the LENS® process can be applied to any novel cemented carbide combination with the focus on the feasibility of producing commercial components.

Acknowledgements

I would like to express my deepest gratitude to the following people, who assisted me throughout the course of this project.

Prof. Natasha Sacks, who supported me and supervised this project and who encouraged me to attend international conferences which gave me a wonderful opportunity to publish and share my work with other scientists in the field.

Ms. Maritha Theron, for her supervision, helpful discussions and practical assistance.

Prof. Josias Van Der Merwe, for his supervision.

The **Department of Science and Innovation** and the **National Research Foundation** in South Africa for financial support.

To the **Centre of Excellence in Strong Materials** (CoE-SM), for financial support.

The **National Laser Centre (NLC)** at the Council for Scientific and Industrial Research (CSIR) is acknowledged for use of the LENS® machine as well as technical support.

The **Microscopy and Microanalysis Unit** at the University of the Witwatersrand is acknowledged for use of microscopy equipment.

Brayner Nelwalani for assistance with FESEM imaging and **Gerrard Peters** for SEM assistance.

Dr. Rudolph Erasmus for assistance with the Raman spectrum acquisitions.

My family for their love, support and constant encouragement.

Table of Contents

Declaration ii

Abstract iii

Acknowledgements iv

List of Acronyms vii

List of Figures viii

List of Tables xiii

Chapter 1 Introduction 1

1.1 Background and motivation for research 1

1.2 Research aim and objectives 4

1.3 Contribution to knowledge 4

1.4 Structure of the thesis 5

Chapter 2 Literature Review 6

2.1 Cemented tungsten carbides 6

2.2 Additive Manufacturing of Cemented Tungsten Carbides 16

2.3 LENS® Process 19

2.4 LENS® of Cemented Tungsten Carbides 29

Chapter 3 Experimental Procedures 42

3.1. Feedstock Powders 42

3.2 LENS® production of alloys 47

Chapter 4 Results and Discussion 61

4.1. Design of Experiments: Thin Walls 61

4.1.1 Height Analysis 65

4.1.2 Width Analysis 69

4.2 Parameter refinement: Cubes 73
4.3 Hardness 82
4.3.1 Design of Experiments: Thin walls 82
4.5.2 Cubes 86
4.5.3 Crack analysis 91
4.4 Microstructural Characterisation 95
4.4.1 XRD 95
4.4.2 Microstructure 102
4.4.3 Raman Spectroscopy 130
4.5 Drill bit 133
Chapter 5 Conclusions 153
Chapter 6 Recommendations for Future Work 156
References 157
Appendix A 198
Research Outputs 198

List of Acronyms

AM-Additive Manufacturing

ANOVA- Analysis of Variance

EDS- Energy Dispersive Spectroscopy

EPMA- electron probe microanalysis

FESEM- Field Emission Scanning Electron Microscopy

LENS®-Laser engineered net shaping

TEM-Transmission Electron Microscopy

WC- Tungsten Carbide

WDS- Wavelength Dispersive Spectroscopy

XRD- X-ray diffraction

List of Figures

Fig. 1.1 :Different methods of additive manufacturing [15]. 2

Fig. 2.1: Phase diagram for W and C [69]. 7

Fig. 2.2: Schema of WC grain shape in Co binder (left) and the atomic structure of WC crystal (right) [78]. 8

Fig. 2.3: Corrosion rate of Ni based and Co based cemented carbides for various pH values [160]. 11

Fig. 2.4: Phase diagram of W-C-10%Ni (left) and Ni-Cu [162] [163]. 14

Fig. 2.5: Schematic of the LENS® process [204] and a layer-by-layer CAD model example. 20

Fig. 2.6: NSTF trophy produced by CSIR (left) and impeller produced by Sandia Laboratories (right)..... 21

Fig. 2.7: Schematic describing the formation mechanism of W-rim/Cu-core structure [244]. 24

Fig. 2.8:The effect of G and R on the solidification morphology and size [126]. 25

Fig. 2.9: Influence of laser power on sample height [284]. 31

Fig. 2.10: Influence of powder feed rate on sample height [284]..... 32

Fig. 2.11: (a)-(d) Change in sample height and profile with an increase in powder feed rate for WC-13wt%Co [60]. 32

Fig. 2.12: Influence of traverse speed on sample height [284]..... 33

Fig. 2.13: Influence of traverse speed on sample height and profile: (a) 4.2 mm/s, (b) 6.4 mm/s, (c) 10.6 mm/s [284]. 33

Fig. 2.14: SEM SE images of nanocrystalline WC-10%Co powder..... 35

Fig. 2.15: A thermal image of a WC-Co thick-walled sample looking from the deposition of layer 5 [286]. 38

Fig. 2.16: Temperature profile in selected deposition layers [286]. 39

Fig. 2.17: Life-cycle of a WC-Co cermet product manufactured by either the P/M or the LENS® process [287]. 40

Fig. 3.1: Size distribution of a) WC Powder b), Monel 400, c) WC-9.2wt% Monel 400 43

Fig 3.2: SEM micrographs of the a) tungsten carbide, b) surface of WC particle, c) cross-section of cast WC particle and d) Monel powder. 45

Fig. 3.3: XRD pattern of the mixed WC-9.2wt%Ni feedstock powder..... 47

Fig. 3.4: Framework for component fabrication from novel binder. 48

Fig. 3.5: a) general schematic for cubic structure and b) as-deposited cube and 52

Fig. 3.6: Representation of the region used to quantify porosity. 55

Fig. 3.7: a) CAD model of drill bit and b) diagram indicating a perfect circle fitted to a hole drilled by the purchased drill bit. 59

Fig 4.1: Calibration curve for LENS® hopper rpm to g/min. 62

Fig 4.2: Design of experiments' thin walls (left) and single thin wall (right). 62

Fig. 4.3: Average height as a function of laser beam power and powder feed rate at traverse speeds of 2 mm/s, 3 mm/s and 4 mm/s. 65

Fig 4.4: Residuals plot from ANOVA analysis. 67

Fig. 4.5: Optimization of powder feed rate for parameter set. 68

Fig. 4.6: Average width as a function of laser beam power and powder feed rate at traverse speeds of 2 mm/s, 3 mm/s and 4 mm/s. 69

Fig. 4.7: Residuals plot from ANOVA analysis. 71

Fig. 4.8: Minimum wall width with optimized traverse speed. 72

Fig. 4.9: Porosity of cubes a) 1, b) 2, c) 5, d) 6, e) 7, f) 8, g) 9, h) 11, i) 12, j) 14 73

Fig. 4.10: Porosity of cubes a) 15, b) 17, c) 18, d) 19, e) 21, f) 28, g) 27, h) Monel 400 74

Fig. 4.11: Representation of the optimized process parameters and the region used to quantify porosity. 75

Fig. 4.12: Diagram representing the surface roughness on the samples. 75

Fig. 4.13: EDS spectra of four regions around the lack-of-porosity region. 76

Fig. 4.14: Change in layer thickness when the hatch % is changed from 50% overlap to 75% overlap. 79

Fig. 4.15: Vickers hardness averaged over five indentations on each of the DoE thin walls. 83

Fig 4.16: Residuals plot from ANOVA analysis. 84

Fig. 4.17: Vickers hardness averaged over five indentations on the surface layer of the cubes (with error bars) and porosity recorded for each sample. 86

Fig. 4.18: Microhardness of four regions of different composition. 88

Fig. 4.19: Hardness profiles for 3 cubes (a) 220 W, 5.2 mm/s, 11.5 g/min, 50% hatch spacing, (b) 300 W, 7 mm/s, 19.1 g/min, 75% hatch spacing, (c) 220 W, 4.5 mm/s, 11.9 g/min, 50% hatch spacing. 91

Fig. 4.20: a)-d) micrographs of hardness indentations, e) BSE image of indentation, f)-g) BSE image magnified into crack region. 93

Fig. 4.21: a) XRD patterns of a) Sample OP, b) Sample HS, c) Sample RM. 96

Fig. 4.22: a) 220 W, 5.2 mm/s, 11.5 g/min, 50% hatch, 0.2 z-increment, b) 270 W, 6.3 mm/s, 17.2 g/min, 75% hatch, 0.2 z-increment, c) 220 W, 5.2 mm/s, 12.6 g/min, 50% hatch, 0.31 z-increment, d) 220 W, 5.2 mm/s, 13.3 g/min, 0.5 z-increment. .. 100

Fig. 4.23: Dilution of Fe and Cr into the deposition a) and c) Sample OP, b) and d) Sample 2. 102

Fig. 4.24: Eutectoid lamella within spheroids (left) and magnified eutectoid lamella structure (right) 103

Fig. 4.25: SEM micrographs of a) and b) fusion region, c) close to the fusion region, d) central to top region, e) multiple regions of Sample HS and f) top region of Sample RM. 104

Fig. 4.26: a) SEM of region of interest and elemental mapping of b) W, c) Ni, d) Fe, e) Cu 107

Fig. 4.27 a) SEM of region of interest and elemental mapping of b) W, c) Ni, d) Fe, e) Cu 109

Fig. 4.28: EDS analysis of light and dark phases. 110

Fig. 4.29: a) SEM of region of interest and elemental mapping of b) W, c) Ni, d) Fe, e) Cu 113

Fig. 4.30: a) SEM of region of interest and elemental mapping of b) W, c) Ni, d) Fe, e) Cu 115

Fig. 4.31: EPMA of Sample HS a) oxygen, b) tungsten and c) nickel. 117

Fig. 4.32: EPMA of fusion region of a) Sample 2 b) Sample OP and c) Sample HS. 118

Fig. 4.33: EPMA of a) W of Sample RM, b) Ni of Sample RM, c) W of Sample OP and d) Ni of Sample OP, e) W of Sample 2 and f) Ni of Sample 2, g) W of Sample 14 and h) Ni of Sample 14. 120

Fig. 4.34: Binder of Sample HS (left) and binder of Sample OP (right). 121

Fig. 4.35: Cracks present in the binder region (left) and WC particles (right). 123

Fig. 4.36: Core-rim WC particle after laser deposition. 127

Fig. 4.37: Change in W, Ni and Cu content with radial position in WC particle in sample 21(OP), (selected data from Table 4,10) 128

Fig. 4.38: Raman spectrum and a representative point micrograph [I] Binder region, [II] Inside embedded WC spheroid, [III] A-dark region on boundary of spheroid, B-interface region, [IV] oxide region, [V] Blocky microstructure..... 131

Fig. 4.39: XRD pattern of a drill bit segment 133

Fig. 4.40: a) Printed drill bit, b) CAD used to fabricate drill bit..... 134

Fig. 4.41: Fractured a) DB1, b) DB2, c) DB3, d) DB4, e) CAD model approximation of sharpened drill bit, f) CAD approximation of unsharpened drill bit. 137

Fig. 4.42: von Mises stress simulations for a) original CAD model, b) unsharpened CAD model, c) sharpened CAD model and displacement simulations of d) original CAD model, e) unsharpened CAD model, f) sharpened CAD model. 139

Fig. 4.43: Calculated circularity of each drilled hole by the corresponding drill bit. 140

Fig. 4.44: Diameter and depth of each drilled hole for the corresponding drill bit... 141

Fig. 4.45: Tip length, flute length and total length of the drill bit compared to the true value of the CAD model. 143

Fig. 4.46: Diameter of a) Tip, b) flute and c) shank in (mm) 144

Fig. 4.47: Hole of purchased drill bit, SEM of region on boundary. 145

Fig. 4.48: DB1 a) first drilling attempt, b) second attempt, c) third attempt with drill bit failure, d) embedded drill bit tip in the aluminium disk. 146

Fig. 4.49: SEM images of the hole drilled by DB1 showing a) the boundary of the hole, b) the embedded drill tip, c) the rim of the hole, d) and e) the inner rim of the hole. 147

Fig. 4.50: Two drilling attempts by DB2 before failure..... 148

Fig. 4.51: a) first attempt by drill bit DB3, b) second attempt by DB3 and the tip failure, c) SEM image of striations from a), d) and e) inner wall of the hole, f) bottom of the drilled hole..... 149

Fig. 4.52: Striations made by DB4. 150

Fig. 4.53: Fractured region of DB3 a) fractured cast WC, b) surface cracks on cast WC and c) high- and low-density regions in fracture zone. 151

Fig. 4.54: a) and b) cracks in the fracture zone of DB1 and c) rough surface after fracture..... 152

List of Tables

Table 2.1: Additive manufacturing processes used for WC-alloys. 16

Table 2.2: Materials which have been fabricated using the LENS® process. 27

Table 2.3: Summary of LENS® literature findings for various cemented WC compositions. 30

Table 2.4: Parameter range used for optimization of LENS® process. 31

Table 2.5: Optimized LENS® parameters for WC-Co. 34

Table 2.6: Micro and ultra-micro hardness test results (mean values) amended from [47] 36

Table 3.1: Elemental composition of Monel 400. 42

Table 3.2: Values used in constructing the design of experiments matrix. 50

Table 3.3: The refinement of paraments through deposition of cubic samples. 53

Table 4.1: Design of experiments parameters and resultant average height and average width 64

Table 4.2: Coefficients for Equation 4.1. 66

Table 4.3: Coefficients for Equation 4.2. 70

Table 4.4: Atomic % analysis of four regions in Fig. 4.13. 77

Table 4.5: Process parameters for the respective samples and the porosity which was obtained for these parameter sets. 78

Table 4.6: Coefficients for Equation 4.3. 84

Table 4.7: Recorded hardness values for each indentation in Fig. 4.18. 88

Table 4.8: Atomic percentage of elements for different defined microstructures. 105

Table 4.9: EDS results for the five spectra in Fig. 5.6. 110

Table 4.10: Atomic % of elements at various points along the scan line in Fig. 4.36. 127

Table 4.11: Average cost to produce a drill bit 135

Chapter 1 Introduction

1.1 Background and motivation for research

“Additive manufacturing” (AM) is the standard term used for all rapid prototyping applications in accordance with ASTM F2792 [1]. Commonly known as additive techniques, layer manufacturing or freeform fabrication this method is the process of joining materials, usually layer by layer, to create an object from a 3D computer aided design model. The additive manufacturing economy was worth $1.7 billion in 2011 and its projected worth for 2025 was $10+ billion [2], [3]. In the 2015 Wohler’s Report, AM products contributed $4.1 billion in 2014 and a revised projection of $21+ billion by 2020 was made [4]. Based on this rapid global growth in the AM field, it is critical for South Africa to explore the employment of this technology within the local manufacturing industry. By November 2015 there was an estimated 3500 AM machines in South Africa, with 87% being termed entry level [5]. Only nine of the 3500 setups can produce metal AM components, with a mere six being used for metal component production and the remaining three for refurbishment purposes.

In 2016 the Department of Science and Technology, in conjunction with the Council for Scientific and Industrial Research (CSIR), released an additive manufacturing strategy for South Africa to enable exploitation of AM processes and to become competitive in the global manufacturing market [5]. The idea of incorporating lasers to melt powders and produce a “bulk” near-net shape rapidly solidified structure can be traced back to Breinan and Kear [6] who developed Laserglaze™ technique. Solid free form capabilities have been revolutionized by the advances in laser technology, computers, Computer Aided Design (CAD) software, motion control systems and materials which are available to users and additive manufacturing machine manufacturers [6]–[13].

Rapid prototyping, an earlier form of additive manufacturing was developed in the 1980's to produce functional printed parts and not just models [14]. The first widely used form of rapid prototyping was developed by 3D Systems, Inc and was known as Stereolithography (SL). The process started with a computer aided design (CAD) which would be converted into a .STL file which "cuts" the CAD model into slices containing the relevant printing information for each successive layer of the build. A platform is used to anchor the part that is being produced. Since the process is liquid-based, a UV laser is applied to a photosensitive polymer to induce curing and resultantly producing a single layer on the platform. When the layer is complete, the platform is lowered, and the process continues until the complete CAD model has been printed from the polymer. The excess photosensitive polymer is drained and used for further projects[15]–[17]. From this layer-based process followed many other three-dimensional printing processes developed to produce components from liquids, solids and powder-based systems.

The different forms of additive manufacturing are shown in Fig. 1.1. With these methods CAD designs can be used to produce functional parts spanning polymers, metals and ceramics [18]–[20].

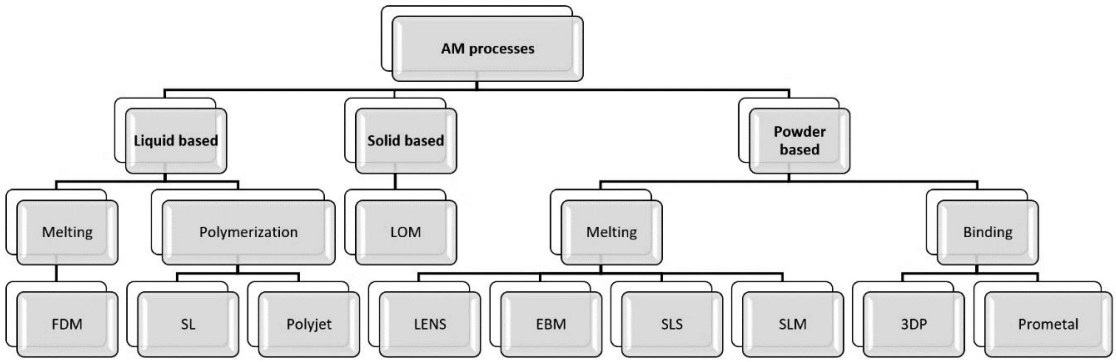


Fig. 1.1 :Different methods of additive manufacturing [15].

While additive manufacturing of many materials has been actively researched and even commercially employed, its application in the field of cemented tungsten carbides to date has been confined to research and development wherein limited studies have been undertaken. There are currently several conventional techniques to synthesize tungsten carbide-cobalt (WC-Co) cermet bulk and coating materials. These include conventional powder metallurgy (P/M) processes such as liquid phase sintering and machining [21]–[25], thermochemical techniques [24], [26]–[29], spark plasma sintering (SPS) [30]–[38], vacuum plasma spraying [39]–[46] and high velocity oxy-fuel (HVOF) [47]–[55]. Additive manufacturing methods have not been studied enough to compete with these conventional and tested methods.

Laser engineered net shaping (LENS®) is a form of AM which has been used to produce a variety of alloys, with the predominant focus being on titanium alloys, Inconel and stainless steel [56]–[58]. Limited research and no commercialization process has been done using the LENS® process to manufacture cemented tungsten carbides, with only cobalt (Co) being utilized as a binder phase [7], [59], [60]. Therefore, the focus of the current research study was to investigate the feasibility of using the LENS® technology to manufacture cemented tungsten carbides having a Ni-based binder. A Ni-alloy was selected as the binder material since it has been shown that the alloys are stronger than pure nickel and are resistant to many corrosive agents, e.g. rapidly flowing seawater [61]. By combining these properties of Ni-alloys with the excellent hardness and wear resistance of WC, it may be possible to produce a viable LENS® component for a wide range of commercial applications.

1.2 Research aim and objectives

The aim of this research project was to broaden the knowledge and understanding of laser sintered WC-Ni-alloy components and to aid in the advancement of WC-Ni-alloy additive manufacturing endeavors, specifically in the field of LENS® technology.

This aim was achieved through the following objectives:

- The effectiveness of Nickel-alloys as a binder phase for tungsten carbide was determined from the ability to produce depositions and the porosity of the depositions.
- The optimal processing parameters for WC-Ni-alloys was determined using a full factorial design of experiments.
- The microstructural, physical and mechanical properties of the LENS® materials were characterised.
- The LENS® process was used to produce a WC-Ni-based commercial product which was benchmarked against a conventionally produced product.

1.3 Contribution to knowledge

The LENS® process, although established commercially for other materials, is significantly lacking with regards to cemented tungsten carbides. There are limited available research publications and currently there is no defined commercial process employing the LENS® technique for the fabrication of mainstream cemented tungsten carbide components. Due to these deficits the current research study provides new scientific information on the feasibility of using the LENS® technology in the production of cemented tungsten carbides. The investigation of a Ni-based alloy, specifically Monel 400, in the additive manufacturing processes of these materials is also novel. Additional outcomes of this research were to address whether LENS® can manufacture dense WC-Ni-alloy materials without the

aid of post processing techniques, whether the microstructural and mechanical properties are similar in nature to those of WC-Ni-alloys in literature, and ultimately if a commercial product could be manufactured using the LENS® process.

1.4 Structure of the thesis

The thesis is structured in the following manner: Chapter 1 explains the importance of the research. Chapter 2 provides an in-depth literature review on the LENS® process as well as the application to various materials and WC-based cemented carbides. Chapter 3 describes the experimental procedures used to investigate the LENS® deposition process, the mechanical and microstructural properties of the fabricated thin walls, cubes and drill bits. Chapter 4 presents the characterisation results which are integrated with their interpretation and discussion. Chapters 5 and 6 provide conclusions and recommendations for future work followed by a list of cited references.

Chapter 2 Literature Review

This chapter describes the laser engineered net shaping process and provides a review of the materials which have been deposited using the LENS® process. The published work on the additive manufacturing of cemented carbides is also discussed in this chapter.

2.1 Cemented tungsten carbides

Cemented tungsten carbides are available in a variety of different grades with extensive usage in the mining, cutting tool and high wear environments [62]. Cemented tungsten carbides comprise of a hard particle phase, the tungsten carbide (WC), which have been “cemented” due to the binder phase becoming a liquid during sintering and thereby surrounding the hard phase before solidifying. The sintering process can produce multiple complex phases which can only be reduced if the relevant temperatures of formation and elemental composition are understood. The importance of carbon content in the WC system is observed in Fig. 2.1 which is the W-C phase diagram. Research has shown that the carbon content has a critical impact on the formation of WC-based composites during sintering [33], [34], [41], [43], [44], [49]. For monotungsten carbides WC, the stoichiometric value is 6.13 wt.%. If there is excess carbon then free graphite will form and if there is a carbon deficiency W_2C and WC_{1-x} are the main phases that would form [68].

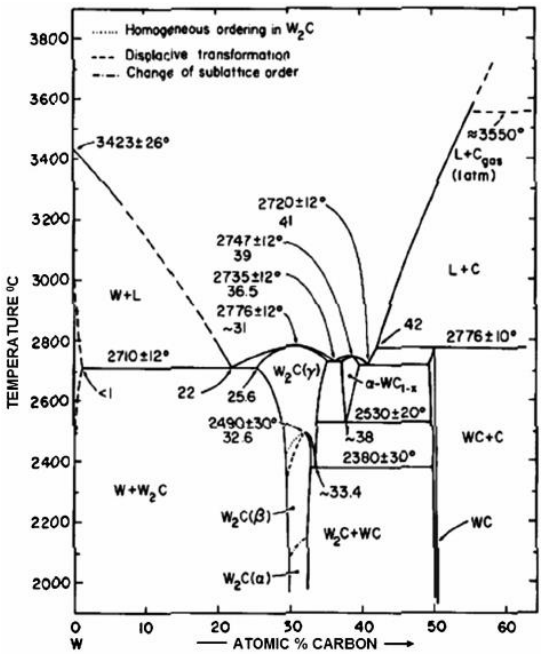


Fig. 2.1: Phase diagram for W and C [69].

The W-C phase diagram begins at a much higher temperature because tungsten, carbon and their different elemental combinations have remarkably high melting points [70]. Many different chemical variations are possible for W and C with most comprising of different combinations of WC, W_2C and graphite. Equations 2.1 and 2.2 show how tungsten carbide combines to form W_2C while creating a localized increase in the carbon content. The eta phase W_2C, can decompose to yield twice the amount of metallic tungsten when compared to carbon which creates a high local concentration and promotes the growth of microstructures that have an affinity for W.

$$2WC \rightarrow W_2C + C \qquad \text{(Equation 2.1)}$$

$$W_2C \rightarrow 2W + C \qquad \text{(Equation 2.2)}$$

Fig. 2.2 shows schematics of the WC crystal structure. Tungsten carbide has a hexagonal crystal structure of the form P6m2 crystal symmetry [71], [72] and a c/a ratio of 0.976 (a=0.2906nm) [73] .The W atoms are in the (0,0,0) positions while the carbon take the asymmetrical positions (1/3,2/3,1/2) in the unit cell and due to this asymmetry the prismatic planes are divided into two families of planes with different arrangements. These two families have different affinities to carbon because W atoms on each plane have a different number of W-C bonds. The planes which have the high affinity to carbon will grow preferentially in the saturated carbon environment which results in the triangular prismatic shape shown in Fig. 2.2 (a) [74] [67], [68], [75]–[77] [67].

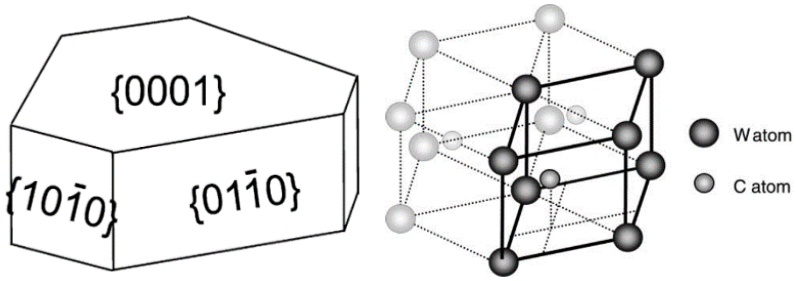


Fig. 2.2: Schema of WC grain shape in Co binder (left) and the atomic structure of WC crystal (right) [78].

Each W atom is coordinated by six C atoms and each carbon by six W atoms [79]. The atoms are arranged in alternate close-packed layers of W and C in (0001) planes. Tungsten carbide has three types of dense planes, the base plane {0001} and two different prismatic planes $\{10\bar{1}0\}$ and $\{01\bar{1}0\}$. Hardness of (0001) planes are up to twice as much as other planes [80] and cleavage strength is the lowest in the (0001) planes [81]. The grain coarsening is limited by interfacial reactions or long-range diffusion. A coarsening process is predicted to obey a rate equation according to [82]:

$$r^n - r_0^n = 2Kt \quad \text{(Equation 2.3)}$$

Where r is the average grain radius, r_0 is the initial average grain radius, K is the coarsening rate constant dependent on the controlling mechanism, and t is time. If the growth is controlled by an interface reaction then the exponent n will be 2, whereas for diffusion-controlled growth, n = 3. The grain growth is known to be limited by the interface reaction rather than the diffusion reaction [83].

Grain growth kinetics of tungsten carbide cermets in the sintering process and the activation energy has been studied by several researchers [84], [85]. Growth kinetics based on classical kinetic theory has been applied to the investigations of growth in films and coatings [76], [85]–[91]. Growth kinetics differ from densification kinetics since it is controlled by a diffusion mechanism while densification is controlled by power law creep and linear diffusional creep at different stages [84]. Due to this the activation energy of WC growth has been found to be approximately one-third of densification activation energy [39], [41].

Grain size of the sintered part has been found to be very dependent on the size of the initial powders [92]. During sintering the average WC grain growth is through Ostwald ripening [93], in which large grains grow and small grains dissolve [94]. It has been found that the morphology [64], [65], [95]–[102] , grain size [63], [64], [66], [67], [98], [103]–[108] and abnormal grain growth [100], [101], [105], [109] of WC grains are sensitive to carbon content [63]–[67], inhibitor type (Cr or V)[67], [102] binder contents [110], [111] ,sintering parameters [112] and the thermal stability of the phase [113]–[115]. The average size of WC grains has been found to increase with an increase in Ni content since the solubility of WC is higher in nickel than cobalt [116],[117]. The coarsening of WC is a reaction controlled growth process which is determined by dissolution at interfaces dissolving small

grains[98], [118], [119].The coarser microstructures and the dilution of elements from the substrate material have a significant effect on the observed hardness [95], [120], [121]. This hardness variation due to the change in grain size is well defined by the Hall-Petch relationship shown in Equation 2.4 [122].

$$\sigma_0 = \sigma_i + k/\sqrt{D} \quad \text{(equation 2.4)}$$

This relationship indicates that the strength of a metal is equal to the frictional stress plus a factor (k) multiplied by the inverse of the square root of the grain size (D). Hence, by reducing the grain size the material will become stronger and increase the toughness [122].

Hardness is mainly dictated by three different factors, namely solid solution alloying [95], [121], [123], [124], carbide fraction [70] and dendrite arm spacing [125], [126]. A low carbon content in the substrate will lead to a low fraction of formed carbides. Slower solidification rates will result from lower thermal conductivity of the substrate and consequently larger dendrite arm spacing. Mechanical properties, such as hardness [127] , fracture toughness [127] and ultimate tensile strength [127], are also affected by the thermal history of each point in the deposition, the heating and cooling cycles, which ultimately affect the microstructures that are observed in different regions of a laser deposited sample. The shape of the WC microstructure has also been found to have a strong effect on the mechanical properties [96], [128], [129] with thin WC platelets with high aspect ratios [20] improving toughness and hardness of WC-Co cemented carbides.

It is well-known that the tungsten carbide (WC) phase is responsible for hardness and wear resistance and the Co binder for toughness and bending strength [130], [131]. However, Co is toxic by inhalation and is under consideration for addition to the suspected human carcinogenic list [132], [133]. Due to the apparent carcinogenic nature of Co, alternate binders, comprising of nickel (Ni) [134]–[141] and iron (Fe) [132], [134], [135], [142]–[145] alloys have been investigated. Fig. 2.3 shows that with the replacement of Co with Ni as the binder substantially lowers the corrosion rates across all pH values that were tested especially the highly acidic environments, although the mechanical properties appear to be lower than when Co is used [30]–[33], [146]–[157]. At least two patents exist for replacing Co binder with Ni [133], [158], [159] .

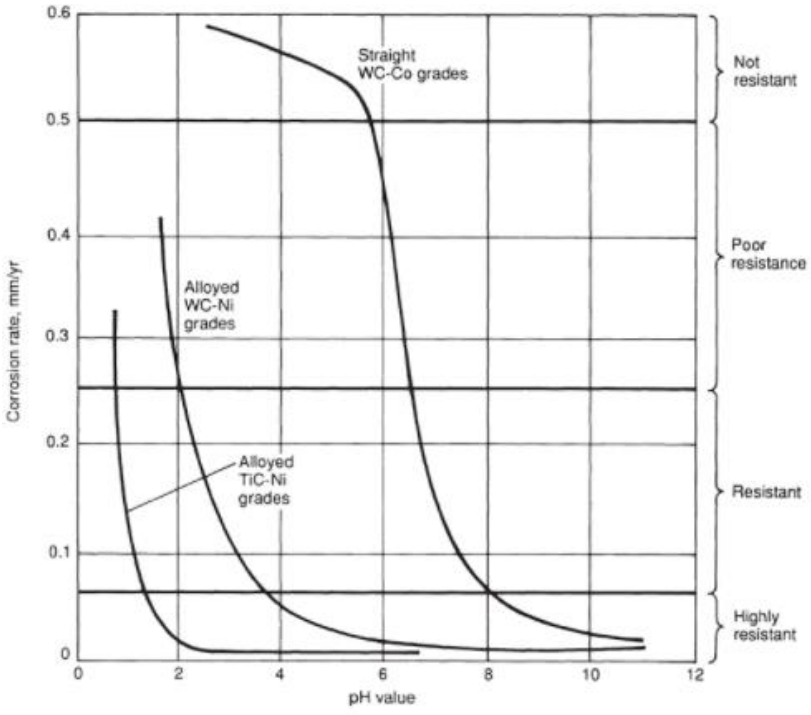


Fig. 2.3: Corrosion rate of Ni based and Co based cemented carbides for various pH values [160].

Some other binder combinations have also been tested by various researchers. Hanyaloglu et al. [142] studied the possibility of using WC/Fe-Mn as a cheaper, non-toxic alternative to WC/Co. It could also be a cheaper alternative for Fe-Ni binders which include the more costly nickel. Two stoichiometric alloys were produced, WC15%FeMn, 0.75wt%C and WC25%FeMn, 0.85wt%C respectively. For the reduction of η-phase the sintering was performed in a high carburizing atmosphere. Cermets having 15%binder were found to possess similar hardness properties to WC-Co alloys with a slightly lower toughness. Various binders were studied by Schubert et al. [134], including variations of FeNi, Fe/Ni/Co and Fe/Mn. A FeNi binder ratio of 8.5:1.5 was found to have the optimal hardness and toughness properties. This corresponded to a nickel content of 15% with respect to the binder alloy. The FeNi binder at optimal conditions resulted in a hardness of approximately 1680 HV_{50}. Even though suitable properties were present for the FeNi binder there was a very small carbon window in which to maintain the austenitic microstructure and inhibit the martensitic transformation. In the binder region of 10 mass% to 20 mass% the carbon window is $\Delta C = 0.05 \pm 0.01$. An FeMn binder showed a high hardness between 1800 HV_{50} and 1900 HV_{50} although it also exhibited the lowest toughness. The manganese is also prone to vaporizing during sintering which reduces the Mn content in the final sintered product. The formation of M_6C was evident which dominated the important WC-FeMn phases. Another impeding factor was the formation of oxides when using manganese.

Bolelli et al. [132] studied the WC-15wt%FeCrAl system as an alternative binder to CoCr using HVOF. Under the spraying method FeCrAl showed a larger degree of oxidation than CoCr. It was also found that in dry particle abrasion (such as mills, crushers and conveyers) excessive oxidation-induced brittleness was recorded for the FeCrAl binder. Liu [161] studied the possibilities of using alternative binders to form cemented carbides. It was found that WC-20vol%(15Fe85Ni) and WC-20vol%(72Fe-28Ni) alloys have relatively higher

toughness than WC-20(15Fe 85Ni). WC-20(82Fe 18Ni) was found to have a better combination of hardness and fracture toughness, with a hardness between WC-20Co and WC-20(70Fe-12Co-18Ni) and a fracture toughness higher than both composites.

Brookes et al. [145] observed that in a pure Fe binder the addition of carbon had simple effects; when no carbon was added the eta phase was present and when 2% carbon was added there were graphite inclusions. When 1% carbon was added a homogenous distribution of Fe and WC was observed. A 28% Cr addition to the binder, resulted in defects regardless of the addition of carbon. Comparable results were observed for the Fe18%Cr binder. The FeCr binder resulted in a higher hardness and lower toughness than the pure Fe binder. The addition of 1% carbon to the binder materials resulted in a 25-30% increase in toughness. The FeCr binders were very brittle compared to WC-Co cemented carbides which have an indentation fracture toughness(K_1C) in the range of 9-24MPa.$m^{1/2}$.

The W-C-Ni phase diagram, Fig. 2.4, shows that the carbon percentage is particularly important to the phases which form. If the carbon is maintained below approximately 5.2% then the carbon deficient eta phase will be present along with WC and FCC nickel. To have an eta phase free deposition the carbon would have to be between approximately 5.2 and 5.4 mass percentage. Anything larger than this range would result in FCC nickel, WC and the graphite phase, formed by the superfluous carbon.

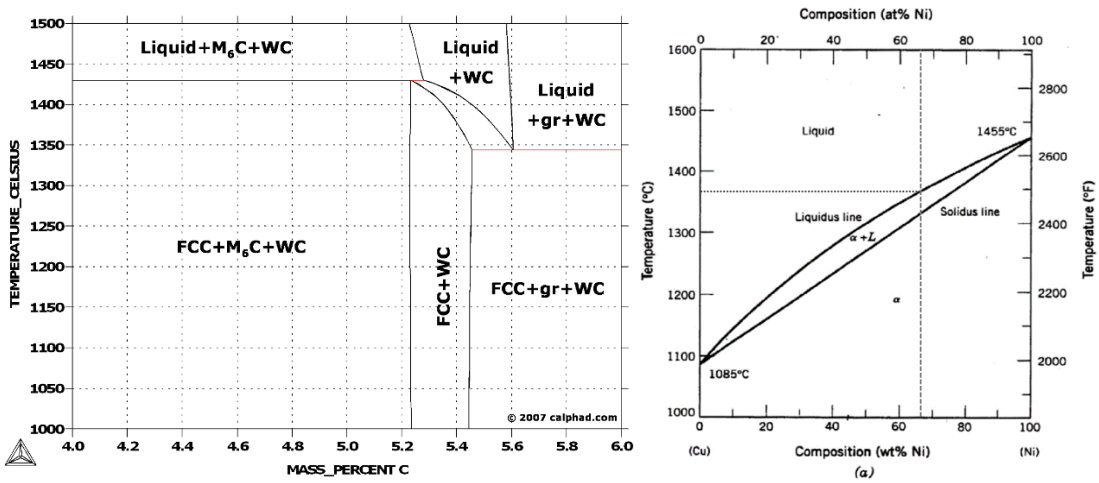


Fig. 2.4: Phase diagram of W-C-10%Ni (left) and Ni-Cu [162] [163].

All three scenarios are possible since from equations 2.1 and 2.2 there may be localized high or low carbon or tungsten regions [138], [164]–[166]. Equations 2.5-2.8 show the different eta phases that can potentially form during the sintering process.

$$WC + W + M \rightarrow \eta\text{-}M_6C\ (Ni_2W_4C,\ Fe_3W_3C) \qquad \text{(Equation 2.5)}$$

$$4M + 4WC + O_2 \leftrightarrow 2M_2W_4C + 2CO \qquad \text{(Equation 2.6)}$$

$$3M + 3WC + O_2 \leftrightarrow M_3W_3C + 2CO \qquad \text{(Equation 2.7)}$$

$$12M + 12WC + 5O_2 \leftrightarrow 2M_6W_6C + 10C \qquad \text{(Equation 2.8)}$$

Published research shows a vast array of structures for WC-Fe-Ni alloy system including M_4C and M_6C (Ni_2W_4C, Ni_3W_3C, FeW_3C, Fe_2W_2C, Fe_3W_3C, Fe_6W_6C) [68], [92], [167]–[173]solid solutions ($W_{0.15}Ni_{0.85}$, NiW, Fe_2W) [168], [174], [175],

irregular structures of chromium scattered in blocky, hexagonal and needle like structures [176], [177], and M_3C carbides [68], [174], [178]–[180]. Equations 2.5-2.8 show how the M_6C and $M_{12}C$ carbides form during the sintering process [181]. Cemented carbides are made by liquid phase sintering [92], [95], [120], [121], [127], [128]. The liquid phase is seen to initiate from approximately 1455˚C, Fig. 2.4, although this is for a pure nickel binder, hence, by using Fig. 2.4, it can be seen that all components would be in the liquid phase would at 1367˚C with the Monel 400 melting point listed as 1299-1349ºC [182]. Since copper has a much lower melting point than nickel, even 1% difference in the copper would have a major effect on the melting temperature.

Based on the review of previous studies which showed that nickel is a viable alternative binder for the WC-Co alloys system, a nickel-based alloy Monel 400 was chosen as the binder phase for the current research study. Monel 400 contains the same quantity of nickel and copper as found in a naturally occurring nickel ore mine in Ontario [183]. It has a high strength but can only be hardened by cold working [184]. Its composition is predominantly nickel with about one third copper and lesser amounts of iron and manganese. It is resistant to sea water and steam at elevated temperatures as well as to caustic and salt solutions. It exhibits good corrosion resistance, good weldability and high strength. It has a wide usage in marine environments and other non-oxidizing chloride solutions. In deaerated solutions it has exceptional corrosion resistance to hydrochloric and hydrofluoric acid, although is highly susceptible to nitric acid and ammonia environments. It even retains its good mechanical properties in subzero temperatures up to 550 ˚C. In US Navy tear tests at temperatures as low as -196˚C it showed excellent ductility and tough fracture characteristic over the temperature range with the maximum load increasing considerably with increased temperature [185].

2.2 Additive Manufacturing of Cemented Tungsten Carbides

WC-alloys have been produced using additive manufacturing and cladding processes, with some examples shown in Table 2.1. Various laser setups have been used to process WC with an array of different binder materials. The effect of laser processing parameters on the resultant microstructures was the main research path in many of the articles.

Table 2.1: Additive manufacturing processes used for WC-alloys.

Process	Material	Reference
Selective Laser Melting	Tool grade WC, WC-12wt%Co, 25wt.% WC-75wt.% Co, 50wt.% Co-50wt.% WC WC-Co 88-17, WC-Co 88-12 WC-Co-83-17	[186] [187] [188] [189] [190]
Laser Cladding	30% Colmony 227-F and 70% WC/Co/C WC-17wt% Co WC-Ni-Cr alloy WC-15wt.%Ni-alloy WC-12wt%Co Nano-phased WC-12wt%Co	[191] [192] [193] [194] [195],[196] [197]
Selective Laser Sintering	WC/SS composite WC-12wt%Co	[198] [199]
Direct Metal Laser Sintering	WC-Co/Cu MMC 70:30 ratio of Nickel- base alloy (KGH95) with nickel coated WC (WC-12%Ni)	[200], [201] [202]

Some of the articles, in Table 2.1, are explored in more detail here. A cusing M2 laser was used to produce 35 mm x 35 mm single layer samples of tool grade tungsten carbide powder [186]. Two balling mechanisms were identified, namely shrinkage-induced balling and self-balling where balling is defined as melted metal droplets solidifying before spreading out completely and retaining a ball-like shape

[203]. It was found that a lower scan speed coupled with a high laser power and high hatch spacing resulted in the least amount of balling. Higher hatch spacing resulted in reduced shrinkage which leads to reduced porosity in the layer [186]. In WC-12wt%Co powder [187] both fine and coarse grains were observed which segregated in the melt pool during the deposition process. The formation of W_2C due to the thermal decomposition of WC is evident. The microhardness of the part produced by a nano-phased powder had a slightly increased hardness in both the coarse (~1496 $HV_{0.3}$) and fine (~1542 $HV_{0.3}$) regions when compared to conventional powder (1384 $HV_{0.3}$-coarse),(1515 $HV_{0.3}$-fine) [187]. Khmyrov et al. [188] found that the selective laser melting of 25wt%WC-Co powder was found to have satisfactory porosity without any cracks once deposited on the substrate material, whereas 50%wtWC was found to have considerable cracking due to the formation of the brittle $W_3Co_3C_3$ phase. The 25wt% WC was an alpha-Co solid solution.

A combination of 30% Colmony 227-F (Nickel alloy) and 70% WC/Co/Cr powders were used in a cladding process [191]. The tungsten carbide powder mixture consisted of about 86 wt.% WC, 10 wt.% Co and 4 wt.% Cr which was deposited onto an AISI 304 steel. The deposited layer had a maximum porosity of 0.24% and was crack free. The cladded layer showed good adhesion between the substrate and the layers. For a single layer the CO_2 laser was set to 2.4 KW, with a spot diameter of 2 mm and powder feed rate of 9.3 g/min. With these fixed parameters and the use of a mathematical model the ideal translation speed was found to be 500 mm/min. For multilayer cladding, four layers, a translational speed of 170 mm/min was used with layer height of 0.79 mm [191].

In a study by Pavalache et al. [192] WC-17wt%Co powder was used to test the effects of cladding parameters on the resultant microstructure. The lowest heat input (1.26k J/cm) resulted in smaller and finer dispersed carbide particles

throughout the metal matrix. When the heat input was raised by a small factor a refinement in microstructure was observed. In both cases an undesirable joining effect of the carbide particles was observed in the molten pool [192]. Composite Ni-Cr + WC laser cladding was investigated by St-Georges [193] and the resultant properties compared with those obtained by conventional arc sintering. A WC-50%Ni clad on tool steel resulted in a hardness of 47.5 HRC (480 HV). A laser power of 4 kW was used with a feed rate between 40 and 120 g/min and traverse speed of 400-800 mm/min and spot diameter of 600 µm. A traverse speed of 600 mm/min and a feed rate of 60 g/min resulted in a dense dispersion of WC and a low level of dilution.

Wu et al. [194] determined that the cladding layer produced under optimal parameters had a uniform structure and excellent bonding with the substrate. When a larger power was used the WC particles tended to sink to the bottom of the layer and underwent a greater level of dissolution [194]. Przybylowics and Kusinski [195] tested Stelcar 6297 (25 wt.% WC), (50 wt.% WC) and WC/Co (88 wt.% WC) and found that the best quality clad coatings were obtained using 1200 W of power at a scanning speed of 2 mm/s for powders containing 25 wt.% WC and 1500W at 3 mm/s when WC quantities were higher. The decrease in power or increase in scanning speed resulted in higher porosity and layer cracking. An increase in power resulted in dissolution of WC in the metal matrix.

Gu et al. [200] studied the effect of direct metal laser sintering parameters on the homogenizing on a WC particulate dispersion in a mixed metal matrix. A uniform dispersion was obtained with a laser power between 650W and 750W with a scan speed of greater than 0.04 m/s. Any larger increase in power resulted in balling and a scan speed below 0.04 m/s yielded particulate aggregation due to the particulates being deposited slower than the advancing dendritic front. A study by

Gu et al. [201] found that a powder layer thickness below 0.30 mm allowed for a higher sintering density with superior densification and mechanical properties.

Chen et al. [202] used direct metal laser sintering to sinter a 70:30 ratio of Nickel-base alloy (KGH95) with nickel coated WC. A power of 900 W resulted in the best sintering performance and a scanning rate of 0.7 m/min allowed for well distributed WC particles. A higher scanning rate resulted in defects in layering due to insufficient process time. At 800 W agglomeration of the WC particles was observed with a relative density of 76.5% being obtained due to the high porosity. A power of 900 W resulted in well distributed dendrite crystals and a relative density of 90.4%. The relative density reduced to 82.6% with 1000 W input due to apparent pores and the visible growth in the WC particles [202].

2.3 LENS® Process

Laser engineered net shaping been applied to fundamental materials research since 1996 [58], [204]–[213], with applications as functional prototyping and the addition of material features to existing components such as thin walls, service and repair [214]–[220]. The LENS® process has also been used for medical device manufacturing including development, prototyping, and production of specialty surgical prosthetics [206], [219], [221]–[225]. The LENS® (Laser engineered net shaping) process and equipment was developed by a multi-program including Sandia National Laboratories and United Technologies of Pratt and Whitney (UTPW) [204]. In 1997, the LENS® technology was licensed to Optomec Inc. [226].

Fig. 2.5 is a schematic of a typical LENS® process, which is a ‘powder blown’ form of additive manufacturing. It is a ‘powder blown’ process because an inert gas stream is used to blow the powdered material to the desired location [227]. Fig. 2.5

shows that the entire process is performed in an argon hermetic chamber to prevent oxidation of the material [15]. The typical process to manufacture a part begins with a CAD (Computer Aided Design) solid model which is sliced into a sequence of thin cross-sectional slices and translated into a series of tool path patterns to build each layer. Each layer is fabricated by first generating the outline of the feature, then filling in the cross section with a rastering technique [204].

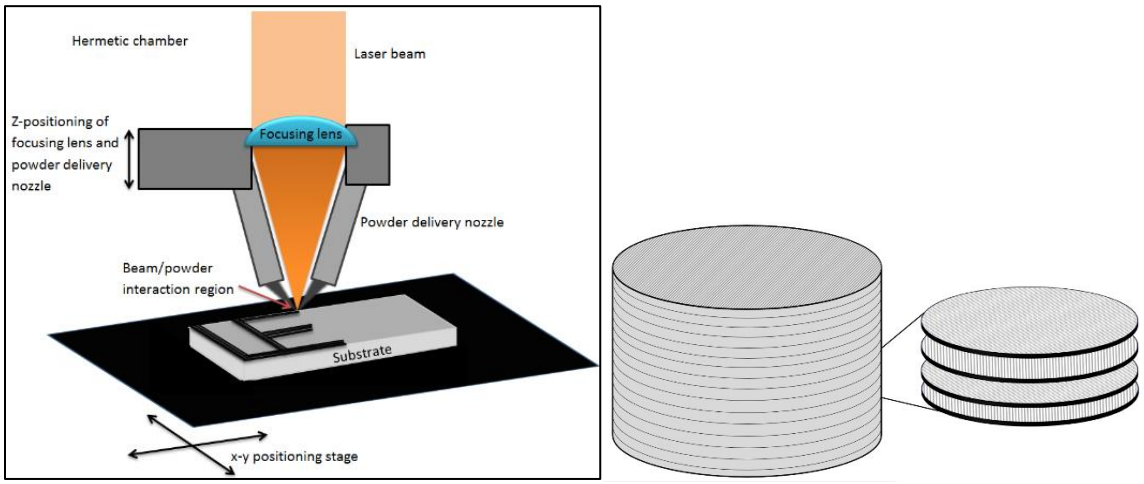


Fig. 2.5: Schematic of the LENS® process [204] and a layer-by-layer CAD model example.

The part is created by melting metal powder, supplied by the four powder delivery nozzles (refer Fig. 2.5), which is injected in a specific location using argon as a carrier gas. It becomes molten when encountering a high-powered laser beam which has been focused through a lens to control the beam size. The molten metal powder cools rapidly after deposition on the substrate, or on the previously deposited layer [15]. Once the layer has been deposited, the powder delivery system and focusing lens are shifted an increment in the positive z-direction to build the three-dimensional component layer-by-layer [15]. The sintered article then undergoes machining, as necessary, to reduce the surface roughness within specification of the intended application.

The LENS® process has been applied in both additive manufacturing and repair applications by several laboratories. Sandia laboratories have fabricated fixtures, component housings and impellers, Fig. 2.6 (right) [228]. RPM Innovations Inc. have done various repairs on components such as bearing housings, turbine compression seals and an atomizer drive coupler gear. They have also done extensive cladding of components to reduce wear [226]. In 2017 the Council for Scientific and Industrial Research, in South Africa, fabricated the National Science and Technology Forum (NSTF) trophies, comprised of titanium, using the LENS® process, as shown in Fig. 2.6 (left) [229].



Fig. 2.6: NSTF trophy produced by CSIR (left) and impeller produced by Sandia Laboratories (right).

Laser engineered net shaping® has a number of advantages including [230]:

- Reduction of material wastage when compared to subtractive manufacturing
- Large working envelope for large components
- Near-net and net-shape capabilities
- Capable of producing functionally graded parts
- Allows for fully customized parts to suit individual requirements
- Effective for both fabrication and repair purposes

The disadvantages of LENS® include [228]:

- High capital cost
- Requires post-sintering machining due to high surface roughness
- Only spherical powders may be used.

Laser powder-fed additive manufacturing, has a large number of processing parameters which include laser power, laser scanning speed, laser absorptivity, laser beam profile, powder feed rate, powder stream profile and carrier and shielding gas flow rate [231]. These parameters are all sensitive to the environmental disturbances and influence each other [232]–[235]. Due to the large possible parameter sets, finite element analysis simulations are performed extensively to reduce the manufacturing costs [236]–[240], although the software and resources required to conduct these simulations add to the cost and duration of the component development. The size of the solidification structure and associaited solidification mode can be affected by the in-situ cooling rate, which is affected by the laser scanning speed, laser power and powder feed rate [241]. A lower linear heat input (laser power/scanning speed) corresponds to a smaller melt pool, larger thermal gradient and higher cooling rate, therefore, resulting in a higher yield strength, larger ultimate tensile strength and higher ductility of 304 L S/S compared to those with a higher linear heat input [234]. For metallic material additive manufacturing the control of microstructure and mechanical properties could be achieved through the manipulation of the local solidification parameters [242], [243].

Marangoni flow is an important phenomenon that can affect the final microstructure which is observed. It is evident when a hardfacing material is present with a binder material which melts at a significantly lower tempertaure. Shen et al. [244]

explained the process using tungsten with a copper binder but any viable combination may result in core-rim structures. In the laser sintering process the duration of the laser beam at any given point depends on the spot size of the beam and the scan speed and is generally below 4 ms [235]. In this short heating cycle the sintering of the powders occurs rapidly, hence a liquid phase sintering mechanism is preferred to a solid state sintering [92], [95], [120], [121], [127], [128].

The liquid nature of the melt pool can be realized through viscous flow or a melting-solidification process. The viscous flow mechanism cannot lead to powder densification of metals since it has no softening phenomena, even at melting temperatures, hence a melting-solidification is the more feasible mechanism [245]. Heating rates in the order of 10^5 ˚C/s are present which causes rapid melting of the Cu and results in a melt pool containing liquid binder phase (Cu) and solid (W) phases. The rapid presence of the liquid phase restricts W-W bonds due to the absence of solid state sintering [246], [247]. A Gaussian beam results in a large temperature gradient between the centre and edges of the sintering pool. It is due to this temperature gradient and the chemical/compositional gradient of the elements that forms surface tension and results in a Marangoni flow [245], [248]–[254]. It is well known than the fluid always moves from low to high surface tension [255].

Studies have shown that the thermal component of the Marangoni flow will lead to a clockwise flow pattern (source flow) whereas the solutal will be anti-clockwise (converging flow). The thermal component is weaker than the solutal component, therefore the overall flow pattern will be counterclockwise [250]. When the W is not completely spherical there will be a torque component due to the misalignment of the particle centre [256] and the action of the thermal Marangoni flow. When a

significant amount of liquid forms a repulsive force is present which keeps the W particles at a certain distance from the centre of the Marangoni flow even if the converging flow pushes them toward the centre [257],which has been found to lead to a core-rim structure [244].

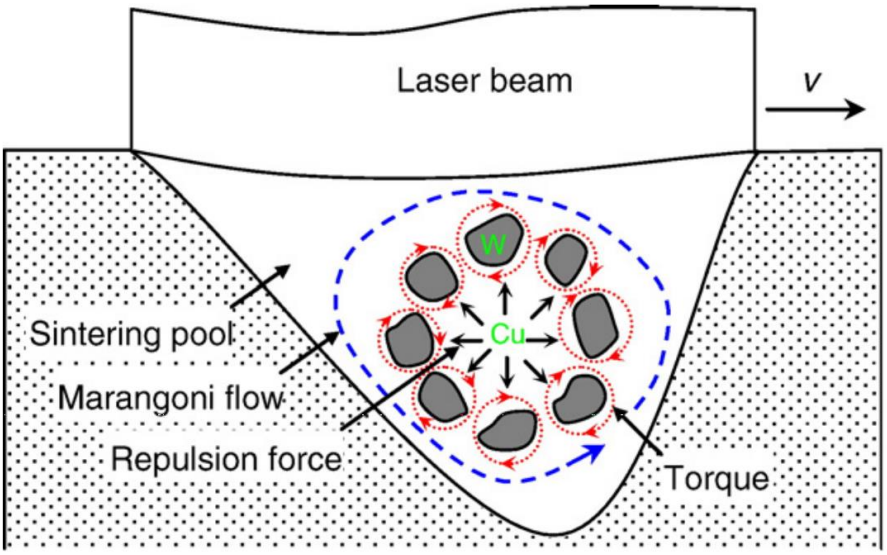


Fig. 2.7: Schematic describing the formation mechanism of W-rim/Cu-core structure [244].

The transformation from liquid to solid and the specific solidification behavior controls the distribution, size and morphology of the final grains [258]. Critical parameters determining the solidification microstructure are the temperature gradient, G, solidification rate, R, undercooling , ΔT and the alloy constitution. If the binder is considered, the microscopic shape varies from planar to cellular dendritic, to columnar and finally equiaxed dendritic. In alloys the solidification is complicated because the redistribution of alloy elements leads to concentration gradients adjacent to solid-liquid interfaces. When the temperature of the liquid ahead of the solidification interface is lower than the equilibrium liquidous temperature corresponding to the compositional variation, the constitutional

supercooling occurs and the planar interface is unstable [255]. The criteria for the stability of the planar solid-liquid interface can be expressed as :

$$\frac{G_L}{R} = \frac{\Delta T_s}{D_L} \quad (Equation\ 2.9)$$

Where G_L is the temperature gradient in the liquid region, R is the solidification rate, ΔT is the solidus and liquidus temperature difference and D_L is the diffusion coefficient in the liquid zone. The size and morphology of the solidified microstructure can be determined using the combined form of the temperature gradient G and the solidification growth rate R, which is shown in Fig. 2.8 [259].

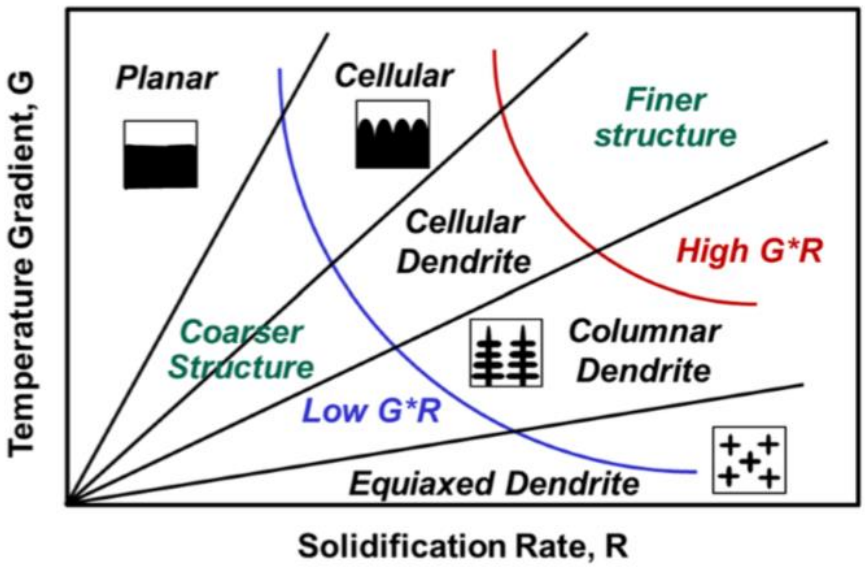


Fig. 2.8:The effect of G and R on the solidification morphology and size [126].

The ratio of G/R indicates the solidification morphology whereas the product of G and R represents the same of the solidification microstructure. Planar growth is when G is extremely high and/ or R is extremely low. As R increases the

solidification morphology can shift to cellular, columnar then equiaxed dendritic. Most metal alloys solidify in cellular or columnar dendritic [125], [126], [213], [260]–[263]. Cellular and columnar structure growth occurs when no secondary dendrite arms form. If the additional arms forms, then the structure shifts to dendritic form. The equiaxed form is only possible when G is exceptionally low. As the cooling rate of the liquid in front of the solidification boundary increases (product of G and R) a finer dendritic microstructure is formed.

From a numerical simulation study, R near the centerline was approximately equal to the beam traverse speed at the top of the weld pool surface. R decreased sharply near the bottom of the weld pool due to the large angle between the boundary normal to the travel vector. At the outermost later edges, the weld pool boundary normal vector was nearly normal to the travel vector at all depths so no notable change in solidification as observed. The simulation predicted an inverse relationship between G and R as seen in Fig. 2.8 and Equation 2.9. The simulation also showed the solidification boundary cooling rate that decreased from top to bottom and from the rear centre to the outermost lateral edge of the weld pool, inverse to the variation of the predicted arm spacing [126]. The melt pool thus has many complex factors that can alter the final microstructure which is observed. That is why research is abundant with numerical simulations in the attempt to model all of these complexities without the need to perform extensive and expensive experimentation [237], [238], [264]–[269].

It is evident from Fig. 2.7 and Fig. 2.8 that many different microstructures may form during the laser sintering process depending on the solidification rates, alloy composition and temperature gradients which are present during the deposition process. It is due to this that the LENS® process has been applied to a variety of materials, all with varying chemical compositions and properties. It can be seen from Table 2.2 that titanium and its alloys are the most studied materials using the

LENS® process. After redesigning the powder feeder capabilities, Griffith et al. [270] proved that LENS® can be used to manufacture both multi-material layered structures as well as graded materials. Using SS316 and Inconel 690 they were able to produce an alternating layered sample as well as a separate graded sample. Dense structures were obtained with the graded material possessing the probability of tailoring final microstructures and hardness.

Table 2.2: Materials which have been fabricated using the LENS® process.

Material	Summary
Inconel 625	By using Inconel-625 and maintaining an energy density of 242.42J/mm^2 and powder density of 0.05g/mm^2 the authors were able to reduce production time by 83 percent. The higher process parameters used resulted in a higher hardness, density and part dimensions although yielding a larger surface roughness compared to lower process parameters [141].
Surface Mod of AISI 410 stainless steel	A 55% increase in surface hardness was reported, when compared to conventionally heat treated samples [56].
Ti-6Al-4V-TiB composites	Homogenous refined dispersion of TiB formed in situ. LENS® composites thermodynamically stable and show limited TiB coarsening [271].
Ti-10%Cr/Ti-10%Nb	A negative enthalpy of mixing, corresponding to the Ti–10% Cr alloy, results in more homogeneous intermixing in the melt pool as well as a rapid rate of solidification. In contrast, a positive enthalpy of mixing, corresponding to the Ti–10%Nb alloy, results in poor intermixing, an inhomogeneous alloy, and a slower rate of solidification [272].
Ti-TiO2	Porous Ti was fabricated with a 50% TiO_2 surface through functional grading. This resulted in a higher wettability of the surface and four times greater hardness [273].
Titanium aluminide matrix composites(carbide reinforced)	Both monolithic and composite feedstocks were susceptible to solid state cracking due to high thermal stresses. Crack-free deposits were obtainable by preheating the substrate material. Fabricated composites exhibited hardnesses twice that of Ti-6Al-4V[274].
TiC/Ti FGM	Functionally graded material was produced from pure Ti to 95 vol% TiC [275].
Ti-6Al-4V	Mass flow rate and scan velocity have the largest effect on deposition rate. Deposition is 2.5 times less sensitive to hatch spacing changes and 4.5 times less sensitive to power changes [276].

Ti alloys and SiAl	Ti burn-resistant alloy and high Si alloy have large processing windows and 100% dense microstructures can be obtained. Ti-6Al-4V has a narrow processing window and can easily become porous [277].
Inconel 625,H13 steel and SS316	Researched alloys have material properties comparable to conventionally processed wrought material and occasionally exceed those of annealed materials [205].
84Ni-14.4Cu-1.6Sn (wt. %)	Thick walls were fabricated with a width of 20-25mm. Dendrites with different characteristics were grown in the three dimensions [278].
Co-Cr-Mo coating on porous Ti-6Al-4V FGM	Crack free coatings were obtained up to a mixture of 86% Co-Cr-Mo depositions on Ti6Al4V as a functionally graded system [279].
High entropy alloy AlCoCrFeNi	The microstructure of the LENS® product was dendritic. The increase in laser scanning rate resulted in the decrease in the average grain size. The average hardness obtained was 543 $HV_{0.5}$ and the increase in cooling rate resulted in the increase in the micro hardness of the alloy [280].

A LENS® 750 was used to fabricate functionally graded samples (FGM) with a diameter of 10 mm on a 3 mm thick Ti substrate [273]. The first hopper was filled with pure Ti and the second with pure TiO_2. The first 10 layers were manufactured with 200 W of laser power to create a 30 % volumetric porosity. The following 5-10 layers were made with the top surface ending with a 50%, 90% and 100% TiO_2 percentage. This was done by using a scan speed of 22.5 mm/s and 300 W of laser power but varying the feed rates in the gradient zone. The Ti powder was initially 100% at a feed rate of 17.5 g/min and gradually decreased to 0% on the surface layer while the TiO_2 was initially 0% and varied to 100% with a feed rate of 23.7g/min. It was found that the sample with 50% TiO_2 on the surface layer resulted in a hardness four times greater than the hardness of laser processed Ti [273].

A 3.175 mm thick Ti64 substrate plate was used as a platform to construct functionally graded Ti/TiC samples using a LENS® 750 system [275]. The FGM samples were 12.7 mm x 12.7 mmx 20 layers. A power of 420 W was used with

a traverse speed of 8.5 mm/s. The layer thickness, hatch spacing, and stand-off distance were set a 0.38, 0.38 and 154.2 mm respectively. The hoppers were set such that the first layer was 100% Ti and gradually became 95% TiC. The hardness of the deposits was found to increase from 200 HV to 2300 HV. When compared to homogenous composite deposits, the FGM created by the LENS® prevented the formation of cracks [275].

Laser engineering net shaping was found to make metallurgically sound FGM of 100% Ti6Al4V on one side gradually fading into 86% Co-Cr-Mo [281]. The FGM process using LENS® results avoids the cracking and delamination which is observed when a Co-Cr-Mo layer was cladded onto the base Ti64. It was found that crack-free coatings were obtained up to 86% Co-Cr-Mo although 50% Co-Cr-Mo resulted in a better coating for biological environments [281].

2.4 LENS® of Cemented Tungsten Carbides

Tungsten carbide-alloys have not been studied to the extent of other alloys using the LENS® process. Literature which has shown the closest correlation to the proposed field of research is summarized in Table 2.3.

Table 2.3: Summary of LENS® literature findings for various cemented WC compositions.

Material	Density (%)	Laser Power (W)	Traverse Speed of laser (mm/s)	Feed Rate (g/min)	Hardness (GPa)
Submicron WC-13wt.% Co and nanocrystalline WC-10wt.% Co[59]	96-97	180-200	2-4	7-10	
Nanocrystalline WC-Co (80wt.% W, 5.1wt.% C, 10wt% Co)[9]	97	200	3	10	13.00 ±1.09
Nanocrystalline WC-Co powder (84wt.% WC , 12wt% Co)[47]	99.5	200	3.2	7.5	12.9-13.7
WC -12%Co [282]	97-98	350 450	10	24	350W 11.58+0.52 450W 11.49+0.56
Nanosized, single phase (Ti, W)C with Ni binder [92]	94-95	260-300	2-4	3-5	

Xiong et al. [59] used the LENS® process to deposit thick walls using a submicron and nanocrystalline powder. Thick wall samples (1.5 mm thick comprising of multiple parallel lines/layers) were prepared using two powder feedstocks, a LENS® 750 OPTOMEC system and varied parameters. Powder A-submicron WC-13 wt.% Co powder (40 µm-110 µm) and Powder B-nanocrystalline WC-10 wt.% Co powder (45 µm – 90 µm), with the submicron powder produced via wet-chemical plus spray-drying process, provided by Infant Corp. Farmington CT.

The effect of process parameters, Table 2.4, on the height of the manufactured thick wall samples was investigated.

Table 2.4: Parameter range used for optimization of LENS® process.

Experimental Parameter	Range
Laser power	140-200W
Powder feed rate	7-21 g/min
Traverse speed	2-11 mm/s
Working plane	Focal plane ±4mm

*Oxygen concentrations were maintained below 5ppm.

With powder A, power values were chosen between 160W and 200 W. The other processing parameters were kept constant at a traverse speed of 2.1 mm/s, feed rate of 7.0 g/min and layer thickness of 0.127 mm. The working distance was set in correlation with the optical focal plane of the laser beam. When 200 W was used the final thick wall had a relative density of 11.7 g/cm^3 which is 81% of the theoretical. An increase in build height was observed with an increase in power as seen in Fig. 2.9.

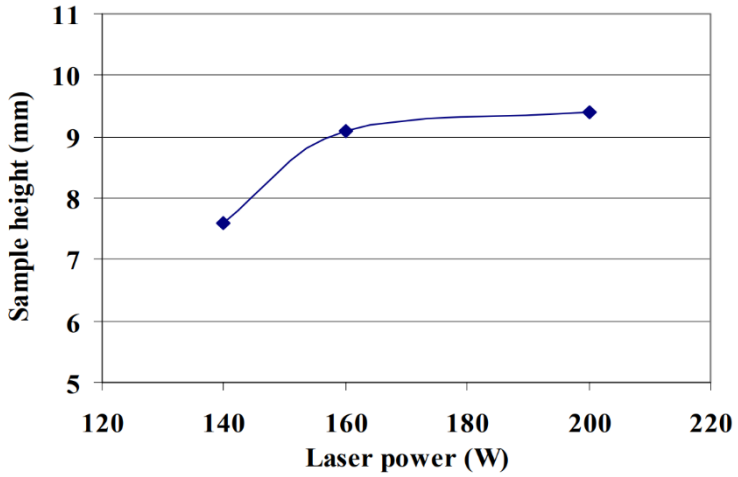


Fig. 2.9: Influence of laser power on sample height [284].

When using constant parameters of 160W, 6.4 mm/s traverse speed, layer thickness of 0.127 mm and working plane set at the focal point of the lens, powder feed rate values of 11, 12.4, 14.9, and 20.4 g/min were used. An increase in build height with an increase in the feed rate was observed as seen in Fig. 2.10 and Fig. 2.11.

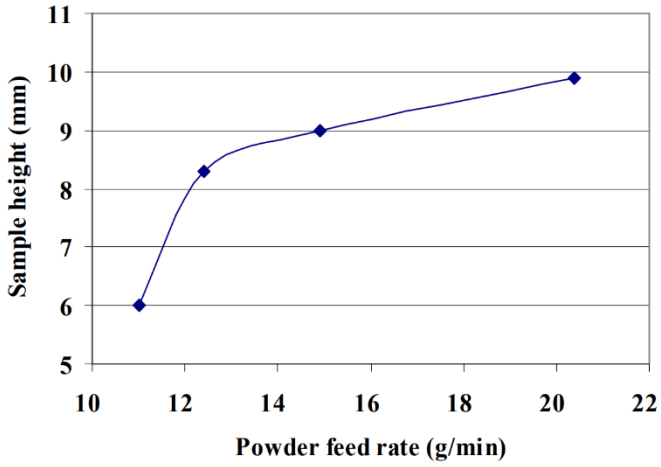


Fig. 2.10: Influence of powder feed rate on sample height [284].

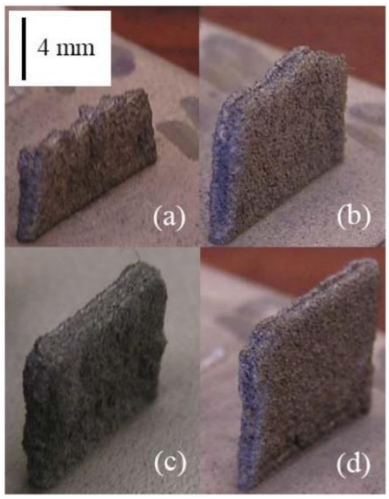


Fig. 2.11: (a)-(d) Change in sample height and profile with an increase in powder feed rate for WC-13wt%Co [60].

With a constant 160W of power, feed rate of 14.9 g/min, layer thickness of 0.127mm and the working plane set at focal plane of the lens high traverse speeds resulted in a rapid decline in sample height due to an inadequate amount of powder being deposited per unit length, as seen in Fig. 2.12 and 2.13.

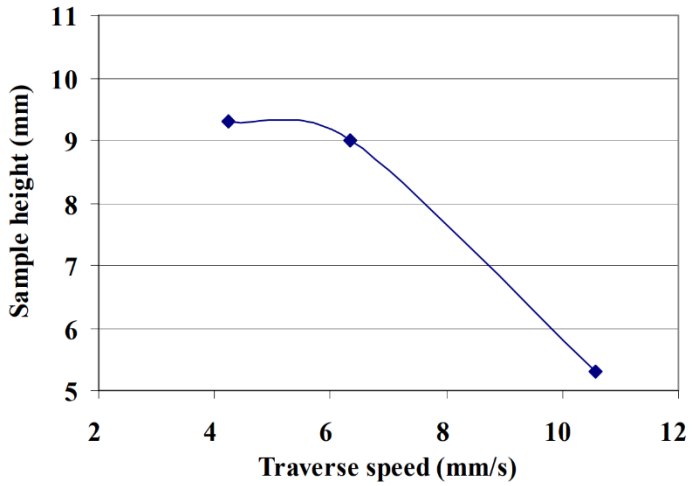


Fig. 2.12: Influence of traverse speed on sample height [284].

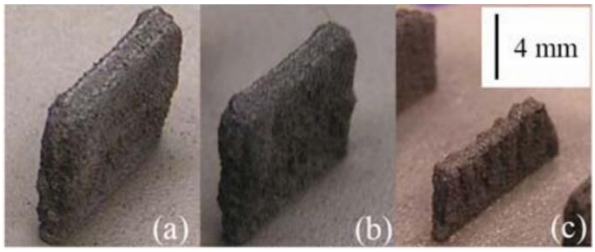


Fig. 2.13: Influence of traverse speed on sample height and profile: (a) 4.2 mm/s, (b) 6.4 mm/s, (c) 10.6 mm/s [284].

Powder B was used with a power of 200 W, feed rate of 10 g/min, traverse speed of 3mm/s and layer thickness of 0.203 mm. When the working plane was set 2 mm higher than the focal plane of the lens it resulted in sample density of 12.9 g/cm^3, 97% of the theoretical density. When the working plane was set 4mm higher than focal plane of lens and layer thickness of 0.127mm it resulted in density of 12.8 g/cm^3, 96% of the theoretical density.

Optimization:

By performing the systematic study an optimal operating range was determined, as shown in Table 2.5. The Z height increment should be set equal to actual layer thickness, deposited by the laser, to keep working distance constant.

Table 2.5: Optimized LENS® parameters for WC-Co.

Experimental parameter	**Range**
Laser Power	180-200W
Powder feed rate	7-10g/min
Traverse speed	2-4mm
Working plane	Focal plane + 2~4mm

It was also found that the decomposition of WC is sensitive to grainsize. No decomposition was observed with the submicron-sized powder however there was occurrence with nano-sized powder. By applying a shorter working distance, a greater specimen density and microstructure was obtained.

Xiong et al. [9] used a nanocrystal line WC-Co (80wt. % W, 5.1wt.% C, 10 wt.% Co) powder, without any grain growth inhibitors, made by MBM Nanomaterialia, was used, as shown in Fig. 2.14.

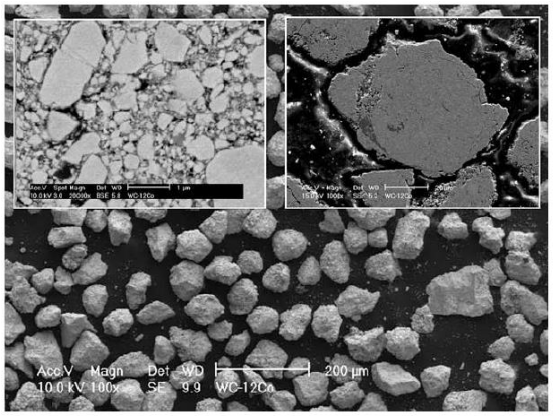


Fig. 2.14: SEM SE images of nanocrystalline WC-10%Co powder.

The powder was produced by high energy ball milling to a granule size range of 45-90 µm. Average grain size of WC was found to be less than 30 nm by manufacturer. The irregular shape of the particles, as seen in the SEM image, is due to the effect of the ball milling. A LENS® 750W (OPTOMEC, Albuquerque, USA) was used to perform the powder deposition of the constructed CAD model. A solid, thin wall design with a nominal length of 20 mm and height of 13 mm was deposited on a stainless-steel substrate. Each layer consisted of four parallel lines as was set to a height of 0.2 mm per layer. The laser parameters were set to a power of 200W, traverse speed of 3 mm/s and a powder feed rate of 10 g/min. Oxygen levels were maintained below 5 ppm. Density was calculated to be 12.9 g/cm^3 which is 97% of theoretical amount. The average wall hardness measured was 1326 ± 111 HV.

An alternating layered microstructure was obtained with one layer having a fine microstructure and the second a course WC microstructure due to the remelting of the surface of the lower layer. The same observations were observed by [285] when studying the influence of working distance on laser deposited WC-Co. Some grains remained below 100 nm and others grew to between 1 and 2 µm.

Picas et al. [47] used three coating consolidation techniques to study the effect of microstructure and wear resistance of WC-Co. One of the coating techniques was performed using a LENS® 750 system (OPTOMEC, USA). A nanocrystalline WC-Co powder (84 wt.% WC, 12 wt.% Co) was used with an agglomerate size distribution (Gaussian) between 20 µm and 90 µm, a laser power of 200 W and a traverse speed of 3.2mm/s with a feed rate of 7.5 g/min. The layer thickness was chosen to be 0.2 mm and three layers were deposited. The properties obtained for the LENS® sintered depositions are shown in Table 2.6.

Table 2.6: Micro and ultra-micro hardness test results (mean values) amended from [47]

Property	Value
Porosity (%)	0.51
Micro hardness $HV_{0.3}$	1315-1397
Universal hardness (GPa)	10.40-10.68
Plastic Hardness (GPa)	16.06-16.34
Young's Modulus (GPa)	416-468
Elastic Recovery (%)	30.2-33.1

The two values are recorded due to the measurements being obtained moving from the coarse carbide zone to the fine carbide zone.

The amount of $Co_XW_YC_Z$ phase depended on the grain size of WC and the heating/cooling rate. The nanostructured WC grains have high surface area per unit volume, which results in a greater likelihood of being dissolved into the liquid phase at high temperature. However, the W_2C and Co_3W_3C phases are limited due to the high cooling rate during the LENS® process. Balla et al. [282] used a cast, crushed WC -12%Co powder (supplied by Powder alloy Corp. Loveland OH with a particle size between 45 and 75µm) as a coating material on a 3 mm 316 stainless steel substrate.

The powder was deposited to a thickness of 1.5 mm-2.0 mm and a diameter of 13-14 mm using a LENS® 750 OPTOMEC system. The laser had a beam diameter of 1.65mm and oxygen levels were maintained below 10 ppm during laser sintering. A laser power of 350W (365 J/mm^3) and 450 W (465 J/mm^3) were used respectively with a traverse speed of 10 mm/s and a feed rate of 24 g/min. A layer thickness of 1.8 mm+ 0.06 mm and 1.35 ± 0.06 mm was obtained for 450 W and 350 W respectively with the 350 W build resulting in approximately 2-3% porosity. The 450 W power resulted in a layer with a hardness of 1172 ± 57 HV while the 350 W resulted in 1181 ± 53 HV.

Xiong et al. [283] used TiO_2 (99% purity, 45 µm average size), WO_3 (99% purity, 20 µm average size) and NiO (99% purity, 45 µm average size) which was mixed with free carbon for the composition equivalent to TiC-15WC-20Ni (wt.%). Powders were subjected to high energy ball milling using a planetary mill. Tungsten carbide balls were mixed with oxide powders at a ball to powder weight ratio of 40:1 and milling was conducted at a speed of 250 rev/min for 20 hours. The oxide powder mixtures were reduced to ($Ti_{0.93}W_{0.07}$) C-20wt%Ni powder at 1300 °C for 1hour in vacuum. The (Ti, W) C-Ni powder was compacted into disc under 150 Pa pressure and sintered at 1510 °C for 1 hour under vacuum. Conventional micrometer sized TiC-15WC-20Ni (wt.%) were sintered for comparison. The conventional samples were prepared from TiC (1-2 µm) and WC and Ni powders (1-4µm).

It was found that core-rim structures were not observed for the (Ti, W) C-Ni cermets made by LENS® and sintering process. LENS® processed (Ti, W) C-Ni resulted in inhomogeneous microstructure with particle coursing whereas the sintered cermets have uniform microstructure. LENS® processed specimens have high hardness and

relative low toughness due to vaporization of the nickel binder during deposition and high porosity.

Xiong et al. [286], conducted a study to investigate the thermal behaviour during LENS® deposition of WC-Co material. A high-speed digital camera system was applied in this work to record the thermal images of a WC-Co thick-walled sample. The CAD model dimensions used for this work were: 20.3 length, 0.8 mm width and a height of 12.7 mm. It was established from the investigation that the highest temperatures are experienced in the centre of the molten pool. As the heat source moves, the previously deposited layers experience a rapid drop in temperature. Fig. 2.15 shows the thermal cycle of a LENS® deposited WC-Co cermet, where the green circle indicates the solid-liquid interface.

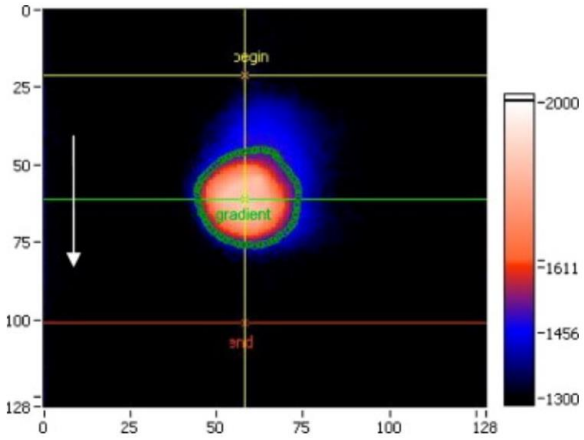


Fig. 2.15: A thermal image of a WC-Co thick-walled sample looking from the deposition of layer 5 [286].

As the deposition layers of WC-Co increases it was established that the highest temperature was not experienced in the centre of the molten pool anymore. A swirling effect was observed as high temperatures where experienced in random

areas within the molten pool, this effect was explained to be caused by the dispersion of WC in the molten pool. In addition, it was seen that as the deposited layers increase the molten pool size and temperature increased, which is attributed to heat build-up from layer to layer. Fig. 2.16 shows the temperature profile in some deposition layers.

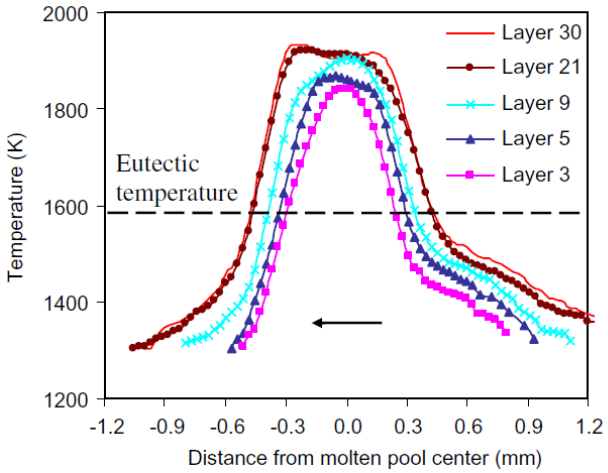


Fig. 2.16: Temperature profile in selected deposition layers [286].

The thermal behavior of WC-Co cermet deposited by the LENS® technology has a correlation to the microstructure with alternating layers and inconsistent hardness with change in specimen height.

A life-cycle assessment of the LENS® process versus conventional powder metallurgy was compiled by Xiong et al. [287]. The life-cycle assessment of WC-Co manufactured by the conventional powder metallurgy (P/M) and LENS® process is shown in Fig. 2.17.

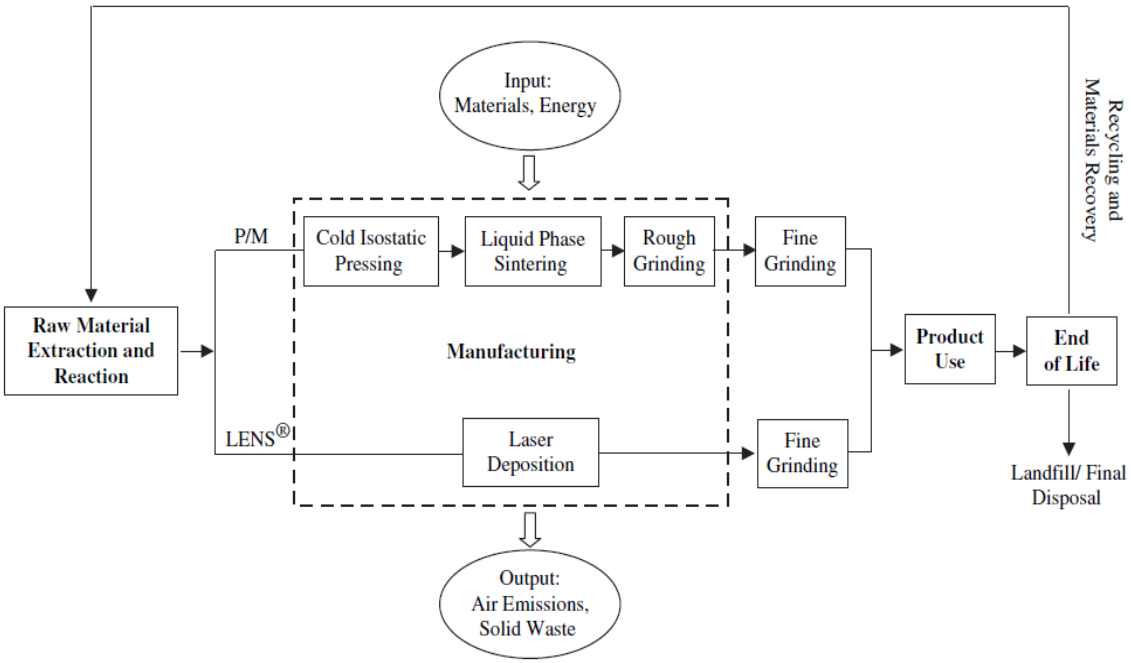


Fig. 2.17: Life-cycle of a WC-Co cermet product manufactured by either the P/M or the LENS® process [287].

It has been observed that the LENS® process consumes more energy and cooling water than the P/M process [287]. However, the LENS® process requires less argon gas, WC and Co consumable materials, provided that the WC-Co powder can be recycled. There is a high scrap rate in P/M processes due to material loss during rough grinding. The LENS® process is beneficial in comparison to P/M processes provided that it is used to produce small volume components, hence low energy consumption [287]. Complex shapes produced with P/M processes leads to increased grinding requirements and hence an increase in the material scrap rate. According to the life-cycle analysis the LENS® process is beneficial if powder recycling is possible, part size is small and part shape is complex [287]. Alternatively, the P/M process is only beneficial for the production of large parts with simple shapes.

The density of the component which is fabricated is not as high as for conventional sintering methods, hence the importance of the laser processing parameters. Fig. 2.13 is an example of the effect of varied process parameters during fabrication using LENS® [60]. By merely changing the powder feed rate, the thin walls exhibited different heights and surface roughness. Once the ideal parameters have been obtained, LENS® can be used to create complex WC-alloy parts for specialized applications in a fraction of the time that would be required for conventional sintering.

Chapter 3 Experimental Procedures

3.1. Feedstock Powders

Spherical tungsten carbide powder from Boda Hard-facing Materials Co, LTD (particle size distribution of -90 /+ 45 µm) and spherical Monel (Ni-alloy) powder from Praxair Surface Technologies (particle size distribution of -90 /+ 45 µm) were used as the feedstock powders. The physical and chemical properties of the powders were verified by means of X-ray diffraction (Bruker D2 Phaser), particle size distribution (Malvern Mastersizer) and scanning electron microscopy (FEI Nova 600 SEM) coupled with energy dispersive spectroscopy (EDS INCA analysis software).

Table 3.1: Elemental composition of Monel 400.

Element	Ni	Cu	Fe	Mn	Si	S	C
Average Wt.%	68.7 ±2.12	27.99 ±2.02	2.32 ±0.25	0.66 ±0.09			
Wt.% (literature) [288]	63.0 min	28.0-34.0	2.50 max	2.00 max	0.50 max	0.024	0.30 max

Particle size was determined by using a Malvern Mastersizer, Fig. 3.1. Particle size analysis was performed to verify that the supplied powder did comply with its data sheet.

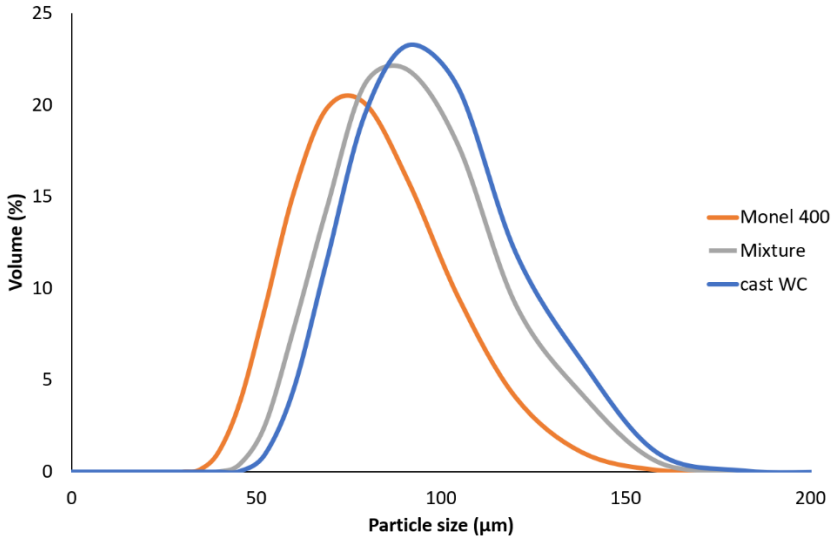


Fig. 3.1: Size distribution of a) WC Powder b), Monel 400, c) WC-9.2wt% Monel 400

A mean particle size of 86.08 µm was obtained for the cast WC powder. There is a 21.76 µm difference between d (0.1) and d (0.5) and 29.38 µm between d (0.9) and d (0.5) which is well within the reported standards of the ordered powder which were -90 µm /+ 45 µm. The Monel 400 powder was found to have a mean particle size of 69.46 µm. There is a 19.70 µm difference between d (0.1) and d (0.5) and 27.08 µm between d (0.9) and d (0.5) which indicates that the mean powder size is approximately 20 µm less than the reported value of -90 µm /+ 45 µm. The larger deviation between d (0.9) and d (0.5) is due to the irregular shape of some of the powder particles as well as the satellite effect which is very prominent in Fig. 3.2(d). When the powders were mixed together a mean of 81.20 µm was obtained. There is a 21.73 µm difference between d (0.1) and d (0.5) and 28.25 µm between d (0.9) and d (0.5) which is within good correlation of the Laser Engineered Net Shaping specifications of -90 µm /+ 45 µm. The larger deviation between d (0.9) and d (0.5) is due to the constituent powders having a slightly larger deviation between d (0.5) and d (0.9).

As shown in Fig. 3.2, the WC powder had smoother, more regular particles than the Monel powder. The latter powder showed a bimodal nature consisting of smaller and larger particles. The smaller particle tends to agglomerate around the larger one during solidification, creating irregular shapes of the powder agglomerates. The grain structure of the Monel 400 and WC powder can be seen as recessed grooves on the surface of the particles [289]. The two powders were mixed in a stainless-steel rotary mill for 2 hours to produce a WC-9.2wt%Monel 400 powder blend. The XRD patterns in Fig. 3 show that the mixed powder has all the peaks that were present in the substituent powders with no mixed phases between the two powders detected. The XRD pattern in Fig. 3.3(c) of the blended powder shows prominent WC, W_2C and W peaks originating from the WC powder with NiCu peaks coming from the Monel powder. No mixed phases between the two powders were detected.

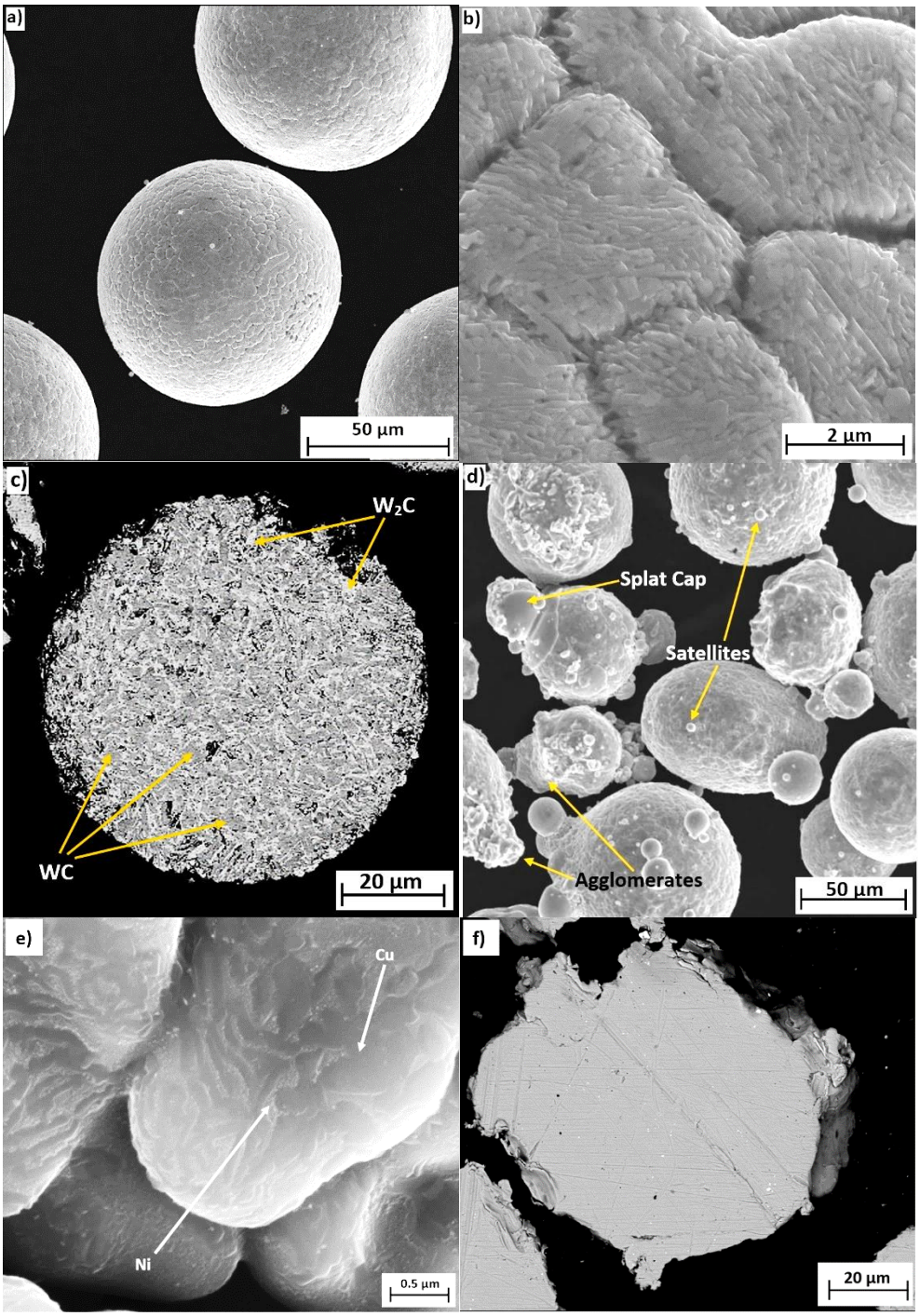
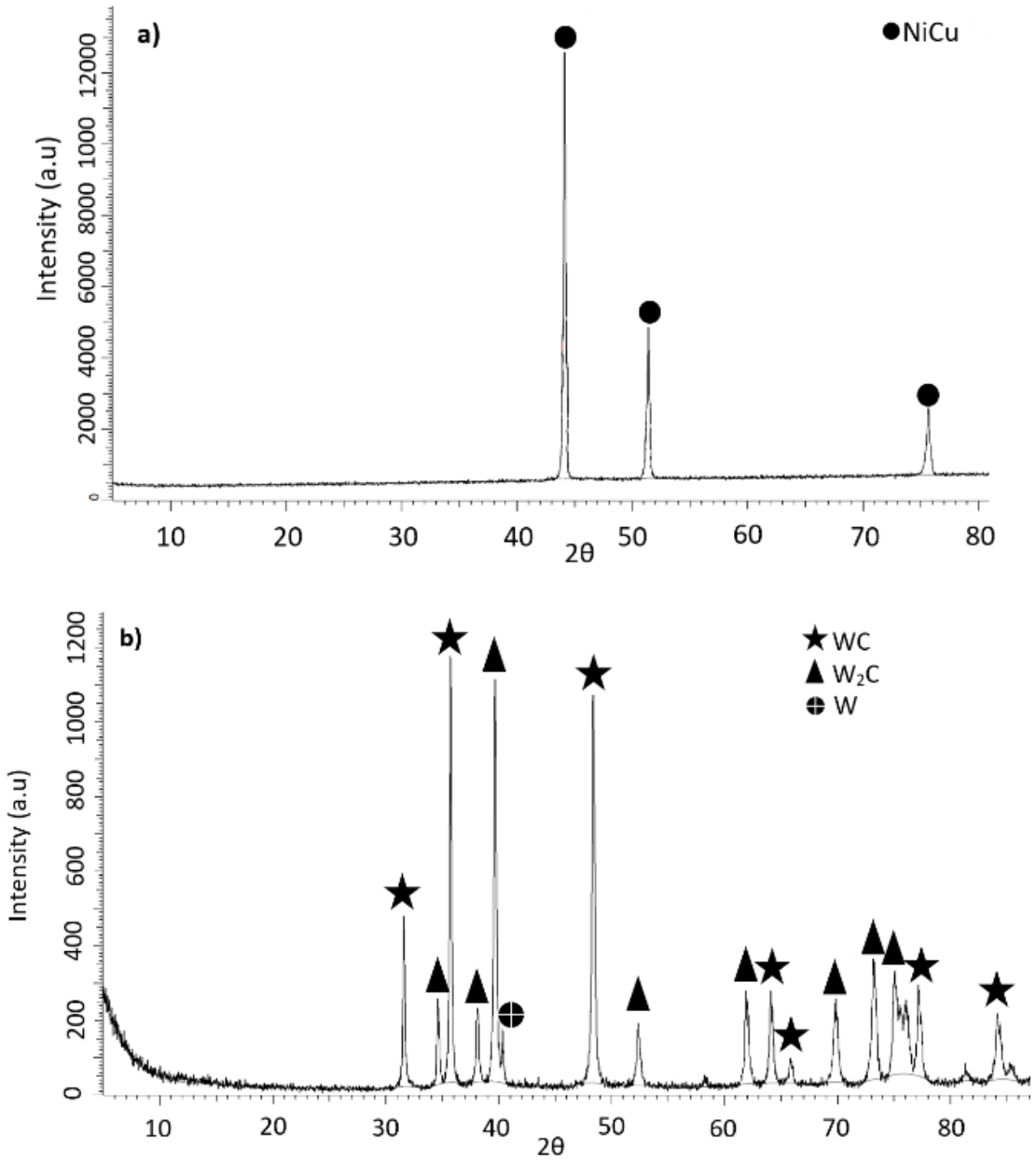


Fig 3.2: SEM micrographs of the a) tungsten carbide, b) surface of WC particle, c) cross-section of cast WC particle and d) Monel powder.


a)
NiCu
Intensity (a.u)
2θ
b)
WC
W2C
W
Intensity (a.u)
2θ

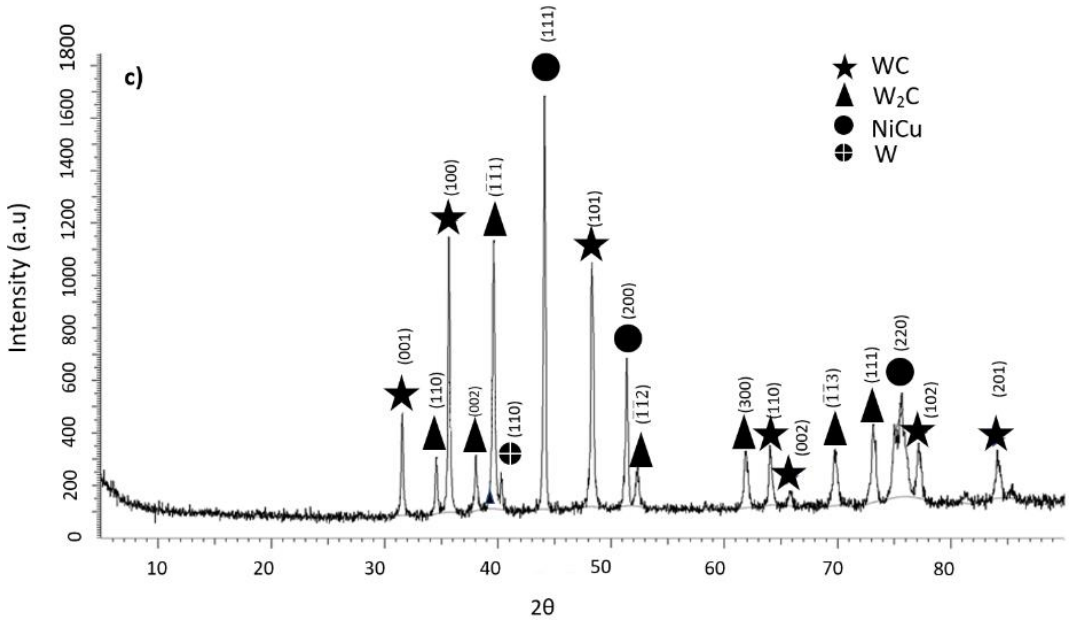


Fig. 3.3: XRD pattern of the mixed WC-9.2wt%Ni feedstock powder.

3.2 LENS® production of alloys

Design of experiments (DoE) and statistical based approaches have been used by numerous researchers [290]–[294] to provide valuable information for the generation of numerical models, machine learning parameter optimizers and finite element analysis models. The framework used in this study is based on these with adaptations made to the optimization process to produce a functional component. It is also provided in a simple layout such that it can be applied in any iterative parameter testing situation.

The framework in Fig. 3.4 was used to optimize the parameters for the deposition of a functional component, i.e. a drill bit, by starting with thin walls and optimizing through small-scale samples. The framework is divided into several phases which are discussed in more detail providing a general overview and the approach used in this study. All depositions were performed using an Optomec LENS® 850-R equipped with a 1kW IPG fibre laser, wavelength of 1.072 µm, a delivery fiber

diameter of 200 µm, a collimator focal length of 60 mm and beam spot size of 1.35 mm. All experiments were conducted in the build chamber under atmospheric conditions and using a mild steel substrate. All samples were sectioned using a diamond cutter (Struers Secotom-10) and the cross-sections were mounted in Struers Polyfast resin using an ATM Opal 410 mounting machine. The samples were polished in accordance with the ASTM B665-08 procedure [295].

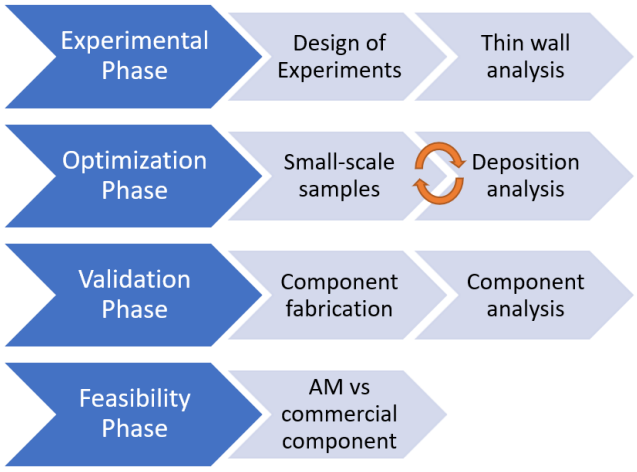


Fig. 3.4: Framework for component fabrication from novel binder.

3.2.1 Experimentation phase

Design of experiments

Design of experiments have been used by multiple researchers to perform optimization experiments [296]–[299], [300]. Many experimental design templates are available within statistical software and are calibrated using the desired outcomes of the study. Two examples of widely used design of experiments are Factorial designs and Taguchi designs. Factorial based designs consider all possible interactions that occur for each of the input factors and results in large experimental sets. Factorial designs allow for interactions between parameters to be determined although one pitfall is that some interactions may be confounded and if not considered can lead to highly erroneous conclusions [301]. Taguchi designs are based on fractional factorial designs as well as factorial designs with

multiple factors being tested. With Taguchi designs, the most significant interactions need to be hypothesized before the experimental processes is commenced. A design of experiments allows for analysis of variance (ANOVA) to be applied to the obtained experimental data and provide results which pertain to the experimental range employed. Any variable sets which are beyond the scope of the study can be extrapolated although this assumes that the mathematical nature of the results is consistent over any variable set, which is not necessarily true. When a novel binder or material is the subject of the research and no defined literature is available, then other materials which have been used for the intended application or the major alloying substituents can provide a guideline as to the manner the material may react and provide beneficial properties in determining feasible initial parameter sets.

For this study a 3x3 full factorial DoE was used including star points. The range which was chosen was hypothesized to contain a local “optimized” set which cannot be defined as a globally “optimized” set due to the restrictive nature of the design of experiments. Three important parameters were considered in the design of experiments as not all parameters can be tested in the design of experiments since the addition of another parameter has an exponential effect on the number of depositions required. The laser beam power (P), traverse speed (v) and powder flow rate (κ) were chosen since literature [233], [302], [303] has identified these as the main deposition parameters. Three parameters at a low, medium and high level for each parameter yields a 3x3 matrix. Three levels provide more information about the interactions of the parameters and the inclusion of star points provides more information about the parameter sets around the “central” values of the design matrix. The design parameters were based on published research for a Co binder (in the absence of data for Ni binders) and the knowledge that Ni has a lower melting point than Co [302], [304], [305]. Table 3.2 lists the range of values used in constructing the DoE matrix.

Table 3.2: Values used in constructing the design of experiments matrix.

Experimental number	Factor level		
	P	v	κ
1	150	2	5
2	150	2	7.5
3	150	2	10
4	150	3	5
5	150	3	7.5
6	150	3	10
7	150	4	5
8	150	4	7.5
9	150	4	10
10	250	2	5
11	250	2	7.5
12	250	2	10
13	250	3	5
14	250	3	7.5
15	250	3	10
16	250	4	5
17	250	4	7.5
18	250	4	10
19	350	2	5
20	350	2	7.5
21	350	2	10
22	350	3	5
23	350	3	7.5
24	350	3	10
25	350	4	5
26	350	4	7.5
27	350	4	10
28*	336.6	3	7.5
29*	163.4	3	7.5
30*	250	4.7	7.5
31*	250	1.3	7.5
32*	250	3	11.8
33*	250	3	3.2

Thin walls provide an ideal deposition design for rapid variable set determination due to low deposition times. The thin walls were 20 mm in length, 25 layers high with a z-increment of 0.2 mm and on a single deposition track.

Thin wall analysis

Once the thin walls have been deposited analysis needs to be performed such that feasible parameters can be obtained for the optimization phase. If there are any visible cracks, agglomerated particles causing surface roughness, poor adherence to the base plate or insufficient build height in the depositions then the parameter sets should be excluded. The properties of interest should be recorded, such as height, width or porosity for each parameter set so that an analysis of variance can be performed and the effect of each parameter as well as parameter interactions can be determined for the desired property. The desired parameter set is then used in the optimization phase with small-scale depositions.

The height, width and Vickers hardness were analyzed and recorded for the 33 DoE trials. The height and width was measured using Vernier Calipers while the Vickers Hardness was determined using 30 kgf with a 10 s dwell time (Future-Tech FV-800) in accordance with ISO 3878 [306]. Vickers hardness was chosen since it can be used on any material and only one type of indenter is used for all Vickers methods. It is limited in the need for specimens to be prepared with a good surface quality due to optically based analysis of the indentations and the relatively long test cycle times [307].

The theoretical height and width of the thin walls were calculated using the z-increment and beam spot size respectively. An ANOVA regression and the resultant quadratic function was used to determine the most feasible parameter set, for the optimization phase. The parameter contributions and interactions in yielding a specific height, width and hardness were also analyzed.

3.2.2 Optimization phase

Small-scale samples

Small-scale samples can now be used to test the best parameter sets obtained from the experimentation phase. Small cubes, as in Fig. 3.5(a), can be deposited and have been used in multiple publications as an optimization standard and many researchers use these as a base to subtractively machine tensile components [308]. The samples are now larger than thin walls and filled with a rastering pattern which introduces different thermal gradients and cooling rates during deposition which allows for the parameter sets to be refined further. The set which performed best on the thin walls may not be the best solution for filled geometries but provided a feasible starting point. There are many parameters which can be altered such as hatch rastering pattern, z-increment, laser beam working distance, spot size and hatch overlap which will change the properties of the final deposition. The thin walls were deposited at a certain laser beam spot size and working distance, for the parameter sets to thus translate more efficiently these should be kept consistent. Depending on the results obtained for the deposition analysis different parameters are changed for each iteration until the required physical or chemical property is obtained.

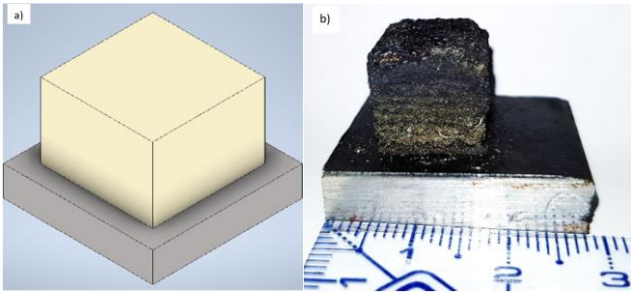


Fig. 3.5: a) general schematic for cubic structure and b) as-deposited cube and

In this study three iteration phases were performed. The first consisted of the laser beam power, traverse speed and powder feed rate being altered although maintaining a fixed energy density [309], as determined from the design of experiment phase with a hatch overlap of 50% and 75% respectively, beam spot size of 1.35 mm and z-increment of 0.2 mm. An as-deposited cube can be seen in Fig. 3.5 (b).

The second iteration used the parameter set from the first iteration which yielded the lowest porosity. Different powder feed rates and z-increments were condensed into a single iteration to reduce redundant testing. The third iteration consisted of minor alterations to the hatch overlap and z-increment with the intention of reducing the final porosity. The experimental matrix of the three iterative refinements are shown in Table 3.3.

Table 3.3: The refinement of paraments through deposition of cubic samples.

Sample	Power (Watts)	Traverse Speed (mm/s)	Powder feed Rate (g/min)	Hatch overlap (%)	z-increment
1	150	3.5	9.5	50	0.2
2	170	4.0	10.9	50	0.2
3	200	4.7	12.8	50	0.2
4	220	5.2	11.5	50	0.2
5	250	6.0	16.35	50	0.2
6	270	6.3	17.2	50	0.2
7	300	7.0	19.1	50	0.2
8	340	8.0	21.8	50	0.2
9	150	3.5	9.5	75	0.2
10	170	4.0	10.9	75	0.2
11	200	4.7	12.8	75	0.2
12	220	5.2	11.5	75	0.2
13	250	6.0	16.35	75	0.2
14	270	6.3	17.2	75	0.2
15	300	7.0	19.1	75	0.2

16	340	8.0	21.8	75	0.2
17	220	5.2	11.5	50	0.31
18	220	4.3	12.5	50	0.55
19	220	4.3	10.9	50	0.5
20	220	5.2	12.6	50	0.31
21	180	3.5	7.7	50	0.5
22	220	4.8	12.7	50	0.5
23	220	5.0	13.3	50	0.5
24 (OP)	220	4.5	11.9	50	0.4
25	220	4.5	11.9	50	0.254
26	220	4.5	11.9	50	0.3
27	220	4.5	11.9	60	0.254
28	220	4.5	11.9	70	0.254
29	310	4.5	11.9	50	0.254
30	310	4.5	11.9	70	0.254
HS	220	4.5	11.9	50	0.4
RM	220	4.5	11.9	50	0.4

For sample HS (heated substrate) the parameters were maintained but the deposition was performed on a stage that was heated to 450˚C before the commencement of the deposition and sustained for the duration of the deposition. Remelting of the final layer was performed on sample RM (remelt) with the laser power and traverse maintained but the powder flow rate set to zero.

Deposition analysis

The final intended use of the component or aim of the research study will determine the analysis performed and desired optimization which will be obtained through the iterative process. Tensile strength, fracture toughness, microstructure, hardness or density are some of the properties that are of general interest [310]–[312].

The porosity was chosen as the deciding factor in the number of iterations required. The porosity was measured for each of the samples of the iteration and based on the values, the viability and necessity of the next iteration was determined. Porosity was determined from images obtained from Olympus stereo and optical microscopes. The porosity measurements were performed across the entire sample to provide an accurate bulk porosity. Fig. 3.6 shows a rectangular region which would be used to determine the porosity.

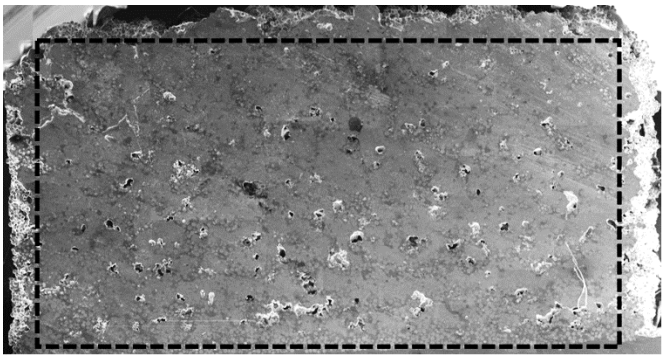


Fig. 3.6: Representation of the region used to quantify porosity.

The parameter changes which would reduce the porosity were hypothesized based on whether porosity or lack-of-fusion was observed [311], [313]. The hardness, chemical composition and microstructures were also studied [314] to understand and explain the deposition process with greater confidence. The Vickers hardness was determined using 30 kgf with a 10s dwell time (Future-Tech FV-800) in accordance with ISO 3878 [306]. Phase identification was done using XRD on a Bruker D2 Phaser (monochromatized Cu Kα, 0.154 nm). X-Ray diffraction was chosen for phase analysis since it is a rapid, non-destructive technique that provides well defined peaks for metallic samples with minimal sample preparation. It is limited by requiring access to standardized reference files and having a detection limit of 2% for mixed samples [315].

Elemental mapping was performed using electron probe microanalysis (EPMA) on a Cameca SX5-FE EPMA. Electron probe microanalysis was selected due to its high sensitivity in chemical analysis and the ability to operate at small spacial scales. It is limited in its ability to distinguish difference valence states and in detecting the three lightest elements which were not incorporated in the samples of this study [316].The microstructures were studied using field emission scanning electron microscopy (Carl Zeiss Sigma) and Energy Dispersive spectroscopy (EDS). Scanning electron microscopy has the advantage of having fast cycle times and the ability to be applied to any material while the main disadvantage apart from the equipment cost is the possibility of artifacts resulting from sample preparation [317]. Raman spectra measurements (0-2000 cm^{-1}) were carried out on a Horiba Jobin-Yvon T64000 Raman Spectrometer. Raman spectroscopy is nondestructive, non-contact and quick acquisition method. It has the disadvantage of not being effective in analyzing metals and alloys and the Raman effect is very weak [318].

3.2.3 Validation phase

Component fabrication

The optimized parameter set obtained from the optimization phase can now be applied to the validation phase. The final component is generally larger than the small-scale samples utilized in the optimization stage, which will affect the resultant cooling rates and thermal gradients during the deposition process [241], [319], [320]. It is important to monitor the first component print process to determine whether in-situ parameter adjustments are required to prevent the damage of the equipment, such as the deposition colliding with the deposition nozzle. These altered parameters can then be applied to the successive deposition process. By lowering the laser power, the powder being fed may not melt adequately and result in lack of fusion porosity, whereas the higher traverse speed will yield less time at each successive point and may also develop porosity. A higher traverse speed is

favorable over a lower laser power since this aids in faster printing, limiting layer thickness and reduces the alterations required to other parameters [233], [303].

Based on the quality control minor changes can be made to the deposition parameters to improve the final product, or the inclusion of post-processing techniques can be employed such as Hot Isotactic Pressing (HIP) to reduce the porosity, surface finish techniques to improve surface roughness or machining processes to enhance features of the final design. If none of these processes show a beneficial change or cause the product cost to elevate excessively then a new alloy should be examined for the process or a different manufacturing process or application should be investigated. The traverse speed was the only parameter which was altered to accommodate for the varied thermal properties and two drill bits were tested on a heated stage to determine the effect on the deposition process. The drill bit CAD design was constructed in Solidworks and once sliced resulted in 151 printable layers. A solid representation of the CAD design is shown in Fig. 3.7. All drill bit depositions were performed with a hatch overlap of 50%, beam spot size of 1.3 mm, z-increment of 0.4 mm and with atmospheric chamber conditions. Table 3.4 shows an overview of the main parameters that were used to fabricate the respective drill bits. All drill bits except DB4 underwent mild sharpening after fabrication.

Table 3.4: Printing parameters for drill bits.

Drill Bit	Power (Watts)	Traverse Speed (mm/s)	Powder feed rate (g/min)	Substrate	Fabrication time (min)
DB1	220,300	8.2	11.9	heated	100
DB2	220	10.25	11.9	heated	60
DB3	220	20.50	11.9	not heated	27
DB4	220	10.25	11.9	not heated	40

Quality control

The surface characteristics of the drill bits were examined and further von Mises simulations were performed to illuminate regions of high stress and indicate possible fracture zones during the quality tests. All von Mises and displacement simulations were performed with a global mesh of 0.77 mm with a tolerance of 0.038 mm. The drill bits were tested on a turn-mill at a rotational speed of 2000 rpm, a penetration depth of 6 mm with a feed rate of 100 mm/min. The holes were drilled into 2011 aluminium alloy which has a hardness of 90-100 $HV_{0.1}$. The holes were named according to the drill bit used and how many holes were drilled. E.g. DB1-1 would be the first hole drilled by drill bit DB1.

The images used to determine circularity were obtained using an Olympus light microscope and the fractured surfaces were studied using a low-resolution scanning electron microscope (TopCon SM-500). The circularity was determined using image analysis software. The image of the drilled hole was uploaded into the software where a circle is fitted to the hole ; the circularity is how close the fitted circle is to being perfect, with a value of one implying a perfect circle. An example is shown in Fig. 3.7 (b).

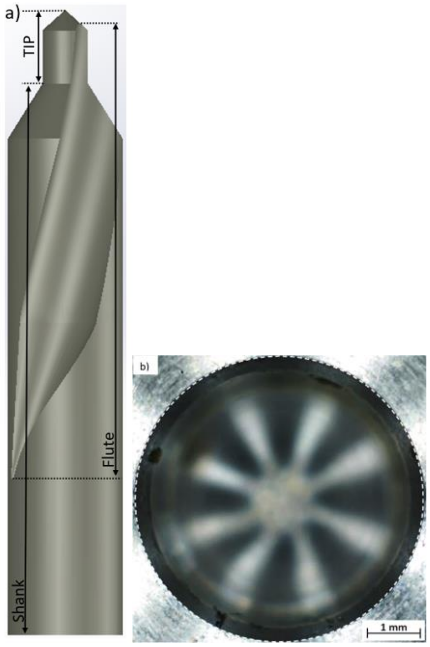


Fig. 3.7: a) CAD model of drill bit and b) diagram indicating a perfect circle fitted to a hole drilled by the purchased drill bit.

3.2.4 Feasibility phase

AM vs commercial component

This is concerned with the volume that needs to be printed, the time to print each component and the cost of the final part. A full cost analysis needs to be applied to the final product to determine whether additive manufacturing is in fact the most cost efficient and suitable method for the part production. Additive manufacturing has its strengths in low volume, highly customizable components, prototyping and concept validation [321]. If high volume is required, then additive manufacturing can be used to design a mold which will allow for rapid manufacturing thereafter using injection molding or metal casting. When accurate features and surface finish is required, a subtractive manufacturing process may be more suitable or even a different type of additive manufacturing such as metal binder jetting.

The manufacturing cost of the additively manufactured drill bit was compared to the price of a commercially available drill bit. The overall performance of the drill bits was also compared and the feasibility of using the additive manufacturing method determined.

Chapter 4 Results and Discussion

4.1. Design of Experiments: Thin Walls

The design of experiments approach is very useful when attempting to determine optimal parameters for further experimentation without excessive waste of material and time [41], [299], [302], [322]–[326]. Thin walls have been used for the design of experiments due to their convenient geometry [302], [305], [327] and have been deposited by means of the Laser Engineered Net Shaping process.

Thin walls were used because they can be deposited rapidly, allow for suitable starting parameters to be determined at minimal cost and provide an initial insight into printing restrictions and challenges. Multiple studies have been performed on cladding [68], [172], [232], [313], [328]–[330], which is effectively a two or three layer thin wall or thin cube. Studies have also deposited two or three layer thin walls and studied the microstructure and mechanical properties and proposed that these are starting parameters and properties for further analyses [232], [325], [331]–[333]. There are many parameters which need to be considered when performing additive manufacturing processes and each affects the deposition in its own unique way but can cause inter parameter effects [232]–[235].

For the DoE laser power, powder feed rate and traverse speed were chosen as the initial parameters to test. The three main parameters were chosen since the addition of each new parameter using a three variable full factorial DoE results in exponential test growth on the scale of 3^x. This implies that from the 27 experiments that were performed in this DoE the next full factorial amount would be 81.

The height of the thin walls was determined as the average of five random points along the wall for each of the DoE experiments in Table 4.1. Before the commencement of the deposition process the hopper had to be calibrated since it operates in revolutions per minute (rpm) and not grams per minute (g/min) for the powder feed rate. Fig. 4.1, shows the calibration curve obtained to convert between rpm and g/min. Every powder would have a different calibration curve since the shape of the powder and the density of the powder affects how readily it will be delivered at a certain hopper rpm.

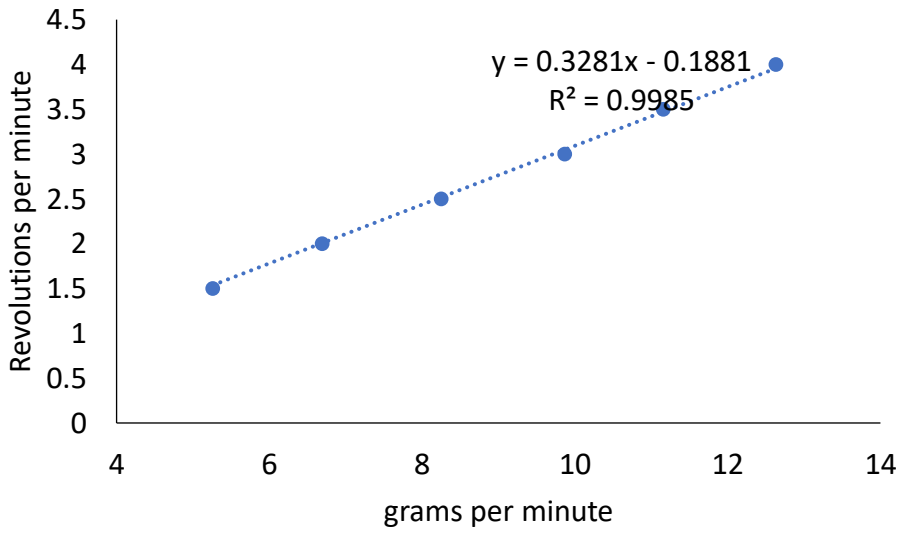


Fig 4.1: Calibration curve for LENS® hopper rpm to g/min.

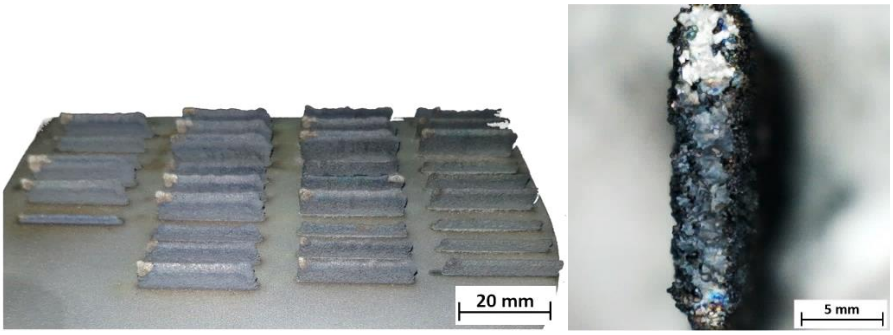


Fig 4.2: Design of experiments' thin walls (left) and single thin wall (right).

The design of experiments' thin walls as deposited on the substrate is shown in Fig. 4.2. The walls have varying roughness and surface properties just from visual observation. One of the thin walls is also shown in Fig. 4.2. The high surface roughness and varying width is evident from the image of the single thin wall. The processing parameters of the thin walls and their resultant average height and average width are shown in Table 4.1. Parameter sets 28-33 which have a small (*) indicates that these points were added to the original full factorial design of experiments and represents the star points. As was provided in the methodology section, the beam spot size was kept constant at 1.35 mm, the z-increment at 0.2 mm for a total of 25 deposited layers.

Table 4.1: Design of experiments parameters and resultant average height and average width.

Sample	Power (W)	Traverse Speed (mm/s)	Powder Flow rate (g/min)	Average Height (mm)	Average width (mm)
1	150	2.12	5.3	5.04	1.69
2	150	2.12	7.5	6.87	1.97
3	150	2.12	10.0	7.74	1.71
4	150	3.17	5.3	2.39	1.50
5	150	3.17	7.5	4.59	1.59
6	150	3.17	10.0	6.20	1.63
7	150	4.23	5.3	2.42	1.51
8	150	4.23	7.5	3.34	1.48
9	150	4.23	10.0	4.62	1.46
10	250	2.12	5.3	6.89	2.24
11	250	2.12	7.5	7.24	2.36
12	250	2.12	10.0	8.36	2.56
13	250	3.17	5.3	4.26	1.80
14	250	3.17	7.5	5.94	2.13
15	250	3.17	10.0	7.04	2.12
16	250	4.23	5.3	3.54	1.66
17	250	4.23	7.5	5.46	1.83
18	250	4.23	10.0	5.67	1.82
19	350	2.12	5.3	6.67	2.77
20	350	2.12	7.5	7.69	2.82
21	350	2.12	10.0	8.30	2.75
22	350	3.17	5.3	5.44	2.23
23	350	3.17	7.5	6.36	2.48
24	350	3.17	10.0	7.40	2.49
25	350	4.23	5.3	4.43	1.98
26	350	4.23	7.5	5.89	2.28
27	350	4.23	10.0	5.84	2.14
28*	340	3.17	5.3	6.24	2.48
29*	160	3.17	7.5	4.35	1.70
30*	250	4.97	10.0	3.45	1.84
31*	250	1.38	5.3	7.74	2.98
32*	250	3.17	11.8	6.06	2.15
33*	250	3.17	3.1	1.88	2.09

4.1.1 Height Analysis

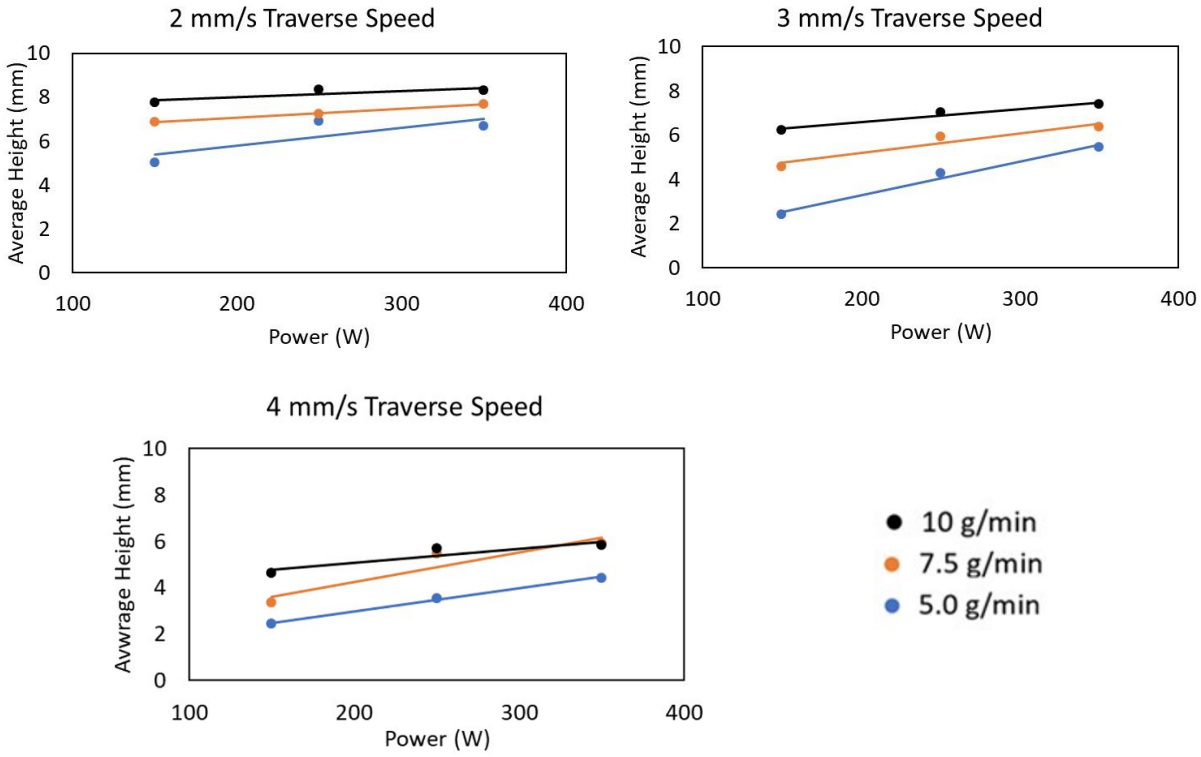


Fig. 4.3: Average height as a function of laser beam power and powder feed rate at traverse speeds of 2 mm/s, 3 mm/s and 4 mm/s.

The average heights of the thin wall specimen deposited at different traverse speeds are plotted in Fig. 4.3 as a function of laser power and powder feed rate. In general, a decrease in the average deposition height was recorded for an increase in traverse speed due to less powder being deposited per unit length. For all three traverse speeds an increase in the laser power and powder feed rate resulted in an increase in the average build height. An increase in laser beam power causes an increase in temperature in the molten pool, hence the height of the molten pool increases and resultantly more powder is included in the deposition [60]. An increase in powder feed rate also resulted in more powder being delivered to the molten pool and consequently being deposited [60].

Multiple linear regression analysis, using ANOVA, was used to determine the prominent factors and relationships between factors. A quadratic model was used to determine the interactions and contribution of each parameter to the deposition height. Traverse speed squared as well as power squared resulted in 0.29 and 0.15 P values respectively which indicates that there are no quadratic relationships concerning these parameters. The main parameters, i.e. power (P=0.0004), traverse speed ($P=6.82x10^{-13}$) and powder feed rate ($P=3.02x10^{-6}$) all had P values that indicated a significant effect on the deposition height. The square of powder feed rate (P=0.0003) and the interaction between laser power and powder feed rate (P=0.03) also had statistically significant effects on the deposition height. With these observations a height predictive model for thin walls was proposed, equation 4.1.

$$y = b_0 + b_1P + b_2v + b_3\kappa + b_4\kappa^2 + b_5P\kappa \quad \text{(Equation 4.1)}$$

Where $b_0 \ldots b_5$ are regression estimates for the coefficients using the least squares method, P is power (watts), v is the traverse speed (mm/s) and κ is the powder feed rate. When the model in Equation 4.1 was applied to the experimental data the regression coefficients were calculated, Table 4.2. The model explains 91.7% of the experimental data.

Table 4.2: Coefficients for Equation 4.1.

b_0	b_1	b_2	b_3	b_4	b_5
-3.15	0.02	-1.37	2.17	-0.09	-0.001

Table 4.2 shows that b_1 is a positive number which implies a protagonist effect between build height and power, the same relationship is observed for b_3, powder

feed rate, which implies that by increasing the laser beam power or the powder feed rate the resultant build height would increase. The coefficient b_5 has a negative value, which is an antagonistic effect between laser power and powder feed rate, hence the laser beam power and powder feed rate cannot both increase to increase the build height since this would cause a decrease in build height. This is due to a powder flux shielding the laser beam and causing insufficient melting of the powder [59], [334]. Traverse speed and the square of traverse speed, b_2 and b_4, have an antagonistic effect with deposition height, by increasing the traverse speed the deposition height will decrease. These observations are consistent with other additive manufacturing research [235], [302], [303], [305], [335].

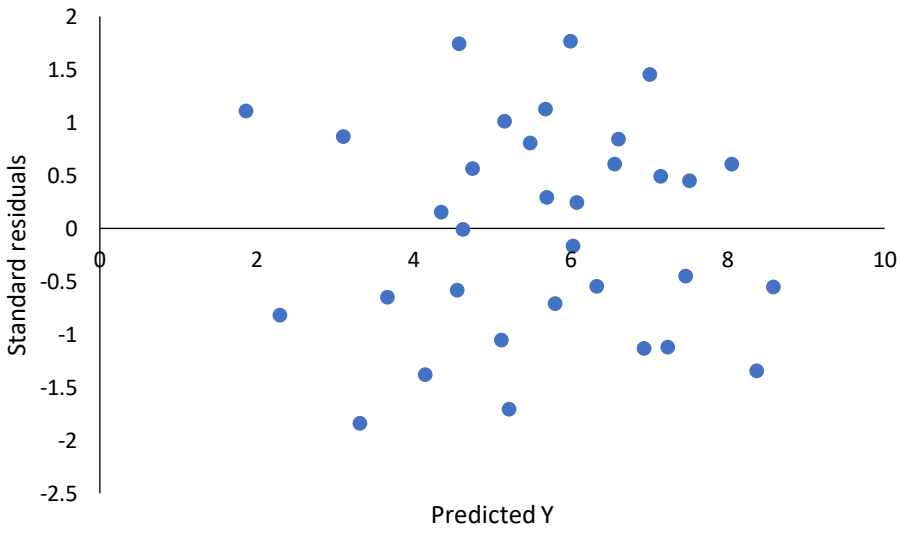


Fig 4.4: Residuals plot from ANOVA analysis.

A residual plot, as in Fig. 4.4, is plotted to determine whether the model fits the data well or if a better model may be evident. A better model is present if a discernible function is evident in the residual plot, such as a cubic or sinusoidal function. Fig. 4.4 does not have any function which can easily be observed. The residuals plot also identifies significant outliers which require retesting since the

outlier is probably due to human error and not experimental error. These outliers are identified when a point is larger than two or less than negative two. No points fit these criteria, hence no significant outliers are present. From equation 4.1 only the traverse speed has a quadratic nature. Thus, an optimum parameter can be obtained by utilising arbitrary power and powder flow rates within the range of the DoE values tested. There were 25 layers and a 0.2 z-increment imply a theoretical build height of 5 mm, hence the deposited layers which were closest give the parameters to be used as a modelling point.

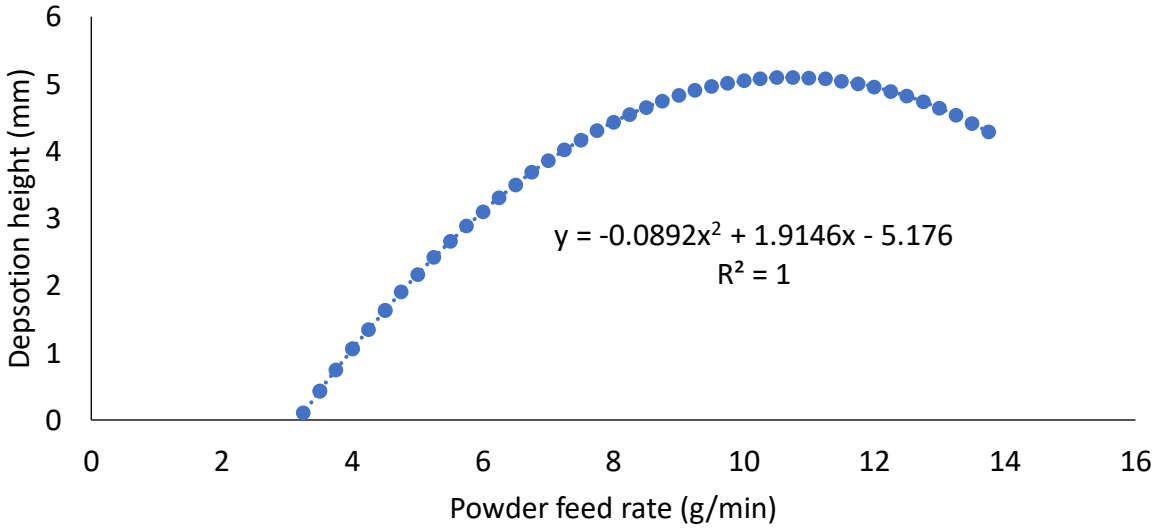


Fig. 4.5: Optimization of powder feed rate for parameter set.

When 170 W laser beam power and a traverse speed of 4 mm/s is used in the model an optimal powder feed rate of 10.9 g/min is obtained.

4.1.2 Width Analysis

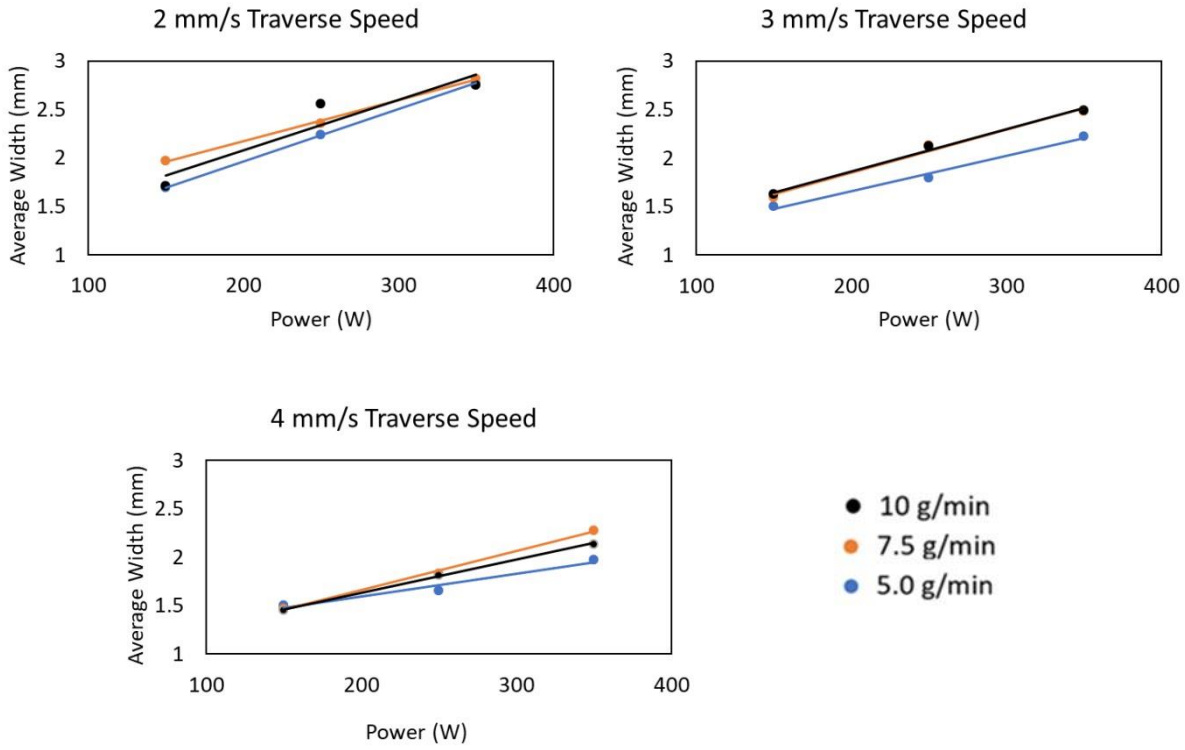


Fig. 4.6: Average width as a function of laser beam power and powder feed rate at traverse speeds of 2 mm/s, 3 mm/s and 4 mm/s.

The average widths of the thin wall specimen deposited at different traverse speeds are plotted in Fig. 4.6 as a function of laser power and powder feed rate. An increase in laser power resulted in a wider wall whereas a decrease in width was observed as the traverse speed increased. The influence of powder feed rate on the wall width did not follow a well-defined trend. For example, at a traverse speed of 3 mm/s a powder feed rate of 10 g/min produced the same wall widths as a powder feed rate of 7.5 g/min. The wall width results were also influenced by the laser power used for each traverse speed and powder feed rate combination.

Multiple linear regression, using ANOVA, was used to determine the prominent factors and relationships between factors. The relationship between laser beam power and powder flow rate (P= 0.7) between powder feed rate and traverse speed (P=0.8) both indicate insignificant statistical interactions. Powder flow rate squared (P=0.77) as well as laser beam power squared (P=0.16) indicates no quadratic relationship between the width of the thin walls and powder flow rate or laser beam power [233]. The main parameters were determined to be power (P= 3.04×10^{-6}), traverse speed (P=0.002), traverse speed squared (P=0.002) and the power and traverse speed interaction (P=0.03). With these observations a width predictive model for thin walls was proposed, equation 4.2.

$$y = b_0 + b_1P + b_2v + b_3v^2 + b_4Pv \quad \text{(Equation 4.2)}$$

Where $b_0 \ldots b_4$ are regression estimates for the coefficients using the least squares method, P is power (watts) and v is the traverse speed (mm/s). When the model in equation 4.2 was applied to the experimental data the regression coefficients were calculated, Table 4.3. The model explains 93.2% of the experimental data.

Table 4.3: Coefficients for Equation 4.2.

b_0	b_1	b_2	b_3	b_4
2.1	0.007	-0.65	0.09	-0.001

Table 4.3 shows that b_1 is a positive number which implies a protagonist effect between build width and power. If the power is increased the width of the thin walls will also increase. The square of the traverse speed also has a positive coefficient, b_3. The traverse speed, b_2, is negative, which implies that when that when the

traverse speed is increased the width of the thin wall will decrease. The coefficient b_4 has a negative value, which is an antagonistic effect between laser power and traverse speed. Hence if the power is increased and the traverse speed increased then the width of the thin wall will not increase since the traverse speed will result in width reduction while the laser beam power in a width increase.

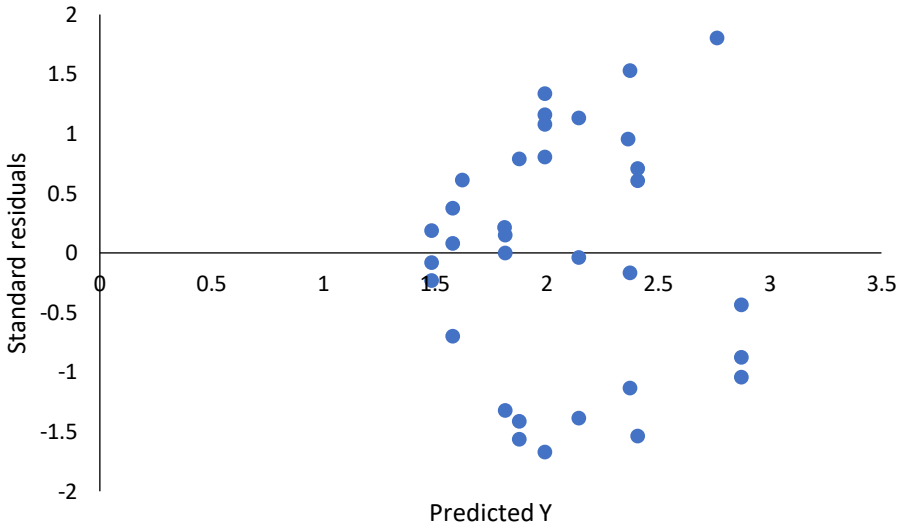


Fig. 4.7: Residuals plot from ANOVA analysis.

A residual plot, as in Fig. 4.7, is plotted to determine whether the model fits the data well or if a better model may be evident. A better model is present if a discernible function is evident in the residual plot, such as a cubic or sinusoidal function. Fig. 4.7 does not have any function which can easily be observed. The residuals plot also identifies significant outliers which require retesting since the outlier is probably due to human error and not experimental error. These outliers are identified when a point is larger than two or less than negative two. No points fit these criteria, hence no significant outliers are present. From equation 4.2 only the traverse speed has a quadratic nature. Thus, an optimum parameter can be obtained by utilising arbitrary power and powder flow rates within the range of the

DoE values tested. The beam diameter is 1.3 mm and only a single track is deposited, hence the deposited layers which were closest give the parameters to be used as a modelling point. The thinnest wall is required to maintain geometrical and structural integrity of the build.

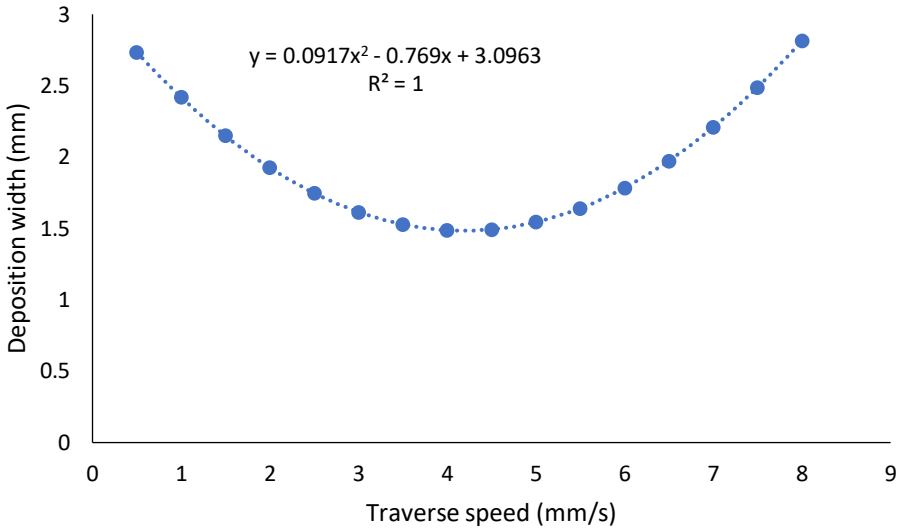


Fig. 4.8: Minimum wall width with optimized traverse speed.

Based on these analyses the optimized wall width parameters are 170 W laser beam power, a traverse speed of 4.5 mm/s and a powder feed rate of 10.4 g/min. When compared to the optimized parameters for the wall height, the required parameters are similar, with only minor deviations noted in the required traverse speed and powder feed rate. These observations are consistent with other additive manufacturing research [233], [325].

4.2 Parameter refinement: Cubes

These thin wall height and width optimized parameters were then used to deposit cubes. Porosity was used as the main indicator to determine viable parameter sets which were then subjected to further refinement and development of the deposition parameters to determine which deposition parameter set would provide the lowest porosity. Porosity is mainly caused by two factors namely trapped gas during solidification and shrinkage of the material during cooling [313], [336]. Lack-of-fusion porosity is due to the insufficient melting of the binder phase [313]. Occasionally powder particles drag gas into the melt as they penetrate the molten surface. If the solidifying velocity of the molten pool is higher than the exit velocity of the gas bubbles, the gas will become trapped and form pores [337]. Table 3.3 lists the parameter sets which were employed to produce the cubes during the refinement process as well as the associated measured porosity.

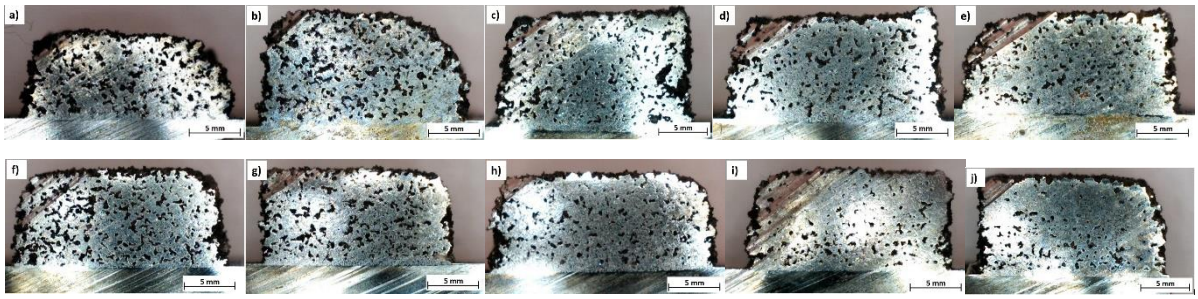


Fig. 4.9: Porosity of cubes a) 1, b) 2, c) 5, d) 6, e) 7, f) 8, g) 9, h) 11, i) 12, j) 14

A selection of cross-sectional micrographs from the deposited cubes are shown in Fig. 4.9. The porosity is evident even at low magnification which indicates a more lack-of-fusion porosity nature as opposed to conventional porosity. Lack-of-fusion porosity is present across the entire sample, not localized to a certain region. In samples 12 and 14, Fig. 4.9 (i and j), the porosity is more localised to the bottom half of the sample. This is due to the thermal gradients and cooling rates as discussed in the microstructure section. The higher laser power also contributes to the reduction of

porosity in the higher regions. The visible nature of the porosity corresponds to the high porosity measurements that were obtained for the samples.

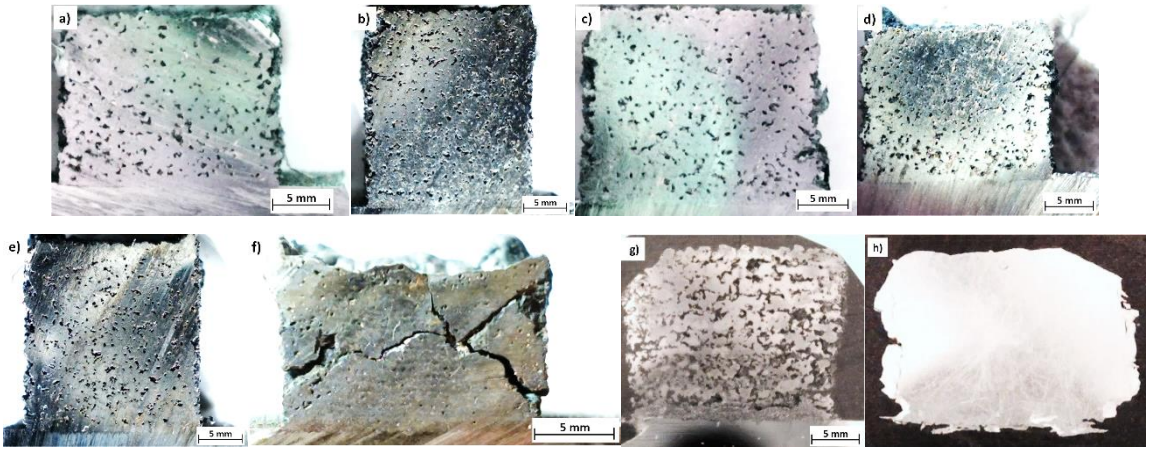


Fig. 4.10: Porosity of cubes a) 15, b) 17, c) 18, d) 19, e) 21, f) 28, g) 27, h) Monel 400

Samples 15 – 21 were part of the second round of parameter refinement. From Fig. 4.10 (a-e) visible porosity is still visible but to a much lesser degree than the porosity observed in Fig. 4.9, the first set of parameter refinement through cubes after the initial thin wall design of experiments. The porosity is still distributed relatively evenly throughout the cube, with the top regions exhibiting slightly less porosity when compared to the base regions.

Sample 28, Fig. 4.10 (f), shows the extensive cracking of the cube when the beam spot size was altered from 1.3 mm to 1.85 mm. The cube did not retain an acceptable geometry with the side walls caving into the sample and the top of the cube has a concave nature and not a straight nature as was observed in the other cubes produced in Fig. 4.10. The heated substrate, Fig. 4.10(g), still shows a high percentage of porosity, but in the fusion zone, directly above the substrate, a denser layer is observed before the general porosity initiates. The Monel 400

binder was deposited by itself, as in Fig. 4.10 (h), and shows a 0% porosity, although the shape is not perfectly square and would require further machining.

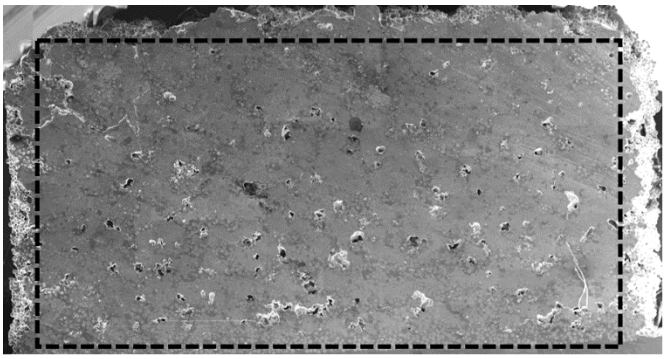


Fig. 4.11: Representation of the optimized process parameters and the region used to quantify porosity.

The porosity measurements were calculated by constructing a rectangular region across the largest percentage of the cube, as in Fig. 4.11, and calculating the porosity for the entire region. A macro level porosity was used since the porosity of a micro region would have a smaller effect on the macro properties of the depositions.

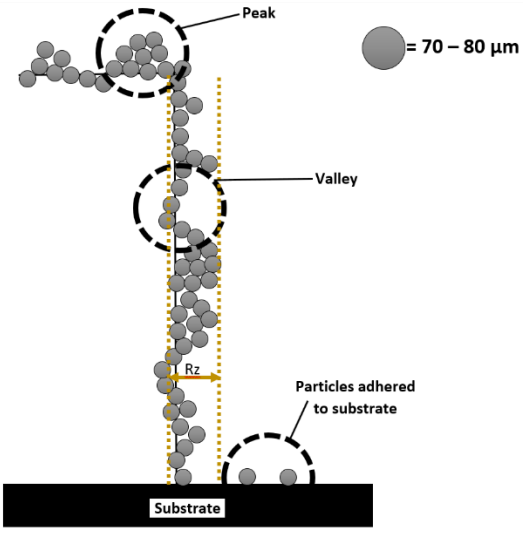


Fig. 4.12: Diagram representing the surface roughness on the samples.

The high surface roughness on the samples can be viewed as in Fig. 4.12. The cast WC particles become embedded in the binder and the binder solidifies with the particles extruding from the surface. The particle form in thinner layers, where a valley forms, in comparison to other regions where multiple particles become attached to each other. The particles have diameter of approximately 70 µm which implies that between the valleys which are approximately 70 µm above the predicted surface and the peaks which can be up to approximately 280 µm an R_z value in the order of 210 µm can be expected with higher values being very plausible due to the unfavorable surface finish which was observed across all of the samples.

The lack-of-fusion regions are of interest, as is the chemistry which is observed in and around these zones. One such region was studied to determine distinct phases that may be present. The lack-of-porosity region is shown in Fig. 4.13 and the results of the chemical analysis in Table 4.4.

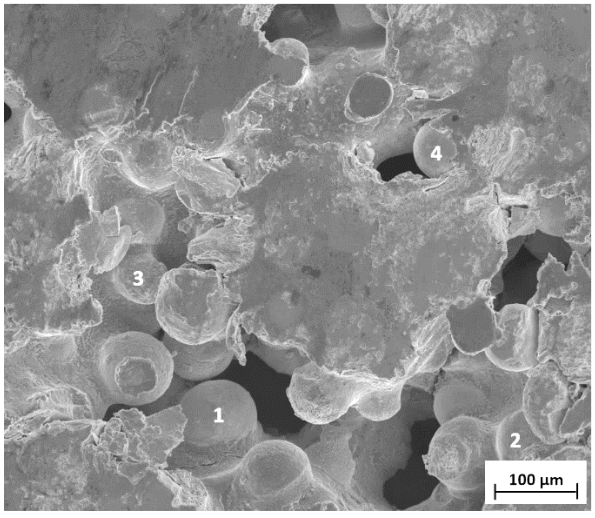


Fig. 4.13: EDS spectra of four regions around the lack-of-porosity region.

Table 4.4: Atomic % analysis of four regions in Fig. 4.13.

Element	Spectrum 1	Spectrum 2	Spectrum 3	Spectrum 4
C				57.60
O	67.51	71.43	64.91	28.35
W	28.46	20.66	6.25	6.42
Ni	1.20	3.79	16.88	3.49
Cu	1.43	1.47	9.43	3.12
Fe	1.40	2.65	2.54	1.01

The microstructure chapter covers the studied microstructural properties of the samples in greater detail. Spectrum 1 shows an exceedingly high oxygen percentage as well as a high tungsten concentration. WO_3 is the most probable structure in the lack-of-fusion regions with some free tungsten due to dissolution also being present. Spectrum 2 has a 3:1 ratio of oxygen to W, WO_3, and the remining oxygen can for trace amounts of iron oxide, nickel oxide and copper oxide. Spectrum 3 has been coated in the binder phase, hence the high nickel and copper concentrations, but there still a high oxygen concentration due to the formation of multiple metallic oxides. Spectrum 4 has a remarkably high oxygen and carbon content, which implies that the metals form oxides and the carbon from the dissolution of the cast WC forms a graphite phase on the surface of the particles in the lack-fusion zones.

Table 4.5: Process parameters for the respective samples and the porosity which was obtained for these parameter sets.

Sample	Power (W)	Traverse Speed (mm/s)	Powder feed Rate (g/min)	Hatch overlap(%)	z-increment (mm)	Porosity
1	150	3.5	9.5	50	0.2	20.0
2	170	4	10.9	50	0.2	12.3
3	200	4.7	12.8	50	0.2	16.5
4	220	5.2	11.5	50	0.2	5.3
5	250	6	16.35	50	0.2	12.2
6	270	63	17.2	50	0.2	12.0
7	300	70	19.1	50	0.2	9.9
8	150	3.5	9.5	75	0.2	12.5
9	170	4	10.9	75	0.2	11.6
10	200	4.7	12.8	75	0.2	10.5
11	220	5.2	11.5	75	0.2	9.8
12	250	6	16.35	75	0.2	9.8
13	270	63	17.2	75	0.2	9.6
14	300	70	19.1	75	0.2	6.7
15	220	5.2	11.5	50	0.31	6.7
16	220	4.3	12.5	50	0.55	8.9
17	220	4.3	10.9	50	0.5	10.4
18	220	5.2	12.6	50	0.31	5.0
19	220	4.8	12.7	50	0.5	11.8
20	220	5	13.3	50	0.5	8.4
21(OP)	220	4.5	11.9	50	0.4	3.9
22	220	4.5	11.9	50	0.254	4.9
23	220	4.5	11.9	50	0.3	5.1
24	220	4.5	11.9	60	0.254	4.8
25	220	4.5	11.9	70	0.254	4.9
26	310	4.5	11.9	50	0.254	
27	310	4.5	11.9	70	0.254	
HS	220	4.5	11.9	50	0.4	20.1
RM	220	4.5	11.9	50	0.4	20.3

Samples 1-14, Table 4.5, were used to determine how the change in hatch % overlap alters the effective layer thickness of the deposited cubes. The resultant change is shown in Fig. 4.14.

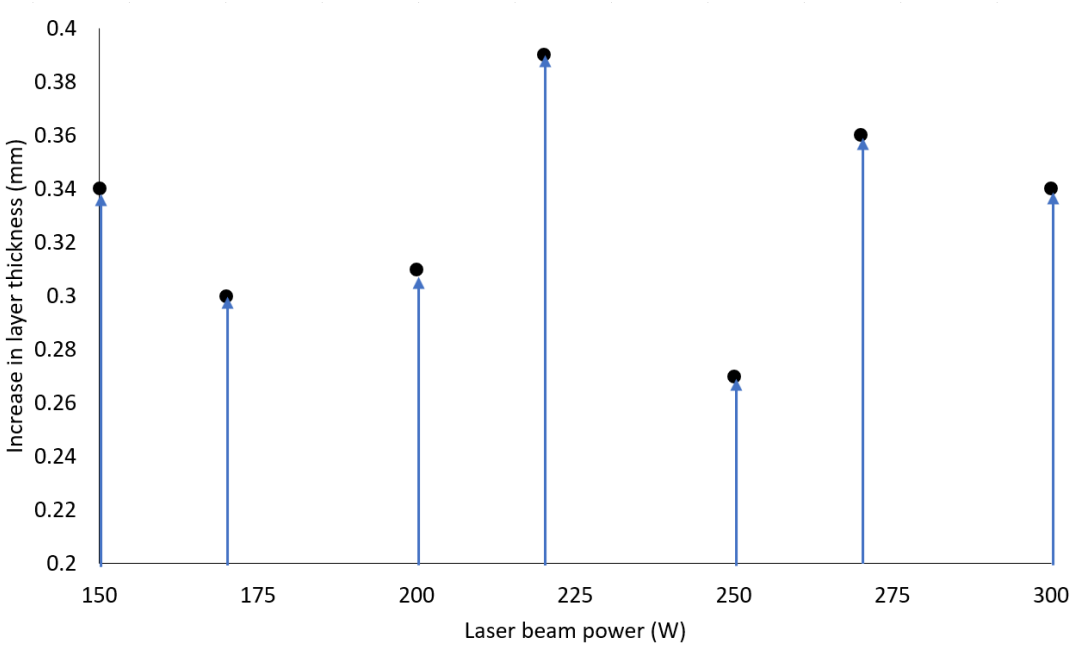


Fig. 4.14: Change in layer thickness when the hatch % is changed from 50% overlap to 75% overlap.

The arrows in Fig. 4.14 indicate the increase in layer thickness for the specific laser power but with a 25% increase in the hatch overlap %. An average layer thickness increase of 0.33 mm was calculated when the hatch overlap is increased by 25%. Thus, by allowing the horizontal tracks to overlap by 25% more the layer thickness of each deposited layer increases by 0.33 mm without any alterations to the z-increment. This is due to more powder being deposited with each layer and the remelting of a larger percentage of the adjacent deposition track. There are also more deposition tracks due to a smaller horizontal increment, hence a thicker layer is obtained.

The parameter sets for samples 1 to 7 were repeated for samples 8 to 14 with only the hatch spacing being varied from 50% to 75% for samples 1 to 7 and samples 8 to 14 respectively. For the 50% hatch spacing the highest porosity was measured for the parameter set which had the lowest laser power, lowest powder feed rate and lowest traverse speed combination. However, there was no direct relationship between porosity and the deposition parameters. The lowest porosity of 5.3% was measured at a laser power of 220 W, a traverse speed of 5.2 mm/s and a powder feed rate of 11.5 g/min. For the 75% hatch spacing there was an indirect relationship between laser power and porosity; as the laser power increased, the porosity decreased. A parameter set of 300 W laser power, a traverse speed of 7 mm/s and a powder feed rate of 19.1 g/min gave the lowest porosity of 6.7%. For both the 50% and 75% hatch overlap an increase in power resulted in a lower porosity due to the higher temperature of the molten pool. The 75% hatch overlap had a lower porosity than the 50% hatch overlap since the previously deposited layers were undergoing more remelting which allowed for some of the defects to be removed.

As the 50% hatch spacing produced a lower porosity compared to the 75% hatch spacing, the parameter set for sample 4 was used as a basis for samples 15-21. Here the laser power and hatch spacing were kept constant at 220 W and 50% respectively, while the z-increment, traverse speed and powder feed rate were adjusted. Lower porosity values were recorded for the lower z-increment value due to increased remelting of previously deposited layers, thereby removing some of the lack of fusion, and maintaining a more stable laser beam spot size [59]. From Table 4.5 parameter set 21 produced the lowest porosity of 2.5%. Using this parameter set attempts were made to investigate if the porosity could be further decreased by maintaining a fixed laser power, traverse speed and powder feed rate of 220 W, 4.5 mm/s and 11.9 g/min respectively while making minor

adjustments to the hatch spacing and z-increment. These results are listed as samples 22 to 25 in Table 4.5 and as shown resulted in an increase in the porosity.

A final attempt to reduce the porosity was done by increasing the laser beam spot size from 1.3 mm to 1.85mm. These results are reflected as samples 26 and 27 in Table 4.5; for both parameter sets severe cracking was observed along with poor cube geometry. Here the melt pool has a poor quality with high instability which is especially prominent at higher energy densities [338]. The increased role of surface tension is also believed to have contributed to the negative effects of the increased beam spot size [338], [339] . Surface remelting and a heated substrate was also tested, but both methods did not decrease the observed porosity. The surface remelting reduced porosity in the top layer which is not the key area where the porosity is situated. The heated substrate did not reduce the observed porosity since 450˚C appears to not be high enough to effectively alter the thermal gradients enough to change microstructural characteristics through dissolution and solidification processes. Thus, there is still a substantial amount of porosity.

On the basis of all the parameter sets tested and the regression analyses of the data the parameter set which consisted of 220 W of laser beam power, a traverse speed of 4.5 m/s, a powder feed rate of 11.9 g/min, hatch overlap of 50% and a z-increment of 0.4 mm produced the lowest porosity of 2.5% for the WC-9.2wt%Ni alloy.

4.3 Hardness

4.3.1 Design of Experiments: Thin walls

Hardness measurements were performed on the 33 design of experiment samples (Table 3.2) with five indentations being performed across the entire sample to obtain an average for the bulk sample. ANOVA analysis was performed on the samples to determine the dominant factors that affect the hardness. The surface hardness of the cube samples was recorded by also performing five indentations across the top of the sample to determine an average surface hardness. At least 80 hardness measurements were performed across the entire cross-section to model a surface plot of the hardness form the substrate to the surface. The hardness properties of the fabricated samples are particularly important since it provides an insight into the viability of industrial applications of the chosen cemented carbide.

The average hardness of each thin wall from the design of experiments matrix in Table 3.2 is plotted in Fig 4.15. It was found that 15% of the samples had an average hardness greater than 1000 HV_{30}, while 66.5% of the samples were between 800 HV_{30} and 1000 HV_{30} while the remaining 18.5% were below 800 HV_{30}. No trends were observed in terms of hardness and the individual deposition parameters. However, the 150 W and 350 W laser power thin walls showed a greater variation in their results compared to the relatively consistent values of the 250 W laser power cubes where all the measured hardness values were in the range of 800 HV_{30} to 1000 HV_{30}. Two of the highest average hardness values were obtained at 150 W laser power which implies that a very high energy density would result in less favorable results. The third highest average hardness value, obtained at 350 W laser power, was deposited at the highest traverse speed which would reduce the energy density used during deposition.

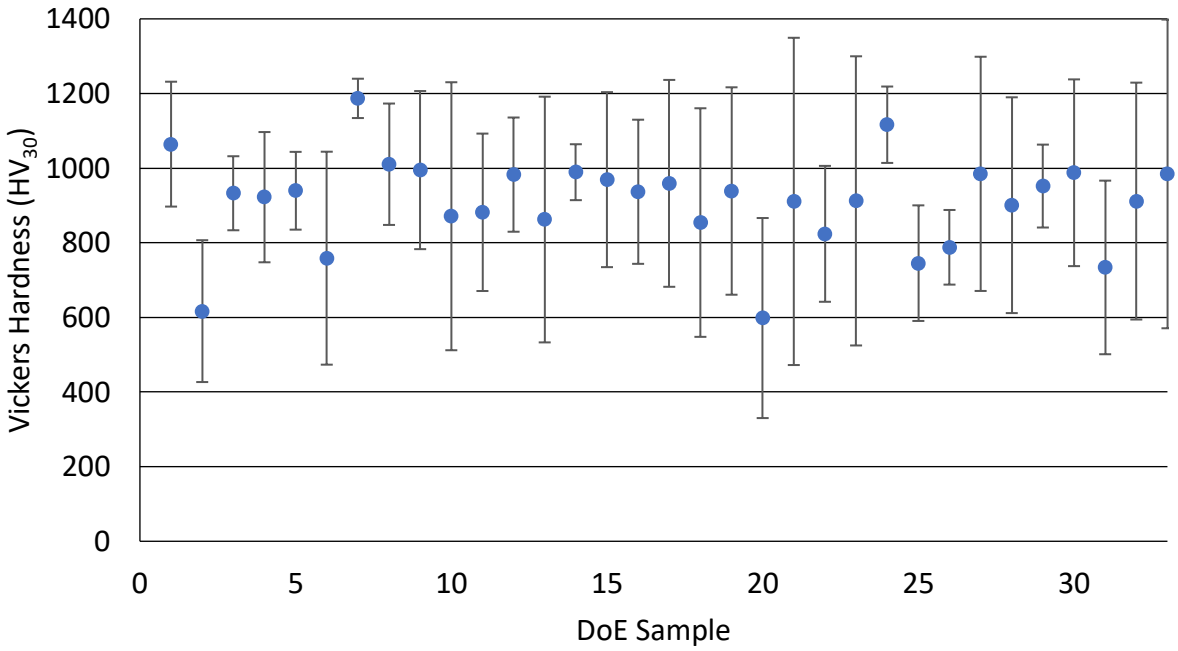


Fig. 4.15: Vickers hardness averaged over five indentations on each of the DoE thin walls.

Multiple linear regression, using ANOVA, was used to determine the prominent factors and relationships between factors. A quadratic model was used to determine the interactions and contribution of each parameter to the deposition average hardness. Power and all the squared contributors were eliminated due to P values greater than 0.05 indicating an insignificant effect on the obtained results. The prominent factors were found to be the traverse speed (P=0.0015), powder feed rate (P=0.026), the interaction between power and traverse speed (P=0.006) and the interaction between power and powder feed rate (P=0.017). Even though power was eliminated as an individual contributor it does affect the hardness in the interactions.

With these observations a hardness predictive model for thin walls was proposed, equation 4.3.

$$y = b_0 + b_1 v + b_2 \kappa + b_3 P v + b_4 P \kappa \quad \text{(Equation 4.3)}$$

Where $b_0 \ldots b_4$ are regression estimates for the coefficients using the least squares method, P is power (watts), v is the traverse speed (mm/s) and κ is the powder feed rate. When the model in equation 4.3 was applied to the experimental data the regression coefficients were calculated, Table 4.6. The model explains 32.5% of the experimental data.

Table 4.6: Coefficients for Equation 4.3.

b_0	b_1	b_2	b_3	b_4
768.6	213.9	-57.3	-0.7	-0.2

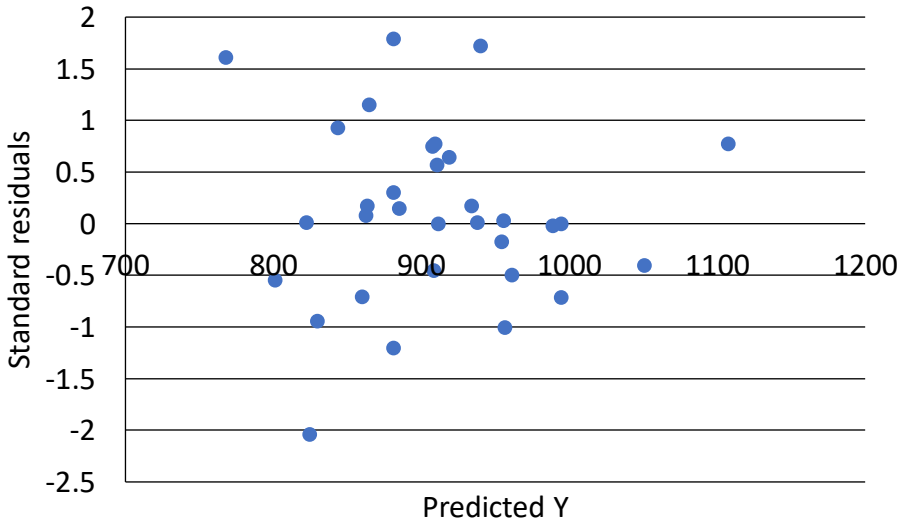


Fig 4.16: Residuals plot from ANOVA analysis.

A residual plot, as in Fig. 4.16, is plotted to determine whether the model fits the data well or if a better model may be evident. A better model is present if a discernible function is evident in the residual plot, such as a cubic or sinusoidal function. Fig. 4.16 does not have any function which can easily be observed. The residuals plot also identifies significant outliers which require retesting since the outlier is probably due to human error and not experimental error. These outliers are identified when a point is larger than two or less than negative two. One point is on the negative two line but is not significantly past it so it can be accepted in the data set. Since there are no squared components no optimal set can be determined which is understandable since equation 4.3 only explains 32.5% of the experimental data.

This implies that power, traverse speed and powder feed rate do affect the obtained hardness, but a very significant factor has not been included. The residual plot shows that the correct model was used. Hardness is highly affected by the microstructural nature and grain refinement of the material being tested as well as the binder content [340]–[346]. The microstructure is affected by the power, powder feed rate and traverse speed, but as see in the microstructure chapter the thermal gradient, cooling rate, solidification rate and different localized conditions including tungsten and carbon content all influence the resultant microstructure that is obtained. With the large number of contributing parameters and variety of microstructures that were obtained the ANOVA analysis has a reasonable conclusion.

4.5.2 Cubes

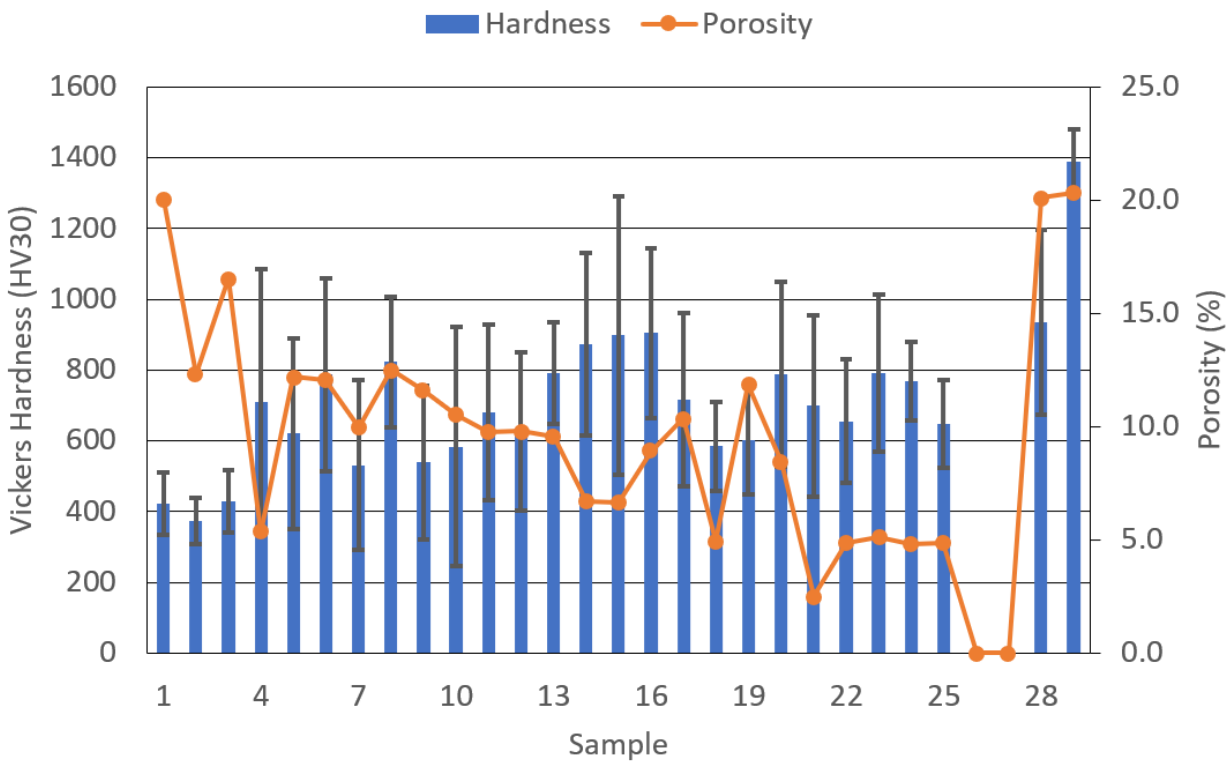


Fig. 4.17: Vickers hardness averaged over five indentations on the surface layer of the cubes (with error bars) and porosity recorded for each sample.

The average hardness of each of the cubes in Table 3.3 is plotted in Fig. 4.17. 26% of the cubes had a hardness below 600 HV_{30}, 52% of the samples had a hardness between 600-800 HV_{30} and 22% of samples had a hardness > 800HV_{30}. Samples 26 and 27 are reported as zero since the samples cracked catastrophically before any tests could be performed and therefore the hardness is irrelevant. Cubes 1-3 show a generally lower average surface hardness than the other samples since they had the lowest laser beam power and high porosity which affected the mechanical integrity of the surface region. The error bars show that there are no statistically significant variations in the recorded hardness values except for sample 29, which has a statistically significant difference from the other 28 samples. Sample 29 underwent surface remelting which greatly altered the surface hardness by changing the

microstructure to a more homogenous nature, decreased binder content and fine WC structures, as was seen in 4.33. The remelting process is typically used to alter the surface microstructure properties and increase the surface hardness of components in high wear environments [332], [347]–[352], as a substitute to cladding. The Monel 400 binder was to have a hardness of 114±3 HV_{10} without any cast tungsten carbide. In other research Inconel 718 was found to have a hardness of 250 HV after direct laser manufacturing [353] and Monel K500 133-152 $HV_{0.5}$ after wire arc additive manufacturing [354]. Both materials have harder component elements than Monel 400, so the value obtained is justified.

The hardness and porosity measurements of samples 1 – 29 do not correlate over the entirety of the data set although in general, the lower the porosity values did have the higher recorded hardness. The lower porosity is associated with more refined process parameters which consequently enhances other deposition properties, such as hardness. In the samples where this is not observed, such as sample 29, the hardness testing procedure needs to be highlighted. The surface hardness is only concerned with the hardness of the final deposited layers, not the bulk of the sample, hence the remelting process improves the hardness and remains unaffected by the high porosity within the bulk. The main type of porosity observed in the bulk of the samples was lack-of-fusion which is simple to avoid when performing measurements. Conventional porosity caused by gas bubbles was not very prominent and therefore the hardness does not readily correlate with the porosity. The surface layers also had the most consistent microstructures, as discussed in Chapter 4.4, hence the most favourable hardness results were obtained in the surface layers. This is also evident in the hardness profiles displayed in Fig. 4.19.

Four microhardness regions were examined to determine the effect of the cast WC on the Monel 400, as shown in Fig. 4.18.

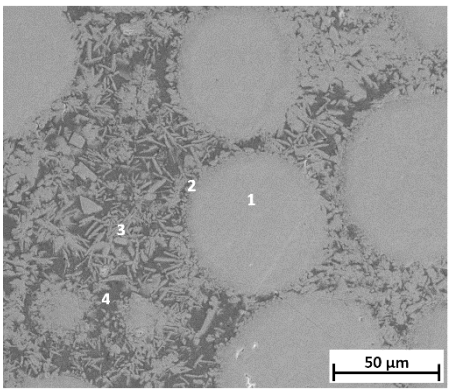


Fig. 4.18: Microhardness of four regions of different composition.

Table 4.7: Recorded hardness values for each indentation in Fig. 4.18.

Region	1	2	3	4
Hardness ($HV_{0.05}$)	2750	1749	1122	683

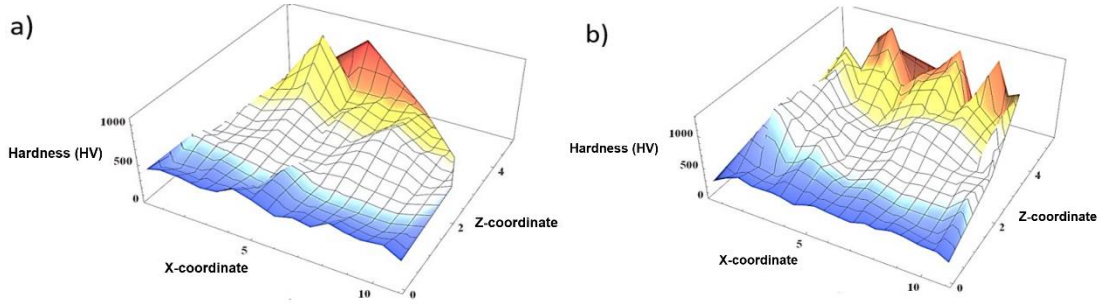
The hardness within the cast WC was the highest, Table 4.7. This was expected because cast tungsten carbide has a very high hardness [355], [261].

Literature cites a higher hardness for W_2C than WC, hence the ratio of WC/W_2C and the carbon percentage have a massive impact on the recorded hardness [356]–[358], [359]. The dilution region had a greatly reduced hardness since the W_2C dissolves into the matrix and the matrix infiltrates the cast WC in the dilution zone and therefore reduces the overall hardness [261] [360]. There are also new carbides formed in the transition zone, such as the eta phase which has a lower hardness than cast WC [361]. The dilution region did have a hardness which was higher than the binder by itself, so the dilution nature of cast WC does promote the hardness [360]. Region 3 had a larger portion of binder but still included needle-like and blocky structures which allowed for a higher hardness, the resultant being less than the dilution zone but more than the isolated binder [261]. The binder had the lowest hardness which was expected. The integration of the hard-facing

particles made a significant difference in increasing the hardness. This can be seen when compared to the hardness of when the binder was deposited by itself, 114±3 HV_{10}, whereas a minimum hardness of 683 HV_{30} was obtained when mixed with the cast WC powder. Similar results have been observed in other research [355], [360], [362].

Hardness profiles were constructed of cube cross-sections and Fig. 4.19 shows three cube profiles which reflect how the hardness varied from the base plate-alloy interface to the surface. The hardness increased from the base plate-alloy interface to the final deposited layer, where values ranged from approximately 280 HV_{30} to 1300 HV_{30}. The surface regions exhibited localized regions of higher hardness than the average trend of the cube. These hardness gradients can be correlated to the microstructural differences observed for the carbide grains, i.e. the higher density of large spheroidal grains in the base region and the bimodal grains in the surface region which has a high concentration of fine carbide platelets interspersed between the spherical carbides. The smaller grains resulted in a higher hardness than the larger grains [70] ,[363], and also contributed to the localized regions of high hardness. Hardness has a general trend toward increased hardness in depositions with increased heat input which has a qualitative agreement with the microstructure[261]. The higher dilution and thermal conductivity of the substrate has been shown to have reduced hardness values. Three different hardness factors have been found to dictate the hardness, namely solid solution alloying, carbide fraction and dendrite structure. Solid solution alloying was reduced when high dilution was observed. A low carbon fraction in the substrate also reduces the formation of carbides. The slower solidification rate from the thermal conductivity of the substrate results in a courser dendrite structure in the binder [95], [120], [121].

Similar results have been observed in other studies[232], [236], [311], [319], [364] with the lower hardness in the fusion zone also being contributed to the dilution of elements from the substrate which was very prominent in the depositions [261]. Commercially WC-6% Ni has a hardness of 1460 HV_{30} [365]. Bulk hardness is substantially below this value due to the different microstructures present, although the localized regions with high hardness are close to the commercial product. Monel 400 is approximately two-thirds nickel but also has about one-third copper which would reduce the hardness of the binder phase. The porosity, as in Table 4.5, did not affect the indentation values but did affect the location of the indents. Readings could not be performed in the lack-of-fusion zones and consequently would be moved to the nearest region of substantial density. In ceramic based materials the presence of pores have minimal resistance to applied stress and the material with a higher porosity will have a lower apparent micro-hardness when compared to the denser counterparts [298], [366].



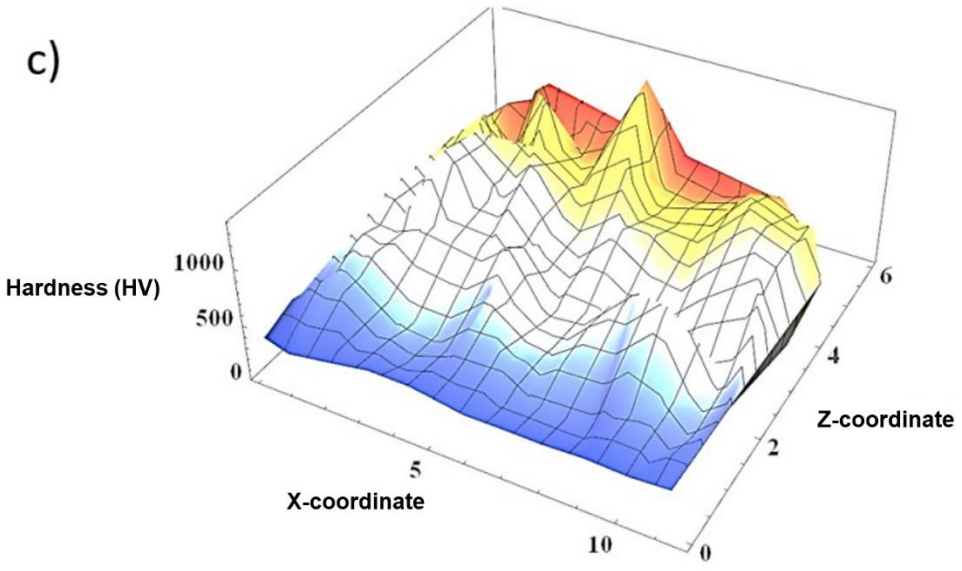
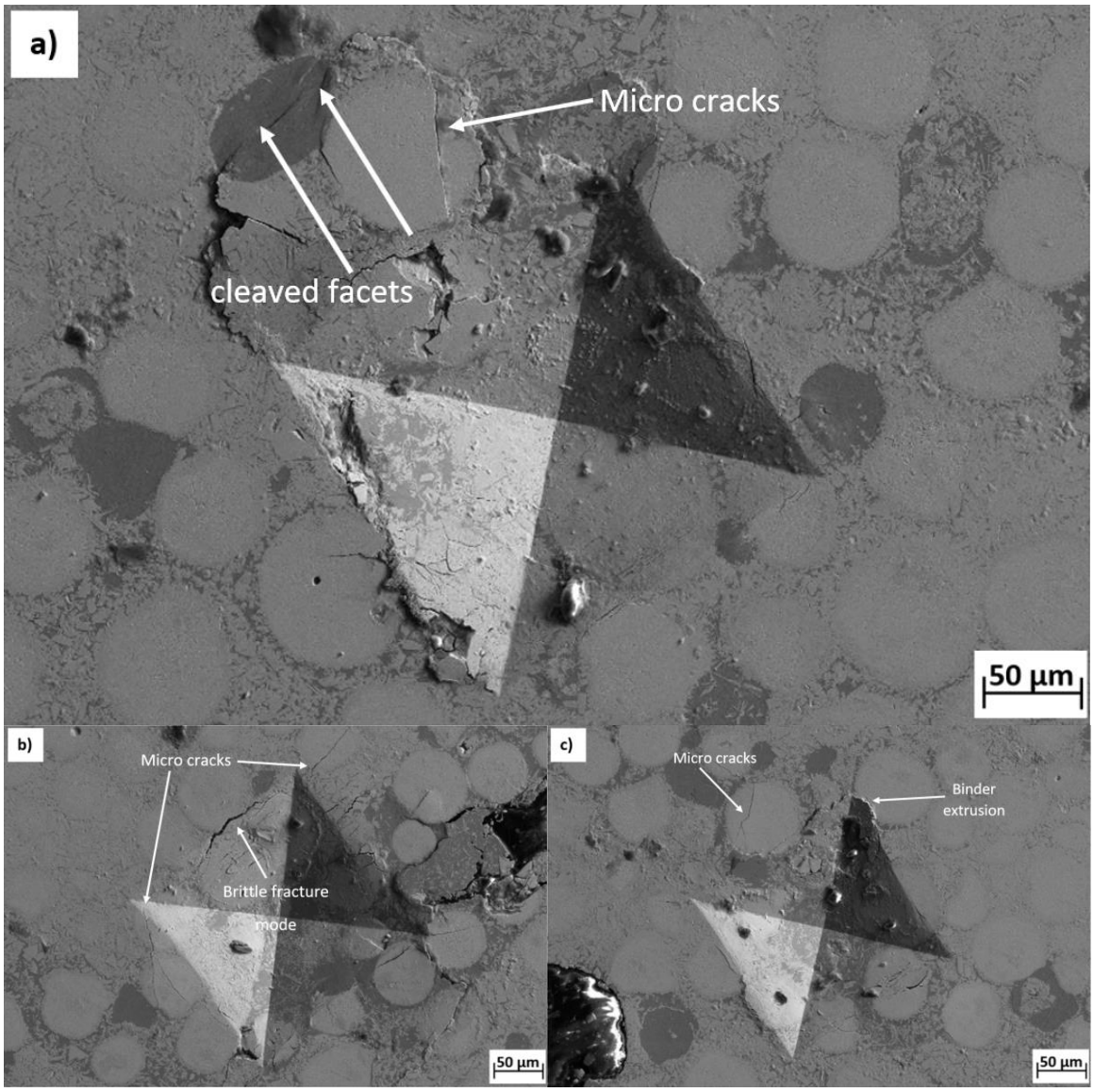


Fig. 4.19: Hardness profiles for 3 cubes (a) 220 W, 5.2 mm/s, 11.5 g/min, 50% hatch spacing, (b) 300 W, 7 mm/s, 19.1 g/min, 75% hatch spacing, (c) 220 W, 4.5 mm/s, 11.9 g/min, 50% hatch spacing.

4.5.3 Crack analysis

The cracks that were formed by the Vickers Hardness indenter were analysed using scanning electron microscopy, as in Fig.4.20.


a)
Micro cracks
cleaved facets
50 µm
b)
Micro cracks
Brittle fracture mode
50 µm
c)
Micro cracks
Binder extrusion
50 µm

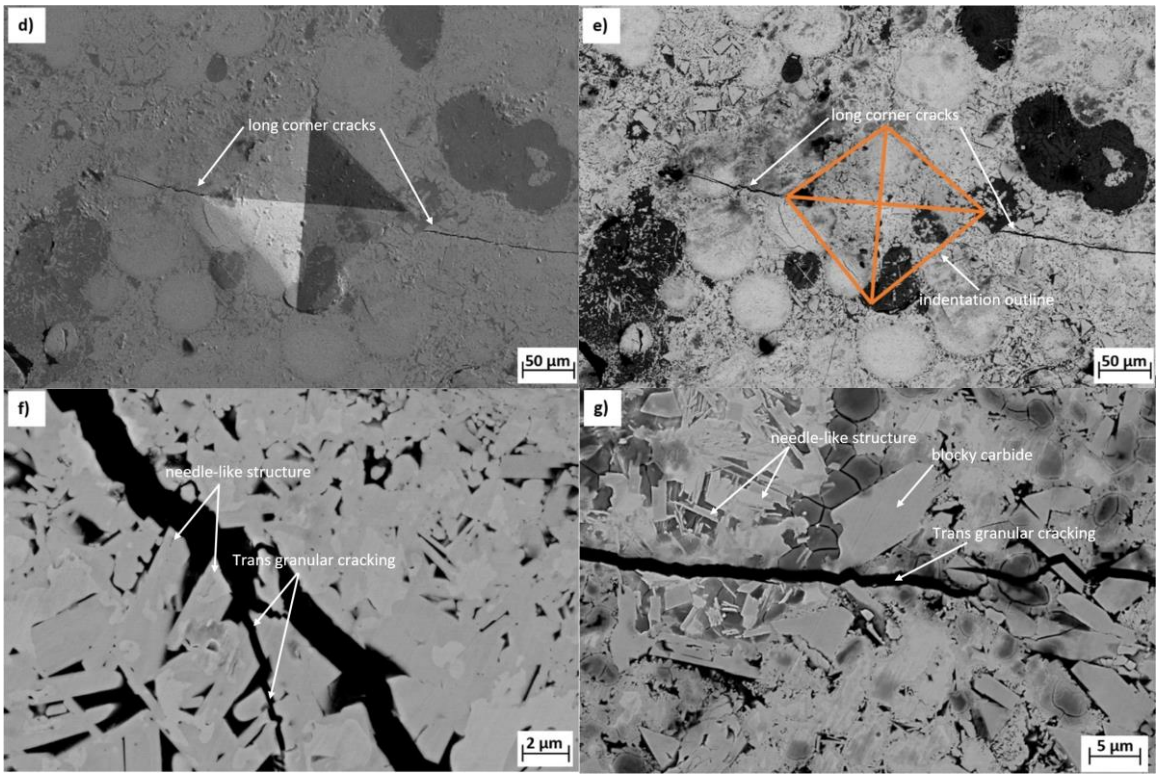


Fig. 4.20: a)-d) micrographs of hardness indentations, e) BSE image of indentation, f)-g) BSE image magnified into crack region.

Fig. 4.20(a) demonstrates how the indenter creates planar cleave facets by pushing large sheet-like planes away from the indent region [367]. The larger, more brittle, cast WC particles show microcracks from the force of the indenter, while the damage observed in the more plastic binder is limited since plastic deformation occurs before severe cracking. Cracks generate easier in WC particles larger than 30 µm compared to smaller particle sizes since the larger grains tend to have more defects [310], [368]. Plastic deformation can be observed in the bottom region where the material has been forced out of the indent region [369]. This can also be form of binder extrusion from the indent zone [370]. The edges of the indent show holes due to the fracturing and removal of brittle cast WC. The Palmqvist fracture toughness method was unsuccessful due to irregular cracking during the hardness indentations, as well as a lack of consistency across

an individual sample as well as multiple samples. This is also attributed to the wide range of microstructures observed within the samples.

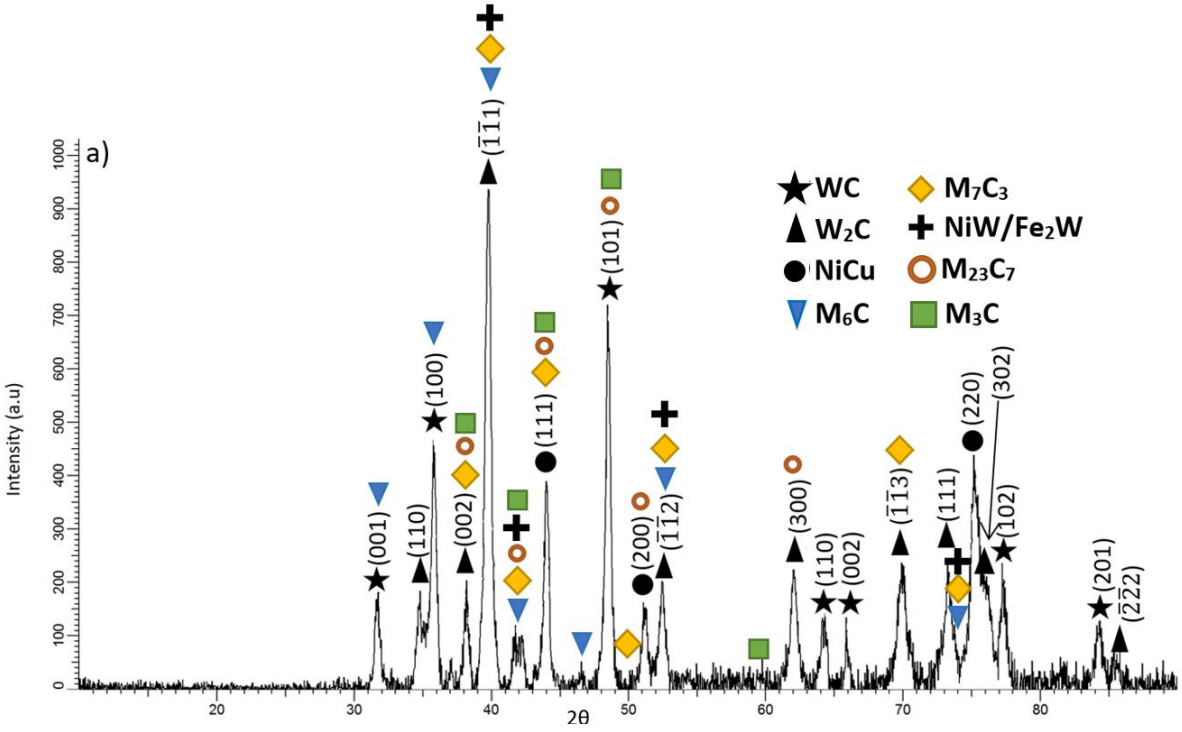
Fig. 4.20(b) also shows microcracks into the WC particles around the indent and multiple larger cracks parallel to the sides of the ident which are characteristic of brittle fracture mode[369]. Fig. 4.20 (c) has the same microcracks but the top corner shows a large amount of material pile-up indicating binder extrusion from the residual impression [369], [370]. Fig. 4.20 (d) and (e) show longer cracks on the sides of the residual impression. The cracks are not seen in the high binder regions and appear only in the brittle phases. On closer examination of the cracks Fig. 4.20(f) and (g) they propagate with a trans granular failure although seldom through a larger blocky structure. The eta phases on the boundaries of the blocky carbides [180], [371] allows the crack to propagate through a more brittle region and continue trans granularly through the smaller needle-like structures[372].

Cemented carbides have complex hardness profiles due to the range of microstructures which are obtained during the laser sintering process. The process parameters only contribute a small component in explaining the hardness, as was seen in the design of experiments. Until certain process parameters produce the same microstructure consistently there will be unavoidable brittle phases which affect the surface hardness and the fracture characteristics of the material.

4.4 Microstructural Characterisation

4.4.1 XRD

X-Ray diffraction was performed on the samples to identify the prominent phases and impurities that formed during the sintering process. These analyses are shown in Fig. 4.21.



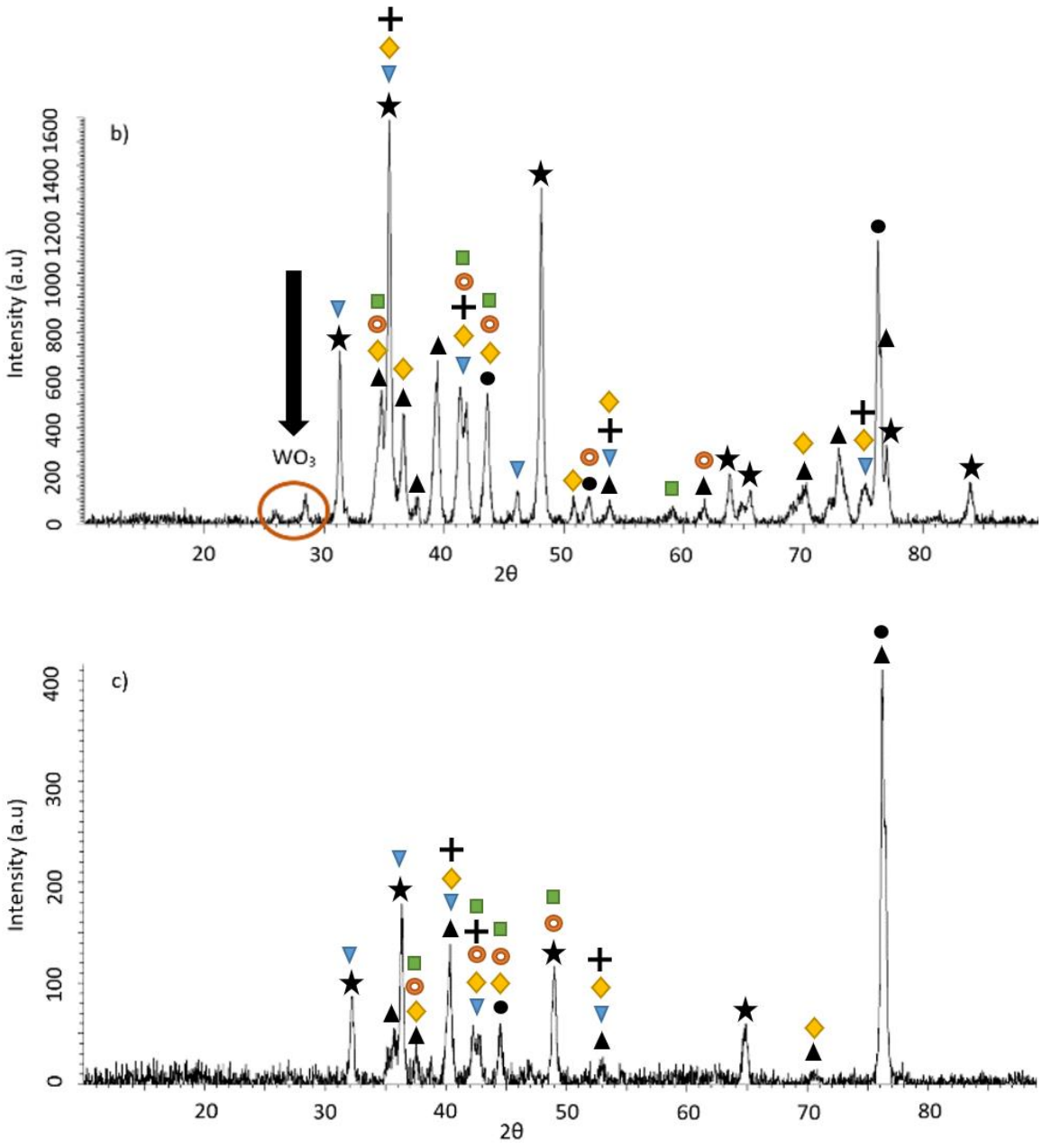


Fig. 4.21: a) XRD patterns of a) Sample OP, b) Sample HS, c) Sample RM.

The obtained XRD patterns are in good agreement with those reported for WC in research [75], [178], [373]. From the XRD patterns of Fig. 4.21, there are two distinct carbide phases detected in the alloys, namely the equilibrium WC phase

and the di-tungsten carbide phase (W_2C). The W and C atoms are in the form of the hexagonal tungsten monocarbide δ-WC ($WC_{1.0}$) (sp.gr. $P\bar{6}m2$, a = 0.2906 nm, c = 0.28375 nm) and the hexagonal lower tungsten carbide β-W_2C ($WC_{0.48}$) (sp.gr. $P6_3/mmc$, a = 0.2996 nm, c = 0.4724 nm) with disordered carbon and vacancy distributions [374], [69].

The main phases will be WC and W_2C since the precursor powder had these two as the dominant phases. Complex carbides require the sintering process to form and grow. When compared to the XRD pattern of the powder, Fig. 3.3, there are two distinct differences, namely no prominent peak for the metallic tungsten as well as the formation of a M_6C ($Ni_2W_4C/Fe_3W_3C/FeW_3C$), which is either due to the dilution of Fe from the base plate into the deposited layers, as shown in the EPMA image of Fig. 4.23, or the formation of Ni_2W_4C during the sintering process. Fig. 4.21 shows that the XRD peaks for many of the phases overlap or are so close that they form shoulders on adjacent peaks. This makes identifying many of the phases exceedingly difficult if only identified by means of XRD. Fig. 4.21(a) shows a small peak at approximately 2θ = 46.5 ˚ which shows the presence of M_6C carbide.

Sample HS, Fig. 4.21(b) shows lower intensity on the W_2C peaks when compared to Sample OP which could imply relatively lower amounts of W_2C when the substrate is heated. Due to the high energy input the oxygen can combine with

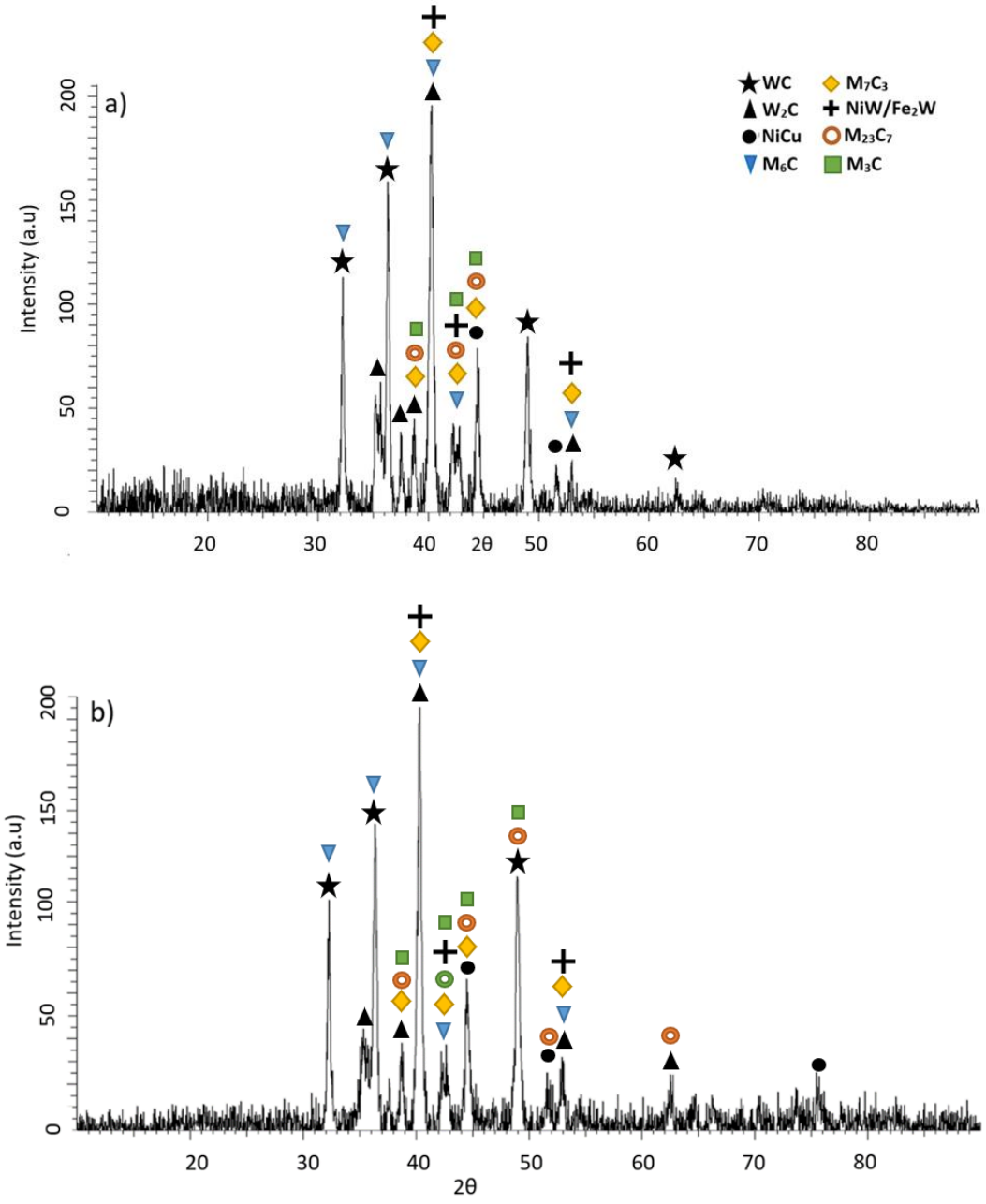
carbon released from the tungsten carbide to form carbon monoxide or carbon dioxide or combine with the tungsten to form tungsten oxide, according to Equations 4.4 and 4.5 [37]. Zhou et al. [38] reported that oxidation of tungsten at higher temperatures is unavoidable and the formation of an oxide layer has a detrimental effect on the wetting of the new melt. Depending on the local oxygen content, either CO_2 or CO will be released on the formation of WO_3 [375], [376].

$$WC + (5/2)\ O_2 = WO_3 + CO_2 \qquad \text{(Equation 4.4)}$$

$$WC + 2O_2 = WO_3 + CO \qquad \text{(Equation 4.5)}$$

The relative intensity of the peak at approximately $2\theta = 42^\circ$ is larger in the heated sample. This peak indicates the presence of complex carbides and solid solution, hence there is a larger amount of these phases present. The peak at $2\theta = 46^\circ$ also has a relatively higher intensity, which indicates the definitive presence of M_6C carbides. The peak at approximately $2\theta = 60^\circ$ indicates that there are M_3C carbides in the microstructure. Sample RM, Fig. 4.21(c) does not show any evidence of WO_3 since the top layer is remelted, limiting the effect of oxidation on the cast tungsten carbide. There is relatively less W_2C present in this sample and a larger amount of WC. Many of the less intense peaks are not present which can be attributed to preferential grain orientation, especially the (102) plane for WC which has a greater intensity than the (100) plane which was the dominant peak for Sample OP and Sample HS.

Four XRD patterns for various parameter sets are shown in Fig. 4.22.



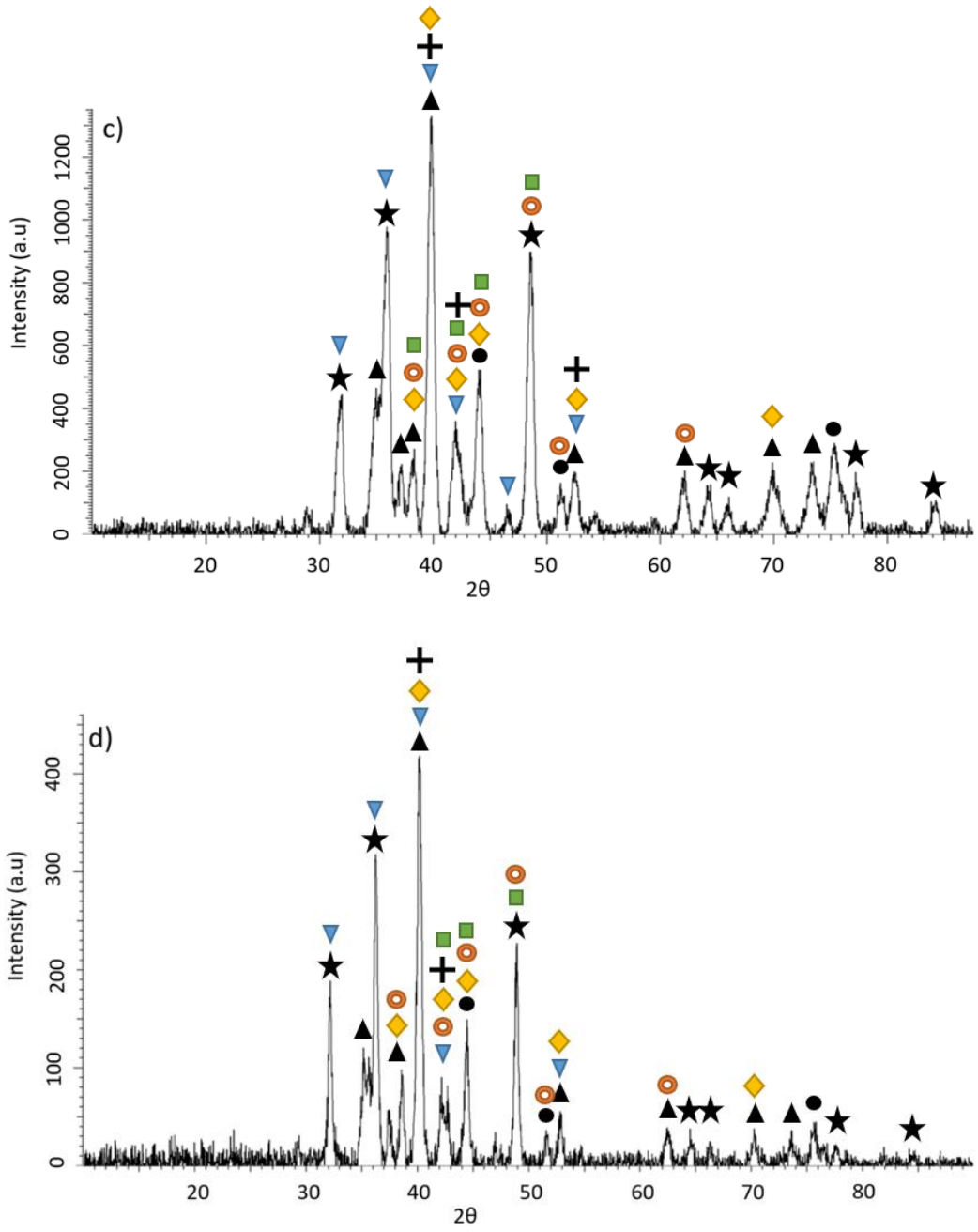


Fig. 4.22: a) 220 W, 5.2 mm/s, 11.5 g/min, 50% hatch, 0.2 z-increment, b) 270 W, 6.3 mm/s, 17.2 g/min, 75% hatch, 0.2 z-increment, c) 220 W, 5.2 mm/s, 12.6 g/min, 50% hatch, 0.31 z-increment, d) 220 W, 5.2 mm/s, 13.3 g/min, 0.5 z-increment.

The XRD patterns in Fig. 4.22 a)-d) show that the patterns remained relatively consistent irrespective of the parameter sets that were used to deposit the samples.

Fig. 4.22(a) and Fig. 4.22 (b) have different laser beam power, hatch overlap, powder feed rate and traverse speed but the XRD patterns have the same prominent peaks for WC, W_2C and the various eta phases as shown in Fig. 4.21. The peaks above 2θ=60˚ are not as prominent in Fig. 4.21 which indicates that the WC and W_2C grew preferentially in the other planes, or the low intensity of the main peaks implies that the weaker peaks are lost in the background noise. The same is observed for Fig. 4.22 (c) and Fig. 4.22 (d) which have a different powder feed rate and z-increment. All the peaks that are present in Fig. 4.21 are present in these samples. Fig. 4.22(c) has a higher overall intensity; hence the weaker peaks are more prominent than observed in Fig. 4.22(a) and Fig. 4.22 (b).

The XRD patterns show that the laser processing parameters did not have a significant effect on the observed patterns and therefore the phases which are present in the samples. Similar phases are present in all the samples and it is the region in which they are observed which might be altered due to the changes in process parameters.

4.4.2 Microstructure

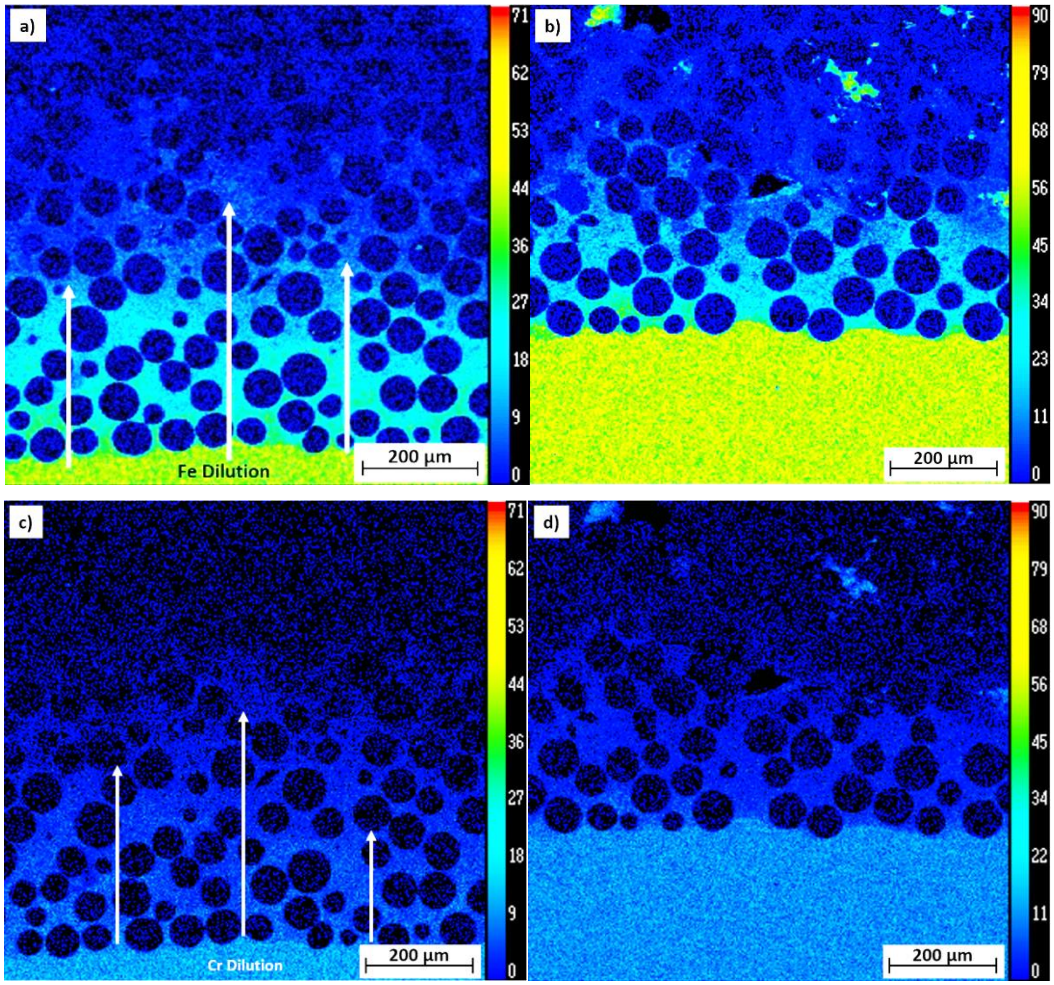


Fig. 4.23: Dilution of Fe and Cr into the deposition a) and c) Sample OP, b) and d) Sample 2.

Fig. 4.23(a) and (b) shows the degree of dilution of Fe from the substrate into the deposition for two samples which were deposited with different processing parameters. The dilution is not homogenous across the entire deposition, with some regions exhibiting more dilution. This being due to the localized thermal gradients and cooling rates. When the laser deposits the first layer it encounters the substrate. It rapidly heats the substrate and applies a layer of WC/W_2C-binder. In the liquid state Fe, can also dissolve and results in a dissolution layer which distributes high concentrations of atoms from the substrate and displaces the

original atoms of the binder. This occurs because iron atoms can easily substitute nickel atoms in solid solution [377]. The diffusion of Fe from the substrate is an indication of a good metallurgical bond between the metal matrix and the substrate[99]. Since the dilution changes the chemical nature of the cemented carbide, it too alters the morphology at the fusion zone[261], [323]. Fig. 4.23(c) and (d) show that Cr dilution also occurs although to a lesser extent since the Cr concentration gradient is less due to less chromium being present in the substrate. The same extent of dilution is observed across different parameter sets.

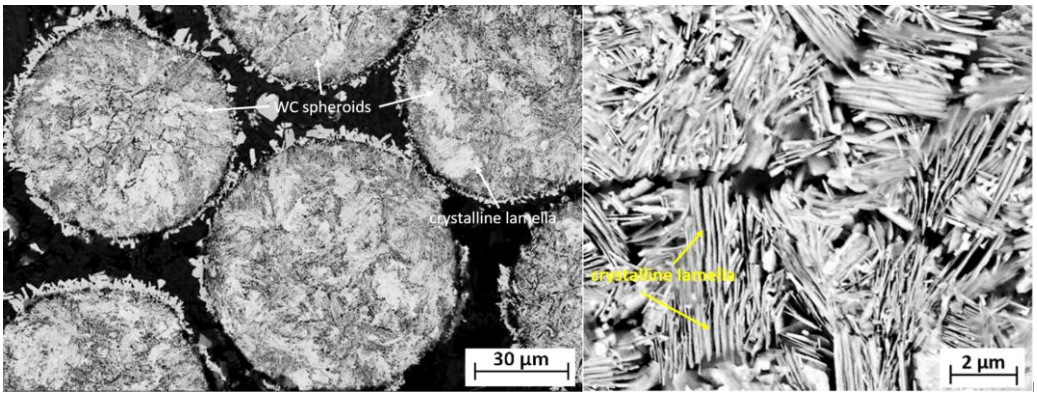


Fig. 4.24: Eutectoid lamella within spheroids (left) and magnified eutectoid lamella structure (right).

In Fig. 4.24(a), grain orientation within the spheroid particles is observed and these grains comprise of lamella. The fine crystalline lamella, Fig. 4.24 (b), within a spheroidal particle is the eutectic mixture of WC-W_2C. The elongation and thickness of the platelets is directly related to the cooling rate during the powder formation process [378] [355]. Many distinct phases are possible, as seen in Fig. 4.21(a), the XRD analysis. In Fig. 4.25, below, multiple microstructural configurations have been identified and the chemical analysis of these structures are represented in Table 4.8.

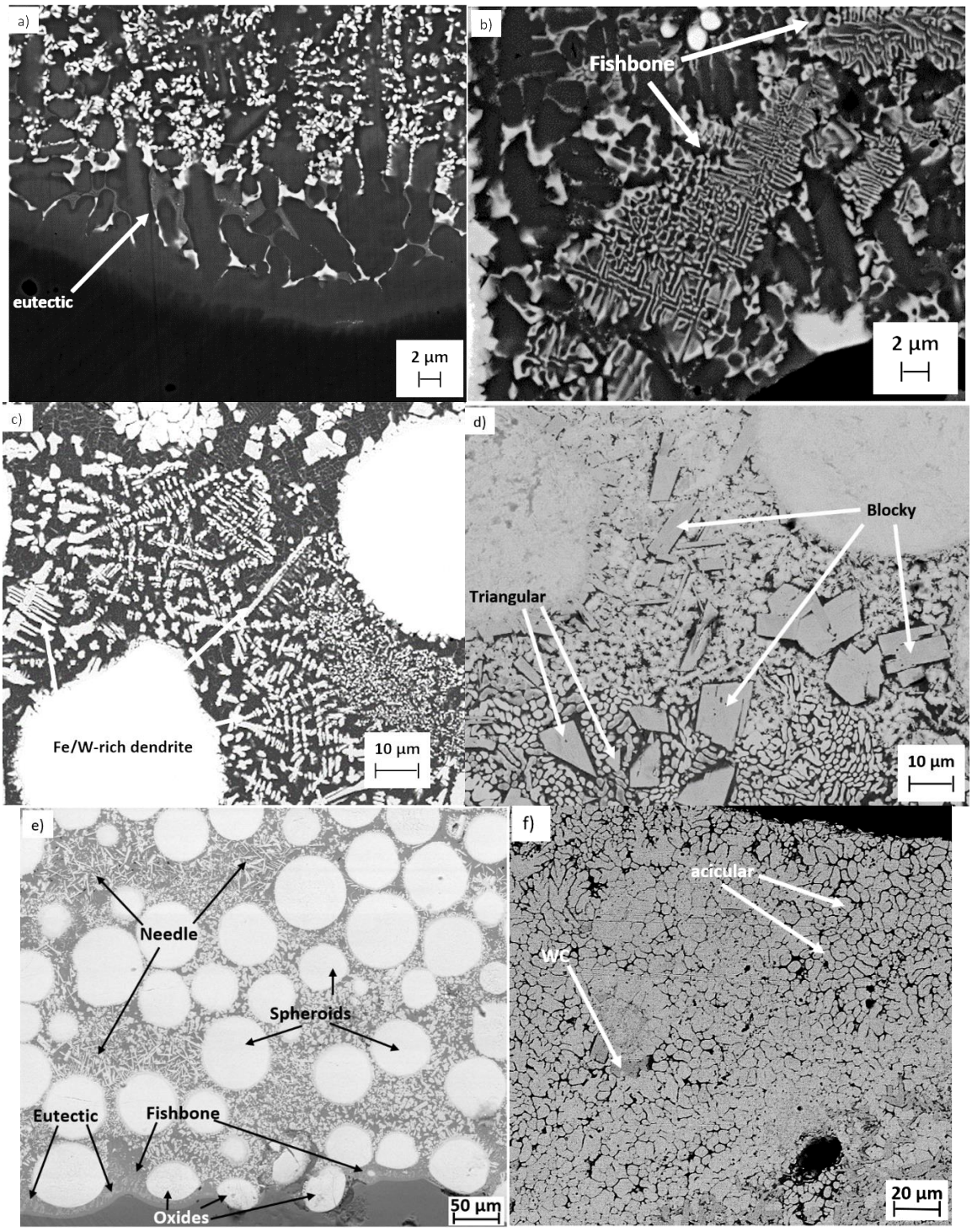


Fig. 4.25: SEM micrographs of a) and b) fusion region, c) close to the fusion region, d) central to top region, e) multiple regions of Sample HS and f) top region of Sample RM.

Table 4.8: Atomic percentage of elements for different defined microstructures.

	W	C	Ni	Cu	Fe	O	Cr
Triangular	46.63 ±0.63	36.93 ±0.34	7.42 ±0.46	2.68 ±0.29		6.33 ±0.33	
Blocky (rectangle)	37.18 ±4.77	8.86 ±2.33	28.34 ±5.88	20.06 ±4.38	1.07 ±0.14	4.18 ±1.11	
Acicular	47.94 ±1.50	24.75 ±3.22	14.14 ±3.64	8.03 ±2.34		5.14 ±1.25	
Fishbone	44.99 ±3.02	5.77 ±0.27	9.10 ±0.64	3.64 ±0.20	26.07 ±1.33	4.06 ±1.78	5.83 ±0.43
Fe/W-Dendrite	39.10 ±2.33	5.55 ±0.30	10.39 ±0.47	4.22 ±0.26	29.64 ±1.35	3.78 ±0.24	6.69 ±0.13
Needle	26.96 ±2.60	5.14 ±0.64	36.77 ±1.84	26.80 ±0.74	1.24 ±0.08	2.66 ±0.73	
Eutectic	10.57 ±3.61	5.82 ±0.88	10.36 ±0.48	1.92 ±0.58	60.54 ±4.63	0.52 ±0.13	9.47 ±0.64
Oxide	53.98 ±3.87	8.94 ±1.64	10.45 ±1.94	5.16 ±1.64	2.92 ±3.11	17.94 ±2.09	
Sample RM- top (acicular)*	56.13 ±2.74	28.28 ±2.49	8.67 ±1.36	0.39 ±0.28		5.76 ±0.87	
Sample RM- top (darker)*	45.75 ±0.80	39.96 ±1.92	7.64 ±1.44	0.45 ±0.15		5.82 ±1.11	

The chemical analysis of the triangular microstructure, as in Fig. 4.25(d), indicates that it is WC, with possible NiW solution impurity. WC grains found with triangular and elongated rectangular faces [67], [68], [75]–[77]. The faceted shape of WC crystals is characteristic of C-rich alloys [104] and is not inconsistent with simultaneous formation of the η-phase which is common in carbon deficient zones. Large grains which are in contact with η-phase in a W rich environment has been found to have similar grain sizes to high carbon concentration regions [379]–[381]. These larger grains are due to a coupled growth of WC-η. Nucleation occurs at the interface since it is less energetic than the WC-binder interface. WC dissolution is stoichiometric and produces supersaturation of both W and C [166]. The growth of

the η phase absorbs more W than C causing a localized high C concentration [104], [382], [383].

WC grains are more triangular in C-rich environments [384]. The truncated trigonal prismatic shape is not an equilibrium form of WC but is determined by the C-content. The blocky carbides, Fig. 4.25(d), observed are due to the truncation of the triangular WC faces. The blocky structure has high concentrations of Ni, Cu and W, and much lower concentrations of Fe than dendrites and fishbone morphologies. Fig. 4.26 (b-d) shows the high W, Ni and Cu content in the localized region. Studies [261], [361],[385] have quantified the blocky structures as tungsten rich eta carbides, M_6C. Therefore, the blocky carbides can be proposed as (M=W, Ni, Cu)$_6$C such as (Ni_2W_4C) and (Ni_3W_3C) which grew into grains with WC due to the analysis of the Raman spectrum, Fig. 4.38(V). The low iron concentration implies that blocky carbides are not observed near the fusion zone due to the high Fe concentration this can also be seen in the EPMA map in Fig. 4.23(d).

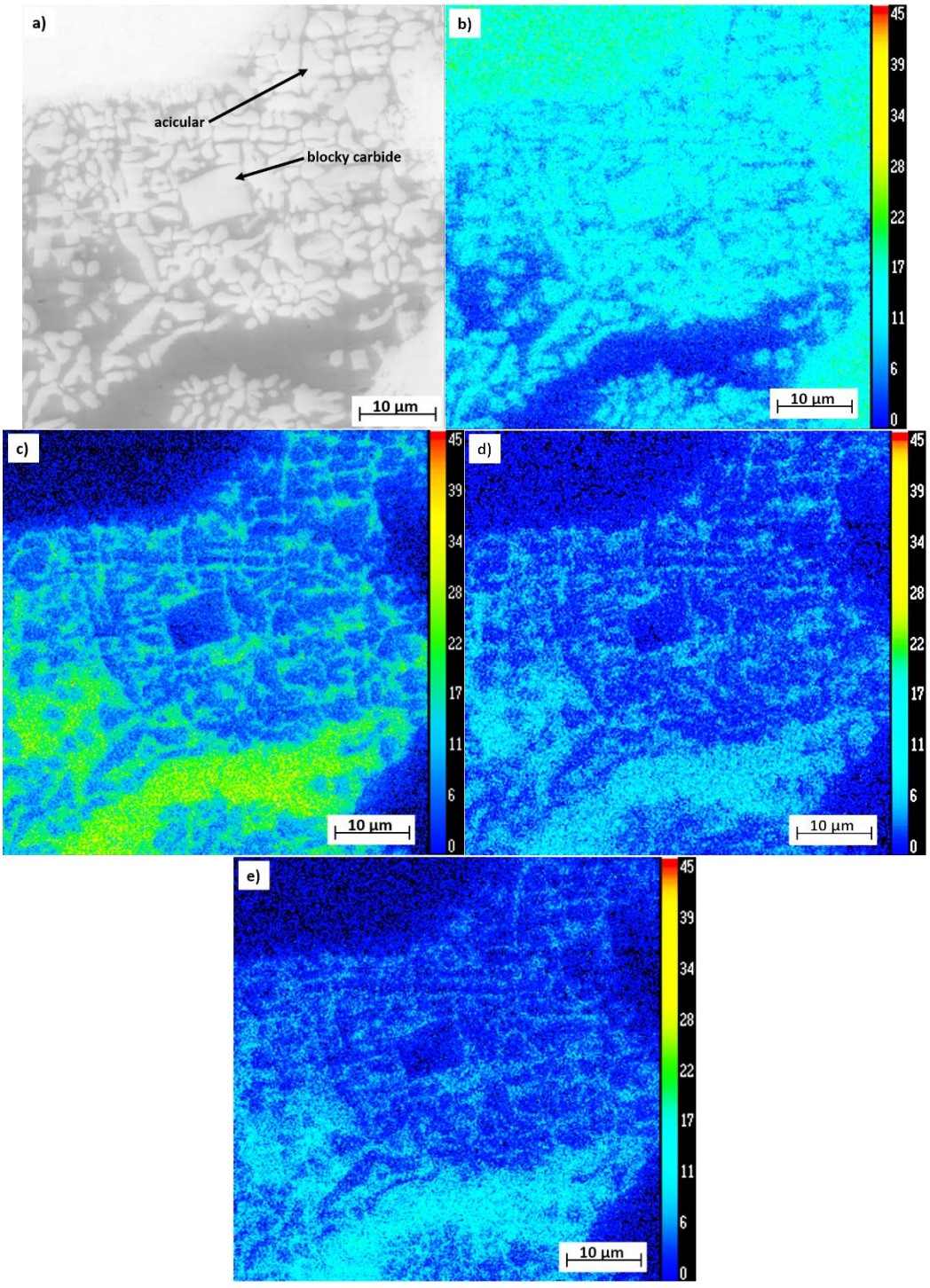


Fig. 4.26: a) SEM of region of interest and elemental mapping of b) W, c) Ni, d) Fe, e) Cu

The tungsten percentage, in the acicular structure, is double that of the carbon content which indicates that the dominant phase is W_2C. W and C accumulate and react with matrix elements, which justifies the presence of Ni and Cu. The acicular structure which is formed is associated with the contact interface [386]. The high W content in the acicular phase is observed in Fig. 4.26(b) and the binder which is present around the phase in Fig. 4.26(c) and (e). Low Fe concentration is observed around the acicular structures, Fig. 4.26(d) and Table 4.8.

The fishbone structure, Fig. 4.25(b), occurs only near the fusion zone because of the high Fe and the high cooling rates [261]. The high Fe concentration is due to the dilution from the substrate during the first layer deposition, where the Fe atoms displace the Ni and Cu from the binder phase, Fig. 4.23(a-b). This effectively creates a Fe binder and hence the fishbone structure which is commonly observed in WC-Fe systems[387]. Table 4.8 shows that there is a high concentration of Fe and W, along with elevated concentrations of Cr which is also from the dilution process of the substrate. The chromium is possibly found as Cr_7C_3 and $Cr_{23}C6$ carbides depending on the localized carbon content. The carbide is surrounded by a solid solution (M-M, M = Fe, W) [388] with the nickel and copper concentrations being due to infiltration of the iron microstructure.

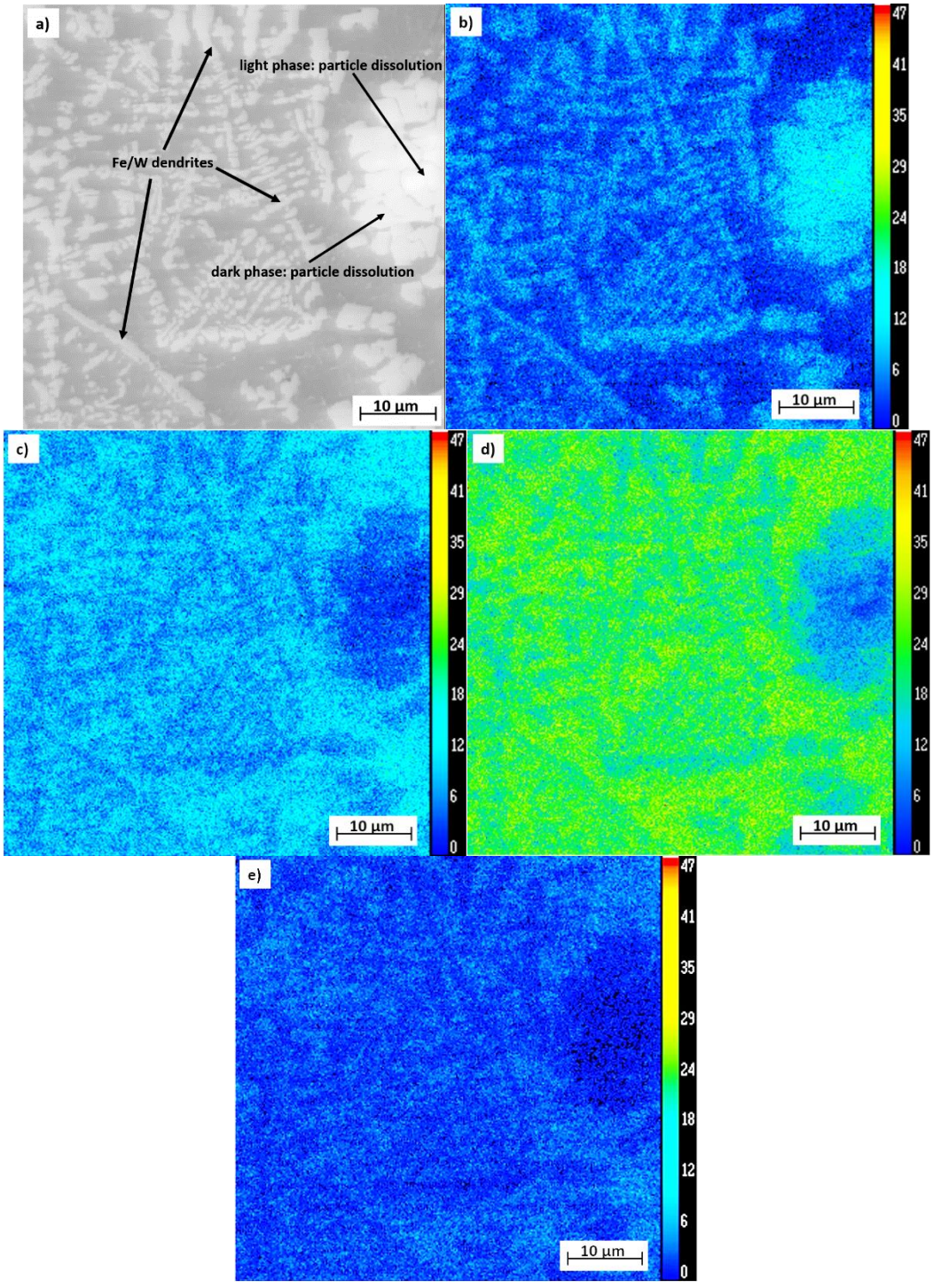


Fig. 4.27 a) SEM of region of interest and elemental mapping of b) W, c) Ni, d) Fe, e) Cu

The Fe/W-dendrite structure, Fig. 4.27(c), is like that of the fishbone with slight variations in the grain growth. A high concentration of Fe is also required, Fig. 4.27(d), limiting this morphology to the dilution region of the deposition. The dendritic structure is found close to the fishbone structure but the differences in the grain growth can be attributed to differences in localized carbon content and slight changes in solidification rate which allows for a courser microstructure to form. The higher Fe concentration results in a decrease in the W concentration, Fig. 4.27(b), which implies that when the solid solution is richer in iron then a dendritic structure will form while a lower Fe concentration will preferentially result in the fishbone structure. The cast WC spheroids dissolve into the surrounding binder and one such spheroid which has almost completely dissolved is seen in Fig. 4.27(a). There are two phases present, a lighter and a darker phase which was further analysed, as in Fig. 4.28.

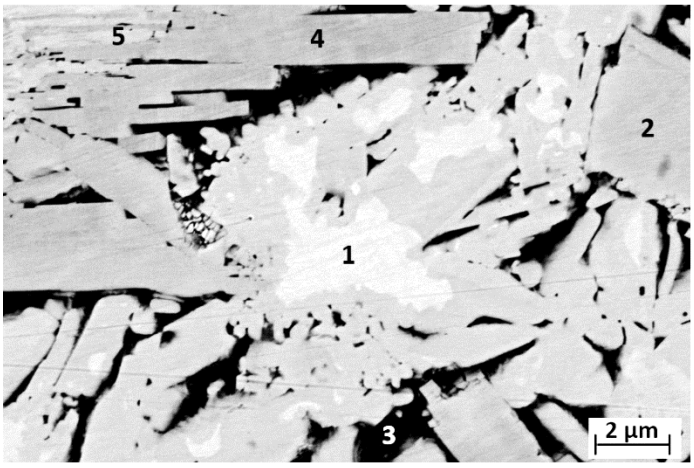


Fig. 4.28: EDS analysis of light and dark phases.

Table 4.9: EDS results for the five spectra in Fig. 5.6.

	W	C	Ni	Cu	Fe	O
Spectrum 1	49.47	42.05	2.68			5.79
Spectrum 2	42.11	57.89				
Spectrum 3	8.44	25.69	47.83	15.49	2.55	
Spectrum 4	41.12	57.21	1.66			
Spectrum 5	44.99	48.56	1.72			4.73

The lighter phase located at point 1 and point 5, Fig. 4.28, has an equal amount of W and C which indicates that the phase represents WC. Point 2 and point 4 has a higher concentration of C when compared to point 1 which indicates that the surplus of carbon could be due to graphite impurities being included in the microstructure or the preferential W dissolution has created a carbon surplus. This carbon surplus results in the darker microstructure. Point 3, is the small binder region between the adjacent dark phases, there is a high Ni and Cu concentration since it is the binder phase.

The low W content is due to W dissolution from the cast WC, but there is a remarkably high C content which implies that a large concentration of carbon has undergone dissolution from the cast WC particles. W_2C undergoes dissolution preferentially to WC thus two times the amount of W is released for each carbon, hence creating a carbon surplus in the adjacent dark phases. Needle like structures, Fig. 4.25(e), have a relatively low W concentrations and are rich in Ni and Cu. Fine rod-like/lamellar structures have been associated with M_2C structures [389] and M_6C carbides in higher carbon content regions with high cooling during solidification [99],[377]. The W and C which is dissolved in the binder grew into grains but before extensive growth can take place the high cooling rates during solidification suspend the fine needle like grains in the binder. These needle-like structures are proposed to be a combination of W_2C, M_6C (M=W, Ni) and a solid solution of Ni-Cu which is attributed to the binder. The needle like structures contribute greatly to the interdendritic carbides found within the binder. Needle-like structures have been found to grow more readily on low concentrations of carbon [68].

The eutectic structure, Fig. 4.25(a) and (e), has the lowest W concentration and highest Fe and Cr concentration of all the morphologies that were studied [390], Fig. 4.29(b) and (c). The nickel and copper, the main components of the binder,

are no longer in relation with the starting powder, as the nickel powder is approximately 5 times more than the copper, Fig. 4.29(d) and (e). This is due to the eutectic structures only being observed in the iron dilution zone, where the iron displaced a significant percentage of the nickel atoms but more of the copper atoms. Cr_7C_3 and $Cr_{23}C_6$ are the carbides in which chromium would be present, with the Cr_7C_3 phase more prominent in the higher carbon rich areas, whereas $Cr_{23}C_6$ could be found in lower carbon, higher chromium concentration regions [377],[388],[390]. The high values of W, Ni and Fe is due to a mixture of M_6C carbides [377] (Fe_3W_3C, Ni_2W_4C) and the Fe rich solid solution of Fe-Ni [175].

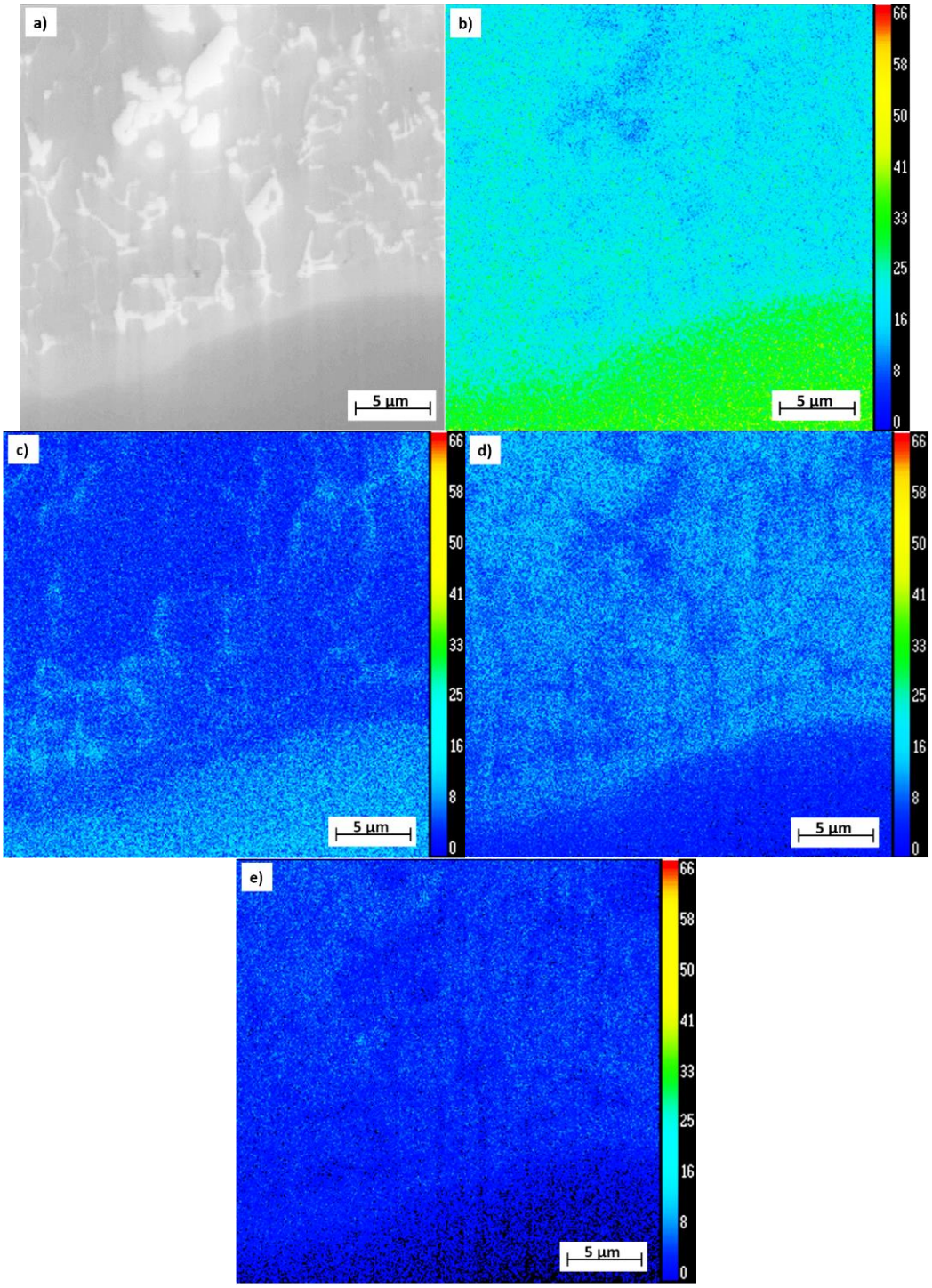


Fig. 4.29: a) SEM of region of interest and elemental mapping of b) W, c) Ni, d) Fe, e) Cu

A small circular microstructure was also observed, as shown in Fig. 4.30(a) which is the remains due to the complete dissolution of a spheroid. The small circular structures have a high W concentration, Fig. 4.30(b), are present in high Ni, Fig. 4.30(c), and high Fe, Fig. 4.30(d), environments. There is also a substantial amount of Cu, Fig. 4.30(e), present. The cooling rates and thermal gradients are still too high for large grains to grow; thus, the remains of the dissolved particle are solidified as small circular particles which show how the dissolution process ends.

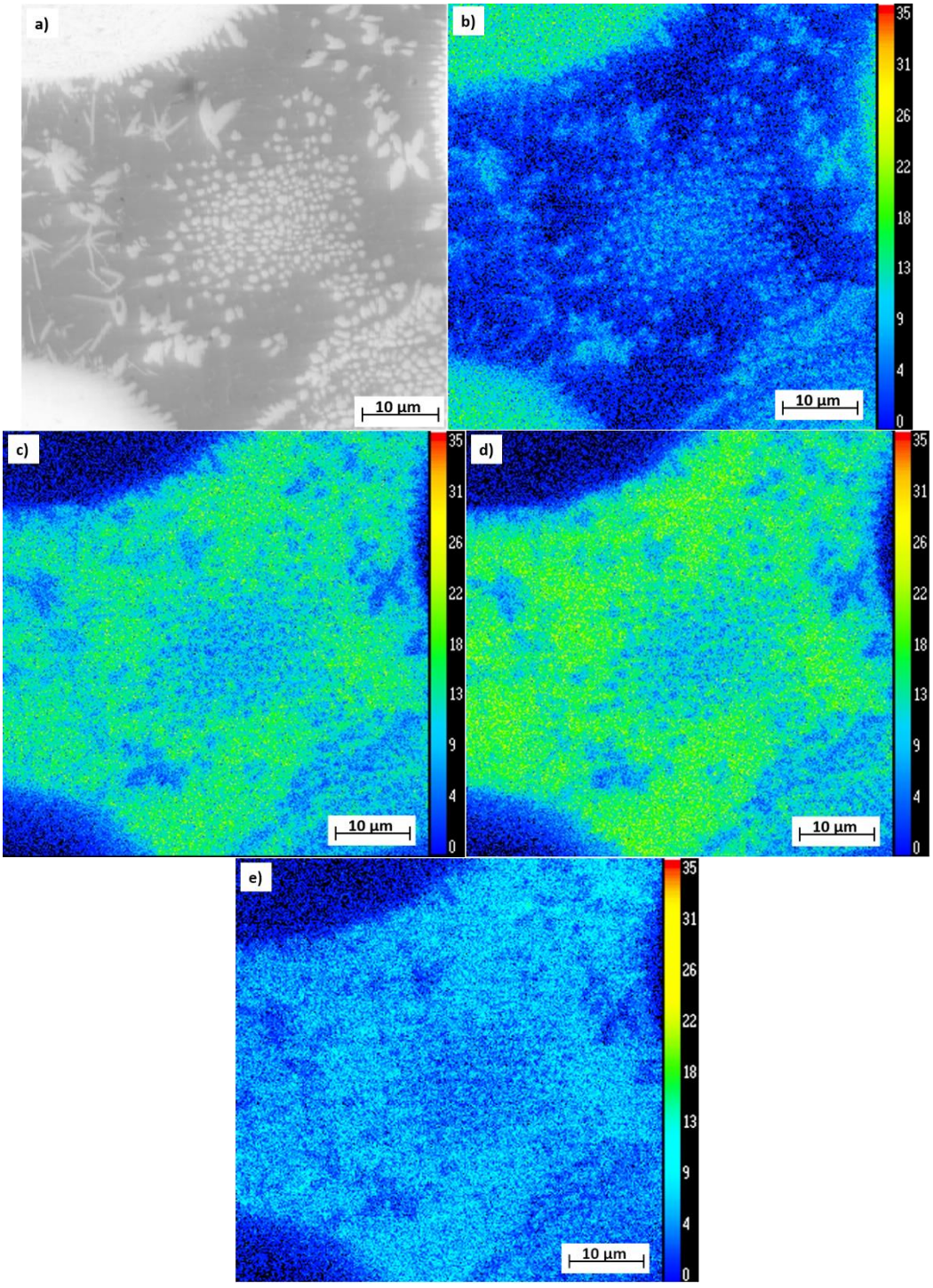


Fig. 4.30: a) SEM of region of interest and elemental mapping of b) W, c) Ni, d) Fe, e) Cu

The use of surface remelting to alter the surface microstructure and improve mechanical properties of the component [348]–[352], [390], [391] and a heated substrate to alter cooling and solidification rates as well as the thermal gradient [172], [177], [180], [236], [330]–[332], [392]–[396] which increased productivity, reduced cracks and pores and improved mechanical strength has been the focus of many studies.

Chemical analysis performed on the top region of Sample RM, Fig. 4.25 (f), showed a ratio of 2:1 between W and C, which indicates that the remelting process promotes the formation of the acicular structure with the same chemical composition as the phase found within the sample. A major difference is observed in the binder metals, i.e. Ni and Cu, the nickel percentage has decreased, and the Cu concentration is basically void. The remelting process causes the evaporation of the copper and a percentage of the nickel due to the high energy input. The darker phase in the remelted region, Fig. 4.25 (f), is due to WC, which is seen from the ratio of W:C which is almost 1:1. Again a low copper content is observed due to the evaporation of copper which has a lower melting point than nickel.

A high concentration of W and O is reported for the oxide phase which grows on spheroids in the fusion zone for Sample HS, Fig. 4.25(f). From Table 4.8 the W:O ratio is almost 3:1 which implies WO_3 is the dominant phase which has formed. The higher carbon content is due to free carbon being present since the WC and W_2C had to undergo a chemical reaction which involved breaking bonds with carbon in favor for bonding to oxygen. An elemental map was recorded for a spheroid particle in the fusion zone on Sample HS, as in Fig. 4.31. The presence of oxygen in the molten pool greatly decreases the wettability of WC in the molten pool [397].

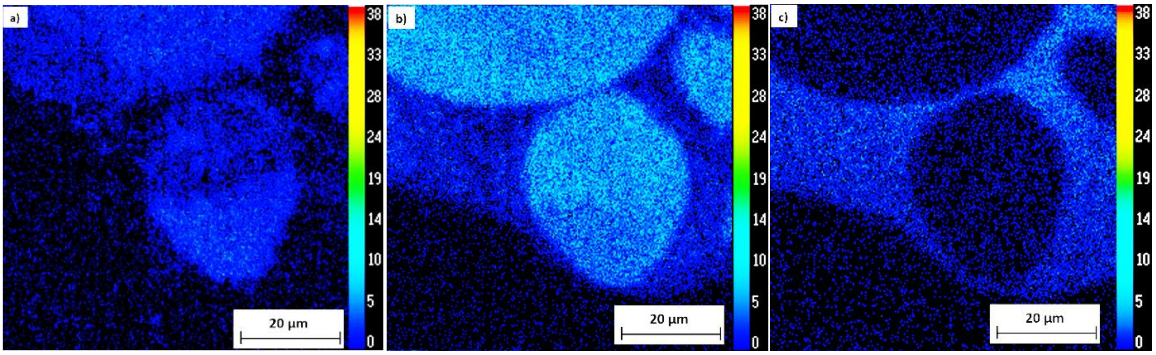


Fig. 4.31: EPMA of Sample HS a) oxygen, b) tungsten and c) nickel.

The oxygen map, Fig. 4.31 (a), shows how the oxide is located on the side closest to the fusion line, which indicates that the temperature is enough to cause oxidation but not enough to cause complete dissolution of the cast WC/W_2C. The tungsten map, Fig. 4.31 (b), reveals that there is a high concentration in the region of the oxygen, hence WO_3 is the main oxide, as found in the XRD, Fig. 4.21(b), and Raman spectroscopy, Fig. 4.38 (IV). No nickel is highly concentrated over the high oxygen concentration, Fig. 4.31(c), hence there is no nickel oxide present. Spheroidal particles in the fusion region was present in all the deposited samples as in Fig. 4.32(a-c).

Sample HS, even though a heated substrate was used, still had spheroidal particles which were solidified in the binder before complete dilution, Fig. 4.25(e) and Fig. 4.32(c). This occurrence is due to the high density of the cast WC compared to the binder phase and the violent stirring and convection driven by a thermocapillary action [398]. There are significant binder regions in between the WC spheroid particles since there are repulsive forces from the Ni and Cu in the binder and this prevent the spheroids form being closer to one another. The Marangoni effect is more visible in the fusion zone than any other region since as the deposition continues the spheroids begin to dissolve and new phases form whereas the fusion zone consists primarily of unaltered solid WC spheroids.

The different processing parameters could not create a fine homogenous structure in the fusion region.

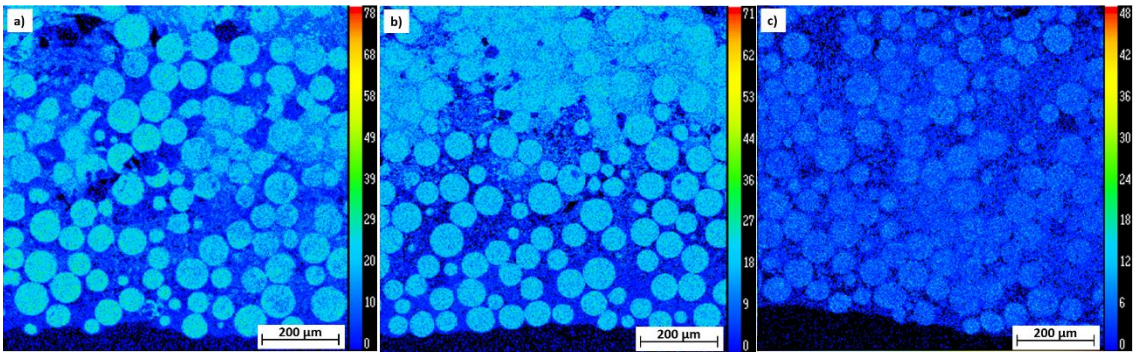
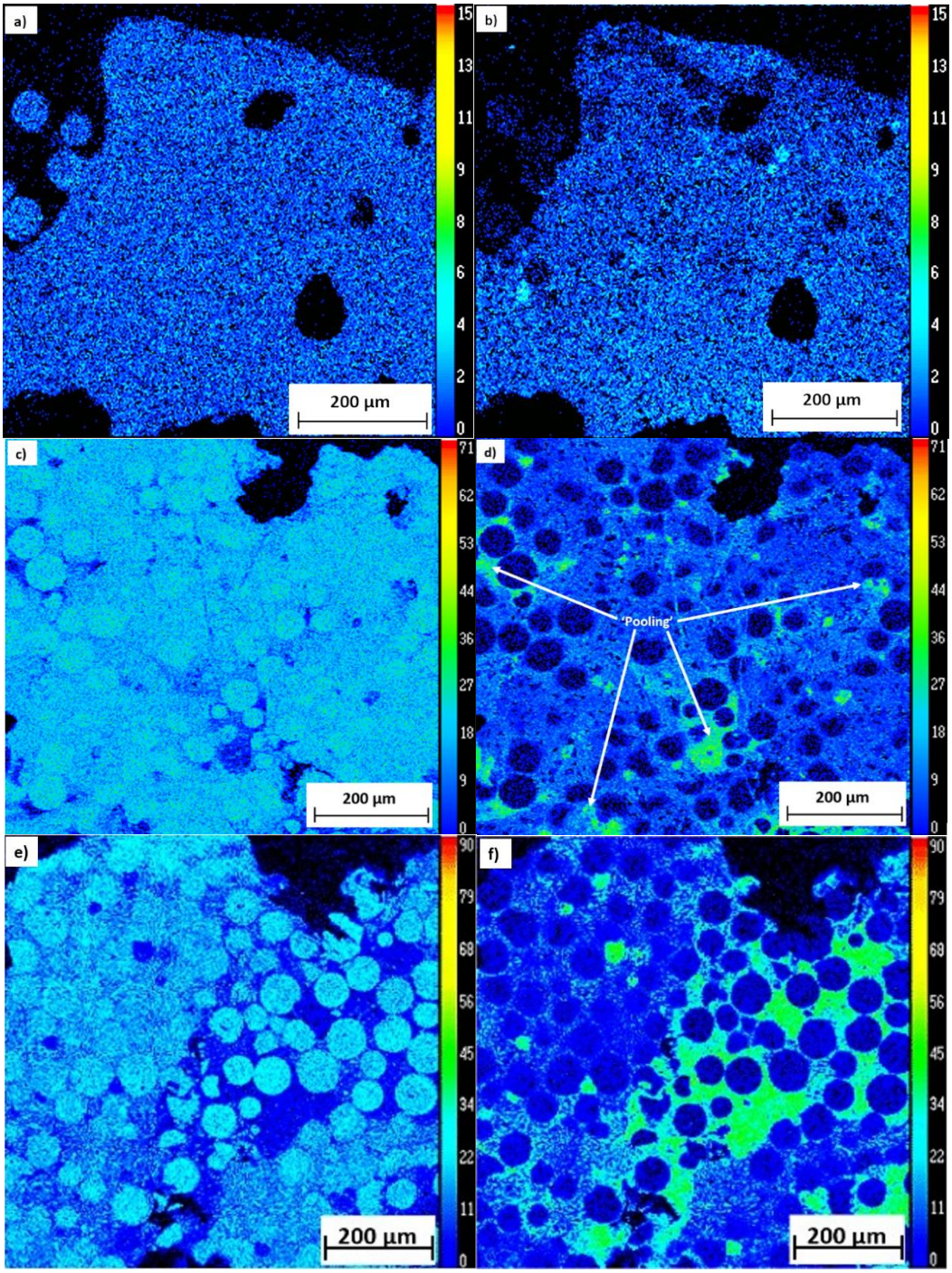


Fig. 4.32: EPMA of fusion region of a) Sample 2 b) Sample OP and c) Sample HS.

The heated substrate still displayed eutectic and fishbone structures in the fusion zone, although more fishbone structures with a larger morphology, than the unheated samples, were observed. The frequency of the eutectic structures reduced as did the Fe/W- rich dendritic structures. The needle-like structures were observed closer to the fusion zone, Fig. 4.25(e), and small particles undergoing complete dissolution were identified significantly closer to the fusion zone than in the unheated samples. The heated substrate affects the cooling rate and temperature gradient that the powder experiences. Therefore, the fishbone structure has a slightly different solidification temperature than the Fe/W-rich dendrites and the eutectic. The lower thermal gradient and slower cooling rates provides more time for grain growth to occur in lower deposited layers.


a)
b)
c)
d)
e)
f)
200 µm
'Pooling'
15
13
11
9
8
6
4
2
0
71
62
53
44
36
27
18
9
90
79
68
56
45
34
22
11

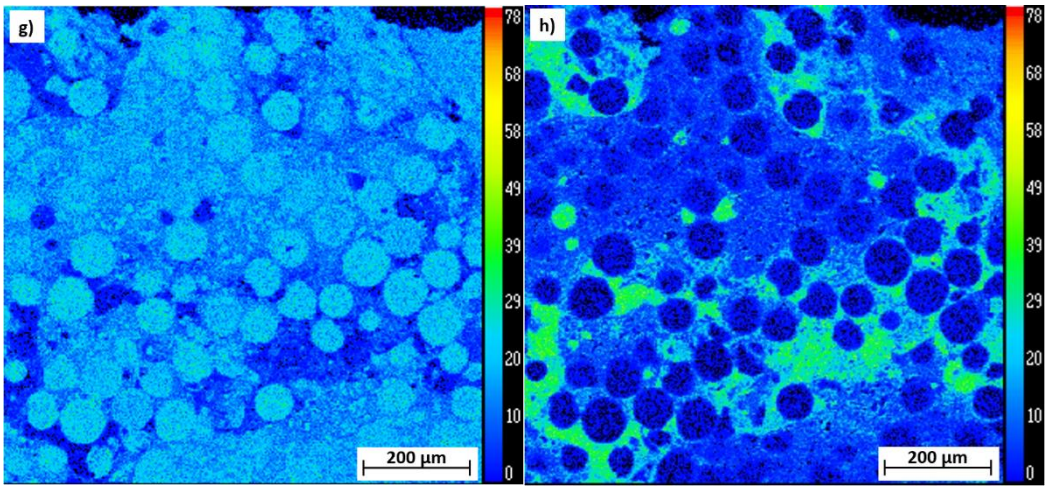


Fig. 4.33: EPMA of a) W of Sample RM, b) Ni of Sample RM, c) W of Sample OP and d) Ni of Sample OP, e) W of Sample 2 and f) Ni of Sample 2, g) W of Sample 14 and h) Ni of Sample 14.

The surface of Sample RM, which underwent a remelting cycle, does not have any unmelted WC/W_2C powder particles, Fig. 4.33(a), whereas Sample OP, Fig. 4.33(c), sample 2, Fig. 4.33(e) and sample 14, Fig.4.33(g) do display undissolved spheroidal particles. Fig. 4.33(a) shows homogenous distribution of W over the entire region [393]. Whereas Sample OP, Fig. 4.33(c), sample 2, Fig. 4.33(e) and sample 14, Fig. 4.33 (g) has a bimodal microstructure with finer structures in between the spheroids.

The different process parameters therefore influenced reducing the number of spheroids in the surface region but could not obtain the same homogeneity as the remelting process. The surface region of the entire remelted sample has acicular microstructure and a blocky darker structure, Fig. 4.33(a). This is due to the remelting process changing the sonification and cooling rate of the surface region which allows for finer microstructure to grow from the completely diluted spherical particles. When assessing the nickel EPMA, which corresponds to the binder distribution, there are minimal localized regions of binder pooling in Sample RM,

Fig. 4.33(b), whereas Sample OP, Fig. 4.33(d), sample 2, Fig. 4.33(f) and sample 14, Fig. 4.33(h) shows multiple regions where high binder pooling has occurred.

The structure in which the binder phase solidifies is highly dependent on cooling and solidification rates and the thermal gradient during deposition.

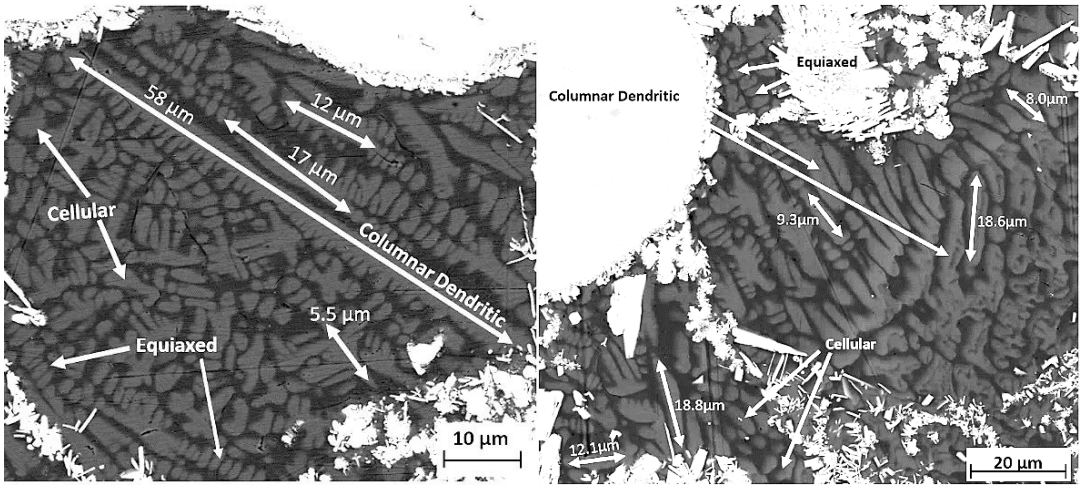


Fig. 4.34: Binder of Sample HS (left) and binder of Sample OP (right).

The binder region in Fig. 4.34 is cellular dendritic in the bottom and central region while the top region, Fig. 4.34 shows columnar dendritic[99],[267],[399] [400]. Columnar dendritic forms in the surface layers since the temperature gradient is low between the deposited layer and the previous layer due to continuous heat and a high solidification rate[99] (cooling rates from 102K.s^{-1} to 103 K.s^{-1} [401]) whereas the bottom region exhibits a large temperature gradient due to the cold substrate plate. The central region still has a large enough temperature gradient to solidify at a lower rate into cellular dendritic structure [126],[402]. The dendrite morphology depends mainly on the cooling rate and thermal gradients inside the build [403]. When the cooling rate is lower a coarser dendritic arm spacing is observed and a faster cooling rate results in a smaller dendritic arm spacing [268]. The dendrite arms were found to be nickel rich and the interdendritic phase rich in copper [99].

Fig. 4.34(a) shows that long columnar dendrites, 58 µm, form alongside much shorter arms, such as 5-17µm. There is also cellular and equiaxed morphologies observed in the same binder region. The molten pool distributes energy in a gaussian manner [236], therefore there are hotter and cooler regions which contributes to different localized cooling properties and allows for multiple microstructures to be observed in a relatively small region. When the binder region was studied for a different sample, Fig. 4.34(b), the same array of morphologies was identified, although for the specific region the dendrite arms had a length of 8.0 µm to 19.0 µm. There were no exceptionally long columnar dendrites as in Fig. 4.34(b), which indicates a different localized cooling rate.

The heated substrate reduces the thermal gradient and therefore affects the cooling rate, but the same binder morphology was found for the heated and unheated substrate. The grain growth directions observed in the binder region will distribute applied forces in a unique manner. The equiaxed and cellular regions will have a homogenous force distribution, while the singular growth direction columnar dendrites will promote an anisotropic force mitigation. This implies that more tensile/ pressure stress can be applied along the grain growth direction and due to their larger size columnar dendrites can accommodate more stress than equiaxed and cellular grains. In the regions were columnar grains grow in multiple directions a mutual constraint is observed, hence there is a greater chance of failure due to an external load since there is distribution conflict between the columnar grains [364].

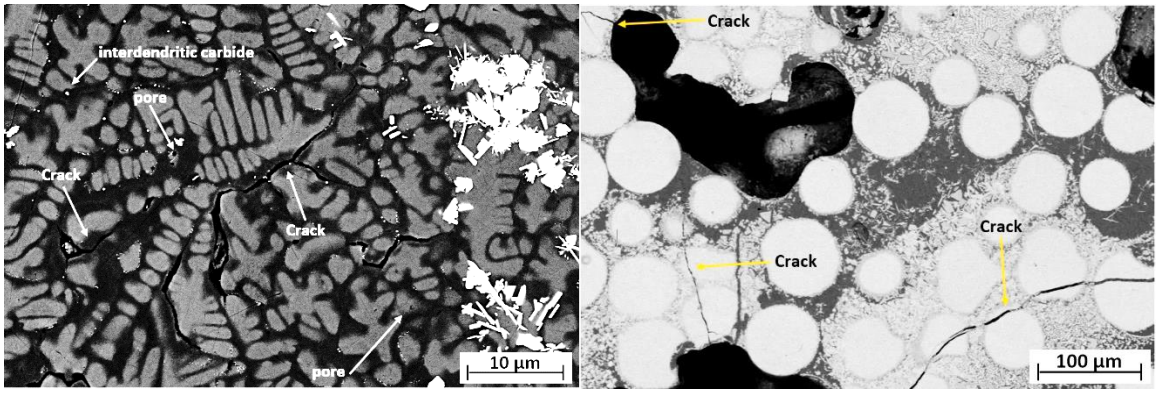


Fig. 4.35: Cracks present in the binder region (left) and WC particles (right).

The formation of cracks during laser cladding has been related to thermophysical properties of the depositing the materials and the substrate, such as the melting point, coefficient of thermal expansion and Young's modulus [404]. The presence of cracks in Ni- based WC cermets has been related to the microstructure as well as the laser processing parameters, such as the laser power and the traverse speed [180]. Residual stresses from the manufacturing process can be a driving force for crack initiation in sites containing pores, regions of fractured WC particles and solidification cracks [178], [371], [404], [405] [406]. Internal stresses of WC particles has been related to the volume fraction [407], with hard facing particles in a metal matrix through the direct metal laser sintering process having an increased crack density after 15% volume percentage of the hard facing particle [408]. This was due to the increasing in reinforcing particle leading to a clustering effect which resisted the flow of the molten material and increase in pore formation [408].

The cracks are only observed in the darker copper rich phase and not in the nickel phase, Fig. 4.35. The boundaries of the Ni phase have small interdendritic carbides, which are hard and brittle and contribute to the propagation of the induced cracks [261],[371]. The high cooling rates and induced stresses are the

main reason of the cracking[264], [328], [409], [410]. When cracks are formed along grain boundaries it is generally due to solidification cracks [196], [411]. The small pores observed, Fig. 4.35, is due to decarburizing reactions in the elevated temperature liquid pool, Equation 4.6 and 4.7 [412], [413]:

$$2WC \rightarrow W_2C + C \qquad \text{(Equation 4.6)}$$

$$C + O_2 \rightarrow 2CO,\ CO + O_2 \rightarrow CO_2 \qquad \text{(Equation 4.7)}$$

The carbon is eliminated from the WC which is transformed into W_2C under high laser power. CO and CO_2 gas bubbles are released into the molten pool which are then trapped by rapid solidification of the layer [196], [411]. These pores add a weakened point and can cause cracks by means of stress concentration. Microcracks were observed through WC particles [391] ,[312], Fig. 4.35. The cracks are due to the high thermal stresses which incur from the WC particles and binder having different coefficients of expansion and once the stresses exceed the yield strength, crack propagation occurs [180].

The WC particles are relatively large since the precursor powder had a d(0.5) of approximately 90 µm. It has been found that WC particles which are larger than 30 µm generate cracks easier since they are more prone to having defects [310], [368]. The larger particles also had larger interfaces with the binder, hence larger stresses are transmitted from the particle to the binder [237], [238]. The crack propagation direction has been found to move along the highest temperature gradient [405], [180], [414], Fig.4.35 shows cracks moving in multiple directions which indicates a very complex temperature gradient in the deposited samples. Research has been conducted to reduce crack formation during laser cladding by

controlling the cladding materials and processing parameters [404], [415]–[418]. An increase in laser power and scan speed affected the formation of cracks [180], [264], [409], as well as reducing the presence of brittle carbides [329].

Dissolution of WC into the surrounding metal binder has been observed for many processing methods such as electrometallurgy, flame spraying and surface cladding in vacuum [103], [361], [419], [420] for temperatures <1200 ºC. Various WC-Ni compositions also had core-rim studies performed on it [421]–[427]. Smaller particles have a relatively larger dissolution percentage than larger particles since the relative surface area is larger for a smaller particle [428]. Three types of interfaces can be identified when there are reinforcing particles and a metal matrix [428]. There is the flat interface where the reinforcing particles (WC/W_2C) do not dissolve or interact with the metal matrix, known as mechanical bonding zone. The second type is the wetting-dissolving interface, where the WC/W_2C and metal matrix dissolve in each other. The third type is when the reinforcing particles and the metal matrix react to form a new interface layer. The third is a chemical reaction and metallurgical change is present [261]. Researchers have studied the kinetics of the interfacial chemical reactions in various alloys and concluded that a simple parabolic growth law, Equation 4.8, can be used to describe the chemical reaction [429]–[432].

$$\bar{X} = K\sqrt{t} \qquad \text{(Equation 4.8)}$$

Where K is the diffusion coefficient and t is the reaction time. The formula provides a theoretical basis for the interfacial reaction control of metal matrix composites. Therefore, by changing the sintering temperature and heat preservation, the thickness of the rim on the outer edge of the WC particles can be controlled [429]–

[432]. Fick's Law, Equation 4.9, can also be used to explain the formation of the interfacial layer [433].

$$J = -D\frac{dc}{dx} \qquad \text{(Equation 4.9)}$$

Where J is the diffusion flux, D is the diffusion coefficient and dc/dx is the concentration gradient. The diffusion flux shows a directly proportional relationship with the concentration gradient, which implies that diffusion reactions will occur if there is a concentration gradient. The diffusion flux shows a directly proportional relationship with the concentration gradient, which implies that diffusion reactions will occur if there is a concentration gradient. In the initial stages of the reaction there is a large concentration gradient between the W and C rich cast powder and the binder. This causes diffusion of W and C with the metal binder matrix [434]. As the reaction progresses the concentration gradient decreases and an interfacial layer forms which prevents the further dissolution of the cast powder, which yields the core-rim structures which are observed.

The elemental nature of the cemented WC particles was tested from within the particle to the interface between the binder and the WC particle. A diagrammatic interpretation is in Fig. 4.36 and the elemental results are shown in Table 4.10.

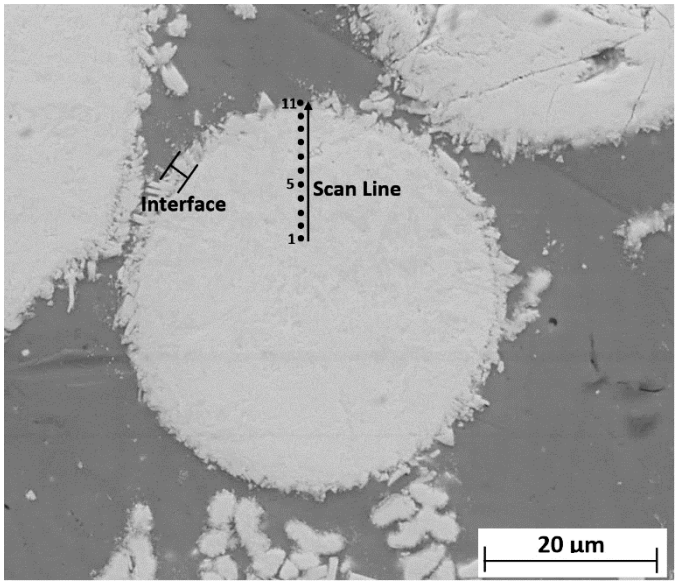


Fig. 4.36: Core-rim WC particle after laser deposition.

Table 4.10: Atomic % of elements at various points along the scan line in Fig. 4.36.

	W	C	Ni	Cu	Fe	O	Mn
1	78.69	12.41	2.85	1.89	0.30	3.85	0.02
2	77.02	12.57	3.95	2.74	0.27	3.37	0.03
3	72.75	12.37	6.72	4.49	0.41	3.22	0.04
4	71.33	12.24	7.80	5.03	0.37	3.13	0.08
5	67.49	11.92	10.29	6.55	0.57	3.07	0.10
6	63.73	12.04	12.69	8.41	0.57	2.46	0.10
7	61.30	11.89	14.28	9.15	0.62	2.63	0.12
8	59.14	11.59	15.82	10.15	0.68	2.50	0.10
9	56.32	11.54	17.72	11.12	0.72	2.41	0.17
10	53.91	11.35	19.36	12.10	0.76	2.34	0.15
11	49.78	11.15	22.02	13.96	0.88	1.98	0.19

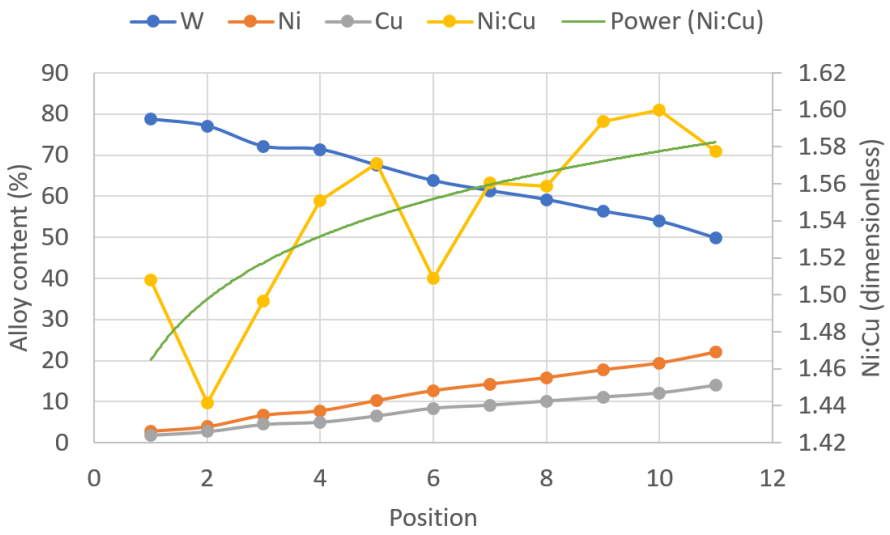


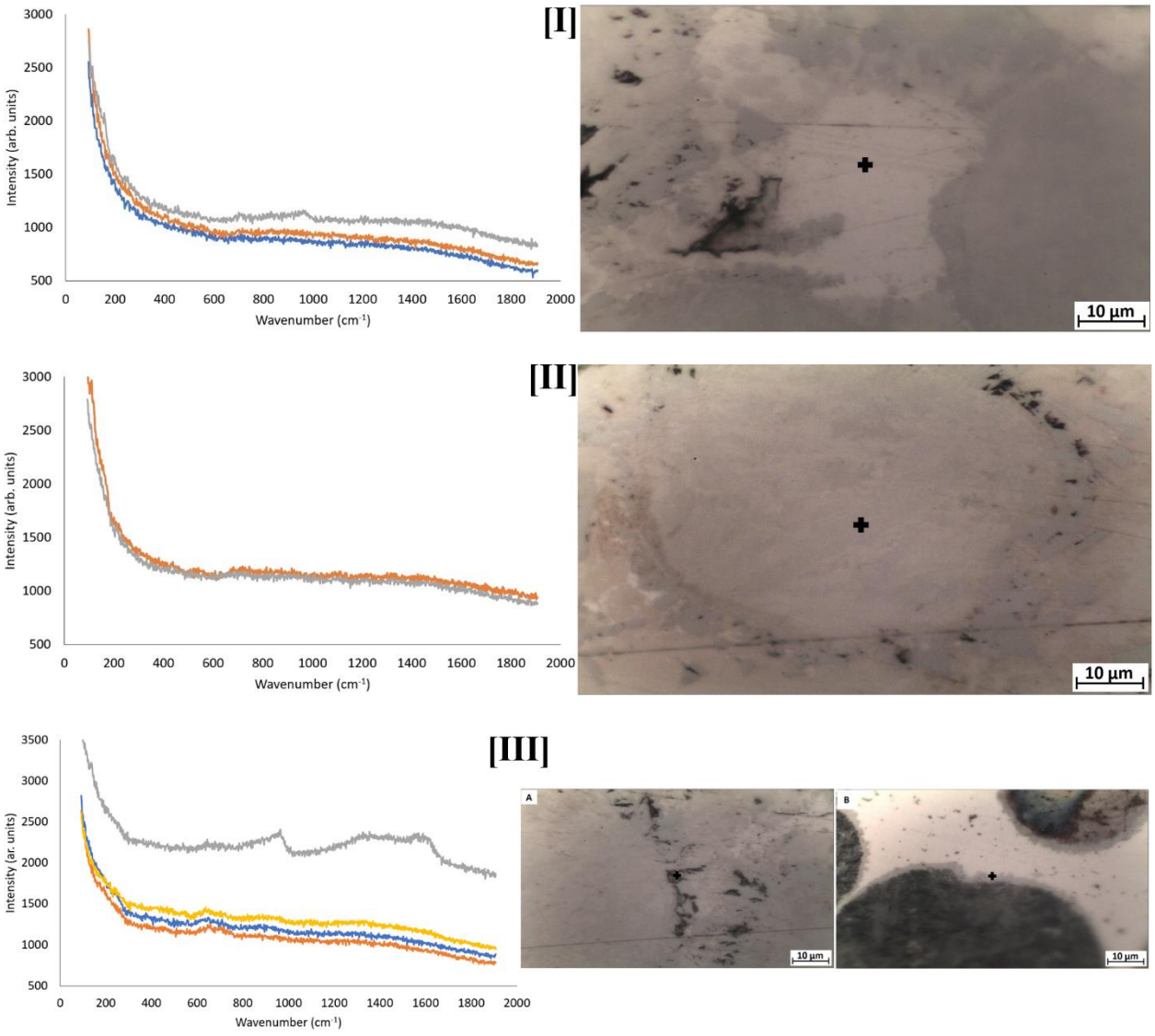
Fig. 4.37: Change in W, Ni and Cu content with radial position in WC particle in sample 21(OP), (selected data from Table 4,10)

From the interior of the cast WC particle to the interface region the W content gradually decreases as the binder content increases. This is due to the dissolution of the cast powder into the surrounding binder which reduces the amount of W which remains in the WC chemical state [386] [434]. The interface region generally possesses sharp edged microstructures due to the decomposition of the cast powders under the heating process and the preservation of heat within the deposition. The tungsten percentage changes more rapidly than the C content since there is a high quantity of W_2C, hence, two W atoms are released for every carbon atom. From the interior of the cast WC particle, point 1, to the exterior of the particle, point 11, there is a consistent increase in the nickel and copper alloy content percentage. The nickel is seen to increase at a faster rate as the binder region is approached since there is a higher nickel than copper percentage in the binder. When the ratio of nickel to copper is considered as in Fig. 4.37, there is a power function relationship which increase from approximately 1.46 at point 1 to 1.58 at point 11. This increase is attributed to the scan line approaching the binder region which has an ideal Ni:Cu ratio of 2.5. The ratio does not maintain 2.5 from

the binder region to the interior of the particle since, as per Fick's law (Equation 4.9), diffusion is concentration based and since nickel begins with a higher concentration difference a higher alloy content is found within the particle. At point 4 the nickel percentage decreases quicker than the Cu due to a higher concentration difference between the Ni and WC existing. Copper shows a more gradual decrease from point 11 to point 1 since a lower initial concentration results in a lower concentration gradient and therefore a lower diffusion rate. Point 11 represents the interfacial region which forms from the high concentration gradient present between the binder and WC particle. The interfacial region forms and prevents any more tungsten and carbon from dissolving into the binder region.

The chemical composition at point 11 shows a C:Ni:W ratio of 1:2:4 which indicates that the main phase is Ni_2W_4C [165] , [360].Research shows that this new granular hard phase can promote dispersion strengthening when smaller than 10 μm [165], [360]. The lower carbon content in the deposited particle could be due to carbon transforming into CO/CO_2 during the deposition process as well as into a graphite like structures seen on the boundaries of the embedded particles, as seen in Fig. 4.38(III(a)).

4.4.3 Raman Spectroscopy



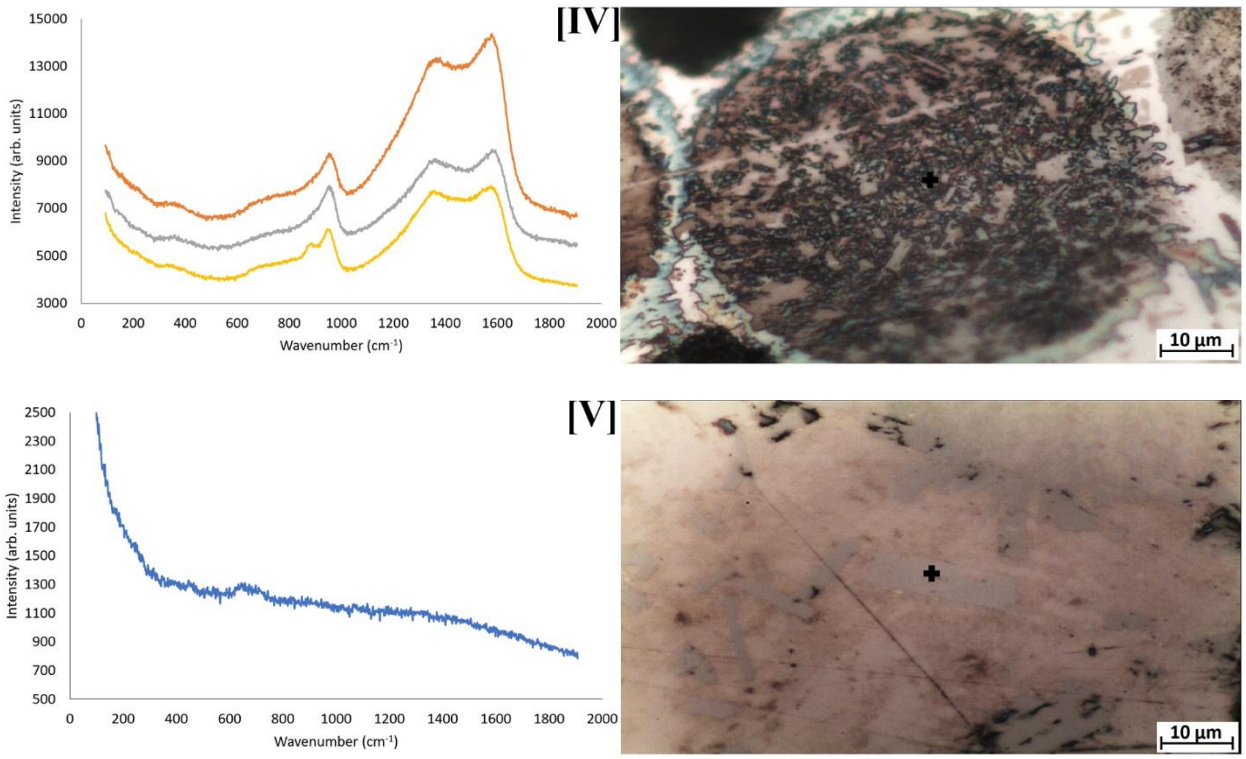


Fig. 4.38: Raman spectrum and a representative point micrograph [I] Binder region, [II] Inside embedded WC spheroid, [III] A-dark region on boundary of spheroid, B-interface region, [IV] oxide region, [V] Blocky microstructure.

The binder region, Fig. 4.38 (I), doesn't show any definitive peaks, except for one of the spectra there is a peak at around 700 cm^{-1}, which is attributed to the stretching mode of WC [435]–[437], due to tungsten and carbon atoms being dissolved in the binder and a second peak at approximately 960 cm^{-1} which is assigned in literature to the stretching of W=O double bonds [438]–[440].

Amorphous and nanostructured WO_6 octahedra of the bulk crystal forming tungsten oxide films are described as being composed of O-W-O units with terminal W=O units on their boundaries. The vibration of the terminal oxygen atoms (i.e. at the grain surface) causes the ~960 cm^{-1} band. It is often associated with the presence of a nanocrystalline structure and usually disappears when the film evolves to a microcrystalline structure [435], [441]–[443]. The intensity can be

related to a high surface-to-volume ratio which indicates the reduces grain dimensions. An alternate view on the 960cm^{-1} band is that is related to the presence of water which has been incorporated into the thin film. This is more probable in films which are porous and have been deposited under high pressures [438], [444]. The centre of the particle, Fig. 4.38 (II) shows no distinct peaks, not even WC modes. This is due to the high presence of W_2C in the cast spheres and therefore a region of high W_2C was analysed, indicating that the darker phase in the cast WC/W_2C is attributed to WC. This agrees with the composition of the original powder which consisted more of W_2C than WC.

The dark region on the interface of the spheroid, Fig. 4.38(III(a)) has a peak at approximately 675 cm^{-1} which is indicative of WC stretching mode [373] [435], [436] [437]. The peak at 960 cm^{-1} is due to the vibrations of the terminal W=O units. There is also a broad peak at approximately 1350 cm^{-1} and 1580 cm^{-1} which indicates the presence of graphite. The broad peak at ~1350 cm^{-1} is the D-band of sp2 carbon (disordered graphite) and the peak at ~1580 cm^{-1} is the G-band of carbon (graphite). These peaks represent the presence of free carbon on the surface and the broadness of the peaks indicates a fairly amorphous structure [373], [435], [436]. The spectra obtained at the interface region, Fig. 4.38(III(b)), show a peak around 675 cm^{-1} which is evident of WC stretching modes. In this region the cast tungsten carbide spheroid is dissolving into the binder. The W_2C dissolves preferentially hence more WC is present on the interface.

The Raman spectra of a potentially oxidized particle, Fig. 4.38 (IV), was obtained in the base region of Sample HS. A small, wide peak is observed between 200cm^{-1} to 400 cm^{-1} which is due to W-O-W bending modes [373], [437], [445], [446]. There is a well-defined peak at approximately 960 cm^{-1} which is due to the stretching of terminal W=O bonds. The D-band and G-band of graphite are also present since the tungsten formed new chemical bonds with the oxygen and therefore leaving a surplus of carbon. Absence of a dominant peak at ~800 cm^{-1}

suggests that there is no monoclinic phase tungsten trioxide and possibly oxygen deficiency [447], [448]. The spectrum for the rectangular blocky structure, Fig. 4.38 (V), has a small peak at approximately 650 cm^{-1} which is attributed to WC stretching [373], [435]–[437].

4.5 Drill bit

The design of experiments and refinement of the parameters by means of multiple cubes culminates in the fabrication of a functional component, i.e. a drill bit. The use of a small-scale parameter optimization design of experiments and the effectiveness to applied to a larger deposition is also being assessed. The cubes consisted of no more than 25 layers, whereas the drill bit consists of 151 layers.

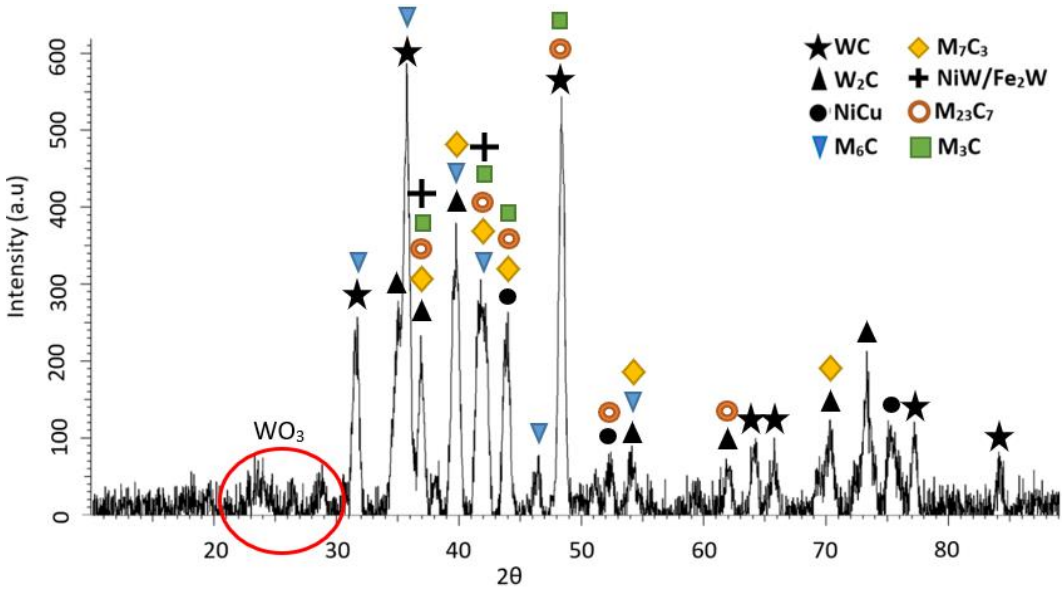


Fig. 4.39: XRD pattern of a drill bit segment

It is clear form Fig. 4.39 that even when 151 layers are deposited the phases which are present remain the same as is evident by the XRD pattern in Fig. 4.39 which has all the same phases present in Fig. 4.21.

The general finish of the fabricated drill bit is shown in Fig. 4.40(a), along with the CAD model which was used as an input during the deposition, Fig. 4.40(b). All the drill bits except for DB4 underwent mild sharpening after fabrication.



Fig. 4.40: a) Printed drill bit, b) CAD used to fabricate drill bit

It is evident from Fig. 4.40 (a), that the surface finish of the drill bit is very rough, due to the WC particles which do not dissolve and merely cool in the binder while protruding from the deposition. The large powder nature (±90 µm) means that if two or three WC particles are solidified upon one another then the surface roughness will increase, thus the nature of the precursor powder is extremely important in the finish of the final product if no post fabrication machining is considered. The top of the drill bit does not have the angled tip as in the CAD model as well as the absence of the flute. This is due to the beam spot size, 1.3 mm, which reduces the overall resolution during the printing process. By reducing

the beam spot size, a better resolution will be obtained, but at the cost of longer printing times, hence more powder usage and more laser time.

The LENS® process does not allow for simple alteration of the beam size, as it can only be done by manually adjusting the internal lens in the workpiece and testing the new beam spot size. Thus, a large beam size for the shank and a small spot size for the tip is not a viable solution. The flute in the thicker section of the drill bit does resemble the CAD model although with surface roughness distortion.

The average cost of producing a drill bit is shown in Table 4.11.

Table 4.11: Average cost to produce a drill bit

Average drill bit mass (g)	**62**
Laser cost (R/hour)	3500
Powder feed rate (g/min)	11.9
Deposition time (min)	25 – 100
WC powder (R/kg)	1196
Monel 400 powder (R/kg)	1835
Powder mixture (9.2wt% Monel)(R/kg)	1251.50
Substrate (R)	30
Purchased drill bit (R)	450
Cost of drill bit (cheapest-expensive)	
Laser cost (R)	1458 - 5834
Drill bit powder (R)	78
Required powder cost (R)	297.5 – 1489
Substrate (R)	30
Extras	####
Total	R1566 - R 5942

The purchased WC centre drill cost R450, which was used as a baseline to compare the fabricated drill bit. Since different printing times were used to deposit

the drill bits a cheapest and expensive amount was calculated where necessary. The average mass of the drill bits was 62 g and the drill bit powder cost was calculated from this amount. To produce the drill bit a constant feed rate is required for the duration of the deposition. An optimal parameter of 11.9 g/min was used in the calculations and it can be seen in Table 4.11, that the cost of the required powder varies between R402 and R1489, although the powder used in the drill bit is R78. Table 4.11 is structured such that the powder can be recycled [449]–[455].

The powder expense was calculated in the ratio used in this study, i.e. WC-9.2wt%Monel 400. The substrate contributes a small portion to the overall cost. It is clear from Table 4.11 that the cost of the laser is by far the contributing factor to the overall cost of the drill bit. To reduce the effect of the laser time the drill bit which was printed approximately 4 times quicker, than the slowest, had a cost which was 3.8 times less. This shows the astounding effect that the laser cost has on the cost of the final product. The cheapest fabricated drill bit was still 3.5 times more expensive than the purchased drill bit. This is due to the entire drill bit comprising of WC-9.2wt% Monel 400 whereas the shank of the purchased drill bit is fabricated from steel and only the tip region from WC based materials. To make the fabricated drill bit competitive the shank should comprise of Monel 400 or steel which is then tipped with a WC-based material, possibly even a functional grading from the steel shank into the tip to remove any adhesion problems between the two dissimilar materials. This would solve the density problems observed within the deposits and limit the WC deposition to a few layers, with a closer nature to a cladding.

An extras row was added to Table 4.11 to indicate that there are many extra costs that may incur apart from the obvious production costs, such as hot isotactic pressing treatment, surface finish machining, performing depositions in an argon

atmosphere, external CAD development and any supplementary simulations. For additive manufactured drill bits, fabricated using WC-9.2wt% Monel 400, to be market competitive with the purchased drill bit it would have to be printed in ten minutes or less.

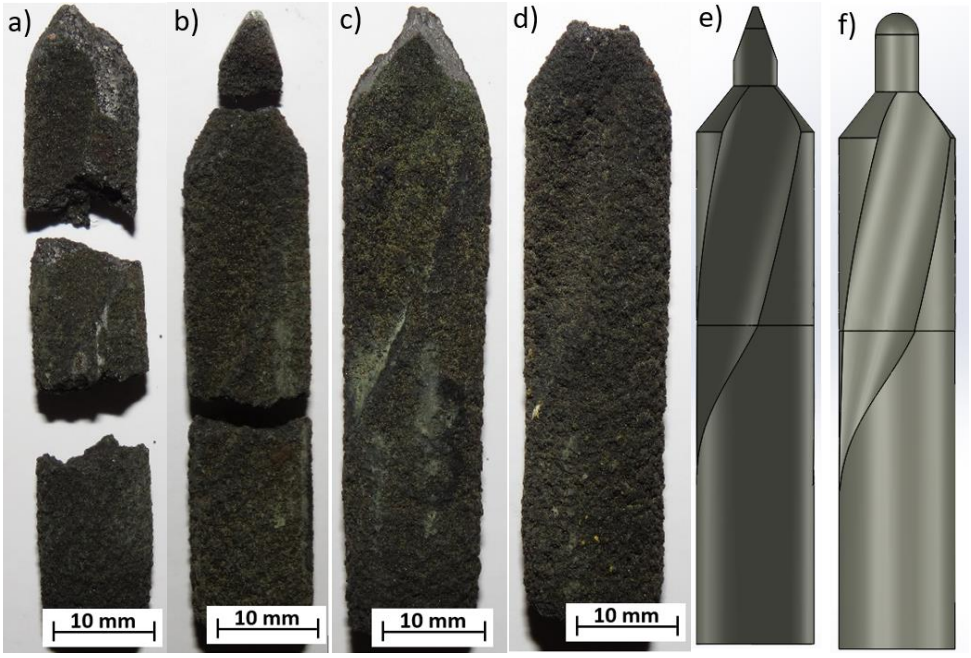
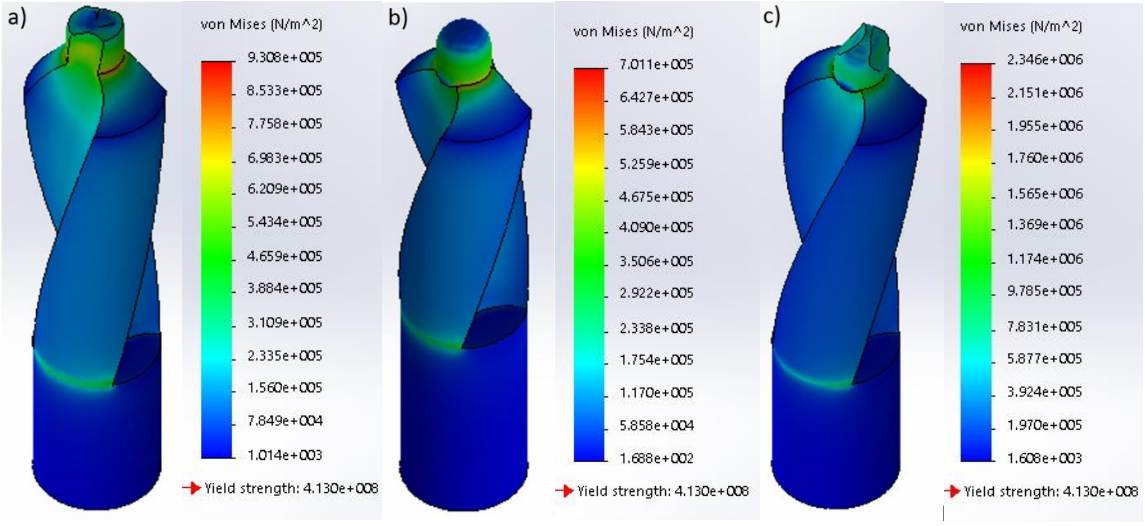


Fig. 4.41: Fractured a) DB1, b) DB2, c) DB3, d) DB4, e) CAD model approximation of sharpened drill bit, f) CAD approximation of unsharpened drill bit.

DB1 shows fractures in three points, Fig. 4.41(a). The tip region did not fracture exactly as the simulation but has the same nature as DB3 and not DB2 and DB4. The fracture did occur near the thin tip region but followed a diagonal trajectory down the side of the drill bit. The two fractures in the flute and shank region are due to the clamping of the drill bit in the CNC machine. The von Mises stress simulations, Fig. 4.42, shows that the second region of high stress is at the bottom of the flute, where the shank begins, and the clamping of the drill bit is performed.

The one closer to the base was from the initial clamping, the shank broke, but the tip was still intact, so it was retested with the top region of the drill bit. It was this second attempt that fractures the tip as well as the flute fracture from the torsional forces on the drill bit at the clamping point. DB2 has the same clamping failure which was observed in DB1 and the same tip failure as seen in DB4. Both fractures perfectly match the von Mises regions of high stress and the most probable regions to undergo stress failure. DB3 has a remarkably similar tip failure to DB1, Fig. 4.41(c). There is a diagonal failure path on the tip which is due to the microstructural properties, as discussed with Fig. 4.41(a). The tip of DB4 was not sharpened and left as a hemispherical shape, as it was after deposition. The tip of the drill bit broke in the exact region which exhibits high von Mises stresses, as in Fig. 4.42(b).

The simulation verified the logical point of failure since this is the narrowest point of the entire drill bit. The rounded surface dissipates the stress in the tip and applies it to the thin basal region of the tip. Without a flute the material was not removed sufficiently hence the surface of the drill bit was compressing into the aluminium disk. DB4 does not show failure at the clamping point since the tip failure occurred rapidly and didn't allow for the fracturing in the lower region.



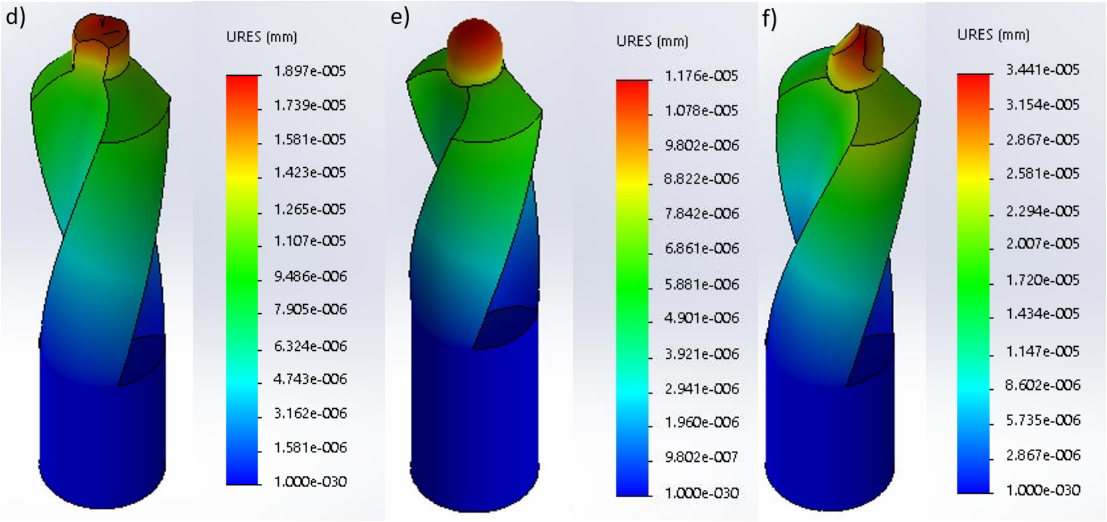


Fig. 4.42: von Mises stress simulations for a) original CAD model, b) unsharpened CAD model, c) sharpened CAD model and displacement simulations of d) original CAD model, e) unsharpened CAD model, f) sharpened CAD model.

The von Mises stress simulations show that the most stress during a loading process occurs at the base of the small tip and the interface between the flute and the shank, where the drill bit is clamped. The top of the drill bit applies the stress to the narrow region in the same way the shank applies the stress to the narrowest region. The binder does allow for the torsion and linear forces to distort the drill bit more than the WC would do by itself, although most conventional drill bits have a steel shank and just a WC tip. This allows for the forces to twist the more ductile drill bit while their hard tip does not affect the properties of the bulk drill bit.

The maximum displacement occurs in the tip regions of all three simulations, Fig. 4.42 (d-f). The displacement continues down to the start of the shank progressively decreasing. This also show the importance of the flute. Not only does it aid in the removal of material while drilling, it guides the stresses such that the torsional displacement allows the top regions of the drill bit to twist, provided the material

has a low enough Young's Modulus, Monel 400 (179Gpa)[182] and cast WC (550GPa) [456].

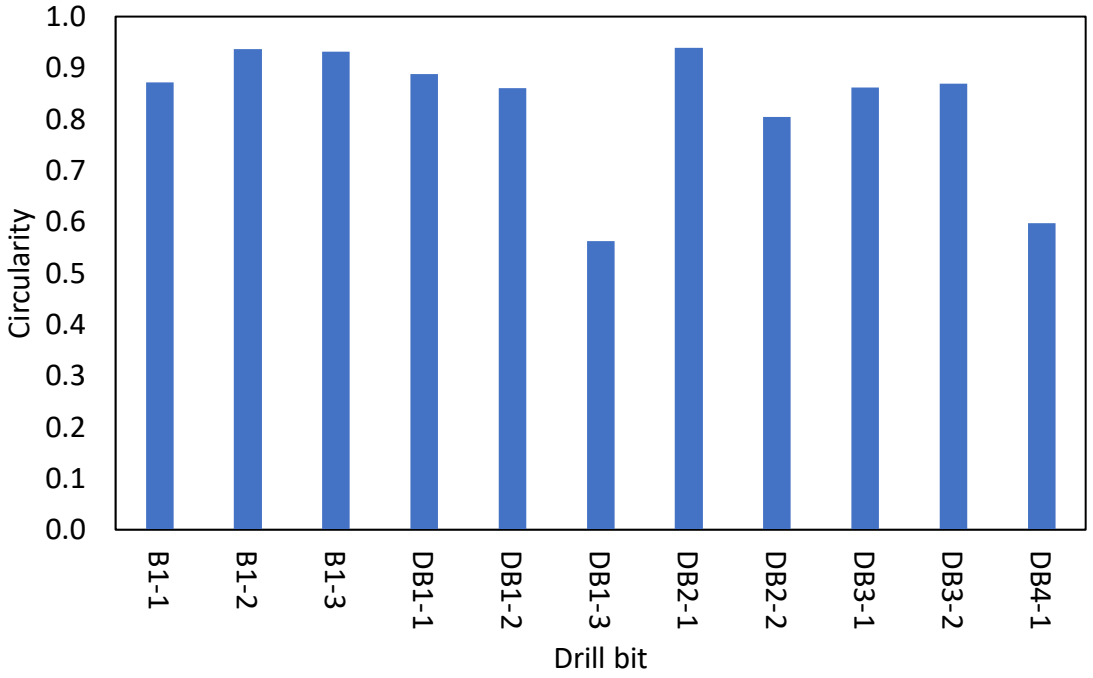


Fig. 4.43: Calculated circularity of each drilled hole by the corresponding drill bit.

It can be seen from Fig. 4.43, that the holes made by the bought drill bit, B1, all exhibited a circularity around 0.9. B1-1 had a lower circularity since the penetration depth was set to 5 mm where as B1-2 and B1-3 the penetration depth was 6 mm. This makes it evident that even with a bought drill bit the depth of the hole affects the circularity that is obtained. DB1-1 and DB1-2 has a circularity close to that of the first trial of the both drill bit. The circularity of between 0.8 and 0.9 is due to the drill bit pushing backward when encountering the aluminium and merely creating some striations on the surface, refer to Fig. 4.48(a). For the third test DB1-3, the calculated circularity was between 0,5 and 0.6 since the tip of the drill bit broke off and became embedded in the aluminium, not before causing damage to the outer region of the hole, Fig. 4.48(d).

DB2-1 had a very high circularity due to the drill bit again pushing backward when contacting the aluminium disk and just creating a few circular striations on the surface. When some penetration occurred, DB2-2, and the drill bit tip fractured, it damaged the hole and decreased the calculated circularity. DB3 showed the most consistency with both tests yielding circularity between 0.85 and 0.9. DB4, the unsharpened sample, yielded a low circularity because the sharpened tip was basically ripping into the aluminium and tearing material away with its high surface roughness.

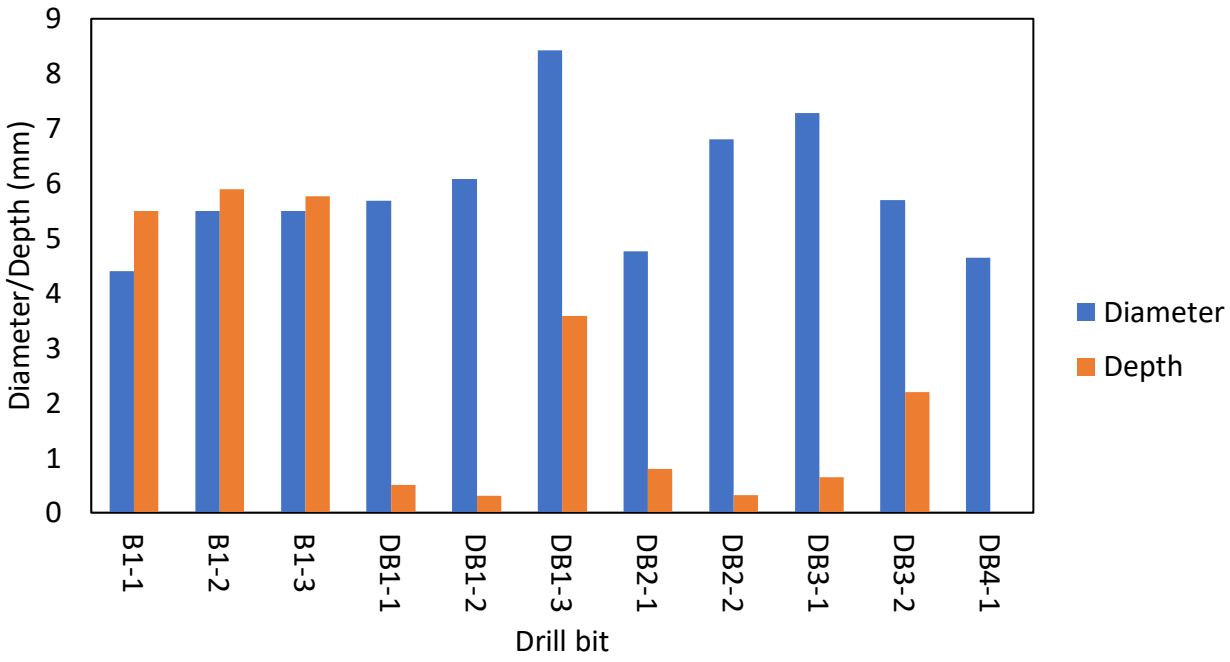


Fig. 4.44: Diameter and depth of each drilled hole for the corresponding drill bit.

The depth of the purchased drill bits was remarkably close to that of the set depth on the CNC machine. B1-1 was set to 5 mm and B1-2 and B1-3 were set to 6 mm which was used for all successive testing. The purchased drill bit showed a good consistency across the depth tests. DB1-1 and DB1-2 were found to have exceptionally low depths, as did DB2-1, DB2-2 and DB3-1 since the drill bit pushed

backward inside the clamp when encountering the aluminium disk. This means that the surface of the aluminium was lightly scratched an no real penetration achieved. DB1-3 and DB3-2 showed a larger decree of penetration since the drill bit started penetrating but the tip broke inside the disk for both drill bits.

DB4 has no depth since the tip broke before even a slight hole had been formed. When considering the diameter size, the purchased drill bit again showed good consistency, with B1-1 having a lower diameter since 5 mm is the tip of the drill bit and when the depth was changed to 6 mm the wider triangular component affects the hole diameter. DB1-1 and DB1-2 was found to have a consistent diameter, but when the tip started boring a hole, DB1-3, the diameter increased, as seen in Fig. 4.48(c), since the tip broke in the sample and damaged the edges of the hole. The same is seen for DB2-1 where the surface is merely scratched in a circular pattern, but when the top of the dill bit fractures the diameter increases due to the damage of caused when the tip breaks.

DB3 was the only sample that improved as the penetration increased, which implies that it was removing material more efficiently than the other drill bits. DB4 had a small diameter since tip broke very soon after contact, hence of only the tip was used to create the scratch striations.

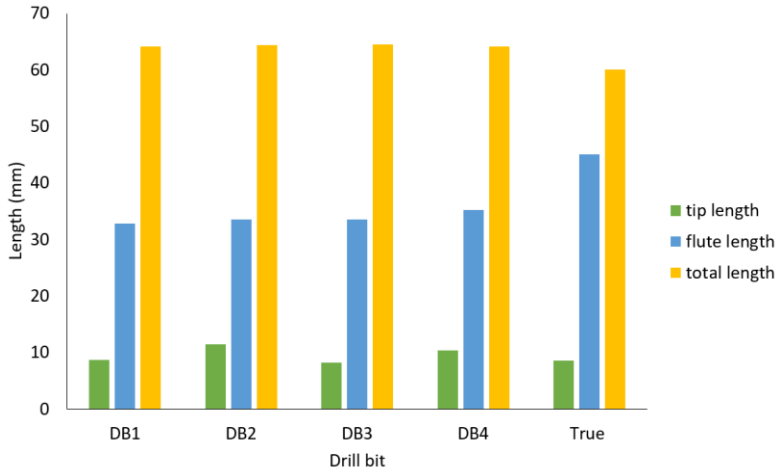


Fig. 4.45: Tip length, flute length and total length of the drill bit compared to the true value of the CAD model.

The tip lengths of DB1, DB2 and DB4 are all longer than the true value of the CAD model, while DB3 is slightly lower. DB3 was printed with the fastest traverse speed which allowed for the tip layers to be deposited quicker and therefore less time for extra powder particles to be included in the melt pool. The flute length was consistent across all the deposited drill bits since the flute did not begin sooner in the shank region but was absent in the tip region due to the beam spot size and the related resolution problems associated with this parameter. All the fabricated samples had similar total lengths, which were all longer than the true expected length from the CAD model. The high surface roughness and extra powder deposition in the tip region due to heat being retained in the tip during deposition resulted in the extra length of the depositions.

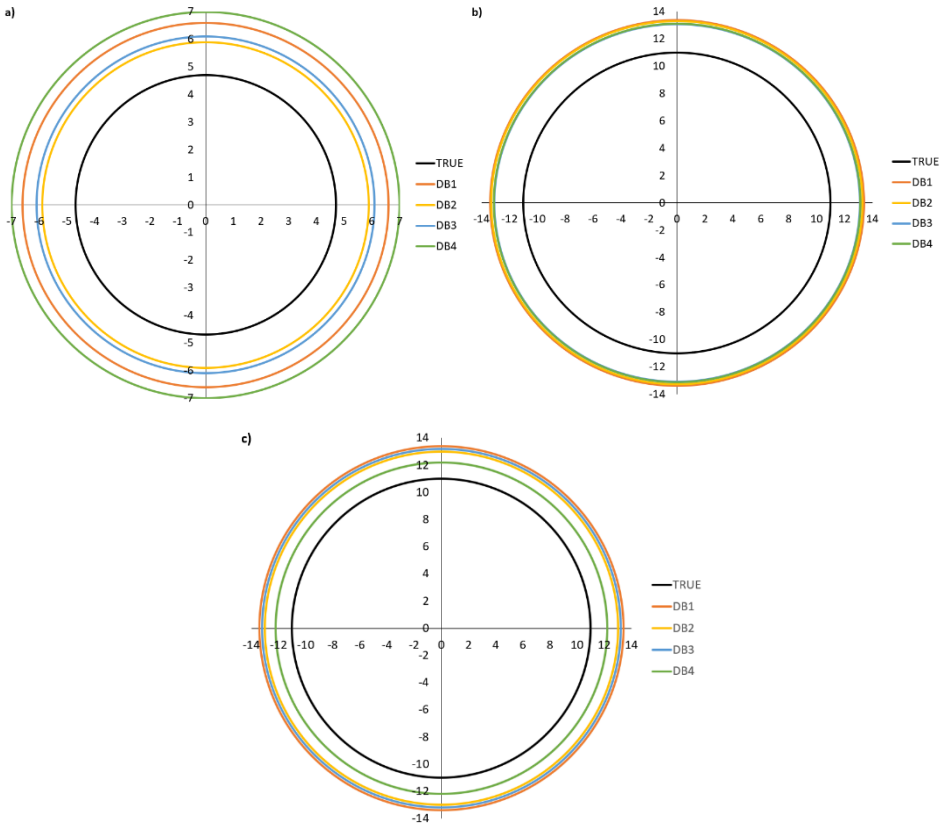


Fig. 4.46: Diameter of a) Tip, b) flute and c) shank in (mm)

The diameters of the different regions of the drill bits are shown in Fig. 4.46. In all three regions, i.e. tip, flute and shank, the fabricated drill bits had a larger circumference than the CAD model. In the tip region the different drill bits had varied increases from the CAD value whereas in the flute region the drill bits were basically identical in their circumference increase. The same was true for the shank region, except for DB4 which had a slightly reduced circumference which could be related to a relatively lower surface roughness. The tip region had the greatest deviations because it had the smallest true circumference, hence an increase in surface roughness or a higher retained heat in the tip would result in a relatively larger increase than in the larger shank and flute regions.

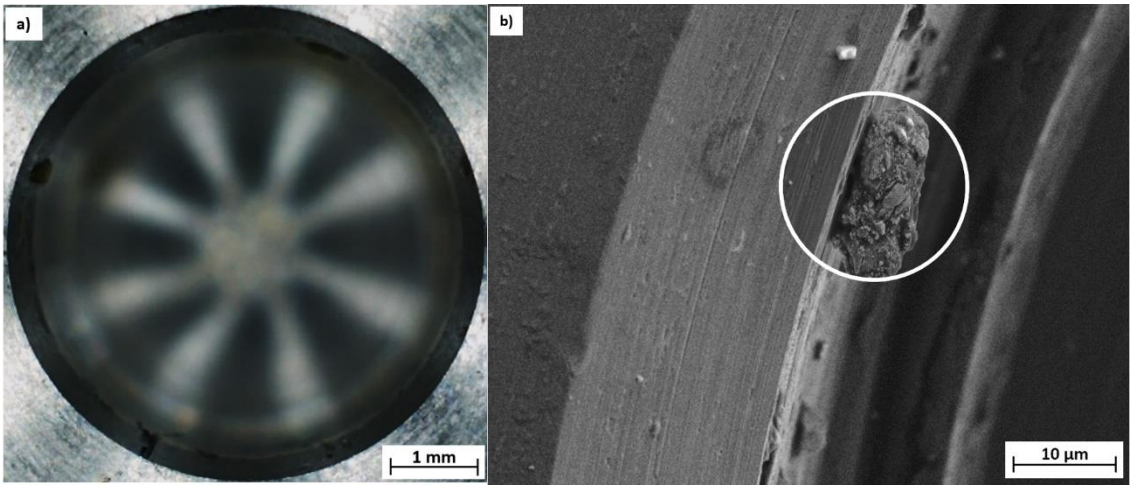
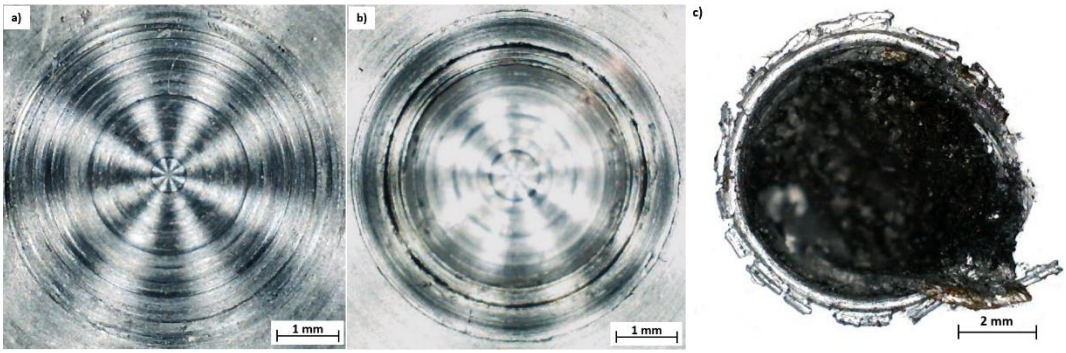


Fig. 4.47: Hole of purchased drill bit, SEM of region on boundary.

The purchased drill bit made a very circular hole, as was calculated for Fig. 4.47(a). The smooth machined exterior of the drill bit with a sharpened and fluted tip allowed for the efficient removal of material during the drilling process. As the triangular region of the drill bit mad contact with the hole it began to compress the aluminium, as seen in Fig. 4.47(b), by the lighter region. The rim of the hole is smooth with few inconsistencies, a small mass of aluminium was removed during the process, Fig. 4.47(b), possibly due to the high revolution speed of the drill bit transferring force to a slightly week region in the aluminium.



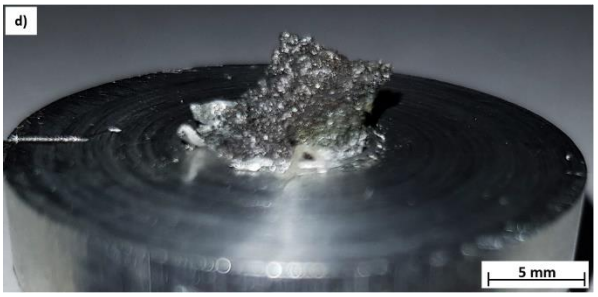
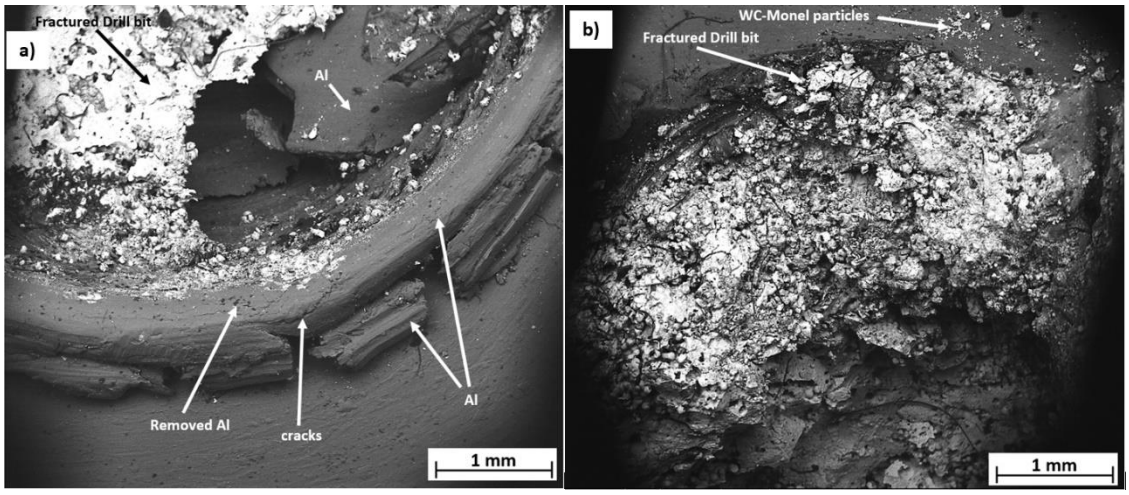


Fig. 4.48: DB1 a) first drilling attempt, b) second attempt, c) third attempt with drill bit failure, d) embedded drill bit tip in the aluminium disk.

It can be seen in Fig. 4.48(a-b), that when the drill bit pushed backward into the clamping device then no depth is achieved, just circular striations are obtained from the hard WC particles surface roughness wearing through the surface of the softer aluminium disk. When the clamping was more efficient as in Fig. 4.48(c), a compressive zone in the outer region of the hole is observed with stress cracks surrounding this zone. There is some depth obtained, although not close to the set value. Tip failure occurred on the third test, Fig. 4.48(d), where the tip broke and was embedded in the sample. The aluminium was curled over the edges during the drilling process which indicates that the tip was not sharp enough and a level of compression was occurring instead of boring and material removal.



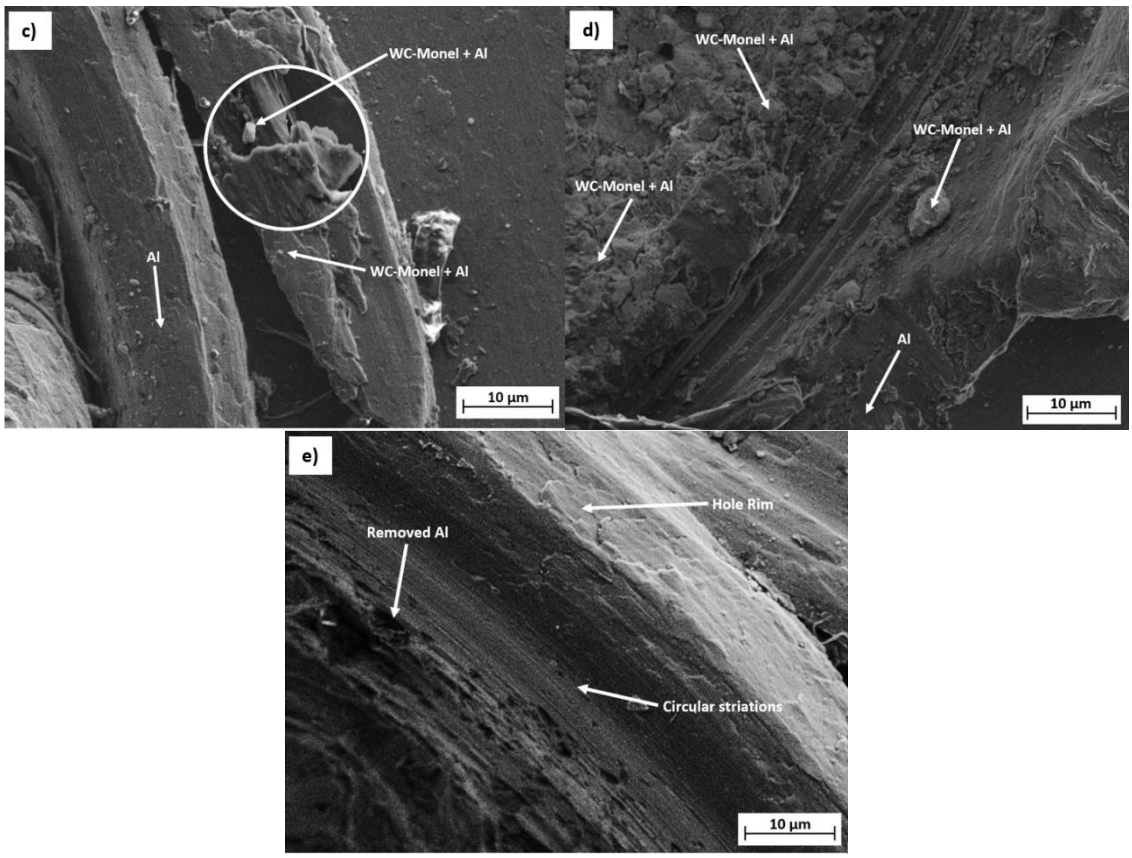


Fig. 4.49: SEM images of the hole drilled by DB1 showing a) the boundary of the hole, b) the embedded drill tip, c) the rim of the hole, d) and e) the inner rim of the hole.

The WC spheroids can be identified in the region where the drill bit was embedded in the aluminium, Fig. 4.49(a-b). WC-binder fragments are also found outside of the hole, on the surface of the aluminium since particles dispersed on the surface when the drill bit fractured. The rim of the hole, Fig. 4.49(c), shows how the aluminium has compressed in the outer region of the hole due to the drill bit forcing the aluminium material out of the drilling zone. It eventually curves over and forms aluminium extrusions from the rim. There are cracks visible in the rim region due to the material compressing and cracking under the strain.

A closer observation of these extrusions shows a sheet-like slipping of the aluminium flakes over previous layers [457]–[459]. There are also small particles of WC-Monel which have been fragmented with aluminium on these sheet-like extrusions. The same WC-Monel-Al combination have been embedded in the walls of the hole-rim, Fig. 4.49(d), which occurred during the failure of the drill bit. Through wear and high surface roughness the drill bits removed aluminium form the hole rim region leaving cavities and small pore like regions. The surface roughness also causes circular striations, as seen in the many of the samples, in the outer rim of the hole.

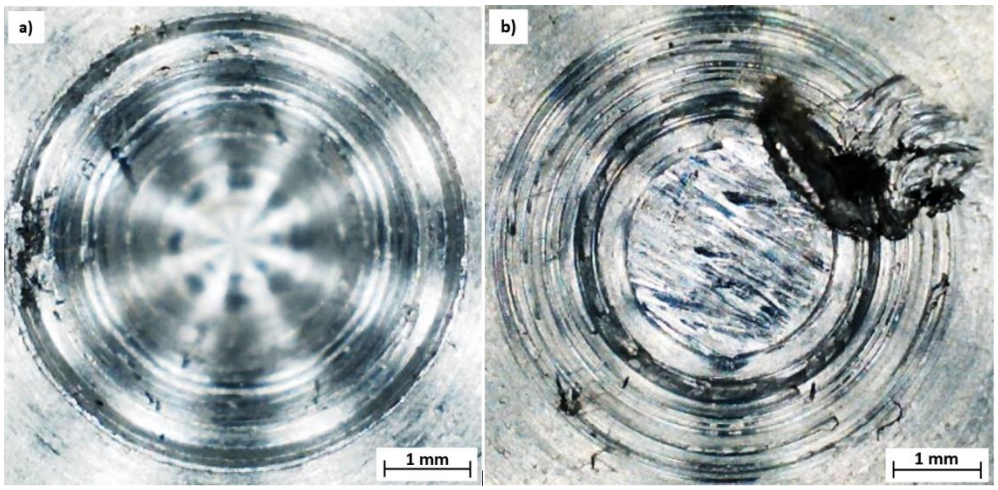


Fig. 4.50: Two drilling attempts by DB2 before failure.

Drill bit DB2 did not obtain a significant depth, as indicated in Fig. 4.50, before the tip failed. As with the other drill bits the surface roughness caused circular striations on the surface of the aluminum and some damage to the wall of the hole, as in Fig. 4.50(a). When the drill bit fractured it left embedded particles in the surface of the aluminium and caused the circular pattern to be disturbed by an anomalous wear path.

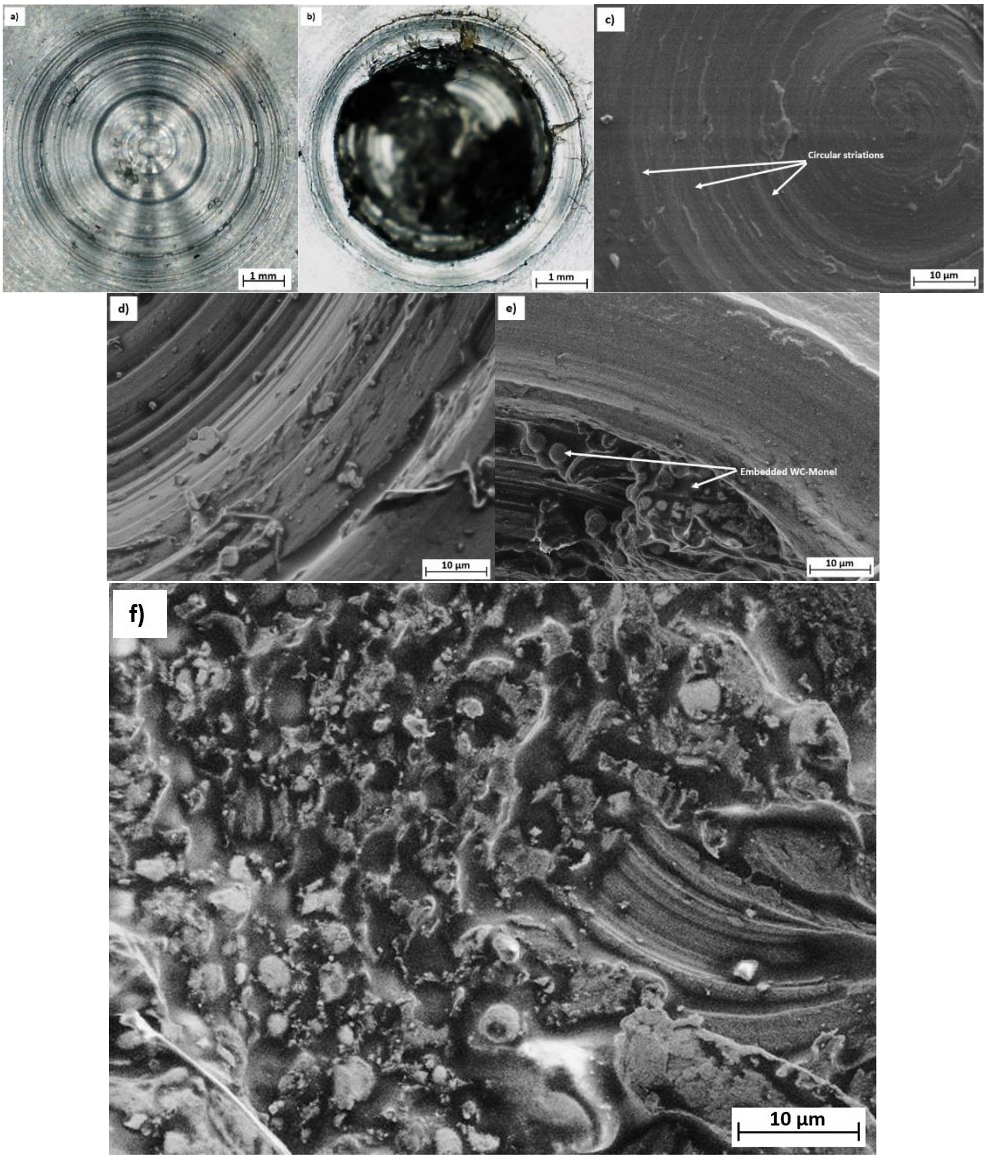


Fig. 4.51: a) first attempt by drill bit DB3, b) second attempt by DB3 and the tip failure, c) SEM image of striations from a), d) and e) inner wall of the hole, f) bottom of the drilled hole.

Similar circular striations were observed for DB-3 as well as a compression-like region around the rim of the hole, as in Fig. 4.51(a-b). When the tip of the drill bit fragmented pieces of the drill bit were embedded into the bottom and sides of the hole, as in Fig. 4.51(b) and (e). The compressive force of the drill bit caused cracks around the edge of the compression rim. The bottom of the hole, Fig. 4.51(f),

shows the rough nature of the hole due to the drill bit tips not being very sharp, hence the holes are formed due to the rough tip compressing and scraping the material.

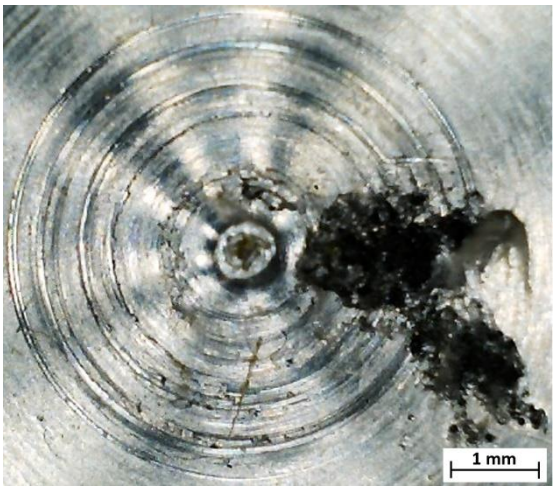


Fig. 4.52: Striations made by DB4.

DB4 didn't make any depth penetration since the tip was not sharpened. The circular striations are form the WC particles contributing to the surface roughness and scratching the aluminium through a wear process. The dark region indicates where WC-binder was embedded in the softer aluminium when the tip of the drill bit catastrophically failed. In the central striations there is a tearing motion observed. The fractured drill bit tips were examined for any indications as to the reason behind failure.

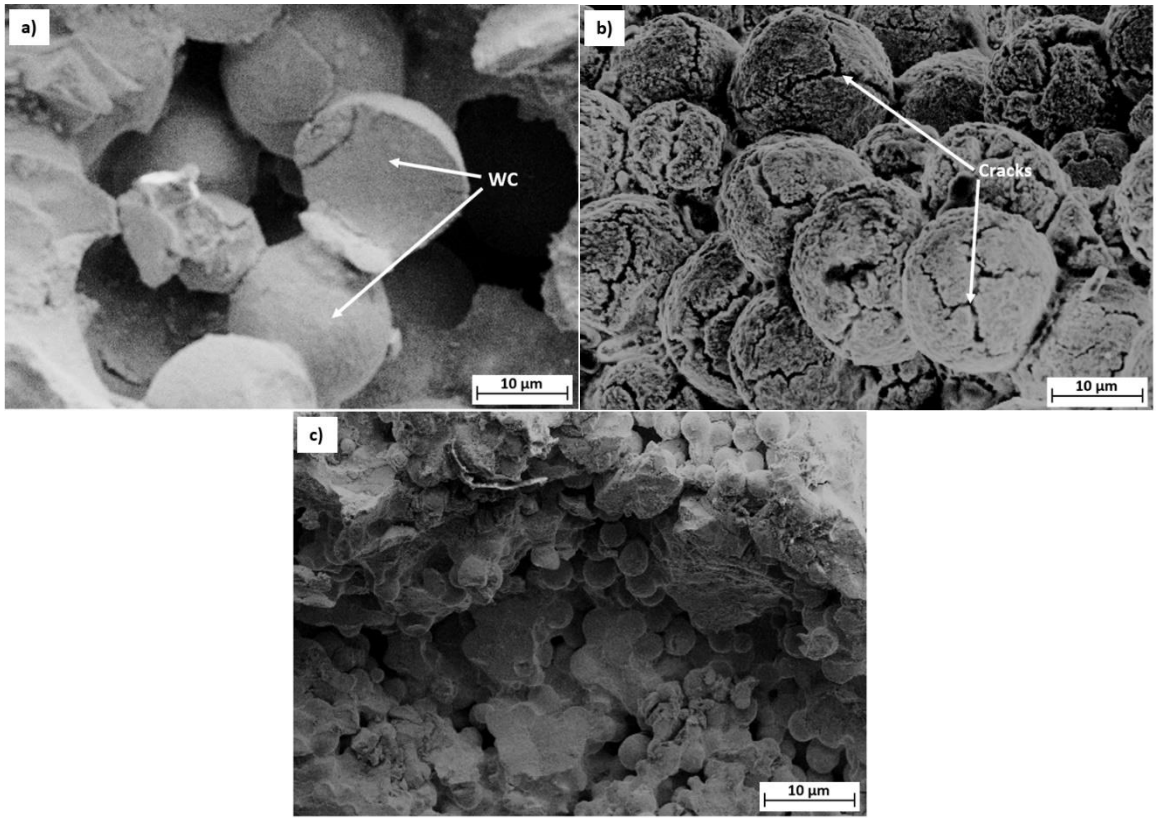


Fig. 4.53: Fractured region of DB3 a) fractured cast WC, b) surface cracks on cast WC and c) high- and low-density regions in fracture zone.

The WC-W_2C spheres showed cracking directly through the particle due to the high hardness and reduced ductility when compared to the binder phase, Fig. 4.53(a). The fracturing of the spheroids can lead to a weaker microstructure since the favorable properties of WC are mostly observed when the hard phase is distributed throughout the binder phase. The spheroidal WC-W_2C particles also had extensive surface cracking due to the energy input during the deposition process and initiation of elemental dilution which creates fissures in the surface of the spheroids, Fig. 4.53(b).

The main reason for the fracturing of the drill bits is due to lack-of-fusion regions and inadequate distribution of the hard phase within the binder phase, as seen in

Fig. 4.53(c). The regions of higher density are surrounded by regions of lower density which creates an imbalance in the mechanical properties and causes the failure to occur on this structural boundary.

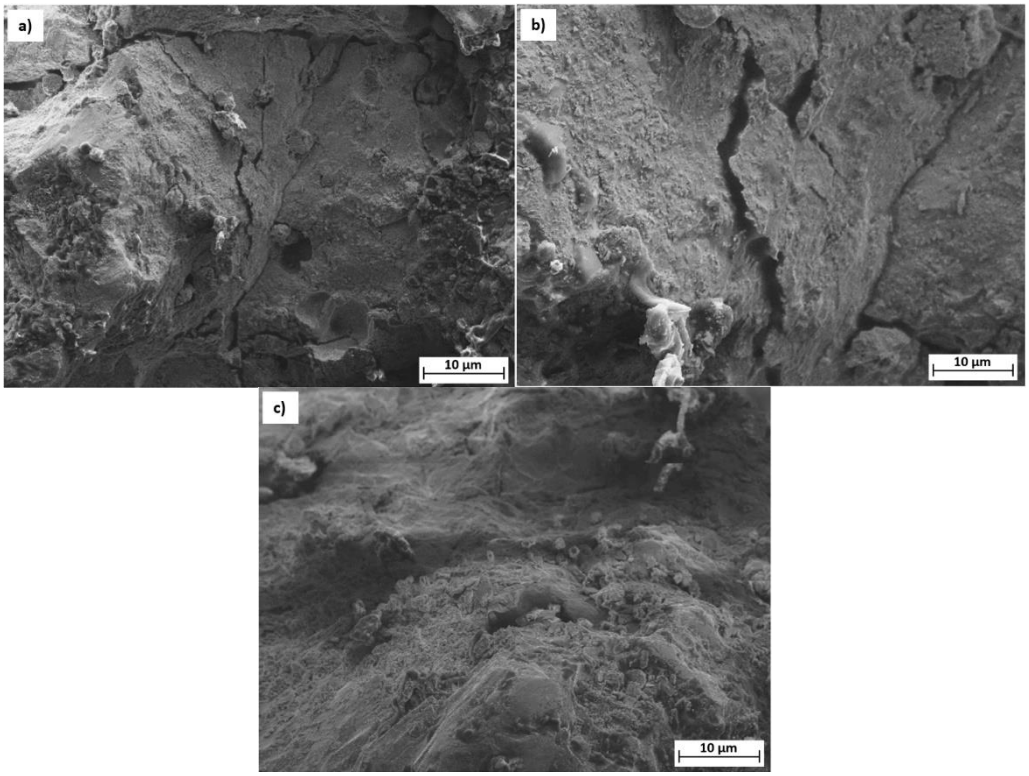


Fig. 4.54: a) and b) cracks in the fracture zone of DB1 and c) rough surface after fracture.

Regions of higher density were observed in the drill bit tips, as in Fig. 4.54(a). The fracturing of the tip caused cracks in the remaining drill bit due to the torque force inducing stresses within the component. The cracks are seen in Fig. 4.54(b) and traverse in the same direction which indicates that the weakness within the microstructure may be directional. Fig. 4.54(c), shows a region of the fractured surface, where there are WC fragments and a highly uneven contoured surface. This is due to the considerable number of parameters which have been observed in previous chapters that affect the localized properties of the deposition and therefore the localized mechanical and microstructural integrity.

Chapter 5 Conclusions

A design of experiment matrix was successfully applied to the LENS® technology to produce a series of thin walls of WC-9.2wt%Monel 400. ANOVA regression and multiple parameter refinements, through the deposition of cube samples, allowed for the production of some high-density depositions. The lowest porosity of 2.5% was obtained using a laser beam power of 220 W, traverse speed of 4.5 mm/s, powder feed rate of 11.9 g/min, hatch overlap of 50%, z-increment of 0.4 mm and a beam spot size of 1.3 mm. Oxygen would need to be limited during processing to reduce oxide formation and porosity. An increase in the laser beam diameter resulted in severe cracking and indicated that depositions retained better geometric and material properties when the laser beam was kept at a reduced diameter. The heated substrate and laser remelted sample did not have any significant improvements to the overall porosity of the samples.

Samples that are fabricated using LENS® technology result in many different microstructures. This is due to the dilution of iron from the substrate, differences in carbon and tungsten in localized regions from variable WC/W_2C dissolution and the changes in the cooling rates from the fusion zone to the top region. At the fusion zone a variety of microstructures were observed with chemical compositions dominated by chromium and iron, such as fishbone-like (26% iron, 6% Cr), Fe/W-dendrites (30% Fe, 7% Cr) and eutectic (61% Fe, 10% Cr). The elevated chromium and iron chemical content is due to the dilution of these alloying elements form the substrate used in the study. Due to these additional elements, structures such as M_6C carbides (Fe_3W_3C, and Fe-Ni solid solution), $Cr_{27}C_6$ and Cr_7C_3 were present even though these elements were not alloyed in the binder. Also forms under high cooling rates.

Needle-like structures which are a combination of W_2C and M_6C structures with a solid solution comprising of Ni-Cu were observed as the centre was approached as the thermal gradient decreased. Tungsten carbide rich triangular (WC with NiW impurities) and blocky structures which are tungsten rich eta phases such as Ni_2W_4C and Ni_3W_3C, were scattered throughout the central regions where stoichiometric conditions were achieved and acicular dominated the top regions where a low thermal gradient was present. The heated substrate resulted in less eutectic and more fishbone and dendritic structures being observed and the spheroidal WC/W_2C particles were still present in the fusion zone, as in the unheated substrate samples. The remelted sample was found to have a very uniform acicular structure, which is predominantly W_2C, with minimal binder pooling in the top region whereas the samples which did not undergo remelting had high binder pooling and regions where spheroidal particles were still present. The remelted sample also had a significantly low Cu composition in the top region due to the remelting process melting causing extensive copper evaporation. The binder throughout the depositions were comprised mainly of Ni and Cu dendrites which changed from cellular dendritic in the bottom and central regions to columnar dendritic in the top regions as the temperature gradient decreased.

The process of remelting was found to cause evaporation of the metal matrix, with all the copper being evaporated. Raman spectroscopy was successful in detecting WC, O-W-O, W=O, D-band and G-band stretching modes in multiple points of interest. The analysis showed that the blocky structure had a WC nature and that the dark regions in some of the interfaces, on the spheroids, are regions where carbon has graphitized. Core-rim structures were observed in the fusion and central regions where the spheroidal powders had not dissolved completely. The W and C content decreased from inside the spheroid to the interface region where the nickel and copper concentrations increased rapidly from the infiltration of the binder matrix into the spheroids.

ANOVA analysis on the hardness of the DoE samples showed that the hardness is affected more by the microstructure than the processing parameters used for the deposition of the sample. In the cube samples the variation of the microstructure yielded an increasing hardness gradient from the fusion zone to the surface of the sample due to microstructural grain refinement. The surface hardness was found to have a broad range although without any significant statistical deviations except for the laser remelted sample which showed a significantly increased value.

Multiple drill bits were successfully fabricated and tested. The drilling process produced hole circularities between 0.55 and 0.9 with the best hole depth of 3 mm and circularity being obtained by the drill bit which was fabricated using a power of 220 W, traverse speed of 20.50 mm/s, powder feed rate of 11.9, beam spot size of 1.3 mm and a z-increment of 0.4 mm. All the drill bits failed due to tip fracture or shank failure and were found to have micro-cracks as well as surface cracking in the cast WC particles in the fracture zone. The tip and shank fractures were all predicted by the von Mises stress simulations which indicated regions of high stress. The drill bits produced holes with diameters ranging between 5 mm and 8.5 mm and were found to have embedded particles from the drill bits as well as significant ripping around the hole. All of the deposited drill bits were longer and thicker than the dimension in the CAD model due to extensive surface roughness.

It can be clearly concluded that Monel 400 is an effective binder for tungsten carbide cemented carbides, although the properties of the LENS® sintered alloys were not quite comparable to the properties reported in literature. The LENS® process was able to sinter the novel cemented carbide into a functional drill bit which needs further refinement to possibly compete with drill bits fabricated through conventional methods.

Chapter 6 Recommendations for Future Work

According to the current research status and results, the following work can be further studied:

- Determine a different end use for LENS® technology where it may lead to more favourable outputs.
- Perform TEM analysis on the different microstructures which are present in the samples.
- Determine process parameters to reduce the surface roughness or apply post-process machining techniques before drill bit testing.
- Hot isostatic press samples before testing.
- Other mechanical properties, such as compression strength and bending strength can be analysed.
- Fabricate a drill bit with a Monel 400 shank and only the tip as WC-based material with a functionally graded nature from the shank to the tip.
- Perform depositions under inert atmospheric conditions.

References

[1] ASTM, “Standard Terminology for Additive Manufacturing Technologies F2792-12a.” ASTM International.

[2] S. S. Muthu and M. M. Savalani, Eds., *Handbook of Sustainability in Additive Manufacturing*. Singapore: Springer Singapore, 2016.

[3] Wohlers, T. and Caffrey, T., “Wohlers Report: Additive manufacturing and 3D printing state of the industry annual worldwide progress report.” Wohlers Associates, 2013.

[4] Wohlers, T. and Caffrey, T., “Wohlers Report:Additive manufacturing and 3D printing state of the industry annual worldwide progress report.” Wohlers Associates, 2015.

[5] DST,CSIR, “South African Additive Manufacturing Strategy,” Apr. 2016. http://www.rapdasa.org/wp-content/uploads/2017/02/South-African-Additive-Manufacturing-Strategy.pdf (accessed Aug. 09, 2017).

[6] “Laser Materials Processing, Volume 3 - 1st Edition.” https://www.elsevier.com/books/laser-materials-processing/bass/978-0-444-86396-6 (accessed Oct. 27, 2019).

[7] Y. Xiong, J. E. Smugeresky, L. Ajdelsztajn, and J. M. Schoenung, “Fabrication of WC – Co cermets by laser engineered net shaping,” vol. 493, pp. 261–266, 2008, doi: 10.1016/j.msea.2007.05.125.

[8] M. L. Griffith *et al.*, “Understanding thermal behavior in the LENS process,” *Mater. Des.*, vol. 20, no. 2–3, pp. 107–113, 1999, doi: 10.1016/S0261-3069(99)00016-3.

[9] K. P. Cooper, “Building components by laser-additive processing,” *JOM*, vol. 53, no. 9, pp. 29–29, Sep. 2001, doi: 10.1007/s11837-001-0065-0.

[10] C. L. Atwood *et al.*, “LASER SPRAY FABRICATION FOR NET-SHAPE RAPID PRODUCT REALIZATION LDRD,” p. 32.

[11] S. Das *et al.*, “Direct SLS Processing for Production of Cermet Composite Turbine Sealing Components,” *Mater. Manuf. Process.*, vol. 13, no. 2, pp. 241–261, Mar. 1998, doi: 10.1080/10426919808935239.

[12] S. Das, M. Wohlert, J. J. Beaman, and D. L. Bourell, “Producing metal parts with selective laser sintering/hot isostatic pressing,” *JOM*, vol. 50, no. 12, pp. 17–20, Dec. 1998, doi: 10.1007/s11837-998-0299-1.

[13] M. Y. Zhou, J. T. Xi, and J. Q. Yan, “Modeling and processing of functionally graded materials for rapid prototyping,” *J. Mater. Process. Technol.*, vol. 146, no. 3, pp. 396–402, Mar. 2004, doi: 10.1016/j.jmatprotec.2003.11.034.

[14] M. Gurr and R. Mülhaupt, “Rapid Prototyping,” in *Reference Module in Materials Science and Materials Engineering*, Elsevier, 2016.

[15] K. V. Wong and A. Hernandez, “A Review of Additive Manufacturing,” *ISRN Mech. Eng.*, vol. 2012, pp. 1–10, 2012, doi: 10.5402/2012/208760.

[16] C. W. Hull, “Apparatus for production of three-dimensional objects by stereolithography,” US4575330 A, Mar. 11, 1986.

[17] F. P. W. Melchels, J. Feijen, and D. W. Grijpma, “A review on stereolithography and its applications in biomedical engineering,” *Biomaterials*, vol. 31, no. 24, pp. 6121–6130, Aug. 2010, doi: 10.1016/j.biomaterials.2010.04.050.

[18] Ph. Bertrand, F. Bayle, C. Combe, P. Goeuriot, and I. Smurov, “Ceramic components manufacturing by selective laser sintering,” *Appl. Surf. Sci.*, vol. 254, no. 4, pp. 989–992, Dec. 2007, doi: 10.1016/j.apsusc.2007.08.085.

[19] K. H. Tan *et al.*, “Scaffold development using selective laser sintering of polyetheretherketone–hydroxyapatite biocomposite blends,” *Biomaterials*, vol. 24, no. 18, pp. 3115–3123, Aug. 2003, doi: 10.1016/S0142-9612(03)00131-5.

[20] Mukesh Agarwala, David Bourell, Joseph Beaman, Harris Marcus, and Joel Barlow, “Direct selective laser sintering of metals,” *Rapid Prototyp. J.*, vol. 1, no. 1, pp. 26–36, Mar. 1995, doi: 10.1108/13552549510078113.

[21] P. Seegopaul, L. E. McCandlish, and F. M. Shinneman, “Production capability and powder processing methods for nanostructured WC-Co powder,” *Int. J. Refract. Met. Hard Mater.*, vol. 15, no. 1, pp. 133–138, Jan. 1997, doi: 10.1016/S0263-4368(96)00044-3.

[22] C. Colin, L. Durant, N. Favrot, J. Besson, G. Barbier, and F. Delannay, “Processing of functional-gradient WC-Co cermets by powder metallurgy,” *Int. J. Refract. Met. Hard Mater.*, vol. 12, no. 3, pp. 145–152, Jan. 1993, doi: 10.1016/0263-4368(93)90064-M.

[23] B. K. Kim, G. H. Ha, and D. W. Lee, “Sintering and microstructure of nanophase WC/Co hardmetals,” *J. Mater. Process. Technol.*, vol. 63, no. 1, pp. 317–321, Jan. 1997, doi: 10.1016/S0924-0136(96)02748-3.

[24] L. E. McCandlish, B. H. Kear, and B. K. Kim, “Processing and properties of nanostructured WC-Co,” *Nanostructured Mater.*, vol. 1, no. 2, pp. 119–124, Mar. 1992, doi: 10.1016/0965-9773(92)90063-4.

[25] A. Parasiris and K. T. Hartwig, “Consolidation of advanced WC–Co powders,” *Int. J. Refract. Met. Hard Mater.*, vol. 18, no. 1, pp. 23–31, 2000, doi: 10.1016/S0263-4368(00)00005-6.

[26] L. E. McCandlish, B. H. Kear, and B.-K. Kim, “Carbothermic reaction process for making nanophase WC-Co powders,” US5230729A, Jul. 27, 1993.

[27] J. He and J. M. Schoenung, “A review on nanostructured WC–Co coatings,” *Surf. Coat. Technol.*, vol. 157, no. 1, pp. 72–79, Aug. 2002, doi: 10.1016/S0257-8972(02)00141-X.

[28] H. Mohammadzadeh, H. Rezaie, H. Samim, M. Barati, and H. Razavizadeh, “Synthesis of WC–Ni composite powders by thermochemical processing method based on co-precipitation,” *Mater. Chem. Phys.*, vol. 149–150, pp. 145–155, Jan. 2015, doi: 10.1016/j.matchemphys.2014.09.057.

[29] B. H. Kear and L. E. McCandlish, “Chemical processing and properties of nanostructured WC-Co materials,” *Nanostructured Mater.*, vol. 3, no. 1, pp. 19–30, Jan. 1993, doi: 10.1016/0965-9773(93)90059-K.

[30] D. Sivaprahasam, S. B. Chandrasekar, and R. Sundaresan, “Microstructure and mechanical properties of nanocrystalline WC–12Co consolidated by spark plasma sintering,” *Int. J. Refract. Met. Hard Mater.*, vol. 25, no. 2, pp. 144–152, Mar. 2007, doi: 10.1016/j.ijrmhm.2006.03.008.

[31] S. I. Cha and S. H. Hong, “Microstructures of binderless tungsten carbides sintered by spark plasma sintering process,” *Mater. Sci. Eng. A*, vol. 356, no. 1–2, pp. 381–389, Sep. 2003, doi: 10.1016/S0921-5093(03)00151-5.

[32] J. Zhao, T. Holland, C. Unuvar, and Z. A. Munir, “Sparking plasma sintering of nanometric tungsten carbide,” *Int. J. Refract. Met. Hard Mater.*, vol. 27, no. 1, pp. 130–139, Jan. 2009, doi: 10.1016/j.ijrmhm.2008.06.004.

[33] B. Huang, L. D. Chen, and S. Q. Bai, “Bulk ultrafine binderless WC prepared by spark plasma sintering,” *Scr. Mater.*, vol. 54, no. 3, pp. 441–445, Feb. 2006, doi: 10.1016/j.scriptamat.2005.10.014.

[34] G. Maizza, S. Grasso, Y. Sakka, T. Noda, and O. Ohashi, “Relation between microstructure, properties and spark plasma sintering (SPS) parameters of pure ultrafine WC powder,” *Sci. Technol. Adv. Mater.*, vol. 8, no. 7–8, pp. 644–654, Jan. 2007, doi: 10.1016/j.stam.2007.09.002.

[35] M. Eriksson, M. Radwan, and Z. Shen, “Spark plasma sintering of WC, cemented carbide and functional graded materials,” *Int. J. Refract. Met. Hard Mater.*, vol. 36, pp. 31–37, Jan. 2013, doi: 10.1016/j.ijrmhm.2012.03.007.

[36] C.-C. Jia, H. Tang, X.-Z. Mei, F.-Z. Yin, and X.-H. Qu, “Spark plasma sintering on nanometer scale WC–Co powder,” *Mater. Lett.*, vol. 59, no. 19, pp. 2566–2569, Aug. 2005, doi: 10.1016/j.matlet.2005.04.002.

[37] M. Omori, “Sintering, consolidation, reaction and crystal growth by the spark plasma system (SPS),” *Mater. Sci. Eng. A*, vol. 287, no. 2, pp. 183–188, Aug. 2000, doi: 10.1016/S0921-5093(00)00773-5.

[38] S. I. Cha, S. H. Hong, and B. K. Kim, “Spark plasma sintering behavior of nanocrystalline WC–10Co cemented carbide powders,” *Mater. Sci. Eng. A*, vol. 351, no. 1, pp. 31–38, Jun. 2003, doi: 10.1016/S0921-5093(02)00605-6.

[39] G. D. Girolamo, F. Marra, L. Pilloni, G. Pulci, J. Tirillò, and T. Valente, “Microstructure and Wear Behavior of Plasma-Sprayed Nanostructured WC–Co Coatings,” *Int. J. Appl. Ceram. Technol.*, vol. 10, no. 1, pp. 60–71, 2013, doi: 10.1111/j.1744-7402.2011.02734.x.

[40] G. D. Girolamo, L. Pilloni, G. Pulci, and F. Marra, “Tribological Characterization of WC–Co Plasma Sprayed Coatings,” *J. Am. Ceram. Soc.*, vol. 92, no. 5, pp. 1118–1124, 2009, doi: 10.1111/j.1551-2916.2009.03023.x.

[41] R. Kingswell, K. T. Scott, and L. L. Wassell, “Optimizing the vacuum plasma spray deposition of metal, ceramic, and cermet coatings using designed experiments,” *J. Therm. Spray Technol.*, vol. 2, no. 2, pp. 179–185, Jun. 1993, doi: 10.1007/BF02652027.

[42] X.-Q. Zhao, H.-D. Zhou, and J.-M. Chen, “Comparative study of the friction and wear behavior of plasma sprayed conventional and nanostructured WC–12%Co coatings on stainless steel,” *Mater. Sci. Eng. A*, vol. 431, no. 1, pp. 290–297, Sep. 2006, doi: 10.1016/j.msea.2006.06.009.

[43] H. J. Kim, Y. G. Kweon, and R. W. Chang, “Wear and erosion behavior of plasma-sprayed WC-Co coatings,” *J. Therm. Spray Technol.*, vol. 3, no. 2, pp. 169–178, Jun. 1994, doi: 10.1007/BF02648274.

[44] D. Tu, S. Chang, C. Chao, and C. Lin, “Tungsten carbide phase transformation during the plasma spray process,” *J. Vac. Sci. Technol. A*, vol. 3, no. 6, pp. 2479–2482, Nov. 1985, doi: 10.1116/1.572862.

[45] Y. Zhu, K. Yukimura, C. Ding, and P. Zhang, “Tribological properties of nanostructured and conventional WC–Co coatings deposited by plasma spraying,” *Thin Solid Films*, vol. 388, no. 1, pp. 277–282, Jun. 2001, doi: 10.1016/S0040-6090(01)00805-7.

[46] Y. C. Zhu, C. X. Ding, K. Yukimura, T. D. Xiao, and P. R. Strutt, “Deposition and characterization of nanostructured WC–Co coating,” *Ceram. Int.*, vol. 27, no. 6, pp. 669–674, Jan. 2001, doi: 10.1016/S0272-8842(01)00016-5.

[47] J. A. Picas, Y. Xiong, M. Punset, L. Ajdelsztajn, A. Forn, and J. M. Schoenung, “Int . Journal of Refractory Metals & Hard Materials Microstructure and wear resistance of WC – Co by three consolidation processing techniques,” *Int. J. Refract. Met. Hard Mater.*, vol. 27, no. 2, pp. 344–349, 2009, doi: 10.1016/j.ijrmhm.2008.07.002.

[48] Q. Wang, Z. H. Chen, and Z. X. Ding, “Performance of abrasive wear of WC-12Co coatings sprayed by HVOF,” *Tribol. Int.*, vol. 42, no. 7, pp. 1046–1051, Jul. 2009, doi: 10.1016/j.triboint.2009.02.011.

[49] Q. Yang, T. Senda, and A. Ohmori, “Effect of carbide grain size on microstructure and sliding wear behavior of HVOF-sprayed WC–12% Co coatings,” *Wear*, vol. 254, no. 1–2, pp. 23–34, Jan. 2003, doi: 10.1016/S0043-1648(02)00294-6.

[50] B. H. Kear, G. Skandan, and R. K. Sadangi, “Factors controlling decarburization in HVOF sprayed nano-WC/Co hardcoatings,” *Scr. Mater.*, vol. 44, no. 8, pp. 1703–1707, May 2001, doi: 10.1016/S1359-6462(01)00867-3.

[51] C. Monticelli, A. Frignani, and F. Zucchi, “Investigation on the corrosion process of carbon steel coated by HVOF WC/Co cermets in neutral solution,” *Corros. Sci.*, vol. 46, no. 5, pp. 1225–1237, May 2004, doi: 10.1016/j.corsci.2003.09.013.

[52] M. M. Lima, C. Godoy, J. C. Avelar-Batista, and P. J. Modenesi, “Toughness evaluation of HVOF WC–Co coatings using non-linear regression analysis,” *Mater. Sci. Eng. A*, vol. 357, no. 1, pp. 337–345, Sep. 2003, doi: 10.1016/S0921-5093(03)00204-1.

[53] D. A. Stewart, P. H. Shipway, and D. G. McCartney, “Abrasive wear behaviour of conventional and nanocomposite HVOF-sprayed WC–Co coatings,” *Wear*, vol. 225–229, pp. 789–798, Apr. 1999, doi: 10.1016/S0043-1648(99)00032-0.

[54] V. V. Sobolev and J. M. Guilemany, “Dynamic processes during high velocity oxyfuel spraying,” *Int. Mater. Rev.*, vol. 41, no. 1, pp. 13–32, Jan. 1996, doi: 10.1179/imr.1996.41.1.13.

[55] R. W. Smith and R. Knight, “Thermal spraying I: Powder consolidation—From coating to forming,” *JOM*, vol. 47, no. 8, pp. 32–39, Aug. 1995, doi: 10.1007/BF03221456.

[56] B. V. Krishna and A. Bandyopadhyay, “Surface modification of AISI 410 stainless steel using laser engineered net shaping (LENS TM),” *Mater. Des.*, vol. 30, no. 5, pp. 1490–1496, 2009, doi: 10.1016/j.matdes.2008.08.003.

[57] M. L. Griffith, L. D. Harwell, J. T. Romero, E. Schlienger, C. L. Atwood, and J. E. Smugeresky, “Multi-material processing by LENS,” in *Proceedings of the Solid Freeform Fabrication Symposium*, 1997, pp. 387–393, Accessed: Feb. 25, 2017. [Online]. Available: http://sffsymposium.engr.utexas.edu/Manuscripts/1997/1997-45-Griffith.pdf.

[58] J. Kummailil, C. Sammarco, D. Skinner, C. A. Brown, and K. Rong, “Effect of Select LENS^{TM} Processing Parameters on the Deposition of Ti-6Al-4V,” *J. Manuf. Process.*, vol. 7, no. 1, pp. 42–50, Jan. 2005, doi: 10.1016/S1526-6125(05)70080-3.

[59] Y. Xiong, J. E. Smugeresky, and J. M. Schoenung, “The influence of working distance on laser deposited WC–Co,” *J. Mater. Process. Technol.*, vol. 209, no. 10, pp. 4935–4941, Jun. 2009, doi: 10.1016/j.jmatprotec.2009.01.016.

[60] Y. Xiong, J. E. Smugeresky, E. J. Lavernia, and J. M. Schoenung, “Processing and microstructure of WC-Co cermets by laser engineered net shaping,” Accessed: Feb. 25, 2017. [Online]. Available: http://edge.rit.edu/edge/P10551/public/SFF/SFF%202008%20Proceedings/Manuscripts/2008-12-Xiong.pdf.

[61] C. I. Corrotherm International Ltd, “Corrosion resistant INCONEL, INCOLOY and MONEL, marine application Nickel Alloy Applications | Corrotherm International,” 2017. https://www.corrotherm.co.uk/applications/corrosion-resistant-inconel-incoloy-and-monel-marine-applications (accessed Jun. 23, 2017).

[62] “Cemented tungsten carbide: material properties - Matmatch.” https://matmatch.com/suppliers/cera-ceratizit/examples/cemented-tungsten-carbide-properties (accessed Jan. 14, 2020).

[63] I. Borgh *et al.*, “Microstructure, grain size distribution and grain shape in WC–Co alloys sintered at different carbon activities,” *Int. J. Refract. Met. Hard Mater.*, vol. 43, pp. 205–211, Mar. 2014, doi: 10.1016/j.ijrmhm.2013.12.007.

[64] A. Delanoë and S. Lay, “Evolution of the WC grain shape in WC–Co alloys during sintering: Effect of C content,” *Int. J. Refract. Met. Hard Mater.*, vol. 27, no. 1, pp. 140–148, Jan. 2009, doi: 10.1016/j.ijrmhm.2008.06.001.

[65] Y. Wang, M. Heusch, S. Lay, and C. H. Allibert, “Microstructure evolution in the cemented carbides WC-Co I. Effect of the C/W ratio on the morphology and defects of the WC grains,” *Phys. Status Solidi Appl. Res.*, vol. 193, no. 2, pp. 271–283, 2002, doi: 10.1002/1521-396X(200209)193:2<271::AID-PSSA271>3.0.CO;2-O.

[66] S. Kim, S.-H. Han, J.-K. Park, and H.-E. Kim, “Variation of WC grain shape with carbon content in the WC–Co alloys during liquid-phase sintering,” *Scr. Mater.*, vol. 48, no. 5, pp. 635–639, Mar. 2003, doi: 10.1016/S1359-6462(02)00464-5.

[67] A. Delanoë and S. Lay, “Evolution of the WC grain shape in WC–Co alloys during sintering: Cumulated effect of the Cr addition and of the C content,” *Int. J. Refract. Met. Hard Mater.*, vol. 27, no. 2, pp. 189–197, Mar. 2009, doi: 10.1016/j.ijrmhm.2008.07.010.

[68] M. Zhong, W. Liu, Y. Zhang, and X. Zhu, “Formation of WC/Ni hard alloy coating by laser cladding of W/C/Ni pure element powder blend,” *Int. J. Refract. Met. Hard Mater.*, vol. 24, no. 6, pp. 453–460, Nov. 2006, doi: 10.1016/j.ijrmhm.2005.09.002.

[69] T. Dash *et al.*, “Preparation and Neutronic Studies of Tungsten Carbide Composite,” *Fusion Sci. Technol.*, vol. 65, no. 2, pp. 241–247, Apr. 2014, doi: 10.13182/FST13-663.

[70] J. García, V. Collado Ciprés, A. Blomqvist, and B. Kaplan, “Cemented carbide microstructures: a review,” *Int. J. Refract. Met. Hard Mater.*, vol. 80, pp. 40–68, Apr. 2019, doi: 10.1016/j.ijrmhm.2018.12.004.

[71] E. Parthé and V. Sadagopan, “Neutronen- und Röntgenbeugungsuntersuchungen über die Struktur des Wolframcarbides WC und Vergleich mit älteren Elektronenbeugungsdaten,” *Monatshefte Für Chem.*, vol. 93, no. 1, pp. 263–270, 1962, doi: 10.1007/BF00908251.

[72] M. Hansen, K. Anderko, and H. W. Salzberg, “Constitution of Binary Alloys,” *J. Electrochem. Soc.*, vol. 105, no. 12, pp. 260C-261C, Dec. 1958, doi: 10.1149/1.2428700.

[73] H. E. Exner, “Physical and chemical nature of cemented carbides,” *Int. Met. Rev.*, vol. 24, no. 1, pp. 149–170, 1979, doi: 10.1179/imtr.1979.24.1.149.

[74] J. F. Nicholas, “Calculation of Surface Energy as a Function of Orientation for Cubic Crystals,” *Aust. J. Phys.*, vol. 21, no. 1, pp. 21–34, 1968, doi: 10.1071/ph680021.

[75] J. Li *et al.*, “Applications of WC-based composites rapid synthesized by consumable electrode in-situ metallurgy to cutting pick,” *Int. J. Refract. Met. Hard Mater.*, vol. 35, pp. 132–137, Nov. 2012, doi: 10.1016/j.ijrmhm.2012.05.005.

[76] Y. Yuan and Z. Li, “Microstructure and tribology behaviors of in-situ WC/Fe carbide coating fabricated by plasma transferred arc metallurgic reaction,” *Appl. Surf. Sci.*, vol. 423, pp. 13–24, Nov. 2017, doi: 10.1016/j.apsusc.2017.06.080.

[77] J. Long *et al.*, “Microstructure evolution of WC grains in WC–Co–Ni–Al alloys: Effect of binder phase composition,” *J. Alloys Compd.*, vol. 710, pp. 338–348, Jul. 2017, doi: 10.1016/j.jallcom.2017.03.284.

[78] A. Duszová *et al.*, “Nanoindentation of WC–Co hardmetals,” *J. Eur. Ceram. Soc.*, vol. 33, no. 12, pp. 2227–2232, Oct. 2013, doi: 10.1016/j.jeurceramsoc.2012.12.018.

[79] T. W. Scharf *et al.*, “Atomic-scale structure and composition of tungsten carbide reinforced diamondlike carbon films,” *Appl. Phys. Lett.*, vol. 93, no. 15, p. 151909, Oct. 2008, doi: 10.1063/1.2995860.

[80] T. Takahashi and E. J. Freise, “Determination of the slip systems in single crystals of tungsten monocarbide,” *Philos. Mag. J. Theor. Exp. Appl. Phys.*, vol. 12, no. 115, pp. 1–8, Jul. 1965, doi: 10.1080/14786436508224941.

[81] S. B. Luyckx and J. Katzourakis, “Preparation and properties of WC–Co textured components,” *Mater. Sci. Technol.*, vol. 7, no. 5, pp. 472–474, May 1991, doi: 10.1179/mst.1991.7.5.472.

[82] I. M. Lifshitz and V. V. Slyozov, “The kinetics of precipitation from supersaturated solid solutions,” *J. Phys. Chem. Solids*, vol. 19, no. 1, pp. 35–50, Apr. 1961, doi: 10.1016/0022-3697(61)90054-3.

[83] K. Mannesson, J. Jeppsson, A. Borgenstam, and J. Ågren, “Carbide Grain Growth in Cemented Carbides,” *Acta Mater. - ACTA MATER*, vol. 59, pp. 1912–1923, Mar. 2011, doi: 10.1016/j.actamat.2010.11.056.

[84] M. S. Kovalchenko, “Pressure sintering kinetics of tungsten and titanium carbides,” *Int. J. Refract. Met. Hard Mater.*, vol. 39, pp. 32–37, Jul. 2013, doi: 10.1016/j.ijrmhm.2013.03.001.

[85] C. J. R. G. Oliver, E. A. Álvarez, and J. L. García, “Kinetics of densification and grain growth in ultrafine WC-Co composites,” *Int. J. Refract. Met. Hard Mater.*, vol. 59, pp. 121–131, Sep. 2016, doi: 10.1016/j.ijrmhm.2016.05.016.

[86] L. Zhong, X. Zhang, X. Wang, Y. Xu, H. Wu, and Y. Fu, “Growth kinetics of WC-Fe layer formed at the surface iron during solid-phase diffusion,” *Ceram. Int.*, vol. 42, no. 15, pp. 16941–16947, Nov. 2016, doi: 10.1016/j.ceramint.2016.07.194.

[87] H. Xu *et al.*, “Behavior of aluminum oxide, intermetallics and voids in Cu–Al wire bonds,” *Acta Mater.*, vol. 59, no. 14, pp. 5661–5673, Aug. 2011, doi: 10.1016/j.actamat.2011.05.041.

[88] B. Sarma, N. M. Tikekar, and K. S. Ravi Chandran, “Kinetics of growth of superhard boride layers during solid state diffusion of boron into titanium,” *Ceram. Int.*, vol. 38, no. 8, pp. 6795–6805, Dec. 2012, doi: 10.1016/j.ceramint.2012.05.077.

[89] U. Sen, “Kinetics of niobium carbide coating produced on AISI 1040 steel by thermo-reactive deposition technique,” *Mater. Chem. Phys.*, vol. 86, no. 1, pp. 189–194, Jul. 2004, doi: 10.1016/j.matchemphys.2004.03.002.

[90] H. Yang, X. Wu, Z. Yang, S. Pu, and H. Wang, “Enhanced boronizing kinetics of alloy steel assisted by surface mechanical attrition treatment,” *J. Alloys Compd.*, vol. 590, pp. 388–395, Mar. 2014, doi: 10.1016/j.jallcom.2013.12.151.

[91] L. Zhong, X. Zhang, S. Chen, Y. Xu, H. Wu, and J. Wang, “Fe–W–C thermodynamics and in situ preparation of tungsten carbide-reinforced iron-based surface composites by solid-phase diffusion,” *Int. J. Refract. Met. Hard Mater.*, vol. 57, pp. 42–49, Jun. 2016, doi: 10.1016/j.ijrmhm.2016.02.001.

[92] C. B. Carter and M. G. Norton, Eds., “Sintering and Grain Growth,” in *Ceramic Materials: Science and Engineering*, New York, NY: Springer New York, 2007, pp. 427–443.

[93] R. M. German, P. Suri, and S. J. Park, “Review: liquid phase sintering,” *J. Mater. Sci.*, vol. 44, no. 1, pp. 1–39, Jan. 2009, doi: 10.1007/s10853-008-3008-0.

[94] K. Mannesson, J. Jeppsson, A. Borgenstam, and J. Ågren, “Carbide grain growth in cemented carbides,” *Acta Mater.*, vol. 59, no. 5, pp. 1912–1923, Mar. 2011, doi: 10.1016/j.actamat.2010.11.056.

[95] Q. Y. Hou, Z. Y. Huang, N. Shi, and J. S. Gao, “Effects of molybdenum on the microstructure and wear resistance of nickel-based hardfacing alloys investigated using Rietveld method,” *J. Mater. Process. Technol.*, vol. 209, no. 6, pp. 2767–2772, Mar. 2009, doi: 10.1016/j.jmatprotec.2008.06.025.

[96] A. V. Shatov, S. S. Ponomarev, and S. A. Firstov, “Modeling the effect of flatter shape of WC crystals on the hardness of WC-Ni cemented carbides,” *Int. J.*

Refract. Met. Hard Mater., vol. 27, no. 2, pp. 198–212, Mar. 2009, doi: 10.1016/j.ijrmhm.2008.07.008.

[97] J. Kim and S. Kang, “WC platelet formation via high-energy ball mill,” *Int. J. Refract. Met. Hard Mater.*, vol. 47, pp. 108–112, Nov. 2014, doi: 10.1016/j.ijrmhm.2014.06.024.

[98] I. Konyashin *et al.*, “On the mechanism of WC coarsening in WC–Co hardmetals with various carbon contents,” *Int. J. Refract. Met. Hard Mater.*, vol. 27, no. 2, pp. 234–243, Mar. 2009, doi: 10.1016/j.ijrmhm.2008.09.001.

[99] Y. Wei, X. Wei, B. Chen, J. Zuo, T. Ma, and J. Shen, “Parameter optimization for tungsten carbide/Ni-based composite coating deposited by plasma transferred arc hardfacing,” *Trans. Nonferrous Met. Soc. China*, vol. 28, no. 12, pp. 2511–2519, Dec. 2018, doi: 10.1016/S1003-6326(18)64897-6.

[100] Y. J. Park, N. M. Hwang, and D. Y. Yoon, “Abnormal growth of faceted (WC) grains in a (Co) liquid matrix,” *Metall. Mater. Trans. Phys. Metall. Mater. Sci.*, vol. 27, no. 9, pp. 2809–2819, 1996, doi: 10.1007/BF02652373.

[101] H. S. Ryoo and S. K. Hwang, “Anisotropic atomic packing model for abnormal grain growth mechanism of WC-25wt.%Co alloy,” *Scr. Mater.*, vol. 39, no. 11, pp. 1577–1583, Nov. 1998, doi: 10.1016/S1359-6462(98)00354-6.

[102] K. Choi, N. M. Hwang, and D.-Y. Kim, “Effect of VC addition on microstructural evolution of WC-Co alloy: Mechanism of grain growth inhibition,” *Powder Metall.*, vol. 43, no. 2, pp. 168–172, 2000, doi: 10.1179/003258900665943.

[103] B.-K. Yoon, B.-A. Lee, and S.-J. L. Kang, “Growth behavior of rounded (Ti,W)C and faceted WC grains in a Co matrix during liquid phase sintering,” *Acta Mater.*, vol. 53, no. 17, pp. 4677–4685, Oct. 2005, doi: 10.1016/j.actamat.2005.06.021.

[104] S. Lay, C. H. Allibert, M. Christensen, and G. Wahnström, “Morphology of WC grains in WC–Co alloys,” *Mater. Sci. Eng. A*, vol. 486, pp. 253–261, Jul. 2008, doi: 10.1016/j.msea.2007.09.019.

[105] M. Sommer, W.-D. Schubert, E. Zobetz, and P. Warbichler, “On the formation of very large WC crystals during sintering of ultrafine WC–Co alloys,” *Int. J. Refract. Met. Hard Mater.*, vol. 20, no. 1, pp. 41–50, Jan. 2002, doi: 10.1016/S0263-4368(01)00069-5.

[106] M. Christensen, G. Wahnström, S. Lay, and C. H. Allibert, “Morphology of WC grains in WC–Co alloys: Theoretical determination of grain shape,” *Acta Mater.*, vol. 55, no. 5, pp. 1515–1521, Mar. 2007, doi: 10.1016/j.actamat.2006.10.013.

[107] R.-P. Herber, W.-D. Schubert, and B. Lux, “Hardmetals with ‘rounded’ WC grains,” *Int. J. Refract. Met. Hard Mater.*, vol. 24, no. 5, pp. 360–364, Sep. 2006, doi: 10.1016/j.ijrmhm.2005.11.014.

[108] I. Borgh, P. Hedström, A. Borgenstam, J. Ågren, and J. Odqvist, “Effect of carbon activity and powder particle size on WC grain coarsening during sintering

of cemented carbides," *Int. J. Refract. Met. Hard Mater.*, vol. 42, pp. 30–35, Jan. 2014, doi: 10.1016/j.ijrmhm.2013.10.004.

[109] K. Mannesson, I. Borgh, A. Borgenstam, and J. Ågren, "Abnormal grain growth in cemented carbides — Experiments and simulations," *Int. J. Refract. Met. Hard Mater.*, vol. 29, no. 4, pp. 488–494, Jul. 2011, doi: 10.1016/j.ijrmhm.2011.02.008.

[110] I. Borgh *et al.*, "On the three-dimensional structure of WC grains in cemented carbides," *Acta Mater.*, vol. 61, no. 13, pp. 4726–4733, Aug. 2013, doi: 10.1016/j.actamat.2013.05.008.

[111] A. V. Shatov, S. A. Firstov, and I. V. Shatova, "The shape of WC crystals in cemented carbides," *Mater. Sci. Eng. A*, vol. 242, no. 1, pp. 7–14, Feb. 1998, doi: 10.1016/S0921-5093(97)00509-1.

[112] D.-Y. Yang and S.-J. L. Kang, "Suppression of abnormal grain growth in WC–Co via pre-sintering treatment," *Int. J. Refract. Met. Hard Mater.*, vol. 27, no. 1, pp. 90–94, Jan. 2009, doi: 10.1016/j.ijrmhm.2008.04.001.

[113] J.-P. Palmquist, Zs. Czigany, M. Odén, J. Neidhart, L. Hultman, and U. Jansson, "Magnetron sputtered W–C films with C60 as carbon source," *Thin Solid Films*, vol. 444, no. 1, pp. 29–37, Nov. 2003, doi: 10.1016/S0040-6090(03)00937-4.

[114] B. Trindade, M. T. Vieira, and E. Bauer-Grosse, "Characaterization of W□Me□C (Me□Fe, Co) films and their structural behaviour with temperature," *Mater. Sci. Eng. A*, vol. 174, no. 2, pp. 165–171, Feb. 1994, doi: 10.1016/0921-5093(94)91085-5.

[115] B. Trindade, M. T. Vieira, and E. Bauer-Grosse, "Amorphous phase forming ability in(W–C)-based sputtered films," *Acta Mater.*, vol. 46, no. 5, pp. 1731–1739, Mar. 1998, doi: 10.1016/S1359-6454(97)00336-4.

[116] H. R. de Macedo, A. G. P. da Silva, and D. M. A. de Melo, "The spreading of cobalt, nickel and iron on tungsten carbide and the first stage of hard metal sintering," *Mater. Lett.*, vol. 57, no. 24, pp. 3924–3932, Aug. 2003, doi: 10.1016/S0167-577X(03)00242-8.

[117] W. Su, Y. Sun, J. Liu, J. Feng, and J. Ruan, "Effects of Ni on the microstructures and properties of WC–6Co cemented carbides fabricated by WC–6(Co, Ni) composite powders," *Ceram. Int.*, vol. 41, no. 2, pp. 3169–3177, Mar. 2015, doi: 10.1016/j.ceramint.2014.10.165.

[118] C. M. Fernandes, A. M. R. Senos, M. T. Vieira, and J. V. Fernandes, "Composites from WC powders sputter-deposited with iron rich binders," *Ceram. Int.*, vol. 35, no. 4, pp. 1617–1623, May 2009, doi: 10.1016/j.ceramint.2008.09.009.

[119] S. Kim, J.-K. Park, and D. Lee, "Effect of Grain Motion on the Coarsening of WC Grains in the Carbon-Saturated Liquid Matrix During Liquid Phase Sintering of

WC-Co Alloys," *Scr. Mater.*, vol. 38, no. 10, pp. 1563–1569, Apr. 1998, doi: 10.1016/S1359-6462(98)00070-0.

[120] "Nickel and Nickel Alloys," in *Properties and Selection: Nonferrous Alloys and Special-Purpose Materials*, ASM International, 1990, pp. 428–445.

[121] T. J. Antoszczyszyn, R. M. G. Paes, A. S. C. M. de Oliveira, and A. Scheid, "Impact of dilution on the microstructure and properties of Ni-based 625 alloy coatings," *Soldag. Amp Insp.*, vol. 19, no. 2, pp. 134–144, Jun. 2014, doi: 10.1590/0104-9224/SI1902.05.

[122] "Hall Petch Equation." http://inside.mines.edu/HallPetchEquation (accessed Oct. 23, 2019).

[123] D. Kesavan and M. Kamaraj, "Influence of aging treatment on microstructure, wear and corrosion behavior of a nickel base hardfaced coating," *Wear*, vol. 272, no. 1, pp. 7–17, Oct. 2011, doi: 10.1016/j.wear.2011.05.041.

[124] C. Guoqing, F. Xuesong, W. Yanhui, L. Shan, and Z. Wenlong, "Microstructure and wear properties of nickel-based surfacing deposited by plasma transferred arc welding," *Surf. Coat. Technol.*, vol. 228, pp. S276–S282, Aug. 2013, doi: 10.1016/j.surfcoat.2012.05.125.

[125] Y. Wang, J. Shi, and Y. Liu, "Competitive grain growth and dendrite morphology evolution in selective laser melting of Inconel 718 superalloy," *J. Cryst. Growth*, vol. 521, pp. 15–29, Sep. 2019, doi: 10.1016/j.jcrysgro.2019.05.027.

[126] Y. Lee, M. Nordin, S. S. Babu, and D. F. Farson, "Effect of Fluid Convection on Dendrite Arm Spacing in Laser Deposition," *Metall. Mater. Trans. B*, vol. 45, no. 4, pp. 1520–1529, Aug. 2014, doi: 10.1007/s11663-014-0054-7.

[127] M. Akbari and R. Kovacevic, "An investigation on mechanical and microstructural properties of 316LSi parts fabricated by a robotized laser/wire direct metal deposition system," *Addit. Manuf.*, vol. 23, pp. 487–497, Oct. 2018, doi: 10.1016/j.addma.2018.08.031.

[128] L. L. Shaw, H. Luo, and Y. Zhong, "WC-18wt.% Co with simultaneous improvements in hardness and toughness derived from nanocrystalline powder," *Mater. Sci. Eng. A*, vol. 537, pp. 39–48, Mar. 2012, doi: 10.1016/j.msea.2012.01.005.

[129] V. Bonache *et al.*, "Synthesis and processing of nanocrystalline tungsten carbide: Towards cemented carbides with optimal mechanical properties," *Int. J. Refract. Met. Hard Mater.*, vol. 29, no. 1, pp. 78–84, Jan. 2011, doi: 10.1016/j.ijrmhm.2010.08.003.

[130] H.-C. Kim, I.-J. Shon, J.-K. Yoon, and J.-M. Doh, "Comparison of sintering behavior and mechanical properties between WC−8Co and WC−8Ni hard materials produced by high-frequency induction heating sintering," *Met. Mater. Int.*, vol. 12, no. 2, pp. 141–146, 2006, doi: 10.1007/BF03027470.

[131] G. Jiang, H. Zhuang, and W. Li, “Parameters investigation during simultaneous synthesis and densification WC–Ni composites by field-activated combustion,” *Mater. Sci. Eng. A*, vol. 360, no. 1–2, pp. 377–384, Nov. 2003, doi: 10.1016/S0921-5093(03)00505-7.

[132] G. Bolelli, T. Börner, F. Bozza, V. Cannillo, G. Cirillo, and L. Lusvarghi, “Cermet coatings with Fe-based matrix as alternative to WC–CoCr: Mechanical and tribological behaviours,” *Surf. Coat. Technol.*, vol. 206, no. 19–20, pp. 4079–4094, May 2012, doi: 10.1016/j.surfcoat.2012.03.094.

[133] J. R. Davis, *Alloying: Understanding the Basics*. ASM International, 2001.

[134] W. D. Schubert, M. Fugger, B. Wittmann, and R. Useldinger, “Aspects of sintering of cemented carbides with Fe-based binders,” *Int. J. Refract. Met. Hard Mater.*, vol. 49, pp. 110–123, Mar. 2015, doi: 10.1016/j.ijrmhm.2014.07.028.

[135] E. O. Correa, J. N. Santos, and A. N. Klein, “Microstructure and mechanical properties of WC Ni–Si based cemented carbides developed by powder metallurgy,” *Int. J. Refract. Met. Hard Mater.*, vol. 28, no. 5, pp. 572–575, Sep. 2010, doi: 10.1016/j.ijrmhm.2010.04.003.

[136] R. M. Genga, L. A. Cornish, and G. Akdogan, “Effect of Mo2C additions on the properties of SPS manufactured WC–TiC–Ni cemented carbides,” *Int. J. Refract. Met. Hard Mater.*, vol. 41, pp. 12–21, Nov. 2013, doi: 10.1016/j.ijrmhm.2013.01.008.

[137] S.-H. Chang and S.-L. Chen, “Characterization and properties of sintered WC–Co and WC–Ni–Fe hard metal alloys,” *J. Alloys Compd.*, vol. 585, pp. 407–413, Feb. 2014, doi: 10.1016/j.jallcom.2013.09.188.

[138] T. E. Abioye, P. K. Farayibi, D. G. McCartney, and A. T. Clare, “Effect of carbide dissolution on the corrosion performance of tungsten carbide reinforced Inconel 625 wire laser coating,” *J. Mater. Process. Technol.*, vol. 231, pp. 89–99, May 2016, doi: 10.1016/j.jmatprotec.2015.12.023.

[139] C. M. Fernandes, A. M. R. Senos, M. T. Vieira, and J. M. Antunes, “Mechanical characterization of composites prepared from WC powders coated with Ni rich binders,” *Int. J. Refract. Met. Hard Mater.*, vol. 26, no. 5, pp. 491–498, Sep. 2008, doi: 10.1016/j.ijrmhm.2007.12.001.

[140] E. A. Almond and B. Roebuck, “Identification of optimum binder phase compositions for improved WC hard metals,” *Mater. Sci. Eng. A*, vol. 105, pp. 237–248, 1988.

[141] A. R. Vinod, C. K. Srinivasa, R. Keshavamurthy, and P. V. Shashikumar, “A novel technique for reducing lead-time and energy consumption in fabrication of Inconel-625 parts by laser-based metal deposition process,” *Rapid Prototyp. J.*, vol. 22, no. 2, pp. 269–280, 2016, doi: 10.1108/RPJ-07-2013-0070.

[142] C. Hanyaloglu, B. Aksakal, and J. D. Bolton, “Production and indentation analysis of WC/Fe–Mn as an alternative to cobalt-bonded hardmetals,” *Mater. Charact.*, vol. 47, no. 3, pp. 315–322, 2001.

[143] Z. Zhao, J. Liu, H. Tang, X. Ma, and W. Zhao, “Investigation on the mechanical properties of WC–Fe–Cu hard alloys,” *J. Alloys Compd.*, vol. 632, pp. 729–734, May 2015, doi: 10.1016/j.jallcom.2015.01.300.

[144] M. Tarraste, K. Juhani, J. Kübarsepp, J. Pirso, and V. Mikli, “Hard Materials-Alternative Binders: The Effect of Cr and C on the Characteristics of WC-FeCr Hardmetals,” in *European Congress and Exhibition on Powder Metallurgy. European PM Conference Proceedings*, 2015, p. 1, Accessed: Apr. 10, 2017. [Online]. Available: http://search.proquest.com/openview/f2c98f3aee76ce58862650dbda2ef593/1?pq-origsite=gscholar&cbl=596295.

[145] K. J. A. Brookes, *World Directory and Handbook of Hardmetals and Hard Materials: Sixth Ed*. 1996.

[146] M. Prathabrao, S. Y. M. Amin, and M. H. I. Ibrahim, “Review on Sintering Process of WC-Co Cemented Carbide in Metal Injection Molding Technology,” *IOP Conf. Ser. Mater. Sci. Eng.*, vol. 165, p. 012017, Jan. 2017, doi: 10.1088/1757-899X/165/1/012017.

[147] L. Sun, C. Jia, R. Cao, and C. Lin, “Effects of Cr3C2 additions on the densification, grain growth and properties of ultrafine WC–11Co composites by spark plasma sintering,” *Int. J. Refract. Met. Hard Mater.*, vol. 26, no. 4, pp. 357–361, Jul. 2008, doi: 10.1016/j.ijrmhm.2007.08.009.

[148] V. Bonache, M. D. Salvador, A. Fernández, and A. Borrell, “Fabrication of full density near-nanostructured cemented carbides by combination of VC/Cr3C2 addition and consolidation by SPS and HIP technologies,” *Int. J. Refract. Met. Hard Mater.*, vol. 29, no. 2, pp. 202–208, Mar. 2011, doi: 10.1016/j.ijrmhm.2010.10.007.

[149] V. Bonache, M. D. Salvador, V. G. Rocha, and A. Borrell, “Microstructural control of ultrafine and nanocrystalline WC–12Co–VC/Cr3C2 mixture by spark plasma sintering,” *Ceram. Int.*, vol. 37, no. 3, pp. 1139–1142, Apr. 2011, doi: 10.1016/j.ceramint.2010.11.026.

[150] H.-C. Kim, I.-J. Shon, J. E. Garay, and Z. A. Munir, “Consolidation and properties of binderless sub-micron tungsten carbide by field-activated sintering,” *Int. J. Refract. Met. Hard Mater.*, vol. 22, no. 6, pp. 257–264, Nov. 2004, doi: 10.1016/j.ijrmhm.2004.08.003.

[151] H.-C. Kim, J.-K. Yoon, J.-M. Doh, I.-Y. Ko, and I.-J. Shon, “Rapid sintering process and mechanical properties of binderless ultra fine tungsten carbide,” *Mater. Sci. Eng. A*, vol. 435–436, pp. 717–724, Nov. 2006, doi: 10.1016/j.msea.2006.07.127.

[152] H.-C. Kim, I.-J. Shon, J.-K. Yoon, J.-M. Doh, and Z. A. Munir, “Rapid sintering of ultrafine WC–Ni cermets,” *Int. J. Refract. Met. Hard Mater.*, vol. 24, no. 6, pp. 427–431, Nov. 2006, doi: 10.1016/j.ijrmhm.2005.07.002.

[153] H.-C. Kim, D.-K. Kim, K.-D. Woo, I.-Y. Ko, and I.-J. Shon, “Consolidation of binderless WC–TiC by high frequency induction heating sintering,” *Int. J. Refract. Met. Hard Mater.*, vol. 26, no. 1, pp. 48–54, Jan. 2008, doi: 10.1016/j.ijrmhm.2007.01.006.

[154] H.-C. Kim, H.-K. Park, I.-K. Jeong, I.-Y. Ko, and I.-J. Shon, “Sintering of binderless WC–Mo2C hard materials by rapid sintering process,” *Ceram. Int.*, vol. 34, no. 6, pp. 1419–1423, Aug. 2008, doi: 10.1016/j.ceramint.2007.03.029.

[155] S. G. Huang, K. Vanmeensel, O. Van der Biest, and J. Vleugels, “Binderless WC and WC–VC materials obtained by pulsed electric current sintering,” *Int. J. Refract. Met. Hard Mater.*, vol. 26, no. 1, pp. 41–47, Jan. 2008, doi: 10.1016/j.ijrmhm.2007.01.002.

[156] D. Zheng, X. Li, X. Ai, C. Yang, and Y. Li, “Bulk WC–Al2O3 composites prepared by spark plasma sintering,” *Int. J. Refract. Met. Hard Mater.*, vol. 30, no. 1, pp. 51–56, Jan. 2012, doi: 10.1016/j.ijrmhm.2011.07.003.

[157] O. Malek, B. Lauwers, Y. Perez, P. De Baets, and J. Vleugels, “Processing of ultrafine ZrO2 toughened WC composites,” *J. Eur. Ceram. Soc.*, vol. 29, no. 16, pp. 3371–3378, Dec. 2009, doi: 10.1016/j.jeurceramsoc.2009.07.013.

[158] J. Hong, “Corrosion resistant cemented carbide,” US4963183 A, Oct. 16, 1990.

[159] H. Holleck, “Hard alloy comprising one or more hard phases and a binary or multicomponent binder metal alloy,” US4432794 A, Feb. 21, 1984.

[160] S. D. Cramer and B. S. Covino, Eds., “Corrosion of Cemented Carbides,” in *Corrosion: Materials*, ASM International, 2005, pp. 513–525.

[161] C. Liu, *Alternative binder phases for WC cemented carbides*. 2014.

[162] “Tungsten-Nickel-Carbon (W-Ni-C) Phase Diagram.” http://www.calphad.com/tungsten-nickel-carbon.html (accessed Oct. 28, 2019).

[163] Y. Zhang *et al.*, “Microstructures and properties of high-entropy alloys,” *Prog. Mater. Sci.*, vol. 61, pp. 1–93, Apr. 2014, doi: 10.1016/j.pmatsci.2013.10.001.

[164] Z. Li, Y. Jiang, X. Ye, and R. Zhou, “Dissolution of tungsten carbide particulates (WC) in the matrix of WC reinforced gray cast iron matrix composite,” *Fuhe Cailiao XuebaoActa Mater. Compos. Sin.*, vol. 24, pp. 13–17, Apr. 2007.

[165] P. Xu, J. Ren, P. Zhang, H. Y. Gong, and S. L. Yang, “Analysis of Formation and Interfacial WC Dissolution Behavior of WC-Co/Invar Laser-TIG Welded Joints,” *J. Mater. Eng. Perform.*, vol. 22, Feb. 2012, doi: 10.1007/s11665-012-0279-z.

[166] O. Lavergne and C. H. Allibert, “Dissolution mechanism of tungsten carbide in cobalt-based liquids,” *High Temp. - High Press.*, vol. 31, no. 3, pp. 347–355, 1999, doi: 10.1068/htrt181.

[167] J. Matějíček, H. Boldyryeva, V. Brožek, P. Sachr, T. Chráska, and Z. Pala, “W–steel and W–WC–steel composites and FGMs produced by hot pressing,” *Fusion Eng. Des.*, vol. 100, pp. 364–370, Nov. 2015, doi: 10.1016/j.fusengdes.2015.06.154.

[168] E. Kimmaria, I. Hussainova, A. Smirnov, R. Traksmaa, and I. Preis, “Processing and microstructural characterization of WC-based cermets doped by ZrO 2,” *Est. J. Eng.*, vol. 15, Jan. 2009, doi: 10.3176/eng.2009.4.04.

[169] P. Gustafson, “A thermodynamic evaluation of the C-Fe-W system,” *Metall. Trans. A*, vol. 18, no. 2, pp. 175–188, 1987, doi: 10.1007/BF02825699.

[170] B. Uhrenius and H. Harvig, “A Thermodynamic Evaluation of Carbide Solubilities in the Fe–Mo–C, Fe–W–C, and Fe–Mo–W–C Systems at 1000°C,” *Met. Sci.*, vol. 9, no. 1, pp. 67–82, Jan. 1975, doi: 10.1179/030634575790444379.

[171] Y. Liu, Y. Jiang, R. Zhou, and J. C. Feng, “First-principles calculations of the mechanical and electronic properties of Fe–W–C ternary compounds,” 2014, doi: 10.1016/j.commatsci.2013.09.040.

[172] S. Zhou, J. Lei, X. Dai, J. Guo, Z. Gu, and H. Pan, “A comparative study of the structure and wear resistance of NiCrBSi/50 wt.% WC composite coatings by laser cladding and laser induction hybrid cladding,” *Int. J. Refract. Met. Hard Mater.*, vol. 60, pp. 17–27, Nov. 2016, doi: 10.1016/j.ijrmhm.2016.06.019.

[173] X. Wang *et al.*, “Evaluation and mechanisms on heat damage of WC particles in Ni60/WC composite coatings by laser induction hybrid cladding,” *Int. J. Refract. Met. Hard Mater.*, vol. 64, pp. 234–241, Apr. 2017, doi: 10.1016/j.ijrmhm.2016.11.001.

[174] Ad. Piasecki and M. Popławski, “Microstructure and hardness of Co-based alloy/tungsten carbide padding welds produced by TIG method,” *Inż. Mater.*, p. 4.

[175] H. Yu, R. Ahmed, H. de V. Lovelock, and S. Davies, “Tribo-Mechanical Evaluations of Cobalt-Based (Stellite 4) Alloys Manufactured via HIPing and Casting,” p. 6, 2007.

[176] C. Navas, R. Colaço, J. de Damborenea, and R. Vilar, “Abrasive wear behaviour of laser clad and flame sprayed-melted NiCrBSi coatings,” *Surf. Coat. Technol.*, vol. 200, no. 24, pp. 6854–6862, Aug. 2006, doi: 10.1016/j.surfcoat.2005.10.032.

[177] G. Xu, M. Kutsuna, Z. Liu, and H. Zhang, “Characteristics of Ni-based coating layer formed by laser and plasma cladding processes,” *Mater. Sci. Eng. A*, vol. 417, no. 1, pp. 63–72, Feb. 2006, doi: 10.1016/j.msea.2005.08.192.

[178] J. Wang, L. Li, and W. Tao, “Crack initiation and propagation behavior of WC particles reinforced Fe-based metal matrix composite produced by laser melting deposition,” *Opt. Laser Technol.*, vol. 82, pp. 170–182, Aug. 2016, doi: 10.1016/j.optlastec.2016.03.008.

[179] M. Xia, D. Gu, C. Ma, H. Chen, and H. Zhang, “Microstructure evolution, mechanical response and underlying thermodynamic mechanism of multi-phase strengthening WC/Inconel 718 composites using selective laser melting,” *J. Alloys Compd.*, vol. 747, pp. 684–695, May 2018, doi: 10.1016/j.jallcom.2018.03.049.

[180] S. Zhou, X. Zeng, Q. Hu, and Y. Huang, “Analysis of crack behavior for Ni-based WC composite coatings by laser cladding and crack-free realization,” *Appl. Surf. Sci.*, vol. 255, no. 5, Part 1, pp. 1646–1653, Dec. 2008, doi: 10.1016/j.apsusc.2008.04.003.

[181] J. Yang, X. Miao, X. Wang, and F. Yang, “Influence of Mn additions on the microstructure and magnetic properties of FeNiCr/60% WC composite coating produced by laser cladding,” *Int. J. Refract. Met. Hard Mater.*, vol. 46, pp. 58–64, Sep. 2014, doi: 10.1016/j.ijrmhm.2014.05.010.

[182] “MONEL 400 Alloy (UNS N04400),” *AZoM.com*, Jun. 24, 2013. https://www.azom.com/article.aspx?ArticleID=9338 (accessed Oct. 23, 2019).

[183] “Monel 400 Wire | Monel Wire | Monel Nickel Alloy Wire.” https://www.magellanmetals.com/wire-monel-400 (accessed Feb. 24, 2020).

[184] T. Bell, “Properties of Monel 400, a Nickel-Copper Alloy That Resists Corrosion,” *The Balance*. https://www.thebalance.com/monel-400-properties-and-composition-2340256 (accessed Oct. 24, 2019).

[185] I. Newman, “Monel alloy 400 - strength and hardness.” https://www.corrotherm.co.uk/blog/monel-alloy-400-strength-and-hardness (accessed Oct. 29, 2019).

[186] A. van Staden, “A Fundamental Analysis on Additive Manufacturing of a Cemented Tungsten Carbide.” Mar. 2016.

[187] A. Domashenkov, A. Borbély, and I. Smurov, “Structural modifications of WC/Co nanophased and conventional powders processed by selective laser melting,” *Mater. Manuf. Process.*, vol. 32, no. 1, pp. 93–100, Jan. 2017, doi: 10.1080/10426914.2016.1176195.

[188] R. S. Khmyrov, V. A. Safronov, and A. V. Gusarov, “Obtaining Crack-free WC-Co Alloys by Selective Laser Melting,” *Phys. Procedia*, vol. 83, pp. 874–881, 2016, doi: 10.1016/j.phpro.2016.08.091.

[189] E. Uhlmann, A. Bergmann, and W. Gridin, “Investigation on Additive Manufacturing of Tungsten Carbide-cobalt by Selective Laser Melting,” *Procedia CIRP*, vol. 35, pp. 8–15, 2015, doi: 10.1016/j.procir.2015.08.060.

[190] E. Uhlmann, A. Bergmann, and W. Gridin, “Investigation on Additive Manufacturing of Tungsten Carbide-cobalt by Selective Laser Melting,” *Procedia CIRP*, vol. 35, pp. 8–15, 2015, doi: 10.1016/j.procir.2015.08.060.

[191] A. Angelastro, S. L. Campanelli, G. Casalino, and A. D. Ludovico, “Optimization of Ni-Based WC/Co/Cr Composite Coatings Produced by Multilayer Laser Cladding,” *Adv. Mater. Sci. Eng.*, vol. 2013, pp. 1–7, 2013, doi: 10.1155/2013/615464.

[192] A. C. Pavalache, G. M. Dumitru, E. M. Stanciu, R. López, I. M. Vasile, and D. Petre, “An Experimental Approach to the Robotized Fabrication of WC-Co Based Layers,” *Appl. Mech. Mater.*, vol. 656, pp. 37–42, Oct. 2014, doi: 10.4028/www.scientific.net/AMM.656.37.

[193] L. St-Georges, “Development and characterization of composite Ni–Cr+WC laser cladding,” *Wear*, vol. 263, no. 1–6, pp. 562–566, Sep. 2007, doi: 10.1016/j.wear.2007.02.023.

[194] P. Wu, C. Z. Zhou, and X. N. Tang, “Microstructural characterization and wear behavior of laser cladded nickel-based and tungsten carbide composite coatings,” *Surf. Coat. Technol.*, vol. 166, no. 1, pp. 84–88, 2003.

[195] J. Przybyłowicz and J. Kusiński, “Structure of laser cladded tungsten carbide composite coatings,” *J. Mater. Process. Technol.*, vol. 109, no. 1–2, pp. 154–160, Feb. 2001, doi: 10.1016/S0924-0136(00)00790-1.

[196] C. P. Paul, H. Alemohammad, E. Toyserkani, A. Khajepour, and S. Corbin, “Cladding of WC–12 Co on low carbon steel using a pulsed Nd:YAG laser,” *Mater. Sci. Eng. A*, vol. 464, no. 1–2, pp. 170–176, Aug. 2007, doi: 10.1016/j.msea.2007.01.132.

[197] A. Domashenkov, A. Borbély, and I. Smurov, “Structural modifications of WC / Co nanophased and conventional powders processed by selective laser melting,” *Mater. Manuf. Process.*, vol. 32, no. 1, pp. 93–100, 2017, doi: 10.1080/10426914.2016.1176195.

[198] A. J. Cavaleiro *et al.*, “The role of nanocrystalline binder metallic coating into WC after additive manufacturing,” *Appl. Surf. Sci.*, vol. 427, no. Part A, pp. 131–138, Jan. 2018, doi: 10.1016/j.apsusc.2017.08.039.

[199] R. S. Khmyrov, “Obtaining crack free WC-Co alloys by selective laser melting,” vol. 83, pp. 874–881, 2016, doi: 10.1016/j.phpro.2016.08.091.

[200] D. Gu, Y. Shen, and J. Xiao, “Influence of processing parameters on particulate dispersion in direct laser sintered WC–Cop/Cu MMCs,” *Int. J. Refract. Met. Hard Mater.*, vol. 26, no. 5, pp. 411–422, Sep. 2008, doi: 10.1016/j.ijrmhm.2007.09.005.

[201] D. Gu and Y. Shen, “Processing and microstructure of submicron WC–Co particulate reinforced Cu matrix composites prepared by direct laser sintering,”

Mater. Sci. Eng. A, vol. 435, no. Supplement C, pp. 54–61, Nov. 2006, doi: 10.1016/j.msea.2006.07.105.

[202] J. Chen, Y. Huang, X. Gao, B. Qiao, J. Yang, and Y. He, “Experimental Study on Ni-Base Alloy Bulk Reinforced by Laser Sintered WC Particles,” *Adv. Compos. Mater.*, vol. 20, no. 3, pp. 277–287, Jan. 2011, doi: 10.1163/092430410X547092.

[203] X. Zhou, X. Liu, D. Zhang, Z. Shen, and W. Liu, “Balling phenomena in selective laser melted tungsten,” *J. Mater. Process. Technol.*, vol. 222, pp. 33–42, Aug. 2015, doi: 10.1016/j.jmatprotec.2015.02.032.

[204] C. Atwood *et al.*, “Laser Engineered Net Shaping (lens(tm)): A Tool for Direct Fabrication of Metal Parts,” Sandia National Laboratories, Albuquerque, NM, and, Livermore, CA, SAND98-2473C, Nov. 1998. Accessed: Apr. 19, 2017. [Online]. Available: https://www.osti.gov/scitech/biblio/1549.

[205] M. L. Griffith *et al.*, “Free Form Fabrication of Metallic Components Using Laser Engineered Net Shaping (LENS),” *Proc. 7th Solid Free. Fabr. Symp.*, pp. 125–132, 1996, doi: 10.4028/www.scientific.net/AMR.15-17.175.

[206] A. Bandyopadhyay, B. V. Krishna, W. Xue, and S. Bose, “Application of Laser Engineered Net Shaping (LENS) to manufacture porous and functionally graded structures for load bearing implants,” *J. Mater. Sci. Mater. Med.*, vol. 20, no. S1, pp. 29–34, Dec. 2009, doi: 10.1007/s10856-008-3478-2.

[207] R. Banerjee, C. A. Brice, S. Banerjee, and H. L. Fraser, “Microstructural evolution in laser deposited Ni–25at.% Mo alloy,” *Mater. Sci. Eng. A*, vol. 347, no. 1, pp. 1–4, Apr. 2003, doi: 10.1016/S0921-5093(02)00603-2.

[208] R. Banerjee, P. C. Collins, A. Genç, and H. L. Fraser, “Direct laser deposition of in situ Ti–6Al–4V–TiB composites,” *Mater. Sci. Eng. A*, vol. 358, no. 1–2, pp. 343–349, Oct. 2003, doi: 10.1016/S0921-5093(03)00299-5.

[209] K. I. Schwendner, R. Banerjee, P. C. Collins, C. A. Brice, and H. L. Fraser, “Direct laser deposition of alloys from elemental powder blends,” *Scr. Mater.*, vol. 45, no. 10, pp. 1123–1129, Nov. 2001, doi: 10.1016/S1359-6462(01)01107-1.

[210] D. Keicher, J. W. Sears, J. E. Smugeresky, and Metal Powder Industries Federation, Eds., *Metal powder deposition for rapid manufacturing: proceedings of the 2002 International Conference on Metal Powder Deposition for Rapid Manufacturing sponsored by the Metal Powder Industries Federation in cooperation with the Laser Institute of America (LIA) and APMI International*. Princeton, NJ: Metal Powder Industries Federation, 2002.

[211] B. Zheng *et al.*, “The Influence of Ni-Coated TiC on Laser-Deposited IN625 Metal Matrix Composites,” *Metall. Mater. Trans. A*, vol. 41, no. 3, pp. 568–573, Mar. 2010, doi: 10.1007/s11661-009-0126-5.

[212] T. Gualtieri and A. Bandyopadhyay, “Niobium carbide compostie coatings on SS304 using laser engineered net shaping (LENS^{TM}),” *Mater. Lett.*, vol. 189, pp. 89–92, Feb. 2017, doi: 10.1016/j.matlet.2016.11.071.

[213] B. Onuike, B. Heer, and A. Bandyopadhyay, “Additive manufacturing of Inconel 718—Copper alloy bimetallic structure using laser engineered net shaping (LENS^{TM}),” *Addit. Manuf.*, vol. 21, pp. 133–140, May 2018, doi: 10.1016/j.addma.2018.02.007.

[214] L. Li, “Repair of directionally solidified superalloy GTD-111 by laser-engineered net shaping,” *J. Mater. Sci.*, vol. 41, no. 23, pp. 7886–7893, Dec. 2006, doi: 10.1007/s10853-006-0948-0.

[215] P. S. Korinko, T. M. Adams, S. H. Malene, D. Gill, and J. Smugeresky, “Laser Engineered Net Shaping® for Repair and Hydrogen Compatibility,” p. 12.

[216] I. Palčič, M. Balažic, M. Milfelner, and B. Buchmeister, “Potential of Laser Engineered Net Shaping (LENS) Technology,” *Mater. Manuf. Process.*, vol. 24, no. 7–8, pp. 750–753, May 2009, doi: 10.1080/10426910902809776.

[217] Z. Liu *et al.*, “Feasibility Exploration of Superalloys for AISI 4140 Steel Repairing using Laser Engineered Net Shaping,” *Procedia Manuf.*, vol. 10, pp. 912–922, Jan. 2017, doi: 10.1016/j.promfg.2017.07.080.

[218] C. J. Atwood, J. E. (Sandia N. L. Smugeresky, and D. D. Gill, “Laser engineered net shaping (LENS) for the repair and modification of NWC metal components.,” Sandia National Laboratories, SAND2006-6551, Nov. 2006. doi: 10.2172/901971.

[219] M. Das, V. K. Balla, T. S. S. Kumar, and I. Manna, “Fabrication of Biomedical Implants using Laser Engineered Net Shaping (LENS^{TM}),” *Trans. Indian Ceram. Soc.*, vol. 72, no. 3, pp. 169–174, Sep. 2013, doi: 10.1080/0371750X.2013.851619.

[220] W. W. Wits, J. R. R. García, and J. M. J. Becker, “How Additive Manufacturing Enables more Sustainable End-user Maintenance, Repair and Overhaul (MRO) Strategies,” *Procedia CIRP*, vol. 40, pp. 693–698, 2016, doi: 10.1016/j.procir.2016.01.156.

[221] G. D. Janaki Ram, C. K. Esplin, and B. E. Stucker, “Microstructure and wear properties of LENS® deposited medical grade CoCrMo,” *J. Mater. Sci. Mater. Med.*, vol. 19, no. 5, pp. 2105–2111, May 2008, doi: 10.1007/s10856-007-3078-6.

[222] M. Ziętala *et al.*, “The microstructure, mechanical properties and corrosion resistance of 316L stainless steel fabricated using laser engineered net shaping,” *Mater. Sci. Eng. A*, vol. 677, pp. 1–10, Nov. 2016, doi: 10.1016/j.msea.2016.09.028.

[223] B. Vamsi Krishna, W. Xue, S. Bose, and A. Bandyopadhyay, “Engineered porous metals for implants,” *JOM*, vol. 60, no. 5, pp. 45–48, May 2008, doi: 10.1007/s11837-008-0059-2.

[224] F. A. España, V. K. Balla, S. Bose, and A. Bandyopadhyay, “Design and fabrication of CoCrMo alloy based novel structures for load bearing implants using laser engineered net shaping,” *Mater. Sci. Eng. C*, vol. 30, no. 1, pp. 50–57, Jan. 2010, doi: 10.1016/j.msec.2009.08.006.

[225] M. Buciumeanu, A. Bagheri, N. Shamsaei, S. M. Thompson, F. S. Silva, and B. Henriques, “Tribocorrosion behavior of additive manufactured Ti-6Al-4V biomedical alloy,” *Tribol. Int.*, vol. 119, pp. 381–388, Mar. 2018, doi: 10.1016/j.triboint.2017.11.032.

[226] “Laser Engineered Net Shaping Advances Additive Manufacturing and Repair.” http://www.rpm-innovations.com/laser_deposition_technology_advances_additive_manufacturing_and_repair (accessed Apr. 19, 2017).

[227] “Additive Manufacturing Laboratory | LPD,” *Additive Manufacturing Laboratory*. http://www.additivemanufacturinglaboratory.com/laser-powder-deposition (accessed Sep. 11, 2017).

[228] Sandia National Laboratories, “Laser Engineering Net Shaping.” Oct. 06, 2017, [Online]. Available: http://www.sandia.gov/ms.

[229] Advertorial, “About the NSTF-South 32 Awards trophy,” *The M&G Online*. https://mg.co.za/article/2016-07-01-00-about-the-nstf-south-32-awards-trophy/ (accessed Aug. 11, 2017).

[230] “Laser Metal Deposition | TWI Additive Manufacturing.” http://www.twiadditivemanufacturing.com/capabilities/metal-processing/laser-metal-deposition/ (accessed Aug. 10, 2017).

[231] E. Toyserkani and A. Khajepour, “A mechatronics approach to laser powder deposition process,” *Mechatronics*, vol. 16, no. 10, pp. 631–641, Dec. 2006, doi: 10.1016/j.mechatronics.2006.05.002.

[232] E. Abouda *et al.*, “Effect of Laser Cladding Parameters on the Microstructure and Properties of High Chromium Hardfacing Alloys,” *Phys. Procedia*, vol. 83, pp. 684–696, Jan. 2016, doi: 10.1016/j.phpro.2016.08.070.

[233] N. Fangyong, M. Guangyi, C. Dongsheng, Z. Siyu, and W. Dongjiang, “Influences of Process Parameters on Deposition Width in Laser Engineered Net Shaping,” p. 9.

[234] Z. Wang, T. A. Palmer, and A. M. Beese, “Effect of processing parameters on microstructure and tensile properties of austenitic stainless steel 304L made by directed energy deposition additive manufacturing,” *Acta Mater.*, vol. 110, pp. 226–235, May 2016, doi: 10.1016/j.actamat.2016.03.019.

[235] A. Simchi and H. Pohl, “Effects of laser sintering processing parameters on the microstructure and densification of iron powder,” *Mater. Sci. Eng. A*, vol. 359, no. 1, pp. 119–128, Oct. 2003, doi: 10.1016/S0921-5093(03)00341-1.

[236] P. Balu, S. Hamid, and R. Kovacevic, “Finite element modeling of heat transfer in single and multilayered deposits of Ni-WC produced by the laser-based powder deposition process,” *Int. J. Adv. Manuf. Technol.*, vol. 68, no. 1–4, pp. 85–98, Sep. 2013, doi: 10.1007/s00170-012-4710-2.

[237] H. Shen and C. J. Lissenden, “3D finite element analysis of particle-reinforced aluminum,” *Mater. Sci. Eng. A*, vol. 338, no. 1, pp. 271–281, Dec. 2002, doi: 10.1016/S0921-5093(02)00094-1.

[238] Y. W. Yan, L. Geng, and A. B. Li, “Finite element analysis about effects of particle size on the residual stress of the particle reinforced metal matrix,” *Compos T Nonferr Met. Soc*, vol. 16, pp. 1346–1350, 2006.

[239] Y. Xiong, W. H. Hofmeister, Z. Cheng, J. E. Smugeresky, E. J. Lavernia, and J. M. Schoenung, “In situ thermal imaging and three-dimensional finite element modeling of tungsten carbide–cobalt during laser deposition,” *Acta Mater.*, vol. 57, no. 18, pp. 5419–5429, Oct. 2009, doi: 10.1016/j.actamat.2009.07.038.

[240] G. Vastola, G. Zhang, Q. X. Pei, and Y.-W. Zhang, “Controlling of residual stress in additive manufacturing of Ti6Al4V by finite element modeling,” *Addit. Manuf.*, vol. 12, pp. 231–239, Oct. 2016, doi: 10.1016/j.addma.2016.05.010.

[241] M. H. Farshidianfar, A. Khajepour, and A. P. Gerlich, “Effect of real-time cooling rate on microstructure in Laser Additive Manufacturing,” *J. Mater. Process. Technol.*, vol. 231, pp. 468–478, May 2016, doi: 10.1016/j.jmatprotec.2016.01.017.

[242] W. J. Sames, F. A. List, S. Pannala, R. R. Dehoff, and S. S. Babu, “The metallurgy and processing science of metal additive manufacturing,” *Int. Mater. Rev.*, vol. 61, no. 5, pp. 315–360, Jul. 2016, doi: 10.1080/09506608.2015.1116649.

[243] P. c. Collins, D. a. Brice, P. Samimi, I. Ghamarian, and H. l. Fraser, “Microstructural Control of Additively Manufactured Metallic Materials,” *Annu. Rev. Mater. Res.*, vol. 46, no. 1, pp. 63–91, Jul. 2016, doi: 10.1146/annurev-matsci-070115-031816.

[244] D. Gu, Y. Shen, and X. Wu, “Formation of a novel W-rim/Cu-core structure during direct laser sintering of W–Cu composite system,” *Mater. Lett.*, vol. 62, no. 12, pp. 1765–1768, Apr. 2008, doi: 10.1016/j.matlet.2007.09.087.

[245] D. D. Gu and Y. F. Shen, “Influence of phosphorus element on direct laser sintering of multicomponent Cu-based metal powder,” *Metall. Mater. Trans. B Process Metall. Mater. Process. Sci.*, vol. 37, no. 6, pp. 967–977, 2006, doi: 10.1007/BF02735019.

[246] J. L. Johnson, J. J. Brezovsky, and R. M. German, “Effect of liquid content on distortion and rearrangement densification of liquid-phase-sintered W-Cu,” *Metall. Mater. Trans. A*, vol. 36, no. 6, pp. 1557–1565, Jun. 2005, doi: 10.1007/s11661-005-0247-4.

[247] J. L. Johnson, J. J. Brezovsky, and R. M. German, “Effects of tungsten particle size and copper content on densification of liquid-phase-sintered W-Cu,” *Metall. Mater. Trans. A*, vol. 36, no. 10, pp. 2807–2814, Oct. 2005, doi: 10.1007/s11661-005-0277-y.

[248] D. Gu and Y. Shen, “Influence of reinforcement weight fraction on microstructure and properties of submicron WC–Cop/Cu bulk MMCs prepared by direct laser sintering,” *J. Alloys Compd.*, vol. 431, no. 1, pp. 112–120, Apr. 2007, doi: 10.1016/j.jallcom.2006.05.044.

[249] A. Simchi and H. Pohl, “Direct laser sintering of iron–graphite powder mixture,” *Mater. Sci. Eng. A*, vol. 383, no. 2, pp. 191–200, Oct. 2004, doi: 10.1016/j.msea.2004.05.070.

[250] H. Yin and T. Emi, “Marangoni flow at the gas/melt interface of steel,” *Metall. Mater. Trans. B*, vol. 34, no. 5, pp. 483–493, Oct. 2003, doi: 10.1007/s11663-003-0015-z.

[251] C. R. HEIPLE, “Mechanism for minor element effect on GTA fusion zone geometry,” *Weld. J.*, vol. 61, no. 4, pp. 97s–102s, 1982.

[252] C. R. Heiple, J. R. Roper, R. T. Stagner, and R. J. Aden, “Surface Active Element Effects on the Shape of GTA, Laser, and Electron Beam Welds,” p. 6.

[253] “CHAN: A MODEL FOR FLUID-FLOW IN LASER MELTED POOLS - Google Scholar.” https://0-scholar-google-com.innopac.wits.ac.za/scholar_lookup?author=C.%20Chan&author=J.%20Mazumder&author=MM.%20Chen&journal=J.%20Met.&volume=35&pages=49&publication_year=1983 (accessed Sep. 11, 2019).

[254] S. Kou and Y. H. Wang, “Three-dimensional convection in laser melted pools,” *Metall. Trans. A*, vol. 17, no. 12, pp. 2265–2270, Dec. 1986, doi: 10.1007/BF02645924.

[255] E. D. Hondros *et al.*, “Marangoni effects in welding,” *Philos. Trans. R. Soc. Lond. Ser. Math. Phys. Eng. Sci.*, vol. 356, no. 1739, pp. 911–925, Apr. 1998, doi: 10.1098/rsta.1998.0196.

[256] H. J. Niu and I. T. H. Chang, “Selective laser sintering of gas and water atomized high speed steel powders,” 1999, doi: 10.1016/s1359-6462(99)00089-5.

[257] L. A. Anestiev and L. Froyen, “Model of the primary rearrangement processes at liquid phase sintering and selective laser sintering due to biparticle interactions,” *J. Appl. Phys.*, vol. 86, no. 7, pp. 4008–4017, 1999, doi: 10.1063/1.371321.

[258] S. A. David, S. S. Babu, and J. M. Vitek, “Welding: Solidification and microstructure,” *JOM*, vol. 55, no. 6, pp. 14–20, Jun. 2003, doi: 10.1007/s11837-003-0134-7.

[259] “Welding Metallurgy, 2nd Edition | Metals & Alloys | General & Introductory Materials Science | Subjects | Wiley,” *Wiley.com*. https://www.wiley.com/en-us/Welding+Metallurgy%2C+2nd+Edition-p-9780471434917 (accessed Sep. 11, 2019).

[260] “Cu 70, Ni 30 (wt%), cored dendrites,” Jan. 01, 1970. http://core.materials.ac.uk/search/detail.php?id=1074 (accessed Jan. 28, 2019).

[261] D. Janicki and M. Musztyfaga-Staszuk, “Direct Diode Laser Cladding of Inconel 625/WC Composite Coatings,” *Stroj. Vestn. - J. Mech. Eng.*, vol. 62, no. 6, pp. 363–372, Jun. 2016, doi: 10.5545/sv-jme.2015.3194.

[262] Q. Shi, D. Gu, M. Xia, S. Cao, and T. Rong, “Effects of laser processing parameters on thermal behavior and melting/solidification mechanism during selective laser melting of TiC/Inconel 718 composites,” *Opt. Laser Technol.*, vol. 84, pp. 9–22, Oct. 2016, doi: 10.1016/j.optlastec.2016.04.009.

[263] T. Rong, D. Gu, Q. Shi, S. Cao, and M. Xia, “Effects of tailored gradient interface on wear properties of WC/Inconel 718 composites using selective laser melting,” *Surf. Coat. Technol.*, vol. 307, pp. 418–427, Dec. 2016, doi: 10.1016/j.surfcoat.2016.09.011.

[264] P. Farahmand and R. Kovacevic, “An experimental–numerical investigation of heat distribution and stress field in single- and multi-track laser cladding by a high-power direct diode laser,” *Opt. Laser Technol.*, vol. 63, pp. 154–168, Nov. 2014, doi: 10.1016/j.optlastec.2014.04.016.

[265] B. Liu, B.-Q. Li, Z. Li, P. Bai, Y. Wang, and Z. Kuai, “Numerical investigation on heat transfer of multi-laser processing during selective laser melting of AlSi10Mg,” *Results Phys.*, vol. 12, pp. 454–459, Mar. 2019, doi: 10.1016/j.rinp.2018.11.075.

[266] B. Zheng, Y. Zhou, J. E. Smugeresky, J. M. Schoenung, and E. J. Lavernia, “Thermal Behavior and Microstructural Evolution during Laser Deposition with Laser-Engineered Net Shaping: Part I. Numerical Calculations,” *Metall. Mater. Trans. A*, vol. 39, no. 9, pp. 2228–2236, Sep. 2008, doi: 10.1007/s11661-008-9557-7.

[267] G. Shanthos Kumar, S. Saravanan, R. Vetriselvan, and K. Raghukandan, “Numerical and experimental studies on the effect of varied pulse energy in Nd:YAG laser welding of Monel 400 sheets,” *Infrared Phys. Technol.*, vol. 93, pp. 184–191, Sep. 2018, doi: 10.1016/j.infrared.2018.08.002.

[268] W. Tan, N. S. Bailey, and Y. C. Shin, “Numerical modeling of transport phenomena and dendritic growth in laser conduction welding of 304 stainless steel,” 2011, vol. 1, pp. 243–251, doi: 10.1115/MSEC2011-50219.

[269] F. Liravi, R. Darleux, and E. Toyserkani, “Additive manufacturing of 3D structures with non-Newtonian highly viscous fluids: Finite element modeling and experimental validation,” *Addit. Manuf.*, vol. 13, pp. 113–123, Jan. 2017, doi: 10.1016/j.addma.2016.10.008.

[270] M. L. Griffith, L. D. Harwell, T. Romero, E. Schlienger, C. L. Atwood, and J. E. Smugeresky, “Multi-Material Processing by LENS,” pp. 387–394.

[271] H. L. Fraser, “Direct laser deposition of in situ Ti Á 6Al Á 4V Á TiB composites,” vol. 358, no. v, pp. 343–349, 2003, doi: 10.1016/S0921-5093(03)00299-5.

[272] K. I. Schwendner, R. Banerjee, P. C. Collins, C. A. Brice, and H. L. Fraser, “Direct laser deposition of alloys from elemental powder blends,” vol. 45, pp. 1123–1129, 2001.

[273] V. K. Balla, P. D. Devasconcellos, and W. Xue, “Fabrication of compositionally and structurally graded Ti – TiO 2 structures using laser engineered net shaping (LENS),” *Acta Biomater.*, vol. 5, no. 5, pp. 1831–1837, 2009, doi: 10.1016/j.actbio.2009.01.011.

[274] W. Liu and J. DuPont, “Fabrication of Titanium Aluminide Matrix Composites by Laser Engineered Net Shaping,” pp. 124–132, 2002.

[275] W. Liu and J. N. Dupont, “Fabrication of functionally graded TiC / Ti composites by Laser Engineered Net Shaping,” vol. 48, pp. 1337–1342, 2003, doi: 10.1016/S1359-6462(03)00020-4.

[276] J. Kummailil, C. Sammarco, D. Skinner, C. A. Brown, and K. Rong, “Effect of Select LENS ^{TM} Processing Parameters on the Deposition of Ti-6Al-4V,” 2005.

[277] X. Wu and J. Mei, “Near net shape manufacturing of components using direct laser fabrication technology,” vol. 135, pp. 266–270, 2003.

[278] F. Authors, “Research on laser engineered net shaping of thick-wall nickel-based alloy parts,” 2009, doi: 10.1108/13552540910925036.

[279] B. Vamsi Krishna, W. Xue, S. Bose, and A. Bandyopadhyay, “Functionally graded Co–Cr–Mo coating on Ti–6Al–4V alloy structures,” *Acta Biomater.*, vol. 4, no. 3, pp. 697–706, May 2008, doi: 10.1016/j.actbio.2007.10.005.

[280] I. Kunce, M. Polanski, K. Karczewski, T. Plocinski, and K. J. Kurzydlowski, “Microstructural characterisation of high-entropy alloy AlCoCrFeNi fabricated by laser engineered net shaping,” *J. Alloys Compd.*, vol. 648, pp. 751–758, Nov. 2015, doi: 10.1016/j.jallcom.2015.05.144.

[281] B. Vamsi Krishna, W. Xue, S. Bose, and A. Bandyopadhyay, “Functionally graded Co–Cr–Mo coating on Ti–6Al–4V alloy structures,” *Acta Biomater.*, vol. 4, no. 3, pp. 697–706, May 2008, doi: 10.1016/j.actbio.2007.10.005.

[282] V. K. Balla, S. Bose, and A. Bandyopadhyay, “Microstructure and wear properties of laser deposited WC – 12 % Co composites,” *Mater. Sci. Eng. A*, vol. 527, no. 24–25, pp. 6677–6682, 2010, doi: 10.1016/j.msea.2010.07.006.

[283] Y. Xiong, M. Kim, O. Seo, J. M. Schoenung, and S. Kang, “(Ti,W)C–Ni cermets by laser engineered net shaping,” *Powder Metall.*, vol. 53, no. 1, pp. 41–46, Mar. 2010, doi: 10.1179/174329009X380581.

[284] Y. Xiong, J. E. Smugeresky, E. J. Lavernia, and J. M. Schoenung, “Processing and microstructure of WC-Co Cermets by Laser Engineered Net Shaping,” 2008.

[285] Y. Xiong, J. E. Smugeresky, and J. M. Schoenung, “Journal of Materials Processing Technology The influence of working distance on laser deposited WC – Co,” vol. 209, pp. 4935–4941, 2009, doi: 10.1016/j.jmatprotec.2009.01.016.

[286] Y. Xiong, W. H. Hofmeister, Z. Cheng, J. E. Smugeresky, E. J. Lavernia, and J. M. Schoenung, “In situ thermal imaging and three-dimensional finite element modeling of tungsten carbide–cobalt during laser deposition,” *Acta Mater.*, vol. 57, no. 18, pp. 5419–5429, Oct. 2009, doi: 10.1016/j.actamat.2009.07.038.

[287] Y. Xiong, K. Lau, X. Zhou, and J. M. Schoenung, “A streamlined life cycle assessment on the fabrication of WC–Co cermets,” *J. Clean. Prod.*, vol. 16, no. 10, pp. 1118–1126, Jul. 2008, doi: 10.1016/j.jclepro.2007.05.007.

[288] “Monel 400, Alloy 400, UNS N04400 - MEGA MEX.” http://megamex.com/monel-400-nickel-alloy.htm (accessed Jun. 27, 2019).

[289] M. R. Rokni, S. R. Nutt, C. A. Widener, V. K. Champagne, and R. H. Hrabe, “Review of Relationship Between Particle Deformation, Coating Microstructure, and Properties in High-Pressure Cold Spray,” *J. Therm. Spray Technol.*, vol. 26, no. 6, pp. 1308–1355, Aug. 2017, doi: 10.1007/s11666-017-0575-0.

[290] I. Baturynska, O. Semeniuta, and K. Martinsen, “Optimization of Process Parameters for Powder Bed Fusion Additive Manufacturing by Combination of Machine Learning and Finite Element Method: A Conceptual Framework,” *Procedia CIRP*, vol. 67, pp. 227–232, Jan. 2018, doi: 10.1016/j.procir.2017.12.204.

[291] A. K. Sood, R. K. Ohdar, and S. S. Mahapatra, “Parametric appraisal of fused deposition modelling process using the grey Taguchi method,” *Proc. Inst. Mech. Eng. Part B J. Eng. Manuf.*, vol. 224, no. 1, pp. 135–145, Jan. 2010, doi: 10.1243/09544054JEM1565.

[292] P. K. Jain, P. M. Pandey, and P. V. M. Rao, “Experimental investigations for improving part strength in selective laser sintering,” *Virtual Phys. Prototyp.*, vol. 3, no. 3, pp. 177–188, Sep. 2008, doi: 10.1080/17452750802065893.

[293] A. K. Singh and R. Srinivasa Prakash, “DOE based three-dimensional finite element analysis for predicting density of a laser-sintered part,” *Rapid Prototyp. J.*, vol. 16, no. 6, pp. 460–467, Jan. 2010, doi: 10.1108/13552541011083380.

[294] S. Thipprakmas and W. Phanitwong, “Process parameter design of spring-back and spring-go in V-bending process using Taguchi technique,” *Mater. Des.*, vol. 32, no. 8, pp. 4430–4436, Sep. 2011, doi: 10.1016/j.matdes.2011.03.069.

[295] P. J. Blau, *Microindentation Techniques in Materials Science and Engineering: A Symposium Sponsored by ASTM Committee E-4 on Metallography and by the International Metallographic Society, Philadelphia, PA, 15-18 July 1984*. ASTM International, 1986.

[296] Y. Li, Y. Hu, W. Cong, L. Zhi, and Z. Guo, “Additive manufacturing of alumina using laser engineered net shaping: Effects of deposition variables,” *Ceram. Int.*, vol. 43, no. 10, pp. 7768–7775, Jul. 2017, doi: 10.1016/j.ceramint.2017.03.085.

[297] Z. Liu, H. Kim, W. Liu, W. Cong, Q. Jiang, and H. Zhang, “Influence of energy density on macro/micro structures and mechanical properties of as-deposited Inconel 718 parts fabricated by laser engineered net shaping,” *J. Manuf. Process.*, vol. 42, pp. 96–105, Jun. 2019, doi: 10.1016/j.jmapro.2019.04.020.

[298] Z. Balak, M. Zakeri, M. Rahimipour, and E. Salahi, “Taguchi design and hardness optimization of ZrB2-based composites reinforced with chopped carbon fiber and different additives and prepared by SPS,” *J. Alloys Compd.*, vol. 639, pp. 617–625, Aug. 2015, doi: 10.1016/j.jallcom.2015.03.131.

[299] Y. Liu *et al.*, “Optimization of parameters in laser powder deposition AlSi10Mg alloy using Taguchi method,” *Opt. Laser Technol.*, vol. 111, pp. 470–480, Apr. 2019, doi: 10.1016/j.optlastec.2018.10.030.

[300] Z. Fan *et al.*, “Nanostructured Al2O3-YAG-ZrO2 ternary eutectic components prepared by laser engineered net shaping,” *Acta Mater.*, vol. 170, pp. 24–37, May 2019, doi: 10.1016/j.actamat.2019.03.020.

[301] B. Scibilia, “How Taguchi Designs Differ from Factorial Designs.” https://blog.minitab.com/blog/applying-statistics-in-quality-projects/how-taguchi-designs-differ-from-factorial-designs (accessed Apr. 12, 2020).

[302] Y. Xiong, J. E. Smugeresky, and J. M. Schoenung, “The influence of working distance on laser deposited WC–Co,” *J. Mater. Process. Technol.*, vol. 209, no. 10, pp. 4935–4941, Jun. 2009, doi: 10.1016/j.jmatprotec.2009.01.016.

[303] T. Amine, J. W. Newkirk, and F. Liou, “Investigation of effect of process parameters on multilayer builds by direct metal deposition,” *Appl. Therm. Eng.*, vol. 73, no. 1, pp. 500–511, Dec. 2014, doi: 10.1016/j.applthermaleng.2014.08.005.

[304] Y. Xiong, J. E. Smugeresky, L. Ajdelsztajn, and J. M. Schoenung, “Fabrication of WC–Co cermets by laser engineered net shaping,” *Mater. Sci. Eng. A*, vol. 493, no. 1, pp. 261–266, Oct. 2008, doi: 10.1016/j.msea.2007.05.125.

[305] Y. Xiong, J. E. Smugeresky, E. J. Lavernia, and J. M. Schoenung, “PROCESSING AND MICROSTRUCTURE OF WC-CO CERMETS BY LASER ENGINEERED NET SHAPING,” Accessed: Apr. 06, 2017. [Online]. Available: http://edge.rit.edu/edge/P10551/public/SFF/SFF%202008%20Proceedings/Manuscripts/2008-12-Xiong.pdf.

[306] “ISO 3878 : 1983(R2015) | HARDMETALS - VICKERS HARDNESS... | SAI Global.” https://infostore.saiglobal.com/en-gb/standards/iso-3878-1983-613764_SAIG_ISO_ISO_1408128/ (accessed Mar. 07, 2019).

[307] “Theory of hardness testing.” https://www.emcotest.com/en/the-world-of-hardness-testing/hardness-know-how/theory-of-hardness-testing/vickers-52/advantages-and-disadvantages-of-the-vickers-method-240/ (accessed Jun. 14, 2020).

[308] Y. Zhai, D. A. Lados, E. J. Brown, and G. N. Vigilante, “Understanding the microstructure and mechanical properties of Ti-6Al-4V and Inconel 718 alloys manufactured by Laser Engineered Net Shaping,” *Addit. Manuf.*, vol. 27, pp. 334–344, May 2019, doi: 10.1016/j.addma.2019.02.017.

[309] D.-S. Shim, G.-Y. Baek, J.-S. Seo, G.-Y. Shin, K.-P. Kim, and K.-Y. Lee, “Effect of layer thickness setting on deposition characteristics in direct energy deposition (DED) process,” *Opt. Laser Technol.*, vol. 86, pp. 69–78, Dec. 2016, doi: 10.1016/j.optlastec.2016.07.001.

[310] D. Liu, S. Q. Zhang, A. Li, and H. M. Wang, “Microstructure and tensile properties of laser melting deposited TiC/TA15 titanium matrix composites,” *J. Alloys Compd.*, vol. 485, no. 1, pp. 156–162, Oct. 2009, doi: 10.1016/j.jallcom.2009.05.112.

[311] J. I. Arrizubieta, A. Lamikiz, M. Cortina, E. Ukar, and A. Alberdi, “Hardness, grainsize and porosity formation prediction on the Laser Metal Deposition of AISI 304 stainless steel,” *Int. J. Mach. Tools Manuf.*, vol. 135, pp. 53–64, Dec. 2018, doi: 10.1016/j.ijmachtools.2018.08.004.

[312] J.-S. Xu, X.-C. Zhang, F.-Z. Xuan, F.-Q. Tian, Z.-D. Wang, and S.-T. Tu, “Tensile properties and fracture behavior of laser cladded WC/Ni composite coatings with different contents of WC particle studied by in-situ tensile testing,” *Mater. Sci. Eng. A*, vol. 560, pp. 744–751, Jan. 2013, doi: 10.1016/j.msea.2012.10.028.

[313] B. Borges, L. Quintino, R. M. Miranda, and P. Carr, “Imperfections in laser clading with powder and wire fillers,” *Int. J. Adv. Manuf. Technol.*, vol. 50, no. 1, pp. 175–183, Sep. 2010, doi: 10.1007/s00170-009-2480-2.

[314] B. Davoren, N. Sacks, and M. Theron, “Laser engineered net shaping of WC-9.2wt%Ni alloys: A feasibility study,” *Int. J. Refract. Met. Hard Mater.*, vol. 86, p. 105136, Jan. 2020, doi: 10.1016/j.ijrmhm.2019.105136.

[315] “X-ray Powder Diffraction (XRD),” *Techniques*. https://serc.carleton.edu/research_education/geochemsheets/techniques/XRD.html (accessed Jun. 14, 2020).

[316] “Electron probe micro-analyzer (EPMA),” *Techniques*. https://serc.carleton.edu/research_education/geochemsheets/techniques/EPMA.html (accessed Jun. 14, 2020).

[317] “Scanning Electron Microscope - Advantages and Disadvantages in Imaging,” *MicroscopeMaster*. https://www.microscopemaster.com/scanning-electron-microscope.html (accessed Jun. 14, 2020).

[318] Tzontonel, “Advantages and disadvantages of Raman Spectroscopy,” *Romanian Database of Raman Spectroscopy*, Apr. 19, 2017. http://www.rdrs.ro/blog/articles/advantages-disadvantages-raman-spectroscopy/ (accessed Jun. 14, 2020).

[319] Y. Huang *et al.*, “Rapid prediction of real-time thermal characteristics, solidification parameters and microstructure in laser directed energy deposition (powder-fed additive manufacturing),” *J. Mater. Process. Technol.*, vol. 274, p. 116286, Dec. 2019, doi: 10.1016/j.jmatprotec.2019.116286.

[320] S. J. Wolff, S. Lin, E. J. Faierson, W. K. Liu, G. J. Wagner, and J. Cao, “A framework to link localized cooling and properties of directed energy deposition (DED)-processed Ti-6Al-4V,” *Acta Mater.*, vol. 132, pp. 106–117, Jun. 2017, doi: 10.1016/j.actamat.2017.04.027.

[321] “7 Design for Additive Manufacturing (DfAM) Principles.” https://www.cati.com/blog/2018/12/7-design-additive-manufacturing-dfam-principles/ (accessed Apr. 14, 2020).

[322] V. A. Popovich, E. V. Borisov, A. A. Popovich, V. Sh. Sufiiarov, D. V. Masaylo, and L. Alzina, “Functionally graded Inconel 718 processed by additive manufacturing: Crystallographic texture, anisotropy of microstructure and mechanical properties,” *Mater. Des.*, vol. 114, pp. 441–449, Jan. 2017, doi: 10.1016/j.matdes.2016.10.075.

[323] Y. Huang, M. B. Khamesee, and E. Toyserkani, “A new physics-based model for laser directed energy deposition (powder-fed additive manufacturing): From single-track to multi-track and multi-layer,” *Opt. Laser Technol.*, vol. 109, pp. 584–599, Jan. 2019, doi: 10.1016/j.optlastec.2018.08.015.

[324] T. Bhardwaj, M. Shukla, C. P. Paul, and K. S. Bindra, “Direct Energy Deposition - Laser Additive Manufacturing of Titanium-Molybdenum alloy: Parametric studies, microstructure and mechanical properties,” *J. Alloys Compd.*, vol. 787, pp. 1238–1248, May 2019, doi: 10.1016/j.jallcom.2019.02.121.

[325] A. N. Jinoop, C. P. Paul, S. K. Mishra, and K. S. Bindra, “Laser Additive Manufacturing using directed energy deposition of Inconel-718 wall structures with tailored characteristics,” *Vacuum*, vol. 166, pp. 270–278, Aug. 2019, doi: 10.1016/j.vacuum.2019.05.027.

[326] B. Graf, S. Ammer, A. Gumenyuk, and M. Rethmeier, “Design of Experiments for Laser Metal Deposition in Maintenance, Repair and Overhaul Applications,” *Procedia CIRP*, vol. 11, pp. 245–248, Jan. 2013, doi: 10.1016/j.procir.2013.07.031.

[327] K. Karczewski, M. Dąbrowska, M. Ziętala, and M. Polański, “Fe-Al thin walls manufactured by Laser Engineered Net Shaping,” *J. Alloys Compd.*, vol. 696, pp. 1105–1112, Mar. 2017, doi: 10.1016/j.jallcom.2016.12.034.

[328] M. Alimardani, V. Fallah, A. Khajepour, and E. Toyserkani, “The effect of localized dynamic surface preheating in laser cladding of Stellite 1,” *Surf. Coat. Technol.*, vol. 204, no. 23, pp. 3911–3919, Aug. 2010, doi: 10.1016/j.surfcoat.2010.05.009.

[329] J. M. Amado, M. J. Tobar, A. Yáñez, V. Amigó, and J. J. Candel, “Crack Free Tungsten Carbide Reinforced Ni(Cr) Layers obtained by Laser Cladding,” *Phys. Procedia*, vol. 12, pp. 338–344, 2011, doi: 10.1016/j.phpro.2011.03.043.

[330] P. Farahmand, S. Liu, Z. Zhang, and R. Kovacevic, “Laser cladding assisted by induction heating of Ni–WC composite enhanced by nano-WC and La2O3,” *Ceram. Int.*, vol. 40, no. 10, Part A, pp. 15421–15438, Dec. 2014, doi: 10.1016/j.ceramint.2014.06.097.

[331] L. Meng *et al.*, “A comparison of microstructure and mechanical properties of laser cladding and laser-induction hybrid cladding coatings on full-scale rail,” *Mater. Sci. Eng. A*, vol. 748, pp. 1–15, Mar. 2019, doi: 10.1016/j.msea.2019.01.068.

[332] D. Wang, Q. Hu, and X. Zeng, “Influences of parameters on microstructures and mechanical properties of Cr13Ni5Si2 based composite coating by laser-induction hybrid cladding,” *Surf. Coat. Technol.*, vol. 280, pp. 359–369, Oct. 2015, doi: 10.1016/j.surfcoat.2015.09.029.

[333] M. Ansari, A. Mohamadizadeh, Y. Huang, V. Paserin, and E. Toyserkani, “Laser directed energy deposition of water-atomized iron powder: Process optimization and microstructure of single-tracks,” *Opt. Laser Technol.*, vol. 112, pp. 485–493, Apr. 2019, doi: 10.1016/j.optlastec.2018.11.054.

[334] C. P. Paul, A. Jain, P. Ganesh, J. Negi, and A. K. Nath, “Laser rapid manufacturing of Colmonoy-6 components,” *Opt. Lasers Eng.*, vol. 44, no. 10, pp. 1096–1109, Oct. 2006, doi: 10.1016/j.optlaseng.2005.08.005.

[335] J. Kummailil, C. Sammarco, D. Skinner, C. A. Brown, and K. Rong, “Effect of Select LENS™ Processing Parameters on the Deposition of Ti-6Al-4V,” *J.*

Manuf. Process., vol. 7, no. 1, pp. 42–50, Jan. 2005, doi: 10.1016/S1526-6125(05)70080-3.

[336] C. Zhou, S. Zhao, Y. Wang, F. Liu, W. Gao, and X. Lin, “Mitigation of pores generation at overlapping zone during laser cladding,” *J. Mater. Process. Technol.*, vol. 216, pp. 369–374, Feb. 2015, doi: 10.1016/j.jmatprotec.2014.09.025.

[337] A. Di Schino, I. Salvatori, and J. M. Kenny, “Effects of martensite formation and austenite reversion on grain refining of AISI 304 stainless steel,” *J. Mater. Sci.*, vol. 37, no. 21, pp. 4561–4565, 2002, doi: 10.1023/A:1020631912685.

[338] J. Kim *et al.*, “Effect of beam size in laser welding of ultra-thin stainless steel foils,” *J. Mater. Process. Technol.*, vol. 233, pp. 125–134, Jul. 2016, doi: 10.1016/j.jmatprotec.2016.02.019.

[339] N. Abe, Y. Funada, and M. Ishide, “Micro-welding of thin foil with direct diode laser,” in *Fourth International Symposium on Laser Precision Microfabrication*, Nov. 2003, vol. 5063, pp. 287–292, doi: 10.1117/12.540554.

[340] T. Kresse, D. Meinhard, T. Bernthaler, and G. Schneider, “Hardness of WC-Co hard metals: Preparation, quantitative microstructure analysis, structure-property relationship and modelling,” *Int. J. Refract. Met. Hard Mater.*, vol. 75, pp. 287–293, Sep. 2018, doi: 10.1016/j.ijrmhm.2018.05.003.

[341] L. A. Hanner, J. J. Pittari, and J. J. Swab, “Dynamic hardness of cemented tungsten carbides,” *Int. J. Refract. Met. Hard Mater.*, vol. 75, pp. 294–298, Sep. 2018, doi: 10.1016/j.ijrmhm.2018.05.007.

[342] S. S. Nayak, V. H. Baltazar Hernandez, Y. Okita, and Y. Zhou, “Microstructure–hardness relationship in the fusion zone of TRIP steel welds,” *Mater. Sci. Eng. A*, vol. 551, pp. 73–81, Aug. 2012, doi: 10.1016/j.msea.2012.04.096.

[343] Z. Lei, J. Bi, Y. Chen, X. Chen, X. Qin, and Z. Tian, “Effect of energy density on formability, microstructure and micro-hardness of selective laser melted Sc- and Zr- modified 7075 aluminum alloy,” *Powder Technol.*, vol. 356, pp. 594–606, Nov. 2019, doi: 10.1016/j.powtec.2019.08.082.

[344] A. Wiengmoon, J. T. H. Pearce, and T. Chairuangsri, “Relationship between microstructure, hardness and corrosion resistance in 20wt.%Cr, 27wt.%Cr and 36wt.%Cr high chromium cast irons,” *Mater. Chem. Phys.*, vol. 125, no. 3, pp. 739–748, Feb. 2011, doi: 10.1016/j.matchemphys.2010.09.064.

[345] S. S. Nayak, R. Anumolu, R. D. K. Misra, K. H. Kim, and D. L. Lee, “Microstructure–hardness relationship in quenched and partitioned medium-carbon and high-carbon steels containing silicon,” *Mater. Sci. Eng. A*, vol. 498, no. 1, pp. 442–456, Dec. 2008, doi: 10.1016/j.msea.2008.08.028.

[346] M. Ghasri-Khouzani *et al.*, “Comparing microstructure and hardness of direct metal laser sintered AlSi10Mg alloy between different planes,” *J. Manuf. Process.*, vol. 37, pp. 274–280, Jan. 2019, doi: 10.1016/j.jmapro.2018.12.005.

[347] Z. Wang *et al.*, “Influence of laser surface remelting on microstructure and degradation mechanism in simulated body fluid of Zn-0.5Zr alloy,” *J. Mater. Sci. Technol.*, vol. 35, no. 11, pp. 2705–2713, Nov. 2019, doi: 10.1016/j.jmst.2019.05.019.

[348] Z. Wang, Q. Zhang, P. Guo, X. Gao, L. Yang, and Z. Song, “Effects of laser surface remelting on microstructure and properties of biodegradable Zn-Zr alloy,” *Mater. Lett.*, vol. 226, pp. 52–54, Sep. 2018, doi: 10.1016/j.matlet.2018.04.112.

[349] B. Richter, S. Chen, J. D. Morrow, K. Sridharan, M. Eriten, and F. E. Pfefferkorn, “Pulsed laser remelting of A384 aluminum, part II: Modeling of surface homogenization and topographical effects,” *J. Manuf. Process.*, vol. 32, pp. 230–240, Apr. 2018, doi: 10.1016/j.jmapro.2018.02.009.

[350] J. Vaithilingam, R. D. Goodridge, R. J. M. Hague, S. D. R. Christie, and S. Edmondson, “The effect of laser remelting on the surface chemistry of Ti6al4V components fabricated by selective laser melting,” *J. Mater. Process. Technol.*, vol. 232, pp. 1–8, Jun. 2016, doi: 10.1016/j.jmatprotec.2016.01.022.

[351] Z. Wu, W. Wang, X. Li, M. Yan, and Y. Li, “Microstructure and mechanical properties of Ti-6Al-4V prepared by nickel preplating and electron beam surface remelting,” *J. Mater. Process. Technol.*, vol. 271, pp. 420–428, Sep. 2019, doi: 10.1016/j.jmatprotec.2019.04.017.

[352] C. Cui, F. Ye, and G. Song, “Laser surface remelting of Fe-based alloy coatings deposited by HVOF,” *Surf. Coat. Technol.*, vol. 206, no. 8–9, pp. 2388–2395, Jan. 2012, doi: 10.1016/j.surfcoat.2011.10.038.

[353] E. Hosseini and V. A. Popovich, “A review of mechanical properties of additively manufactured Inconel 718,” *Addit. Manuf.*, vol. 30, p. 100877, Dec. 2019, doi: 10.1016/j.addma.2019.100877.

[354] O. O. Marenych, D. Ding, Z. Pan, A. G. Kostryzhev, H. Li, and S. van Duin, “Effect of chemical composition on microstructure, strength and wear resistance of wire deposited Ni-Cu alloys,” *Addit. Manuf.*, vol. 24, pp. 30–36, Dec. 2018, doi: 10.1016/j.addma.2018.08.003.

[355] S. D. Guest, A. P. Gerlich, and P. F. Mendez, “Depositing Ni-WC wear resistant coatings with hot-wire assisted GTAW,” p. 15.

[356] M. Khechba, F. Hanini, and R. Halimi, “Study of structural and mechanical properties of tungsten carbides coatings,” p. 3.

[357] E. Zeiler, S. Schwarz, S. M. Rosiwal, and R. F. Singer, “Structural changes of tungsten heating filaments during CVD of diamond,” *Mater. Sci. Eng. A*, vol. 335, no. 1, pp. 236–245, Sep. 2002, doi: 10.1016/S0921-5093(01)01933-5.

[358] A. Mukhopadhyay and B. Basu, “Recent developments on WC-based bulk composites,” *J. Mater. Sci.*, vol. 46, no. 3, pp. 571–589, Feb. 2011, doi: 10.1007/s10853-010-5046-7.

[359] R. L. Orban, V. R. Constantinescu, and M. Orban, “Diamond Tools & Ultrahard Materials: Fusion Tungsten Carbide Powder for Matrix of Diamond Drilling Tools,” in *European Congress and Exhibition on Powder Metallurgy. European PM Conference Proceedings; Shrewsbury*, Shrewsbury, United Kingdom, Shrewsbury, 2012, pp. 1–6, Accessed: Sep. 16, 2019. [Online]. Available: http://0.search.proquest.com/docview/1459210920/abstract/368A61BC5F9B4542PQ/1.

[360] H. Cao, W. Ma, H. Chen, Q. Wang, and Y. Wang, “Core-rim microstructure and properties of WC/Ni composites,” *Int. J. Refract. Met. Hard Mater.*, vol. 78, pp. 170–177, Jan. 2019, doi: 10.1016/j.ijrmhm.2018.09.007.

[361] M. Jones and U. Waag, “The influence of carbide dissolution on the erosion–corrosion properties of cast tungsten carbide/Ni-based PTAW overlays,” *Wear*, vol. 271, no. 9, pp. 1314–1324, Jul. 2011, doi: 10.1016/j.wear.2011.01.046.

[362] C. H. Hager, J. Sanders, S. Sharma, A. Voevodin, and A. Segall, “The effect of temperature on gross slip fretting wear of cold-sprayed nickel coatings on Ti6Al4V interfaces,” *Tribol. Int.*, vol. 42, no. 3, pp. 491–502, Mar. 2009, doi: 10.1016/j.triboint.2008.08.009.

[363] S. I. Cha, S. H. Hong, G. H. Ha, and B. K. Kim, “Microstructure and mechanical properties of nanocrystalline WC-10Co cemented carbides,” *Scr. Mater.*, vol. 44, no. 8–9, pp. 1535–1539, May 2001, doi: 10.1016/S1359-6462(01)00835-1.

[364] D. Gu, Q. Shi, K. Lin, and L. Xi, “Microstructure and performance evolution and underlying thermal mechanisms of Ni-based parts fabricated by selective laser melting,” *Addit. Manuf.*, vol. 22, pp. 265–278, Aug. 2018, doi: 10.1016/j.addma.2018.05.019.

[365] “Tungsten Carbide Grade Application Guide by Federal Carbide.” https://www.federalcarbide.com/tungsten_carbide_grade_app_guide.html (accessed Jan. 27, 2019).

[366] Z. Balak, M. Zakeri, M. R. Rahimipur, E. Salahi, and H. Nasiri, “Effect of open porosity on flexural strength and hardness of ZrB2-based composites,” *Ceram. Int.*, vol. 41, no. 7, pp. 8312–8319, Aug. 2015, doi: 10.1016/j.ceramint.2015.02.143.

[367] Q.-W. Huang and L.-H. Zhu, “High-temperature strength and toughness behaviors for reaction-bonded SiC ceramics below 1400 °C,” *Mater. Lett.*, vol. 59, no. 14, pp. 1732–1735, Jun. 2005, doi: 10.1016/j.matlet.2005.01.049.

[368] M. Mabuchi, K. Higashi, and T. G. Langdon, “An investigation of the role of a liquid phase in Al□Cu□Mg metal matrix composites exhibiting high strain rate superplasticity,” *Acta Metall. Mater.*, vol. 42, no. 5, pp. 1739–1745, May 1994, doi: 10.1016/0956-7151(94)90384-0.

[369] X. Rao, F. Zhang, X. Luo, and F. Ding, “Characterization of hardness, elastic modulus and fracture toughness of RB-SiC ceramics at elevated temperature by Vickers test,” *Mater. Sci. Eng. A*, vol. 744, pp. 426–435, Jan. 2019, doi: 10.1016/j.msea.2018.12.044.

[370] C. Jin and K. Plucknett, “The effects of microstructure on Vickers indentation damage in TiC-316L stainless steel cermets,” *Int. J. Refract. Met. Hard Mater.*, vol. 61, pp. 151–161, Dec. 2016, doi: 10.1016/j.ijrmhm.2016.09.006.

[371] C. Lee, H. Park, J. Yoo, C. Lee, W. Woo, and S. Park, “Residual stress and crack initiation in laser clad composite layer with Co-based alloy and WC+NiCr,” *Appl. Surf. Sci.*, vol. 345, pp. 286–294, Aug. 2015, doi: 10.1016/j.apsusc.2015.03.168.

[372] Q. Yang *et al.*, “Fabrication and mechanical properties of WC-10Co cemented carbides with plate-like WC grains,” *J. Alloys Compd.*, vol. 803, pp. 860–865, Sep. 2019, doi: 10.1016/j.jallcom.2019.06.328.

[373] T. Dash and B. B. Nayak, “Preparation of WC–W2C composites by arc plasma melting and their characterisations,” *Ceram. Int.*, vol. 39, no. 3, pp. 3279–3292, Apr. 2013, doi: 10.1016/j.ceramint.2012.10.016.

[374] A. S. Kurlov and A. I. Gusev, “Phase equilibria in the W–C system and tungsten carbides,” *Russ. Chem. Rev.*, vol. 75, no. 7, pp. 617–636, Jul. 2006, doi: 10.1070/RC2006v075n07ABEH003606.

[375] E. Cazzanelli, C. Vinegoni, G. Mariotto, A. Kuzmin, and J. Purans, “Low-Temperature Polymorphism in Tungsten Trioxide Powders and Its Dependence on Mechanical Treatments,” *J. Solid State Chem.*, vol. 143, no. 1, pp. 24–32, Feb. 1999, doi: 10.1006/jssc.1998.8061.

[376] M. Boulova, N. Rosman, P. Bouvier, and G. Lucazeau, “High-pressure Raman study of microcrystalline WO3 tungsten oxide,” *J. Phys. Condens. Matter*, vol. 14, no. 23, pp. 5849–5863, 2002, doi: 10.1088/0953-8984/14/23/314.

[377] L. da S. Ferreira, K. Graf, and A. Scheid, “Microstructure and Properties of Nickel-based C276 Alloy Coatings by PTA on AISI 316L and API 5L X70 Steel Substrates,” *Mater. Res.*, vol. 18, no. 1, pp. 212–221, Feb. 2015, doi: 10.1590/1516-1439.332914.

[378] I. Yu. Trosnikova and P. I. Loboda, “Influence of Obtaining Conditions on Microstructure, Phase Composition and Properties of Eutectic Alloy of WC-W2C System,” *J. Superhard Mater.*, vol. 41, no. 1, pp. 49–52, Jan. 2019, doi: 10.3103/S1063457619010076.

[379] C. H. Allibert, “Sintering features of cemented carbides WC–Co processed from fine powders,” *Int. J. Refract. Met. Hard Mater.*, vol. 19, no. 1, pp. 53–61, Jan. 2001, doi: 10.1016/S0263-4368(01)00004-X.

[380] K. H. Cho, J. W. Lee, and I. S. Chung, “A study on the formation of anomalous large WC grain and the eta phase,” *Mater. Sci. Eng. A*, vol. 209, no. 1, pp. 298–301, May 1996, doi: 10.1016/0921-5093(95)10104-7.

[381] J. Yang, D.-Y. Kim, and K.-Y. Eun, “FORMATION OF ANOMALOUS LARGE GRAINS IN WC-Co ALLOY OBSERVED BY Co INFILTRATION.,” *Powder Metall. Int.*, vol. 18, no. 2, pp. 62–64, 1986.

[382] E. G. Obbard, S. Luyckx, S. Hamar-Thibault, and C. H. Allibert, “Determination of the composition range suitable to the formation of WC–(V,W)Cx–Co materials,” *Int. J. Refract. Met. Hard Mater.*, vol. 19, no. 4, pp. 349–357, Jul. 2001, doi: 10.1016/S0263-4368(01)00047-6.

[383] O. Lavergne, F. Robaut, F. Hodaj, and C. H. Allibert, “Mechanism of solid-state dissolution of WC in Co-based solutions,” *Acta Mater.*, vol. 50, no. 7, pp. 1683–1692, Apr. 2002, doi: 10.1016/S1359-6454(02)00011-3.

[384] S. Kim, S.-H. Han, J.-K. Park, and H.-E. Kim, “Variation of WC grain shape with carbon content in the WC–Co alloys during liquid-phase sintering,” *Scr. Mater.*, vol. 48, no. 5, pp. 635–639, Mar. 2003, doi: 10.1016/S1359-6462(02)00464-5.

[385] B. Maroli and S. Dizdar, “Effect of Type and Amount of Tungsten Carbides on the Abrasive Wear of Laser Cladded Nickel Based Coatings,” p. 9, 2015.

[386] D. Deng, L. Zhang, T. Niu, H. Liu, and H. Zhang, “Microstructures and Wear Performance of PTAW Deposited Ni-Based Coatings with Spherical Tungsten Carbide,” *Metals*, vol. 5, no. 4, pp. 1984–1996, Oct. 2015, doi: 10.3390/met5041984.

[387] M. J. Zhan, X. D. Du, F. C. Wang, J. W. Lang, and W. Z. Shi, “Effect of rare earth on microstructure and carbides in WC-Fe composite coating,” *Tribol. - Mater. Surf. Interfaces*, vol. 9, no. 3, pp. 137–143, Jul. 2015, doi: 10.1179/1751584X15Y.0000000013.

[388] D. Kesavan and M. Kamaraj, “The microstructure and high temperature wear performance of a nickel base hardfaced coating,” *Surf. Coat. Technol.*, vol. 204, no. 24, pp. 4034–4043, Sep. 2010, doi: 10.1016/j.surfcoat.2010.05.022.

[389] H. Li, W. Tong, J. Cui, H. Zhang, L. Chen, and L. Zuo, “Heat Treatment of Centrifugally Cast High-Vanadium Alloy Steel for High-Pressure Grinding Roller,” *Acta Metall. Sin. Engl. Lett.*, vol. 27, no. 3, pp. 430–435, Jun. 2014, doi: 10.1007/s40195-014-0075-x.

[390] S. Zhou *et al.*, “Effect of laser remelting on microstructure and properties of WC reinforced Fe-based amorphous composite coatings by laser cladding,” *Opt.*

Laser Technol., vol. 103, pp. 8–16, Jul. 2018, doi: 10.1016/j.optlastec.2018.01.024.

[391] V. Ocelík, J. A. Vreeling, J. Th, and M. De Hosson, “Computer Methods and Experimental Measurements for Surface Treatment)Effects,” *Surf. Treat. V*, pp. 151–159, 2001.

[392] Y. Huang, “Characterization of dilution action in laser-induction hybrid cladding,” *Opt. Laser Technol.*, vol. 43, no. 5, pp. 965–973, Jul. 2011, doi: 10.1016/j.optlastec.2010.12.005.

[393] S. Zhou and X. Dai, “Laser induction hybrid rapid cladding of WC particles reinforced NiCrBSi composite coatings,” *Appl. Surf. Sci.*, vol. 256, no. 14, pp. 4708–4714, May 2010, doi: 10.1016/j.apsusc.2010.02.078.

[394] F. Brückner, D. Lepski, and E. Beyer, “Modeling the Influence of Process Parameters and Additional Heat Sources on Residual Stresses in Laser Cladding,” *J. Therm. Spray Technol.*, vol. 16, no. 3, pp. 355–373, Sep. 2007, doi: 10.1007/s11666-007-9026-7.

[395] R. C. Gassmann, “Laser cladding with (WC+W2C)/Co–Cr–C and (WC+W2C)/Ni–B–Si composites for enhanced abrasive wear resistance,” *Mater. Sci. Technol.*, vol. 12, no. 8, pp. 691–696, Aug. 1996, doi: 10.1179/mst.1996.12.8.691.

[396] D. Wang, Q. Hu, Y. Zheng, Y. Xie, and X. Zeng, “Study on deposition rate and laser energy efficiency of Laser-Induction Hybrid Cladding,” *Opt. Laser Technol.*, vol. 77, pp. 16–22, Mar. 2016, doi: 10.1016/j.optlastec.2015.08.019.

[397] S. D. Guest, J. Chapuis, G. Wood, and P. F. Mendez, “Non-wetting behaviour of tungsten carbide powders in nickel weld pool: New loss mechanism in GMAW overlays,” *Sci. Technol. Weld. Join.*, vol. 19, no. 2, pp. 133–141, 2014, doi: 10.1179/1362171813Y.0000000178.

[398] P. A. Carvalho and R. Vilar, “Laser alloying of zinc with aluminum: solidification structures,” *Surf. Coat. Technol.*, vol. 91, no. 3, pp. 158–166, May 1997, doi: 10.1016/S0257-8972(96)03185-4.

[399] J. Cai, K. Wang, X. Zhang, and W. Wang, “Characterization of High Temperature Deformation Behavior of BFe10-1-2 Cupronickel Alloy Using Orthogonal Analysis,” *High Temp. Mater. Process.*, vol. 36, no. 7, Jan. 2017, doi: 10.1515/htmp-2016-0018.

[400] P. Liu, S. Sun, M. Cao, J. Gong, and J. Hu, “Microstructural Evolution and Phase Transformation on the X-Y Surface of Inconel 718 Ni-Based Alloys Fabricated by Selective Laser Melting under Different Heat Treatment,” *High Temp. Mater. Process.*, vol. 38, no. 2019, pp. 229–236, Feb. 2019, doi: 10.1515/htmp-2017-0182.

[401] W. H. Hofmeister, M. Wert, J. Smugeresky, J. A. Philliber, M. Griffith, and M. Ensz, “Investigating Solidification with the Laser-Engineered Net Shaping (LENS) Process,” *JOM*, vol. 51, no. 7, Jul. 1999, Accessed: Jan. 28, 2019. [Online]. Available: https://www.tms.org/pubs/journals/jom/9907/hofmeister/hofmeister-9907.html.

[402] V. Ocelík, I. Furár, and J. Th. M. De Hosson, “Microstructure and properties of laser clad coatings studied by orientation imaging microscopy,” *Acta Mater.*, vol. 58, no. 20, pp. 6763–6772, Dec. 2010, doi: 10.1016/j.actamat.2010.09.002.

[403] A. Shah, A. Kumar, and J. Ramkumar, “Analysis of transient thermo-fluidic behavior of melt pool during spot laser welding of 304 stainless-steel,” *J. Mater. Process. Technol.*, vol. 256, pp. 109–120, Jun. 2018, doi: 10.1016/j.jmatprotec.2018.02.005.

[404] P. B. Kadolkar, T. R. Watkins, J. Th. M. De Hosson, B. J. Kooi, and N. B. Dahotre, “State of residual stress in laser-deposited ceramic composite coatings on aluminum alloys,” *Acta Mater.*, vol. 55, no. 4, pp. 1203–1214, Feb. 2007, doi: 10.1016/j.actamat.2006.07.049.

[405] D. Liu, Y. Chen, L. Li, and F. Li, “In situ investigation of fracture behavior in monocrystalline WCp-reinforced Ti–6Al–4V metal matrix composites produced by laser melt injection,” *Scr. Mater.*, vol. 59, no. 1, pp. 91–94, Jul. 2008, doi: 10.1016/j.scriptamat.2008.02.033.

[406] L. Li, D. Liu, Y. Chen, C. Wang, and F. Li, “Electron microscopy study of reaction layers between single-crystal WC particle and Ti–6Al–4V after laser melt injection,” *Acta Mater.*, vol. 57, no. 12, pp. 3606–3614, Jul. 2009, doi: 10.1016/j.actamat.2009.04.021.

[407] L. Babout, Y. Brechet, E. Maire, and R. Fougères, “On the competition between particle fracture and particle decohesion in metal matrix composites,” *Acta Mater.*, vol. 52, no. 15, pp. 4517–4525, Sep. 2004, doi: 10.1016/j.actamat.2004.06.009.

[408] S. K. Ghosh and P. Saha, “Crack and wear behavior of SiC particulate reinforced aluminium based metal matrix composite fabricated by direct metal laser sintering process,” *Mater. Des.*, vol. 32, no. 1, pp. 139–145, Jan. 2011, doi: 10.1016/j.matdes.2010.06.020.

[409] P. Farahmand and R. Kovacevic, “Corrosion and wear behavior of laser cladded Ni–WC coatings,” *Surf. Coat. Technol.*, vol. 276, pp. 121–135, Aug. 2015, doi: 10.1016/j.surfcoat.2015.06.039.

[410] R. Jendrzejewski, G. Śliwiński, M. Krawczuk, and W. Ostachowicz, “Temperature and stress fields induced during laser cladding,” *Comput. Struct.*, vol. 82, no. 7, pp. 653–658, Mar. 2004, doi: 10.1016/j.compstruc.2003.11.005.

[411] S. W. Huang, D. Nolan, and M. Brandt, “Pre-placed WC/Ni clad layers produced with a pulsed Nd:YAG laser via optical fibres,” *Surf. Coat. Technol.*, vol. 165, no. 1, pp. 26–34, Feb. 2003, doi: 10.1016/S0257-8972(02)00700-4.

[412] J. M. Guilemany, J. M. de Paco, J. R. Miguel, and J. Nutting, “Characterization of the W2C phase formed during the high velocity oxygen fuel spraying of a WC + 12 pct Co powder,” *Metall. Mater. Trans. A*, vol. 30, no. 8, pp. 1913–1921, Aug. 1999, doi: 10.1007/s11661-999-0002-3.

[413] C. Verdon, A. Karimi, and J.-L. Martin, “A study of high velocity oxy-fuel thermally sprayed tungsten carbide based coatings. Part 1: Microstructures,” *Mater. Sci. Eng. A*, vol. 246, no. 1–2, pp. 11–24, May 1998, doi: 10.1016/S0921-5093(97)00759-4.

[414] S. Ignat, P. Sallamand, A. Nichici, B. Vannes, D. Grevey, and E. Cicalã, “MoSi2 laser cladding—elaboration, characterisation and addition of non-stabilized ZrO2 powder particles,” *Intermetallics*, vol. 11, no. 9, pp. 931–938, Sep. 2003, doi: 10.1016/S0966-9795(03)00105-5.

[415] K. Van Acker, D. Vanhoyweghen, R. Persoons, and J. Vangrunderbeek, “Influence of tungsten carbide particle size and distribution on the wear resistance of laser clad WC/Ni coatings,” *Wear*, vol. 258, no. 1, pp. 194–202, Jan. 2005, doi: 10.1016/j.wear.2004.09.041.

[416] M. Pilloz, J. M. Pelletier, and A. B. Vannes, “Residual stresses induced by laser coatings: phenomenological analysis and predictions,” *J. Mater. Sci.*, vol. 27, no. 5, pp. 1240–1244, 1992, doi: 10.1007/BF01142030.

[417] F. Wang, H. Mao, D. Zhang, and X. Zhao, “The crack control during laser cladding by adding the stainless steel net in the coating,” *Appl. Surf. Sci.*, vol. 255, no. 21, pp. 8846–8854, Aug. 2009, doi: 10.1016/j.apsusc.2009.06.066.

[418] L.-N. Zhu, B.-S. Xu, H.-D. Wang, and C.-B. Wang, “Microstructure and nanoindentation measurement of residual stress in Fe-based coating by laser cladding,” *J. Mater. Sci.*, vol. 47, no. 5, pp. 2122–2126, Mar. 2012, doi: 10.1007/s10853-011-6012-8.

[419] L. Li and C. Gui, “Dissolving Behavior of Tungsten Carbide in Surface Welded Using Flux-Cored Wire,” *Procedia Eng.*, vol. 27, pp. 823–827, Jan. 2012, doi: 10.1016/j.proeng.2011.12.526.

[420] S. Ahn and S. Kang, “Dissolution phenomena in the Ti(C0.7N0.3)–WC–Ni system,” *Int. J. Refract. Met. Hard Mater.*, vol. 26, no. 4, pp. 340–345, Jul. 2008, doi: 10.1016/j.ijrmhm.2007.08.007.

[421] S.-Y. Ahn and S. Kang, “Formation of Core/Rim Structures in Ti(C,N)-WC-Ni Cermets via a Dissolution and Precipitation Process,” *J. Am. Ceram. Soc.*, vol. 83, no. 6, pp. 1489–1494, 2000, doi: 10.1111/j.1151-2916.2000.tb01415.x.

[422] M. Gao, Y. Pan, F. J. Oliveira, L. Yang, J. L. Baptista, and J. M. Vieira, “The formation of core–rim structures in Fe40Al/(TiC–TiN–WC) cermets produced by pressureless melt infiltration,” *Mater. Sci. Eng. A*, vol. 371, no. 1, pp. 277–282, Apr. 2004, doi: 10.1016/j.msea.2003.12.001.

[423] S. Lemboub *et al.*, “Core-rim structure formation in TiC-Ni based cermets fabricated by a combined thermal explosion/hot-pressing process,” *Int. J. Refract. Met. Hard Mater.*, vol. 70, pp. 84–92, Jan. 2018, doi: 10.1016/j.ijrmhm.2017.09.014.

[424] J. Pörnbacher, H. Leitner, P. Angerer, T. Wojcik, S. Marsoner, and G. Ressel, “TiC-(Ti,M)C core-rim structures in solid-state manufactured steel-based MMCs,” *Mater. Charact.*, vol. 156, p. 109880, Oct. 2019, doi: 10.1016/j.matchar.2019.109880.

[425] N. V. Litoshenko, “Mathematic modeling of diffusion processes of the formation of rim-core structure at sintering TiC–Ni alloys with alloying carbide additions,” *J. Superhard Mater.*, vol. 38, no. 1, pp. 18–24, Jan. 2016, doi: 10.3103/S1063457616010032.

[426] P. Li, J. Ye, Y. Liu, D. Yang, and H. Yu, “Study on the formation of core–rim structure in Ti(CN)-based cermets,” *Int. J. Refract. Met. Hard Mater.*, vol. 35, pp. 27–31, Nov. 2012, doi: 10.1016/j.ijrmhm.2012.03.012.

[427] D. Gu, J. Ma, H. Chen, K. Lin, and L. Xi, “Laser additive manufactured WC reinforced Fe-based composites with gradient reinforcement/matrix interface and enhanced performance,” *Compos. Struct.*, vol. 192, pp. 387–396, May 2018, doi: 10.1016/j.compstruct.2018.03.008.

[428] S.-Y. Guo, X.-J. Li, Q.-H. Yang, J.-L. Yang, and F.-Y. Meng, “Microstructure and tribological properties of laser clad WC-Ni/TiC composite coatings,” pp. 72–75, Jun. 2008.

[429] H.-J. Wang, J. Cai, and Z.-H. Han, “Study on erosion wear of WC-Co coatings prepared by supersonic plasma spray and HVOF spray,” pp. 50–54, Apr. 2005.

[430] H. Berns and S. D. Franco, “Effect of coarse hard particles on high-temperature sliding abrasion of new metal matrix composites,” *Wear*, vol. 203–204, pp. 608–614, Mar. 1997, doi: 10.1016/S0043-1648(96)07427-3.

[431] M. A. Taha, “Practicalization of cast metal matrix composites (MMCCs),” *Mater. Des.*, vol. 22, no. 6, pp. 431–441, Sep. 2001, doi: 10.1016/S0261-3069(00)00077-7.

[432] J. Hashim, L. Looney, and M. S. J. Hashmi, “Particle distribution in cast metal matrix composites—Part II,” *J. Mater. Process. Technol.*, vol. 123, no. 2, pp. 258–263, Apr. 2002, doi: 10.1016/S0924-0136(02)00099-7.

[433] D. R. Askeland and W. J. Wright, *Essentials of Materials Science & Engineering, SI Edition*, 3 edition. Stamford, CT: Cengage Learning, 2013.

[434] “Effects of CTCP Modification on Microstructure and Wear Behavior of CTCP-NiCrBSi/Heat Resistant Steel Composite Layer. - PubMed - NCBI.” https://www.ncbi.nlm.nih.gov/pubmed/30405011 (accessed Aug. 27, 2019).

[435] S. E. Mrabet, M. D. Abad, C. López-Cartes, D. Martínez-Martínez, and J. C. Sánchez-López, “Thermal Evolution of WC/C Nanostructured Coatings by Raman and In Situ XRD Analysis,” *Plasma Process. Polym.*, vol. 6, no. S1, pp. S444–S449, 2009, doi: 10.1002/ppap.200931004.

[436] F. Porrati *et al.*, “Artificial granularity in two-dimensional arrays of nanodots fabricated by focused-electron-beam-induced deposition,” *Nanotechnology*, vol. 21, no. 37, p. 375302, Aug. 2010, doi: 10.1088/0957-4484/21/37/375302.

[437] J. Gabrusenoks, A. Veispals, A. von Czarnowski, and K.-H. Meiwes-Broer, “Infrared and Raman spectroscopy of WO3 and CdWO4,” *Electrochimica Acta*, vol. 46, no. 13, pp. 2229–2231, Apr. 2001, doi: 10.1016/S0013-4686(01)00364-4.

[438] M. Boulova and G. Lucazeau, “Crystallite Nanosize Effect on the Structural Transitions of WO3 Studied by Raman Spectroscopy,” *J. Solid State Chem.*, vol. 167, no. 2, pp. 425–434, Sep. 2002, doi: 10.1006/jssc.2002.9649.

[439] C. Bittencourt, R. Landers, E. Llobet, X. Correig, and J. Calderer, “The role of oxygen partial pressure and annealing temperature on the formation of W=O bonds in thin WO3 films,” *Semicond. Sci. Technol.*, vol. 17, no. 6, pp. 522–525, 2002, doi: 10.1088/0268-1242/17/6/304.

[440] G. A. de Wijs and R. A. de Groot, “Amorphous WO3: a first-principles approach,” *Electrochimica Acta*, vol. 46, no. 13, pp. 1989–1993, Apr. 2001, doi: 10.1016/S0013-4686(01)00377-2.

[441] T. Pagnier, M. Boulova, A. Galerie, A. Gaskov, and G. Lucazeau, “In SituCoupled Raman and Impedance Measurements of the Reactivity of Nanocrystalline SnO2versus H2S,” *J. Solid State Chem.*, vol. 143, no. 1, pp. 86–94, Feb. 1999, doi: 10.1006/jssc.1998.8087.

[442] T. Pagnier, M. Boulova, A. Galerie, A. Gaskov, and G. Lucazeau, “Reactivity of SnO2–CuO nanocrystalline materials with H2S: a coupled electrical and Raman spectroscopic study,” *Sens. Actuators B Chem.*, vol. 71, no. 1, pp. 134–139, Nov. 2000, doi: 10.1016/S0925-4005(00)00598-0.

[443] L. Abello, B. Bochu, A. Gaskov, S. Koudryavtseva, G. Lucazeau, and M. Roumyantseva, “Structural Characterization of Nanocrystalline SnO2by X-Ray and Raman Spectroscopy,” *J. Solid State Chem.*, vol. 135, no. 1, pp. 78–85, Jan. 1998, doi: 10.1006/jssc.1997.7596.

[444] M. Boulova, A. Gaskov, and G. Lucazeau, “Tungsten oxide reactivity versus CH4, CO and NO2 molecules studied by Raman spectroscopy,” *Sens. Actuators B Chem.*, vol. 81, no. 1, pp. 99–106, Dec. 2001, doi: 10.1016/S0925-4005(01)00938-8.

[445] A. Baserga *et al.*, “Nanostructured tungsten oxide with controlled properties: Synthesis and Raman characterization,” *Thin Solid Films*, vol. 515, no. 16, pp. 6465–6469, Jun. 2007, doi: 10.1016/j.tsf.2006.11.067.

[446] A. Kuzmin, J. Purans, E. Cazzanelli, C. Vinegoni, and G. Mariotto, “X-ray diffraction, extended x-ray absorption fine structure and Raman spectroscopy studies of WO3 powders and (1-x)WO3-y·xReO2 mixtures,” *J. Appl. Phys.*, vol. 84, no. 10, pp. 5515–5524, 1998, doi: 10.1063/1.368596.

[447] D. Y. Lu, J. Chen, J. Zhou, S. Z. Deng, N. S. Xu, and J. B. Xu, “Raman spectroscopic study of oxidation and phase transition in W18O49 nanowires,” *J. Raman Spectrosc.*, vol. 38, no. 2, pp. 176–180, 2007, doi: 10.1002/jrs.1620.

[448] D. Y. Lu, J. Chen, S. Z. Deng, N. S. Xu, and W. H. Zhang, “The most powerful tool for the structural analysis of tungsten suboxide nanowires: Raman spectroscopy,” *J. Mater. Res.*, vol. 23, no. 2, pp. 402–408, Feb. 2008, doi: 10.1557/JMR.2008.0056.

[449] V. V. Popov, A. Katz-Demyanetz, A. Garkun, and M. Bamberger, “The effect of powder recycling on the mechanical properties and microstructure of electron beam melted Ti-6Al-4 V specimens,” *Addit. Manuf.*, vol. 22, pp. 834–843, Aug. 2018, doi: 10.1016/j.addma.2018.06.003.

[450] N. E. Gorji, R. O’Connor, A. Mussatto, M. Snelgrove, P. G. M. González, and D. Brabazon, “Recyclability of stainless steel (316 L) powder within the additive manufacturing process,” *Materialia*, vol. 8, p. 100489, Dec. 2019, doi: 10.1016/j.mtla.2019.100489.

[451] B. Melugiri-Shankaramurthy, Y. Sargam, X. Zhang, W. Sun, K. Wang, and H. Qin, “Evaluation of cement paste containing recycled stainless steel powder for sustainable additive manufacturing,” *Constr. Build. Mater.*, vol. 227, p. 116696, Dec. 2019, doi: 10.1016/j.conbuildmat.2019.116696.

[452] H. Asgari, C. Baxter, K. Hosseinkhani, and M. Mohammadi, “On microstructure and mechanical properties of additively manufactured AlSi10Mg_200C using recycled powder,” *Mater. Sci. Eng. A*, vol. 707, pp. 148–158, Nov. 2017, doi: 10.1016/j.msea.2017.09.041.

[453] B. Fullenwider, P. Kiani, J. M. Schoenung, and K. Ma, “Two-stage ball milling of recycled machining chips to create an alternative feedstock powder for metal additive manufacturing,” *Powder Technol.*, vol. 342, pp. 562–571, Jan. 2019, doi: 10.1016/j.powtec.2018.10.023.

[454] C. Fredriksson, “Sustainability of metal powder additive manufacturing,” *Procedia Manuf.*, vol. 33, pp. 139–144, Jan. 2019, doi: 10.1016/j.promfg.2019.04.018.

[455] J. T. Kurasha, “Production of cemented tungsten carbide alloys using zinc recycled tungsten carbide tool grade scrap,” University of the Witwatersrand, 2017.

[456] S. User, “Tungsten Carbide Powder (WC and W2C).” https://www.reade.com/products/tungsten-carbide-powder-wc-and-w2c (accessed Jun. 27, 2019).

[457] V. F. Steier, T. Doca, and J. A. Araújo, “Fretting wear investigation of 1350-H19 aluminum wires tested against treated surfaces,” *Wear*, vol. 414–415, pp. 1–8, Nov. 2018, doi: 10.1016/j.wear.2018.07.012.

[458] E. Huttunen-Saarivirta, V. Heino, A. Vaajoki, T. J. Hakala, and H. Ronkainen, “Wear of additively manufactured tool steel in contact with aluminium alloy,” *Wear*, vol. 432–433, p. 202934, Aug. 2019, doi: 10.1016/j.wear.2019.202934.

[459] N. Idusuyi and J. I. Olayinka, “Dry sliding wear characteristics of aluminium metal matrix composites: a brief overview,” *J. Mater. Res. Technol.*, vol. 8, no. 3, pp. 3338–3346, May 2019, doi: 10.1016/j.jmrt.2019.04.017.

Appendix A

Research Outputs

1) Journal Publication: B. Davoren, N. Sacks, and M. Theron, **"Laser engineered net shaping of WC-9.2wt%Ni alloys: A feasibility study,"** *Int. J. Refract. Met. Hard Mater.*, vol. 86, p. 105136, Jan. 2020
2) Journal Submission: Materials Characterisation: **"Microstructure characterisation of WC-9.2wt% Monel 400 fabricated using laser engineered net shaping." 2019**
3) Oral presentation at 18th Annual International RAPDASA Conference, Johannesburg, 2017.
4) Centre of Excellence in Strong Materials poster presentation, University of the Witwatersrand, 17 May 2017, 4th April 2018, 21st May 2019
5) School of Chemical and Metallurgical Engineering Research day, University of the Witwatersrand 28th September 2017 and 29th August 2019.
6) Oral presentation at International Congress on the Science of Hard Materials, Khao Lak, Thailand, 25th-29th March, 2019.